

# Design, Manufacture and Test of A Magnetic Encoder

Jun Gao

A THESIS SUBMITTED FOR THE DEGREE OF DOCTOR OF PHILOSOPHY IN  
ELECTRICAL ENGINEERING

HERIOT WATT UNIVERSITY  
SCHOOL OF ENGINEERING & PHYSICAL SCIENCES  
APRIL 2018

The copyright in this thesis is owned by the author. Any quotation from the thesis or use of any of the information contained in it must acknowledge this thesis as the source of the quotation or information.

## Abstract

An new eddy current based magnetic position encoder structure is proposed and studied in this thesis. The encoder is composed of one read head and one scale with metal plates placed periodically on a substrate. The read head contains one emitter and two receiver pairs which are all rectangular planar coils. The electromagnetic coupling between the emitter and receivers were affected by the relative position of the scale. A system level analytical model of the proposed encoder structure has been derived, from which three different encoder signals forms were generated.

An amplification and synchronous demodulation circuit has been designed and fabricated. The circuit board was used successfully to process the encoder output signals in the measurement.

Four PCB encoder prototypes were fabricated. These encoder structures were studied using the ANSYS Maxwell™ software package. The simulated and measured results were compared. The best accuracy performance of the PCB encoder is  $-15\text{ }\mu\text{m}$  to  $15\text{ }\mu\text{m}$  from the simulation results and  $-35\text{ }\mu\text{m}$  to  $25\text{ }\mu\text{m}$  from the corresponding measurement.

An alternative manufacturing process of the magnetic encoder based on multilayer Low Temperature Co-fired Ceramic (LTCC) technology has also been presented. The fabrication process of the LTCC encoder and equipment used were described. Two different methods were used to characterise the LTCC encoder with good agreement between all approaches attempted. The best accuracy performance of the LTCC encoder was  $-30\text{ }\mu\text{m}$  to  $25\text{ }\mu\text{m}$  and after lookup table correction the improved accuracy ranged from  $-10\text{ }\mu\text{m}$  to  $10\text{ }\mu\text{m}$ .

## ACADEMIC REGISTRY

### Research Thesis Submission

Name:	JUN GAO		
School:	EPS		
Version: <i>(i.e. First, Resubmission, Final)</i>	Final	Degree Sought:	PhD in Electrical Engineering

### Declaration

In accordance with the appropriate regulations I hereby submit my thesis and I declare that:

- 1) the thesis embodies the results of my own work and has been composed by myself
- 2) where appropriate, I have made acknowledgement of the work of others and have made reference to work carried out in collaboration with other persons
- 3) the thesis is the correct version of the thesis for submission and is the same version as any electronic versions submitted\*.
- 4) my thesis for the award referred to, deposited in the Heriot-Watt University Library, should be made available for loan or photocopying and be available via the Institutional Repository, subject to such conditions as the Librarian may require
- 5) I understand that as a student of the University I am required to abide by the Regulations of the University and to conform to its discipline.
- 6) I confirm that the thesis has been verified against plagiarism via an approved plagiarism detection application e.g. Turnitin.

\* Please note that it is the responsibility of the candidate to ensure that the correct version of the thesis is submitted.

Signature of Candidate:		Date:	
-------------------------	--	-------	--

### Submission

Submitted By <i>(name in capitals)</i> :	
Signature of Individual Submitting:	
Date Submitted:	

### For Completion in the Student Service Centre (SSC)

Received in the SSC by <i>(name in capitals)</i> :			
Chapter 1 Method of Submission <i>(Handed in to SSC; posted through internal/external mail):</i>			
Chapter 2 -thesis Submitted <i>(mandatory for final theses)</i>			
Signature:		Date:	

## Acknowledgements

First and foremost, I would like express my deepest gratitude to my supervisor Professor Marc Desmulliez for his support, encouragement and guidance during my study and research period at Heriot-Watt University. I do very much appreciate his kind advice and help when I encounter problems in the research.

I would like to thank Nick Weston and Iain Gordon-Ingram in Renishaw for their kind help and advice on the project. I would also like to thank Fergus Robertson, Graeme Cunningham and Eric Morgan in Renishaw for their kind help on the measurement. Their help and advice are valuable.

I would like to thank Dr. David Waston, who was also involved in the project and worked with me on design and fabrication. His knowledge and help are priceless.

I would also like to thank my colleagues and friends Dr. Ross Aitken, Dr. Maria Lorente, Dr. Wenxing Tang, Dr. Jia Ni, Zhou Zhou, Julia Faerber, Dr. Shiong Qian, Dr. Rongrong Qian.

Most importantly, I would like to thank my family for their unconditional love, support and encouragement.



# Table of contents

<b>Abstract</b> .....	<b>i</b>
<b>Acknowledgements</b> .....	<b>iii</b>
<b>Academic Publications</b> .....	<b>viii</b>
<b>Glossary of terms</b> .....	<b>ix</b>
<b>Chapter 1 Introduction</b> .....	<b>1</b>
1.1 Introduction to encoders.....	1
1.2 Incremental encoder literature review .....	3
1.2.1 Resistive encoders.....	3
1.2.2 Capacitive encoder .....	5
1.2.3 Magnetic encoders.....	9
1.2.4 Optical encoders.....	12
1.3 Motivation and thesis layout .....	14
References.....	18
<b>Chapter 2 Encoder Specification</b> .....	<b>21</b>
2.1 Introduction.....	21
2.2 Encoder specifications.....	21
2.2.1 Measurement range .....	21
2.2.2 Repeatability .....	21
2.2.3 Accuracy (Encoder output nonlinearity).....	22
2.2.4 Resolution.....	23
2.2.5 Hysteresis .....	23
2.2.6 Drift.....	23
2.2.7 Response time.....	24
2.3 Incremental encoder displacement calculation .....	24
2.3.1 Digital output interpolation .....	24

2.3.2	Analytical modelling of eddy current based magnetic encoder	26
2.3.3	Lissajous curve	27
2.3.4	DC offset	30
2.3.5	Amplitude imbalance	32
2.3.6	Phase error	33
2.3.7	Harmonic distortion	35
2.4	Summary	37
	Reference	39
<b>Chapter 3 Analytical modelling of eddy current based magnetic encoder</b>		<b>42</b>
3.1	Introduction	42
3.2	Eddy currents and eddy currents sensors	42
3.3	Eddy currents based magnetic encoder review	43
3.4	Proposed Structure and working principle	46
3.4.1	Structure and working principle	46
3.5	Modeling of the proposed eddy currents based magnetic encoder	48
3.5.1	Eddy currents in scale	49
3.5.2	Encoder structure simplification	50
3.5.3	Mutual inductance between rectangular planar coils	51
3.5.4	Coupling between coil plates	62
3.6	System output	69
3.6.1	System output	69
3.6.2	Possible reason for the encoder output nonlinearity error	73
3.7	Summary	74
	Reference	76
<b>Chapter 4 Demodulation circuit and PCB encoder prototypes</b>		<b>80</b>
4.1	Introduction	80
4.2	Signal processing circuit	80

4.2.1	Amplification circuit .....	81
4.2.2	Demodulation circuit.....	82
4.3	Prototypes of encoders using PCB technology.....	83
4.3.1	Prototype One.....	84
4.3.2	Prototype Two.....	100
4.3.3	Prototype Three.....	107
4.3.4	Prototype Four .....	113
4.4	Discussion .....	121
4.4.1	Vertical gap .....	122
4.4.2	Rotation around the X-axis.....	123
4.4.3	Rotation around Y-axis.....	124
4.4.4	Rotation around the Z-axis.....	126
4.4.5	Coil Track width.....	127
4.4.6	Scale plate width.....	128
4.5	Conclusions .....	129
<b>Chapter 5</b>	<b>Multi-layer LTCC based encoders.....</b>	<b>131</b>
5.1	Introduction.....	131
5.2	Multi-layer LTCC encoder structure.....	132
5.3	LTCC encoder fabrication.....	133
5.3.1	Definition of LTCC technology .....	134
5.3.2	Fabrication process.....	135
5.3.3	Measurement of the dimensions of the fabricated LTCC encoder ....	142
5.3.4	Impedance measurement.....	144
5.4	PCB board of the amplification and demodulation circuits.....	146
5.5	Characterisation of the LTCC encoder .....	149
5.5.1	Measurement setup .....	149
5.5.2	Measurement results using the Renishaw interpolator.....	151

5.5.3	Measurement results using the oscilloscope.....	152
5.5.4	Comparison of the resulting errors with the two methods.....	155
5.5.5	Correction to the encoder output nonlinearity (accuracy).....	156
5.6	Conclusions .....	160
	Reference .....	161
<b>Chapter 6</b>	<b>Conclusions and future work .....</b>	<b>164</b>
6.1	Conclusions .....	164
6.2	Future work .....	166
<b>Appendix A</b>	<b>Mathematica script for data processing.....</b>	<b>167</b>
<b>Appendix B</b>	<b>Datasheets of ICs used in the project .....</b>	<b>174</b>

## Academic Publications

J. Gao, D. E. Watson, and M. P. Y. Desmulliez, "Simulation of an eddy current based inductive position sensor," in *2015 1st URSI Atlantic Radio Science Conference (URSI AT-RASC)*, 2015, pp. 1–1.

G. Cummins, J. Gao, D. E. Watson, M. P. Y. Desmulliez, R. McPhillips, and S. Cochran, "Optimization and characterisation of bonding of piezoelectric transducers using anisotropic conductive adhesive," in *2017 IEEE International Ultrasonics Symposium (IUS)*, 2017, pp. 1–4.

R. McPhillips, S. Cochran, S. Vinnicombe, D. Watson, J. Gao, M. P. Y. Desmulliez, "The fabrication and integration of a 15 MHz array within a biopsy needle," in *2017 IEEE International Ultrasonics Symposium (IUS)*, 2017, pp. 1–4.

## Glossary of terms

**Encoder** : A position sensor that can provide feedback information of position, speed and direction of movement

**Encoder accuracy** : Specifies how accurate of the encoder measurement is, which is the difference between the measured and actual value.

**Encoder resolution**: Specifies how fine the encoder can measure

**Eddy currents** : occurring in any conductive materials that are subjected to a time-varying magnetic field as a result of Faraday's law of induction

**Lissajous curve** : Also known as Bowditch curve or Lissajous figure, it describes complex harmonic motion. It is often used to get qualitative view of the signal integrity.

**Synchronous demodulation** : A method to demodulate amplitude modulation (AM) signal, it can recover small signal in the presence of noise situation.

**LTCC** : Low Temperature Co-Fired Ceramic, a multilayer ceramic packaging technology.

# Chapter 1 - Introduction

## 1.1 Introduction to encoders

The measurement of angle and distance is a basic requirement in all instruments, machines and installations in which position has to be monitored or adjusted [1]. Most of these measurements are achieved using position encoders which are common devices providing displacement or rotation information of moving objects.

A position encoder is mainly composed of a read head and a scale. In the past, many machines use simple analogue measuring systems, which usually consisted of a scale and a mark or index which moved relative to it. The scale can be in the form of a ruler or disc; the displacement or the rotary readout is indicated by the mark or index on the scale. As it is only a matter of the relative movement between the scale and the mark, the scale can be fixed and the index movable or vice-versa [1].

Most of the analogue mechanical systems were later replaced by digital mechanical counters, which increase the reliability and accuracy of the measurements. However, because of the mechanics involved, mechanical contact was required which resulted often in mechanical wear out, rendering these measurement methods less reliable and limited to medium and low speed applications.

Nowadays, non-contact displacement measurement methods are dominant. In most of these encoders the mark or index is replaced by different electrical and optical sensors, which can provide much higher accuracy and reliability of the movement information.

Encoders can be divided as absolute encoders and incremental encoders, the main difference of which is related to the configuration of the scale. The scale configuration of absolute and incremental rotary encoder is shown in Figure 1.1.

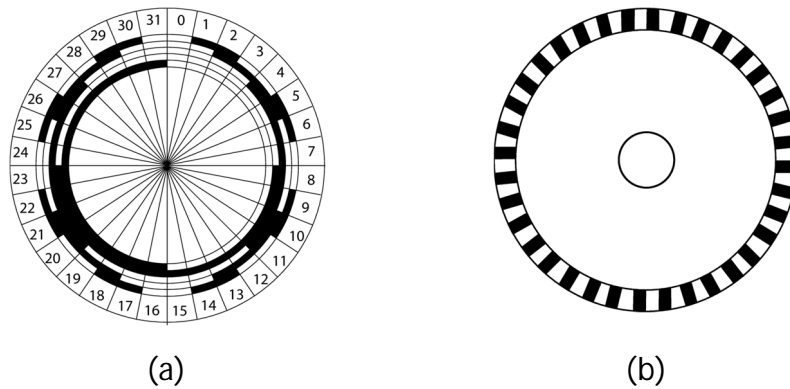


**Figure 1.1 Scale for absolute (left) and incremental (right) encoders**

For the absolute encoder, all pieces of information regarding position are coded on the scale, as shown in Figure 1.1(a). There is usually a start position marked as zero with every other position marked differently on the scale. Absolute encoders are therefore capable of providing a unique position value from the moment that they are switched on. They are also capable of accounting for the movement in the situation of power down, such that correct measurements are generated after power on. Absolute encoders are more suitable for situations where absolute position information is important, such as movement monitoring, robotic arms and computer controlled machines [2].

The scale for incremental encoders, shown in Figure 1.1(b), is simpler than the absolute encoder one. Positions on such a scale are periodically coded and no absolute zero position is defined. The output is usually composed of two quadrature signals ( $90^\circ$  out of phase) from which the relative position is calculated and no two positions on the scale are identical. In order to detect the moving direction, the two receivers are placed with a quarter period length offset which generates two quadrature outputs. The displacement is calculated from the phase using the two signals while the moving direction is determined by the lead signal. Details of calculation method will be discussed in Chapter 2.

Incremental encoders have the advantage to provide higher resolution using a relative simple configuration. Incremental encoders require however a reference mark for determining the absolute positions. Loss position data may occur during power failure or power down.



An incremental encoder is studied in this PhD thesis. As incremental encoders are implemented differently based on the physical sensing principle used such as resistive encoders, capacitive encoders, magnetic encoders and optical encoder, a literature review on these encoders is done here for different working physical principles.

## 1.2 Incremental encoder literature review

### 1.2.1 Resistive encoders

Resistive encoders are very popular, relatively inexpensive, and are also the most easily understood type of position transducer [3]. The structure of a resistive encoder usually consists of a mechanical shaft (scale) contacted with a wiper (read head) that can be angular or linear in its movement. The basic working principle can be understood as a potentiometer. A DC voltage is applied across the resistive element on the shaft and the voltage on the wiper is in proportion to its positions, as the resistance is in ratio to the length of the resistive element according to Ohm's law. The equivalent circuit diagram of potentiometer is shown in Figure 1.2 below,

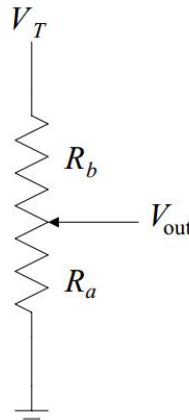


Figure 1.2 Equivalent circuit diagram of potentiometer

As the relative position of the wiper changes the output voltage changes accordingly in ratio and the voltage can be calculated as,

$$V_{out} = \frac{V_T R_a}{R_a + R_b} \quad (1.1)$$

Based on this working principle, different resistive encoder structures have been implemented and can be divided as linear and rotary depending on the

configuration of the shaft (scale). Actually, the earliest linear encoder was brush type [4] as shown in Figure 1.3. The scale contains conducting and insulating segments on its surface; the conducting segments are all connected to a common terminal, a source of excitation voltage is connected between the common contact and the associated signal processing circuit. When the brush is in contact with a conducting segment, a contact closure occurs and an output voltage is seen. When the brush is in contact with an insulating segment, an open contact results and no output is seen [5].

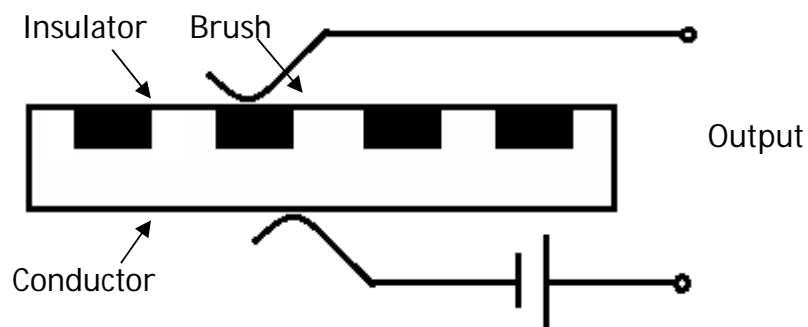


**Figure 1.3 Linear brush-type encoder**

One example of rotary resistive encoder [6] is shown in Figure 1.4. The encoder consists of a ring of resistive material and two electrically independent wipers that are in contact with and move above the ring. A DC voltage is applied across opposite sides of the resistive ring and as the two wipers are mechanically connected to each other at 90 degrees. Two quadrature signals are generated when the wipers move. The signals can be further processed using a microcontroller and the corresponding position and moving direction can be calculated.

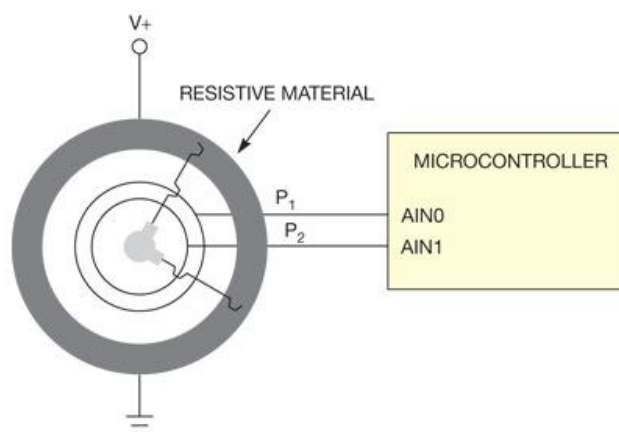


**Figure 1.4 Configuration of a rotary resistive encoder**

Due to the relative low cost, simple wiring and easy understanding of the working principle, the resistive encoder is quite popular. As it requires rubbing contact of two parts, there is a long-term wear out problem preventing its usage in high-reliability and high-speed applications. Other drawbacks of resistive encoder include noise and backlash due to the rubbing contact.

### 1.2.2 Capacitive encoder

Capacitive position encoders are quite popular in the industrial world because they provide a relatively simple technique to implement non-contact measurement [7].

A typical capacitive encoder comprises a variable capacitance sensing element which include the read head and scale, electronics for signal conditioning, and suitable mechanical components for mounting them. The main part of capacitive encoder is the variable capacitor, usually formed by two parallel conductive plates separated by a dielectric material. The capacitance can be calculated by,

$$C = \epsilon_0 \epsilon_r \frac{A}{d} \quad (1.2)$$

Here  $\epsilon_0$  is the vacuum permittivity and  $\epsilon_r$  is the relative permittivity of the dielectric material,  $A$  is the effective area of the plates and  $d$  is the distance between the plates. The capacitive sensing can be based on any change of these parameters. For vertical motion, the capacitance is dependent on the distance  $d$  between the two plates and the impedance is linear with the distance. For transverse motion the capacitance is a linear function of the displacement [8].

The basic working principle is that the electronic circuit drives the capacitive sensing element with an AC current. The two plates of the capacitive sensing element are attached to the two parts in movement working as read and scale respectively. The relative movement of one plate with respect to the other changes the capacitance and therefore the output of the system resulting in a modulated output. The signal is detected and converted to the corresponding displacement by signal processing circuitry. As capacitive encoders require extra driving and conditioning electronic circuits, they are more complex than the resistive encoders.

The displacement or the position is measured from the change of the capacitance due to the relative movement. Similar to resistive encoder, the capacitive encoder can be divided as linear and rotary encoder based on the configuration of the scale. One example of linear capacitive encoder is proposed by Fumitaka [9], as shown in Figure 1.5. In this configuration, the encoder is made of flexible printed circuit films and mainly consists of a long receiver working as a stator and a short transmitter working as a slider. The stator is composed of two induction electrodes on two sides and four-phase receiving electrodes. The slider is composed of two induction electrodes and a two-phase transmitting electrodes.

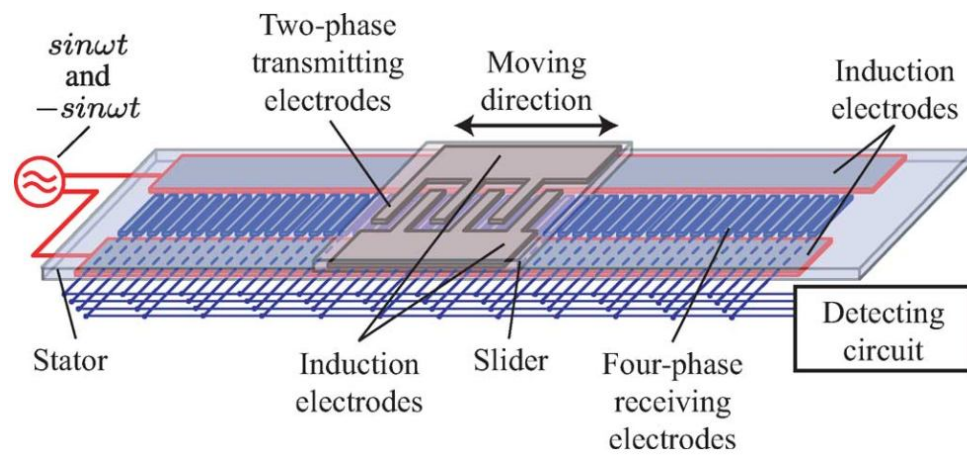


**Figure 1.5 Schematic diagram of capacitive encoder [9]**

The simplified model and corresponding electronic interface is shown in Figure 1.6. Here the labels 7 and 8 correspond to the induction electrodes on the stator, on which two AC voltage with 180° phase difference are applied. The labels 5 and 6 are induction electrodes and two-phase transmitting electrodes of the slider, on which the voltages are induced due to electrostatic effect. The labels 1 to 4 correspond to the four-phase receiving electrodes, the induced voltages on which change at different relative positions of the slider. Labels 1 and 3 working as one receiver; the same with labels 2 and 4. The movement of the slider affects the capacitance of the system thus result in two amplitude modulated outputs from the two receiver pairs. These two signals are further amplified and demodulated, with specified signal processing circuit, to generate the corresponding displacement output. The final

measurement of the prototype device resulted in a  $0.8\ \mu\text{m}$  resolution with  $\pm 4\ \mu\text{m}$  error for an  $800\ \mu\text{m}$  period length.

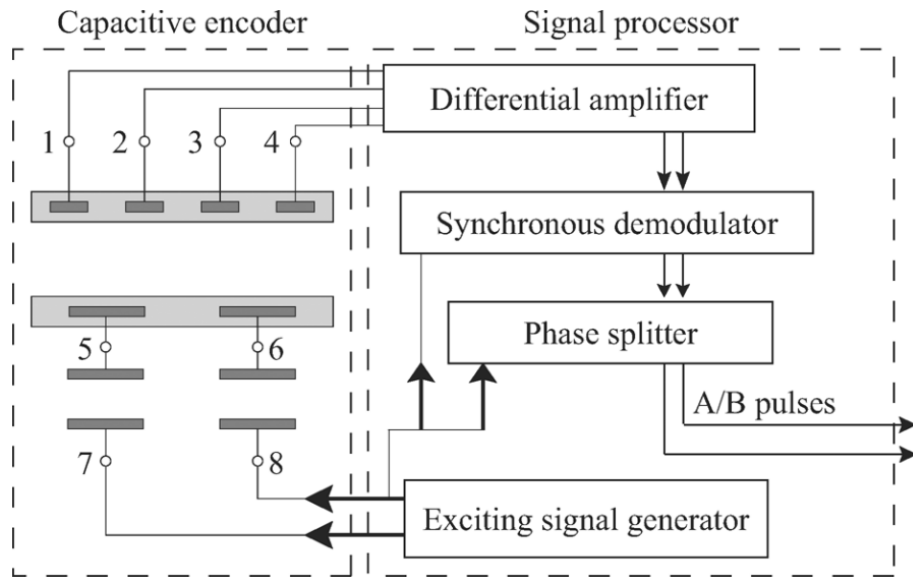


**Figure 1.6 Modelling and corresponding electronics of capacitive encoder**

Bo developed a rotary capacitive encoder, shown in Figure 1.7, and consists of a stator and a rotor, that measures both angular position and angular speed [10]. The stator is composed of excitation electrodes, collection electrodes and guard electrodes, while the rotor has coupling electrodes, sensitive electrodes and guard electrodes. The guard electrodes on both stator and rotor are used for reducing the influence of external interference. An AC voltage is applied on the excitation electrodes, and the voltage is induced on the coupling electrodes and sensitive electrodes, which are electrically connected. The sensitive electrodes on the stator works as pickup elements and the voltage on them changes as the relative position changes.

The schematic view of this encoder is shown in Figure 1.8, here we can also see the corresponding electrically equivalent circuit model. The sensitive electrodes are in sine wave shapes in polar coordinates and divide the circle into six segments. The corresponding collection electrode of each segment is divided into eight parts and two of which are connected composing four groups, as indicated in Figure 1.8(b). The groups A and F, B and E, C and H, D and G are interconnected to form four electrodes sets.

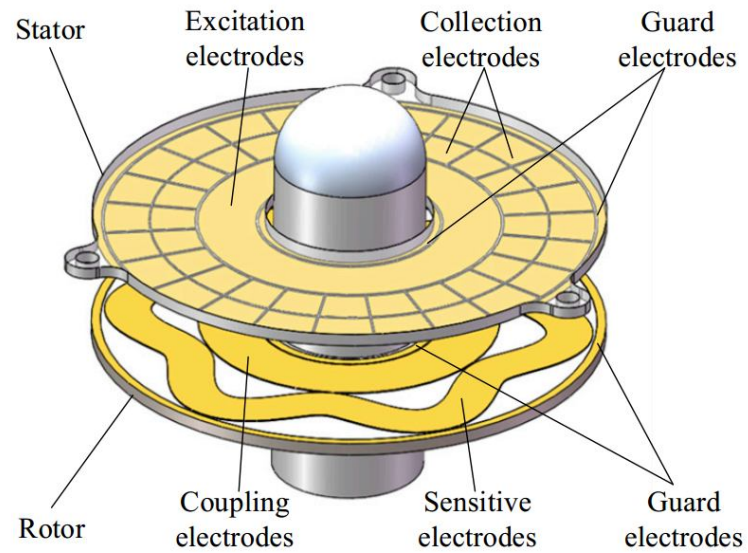
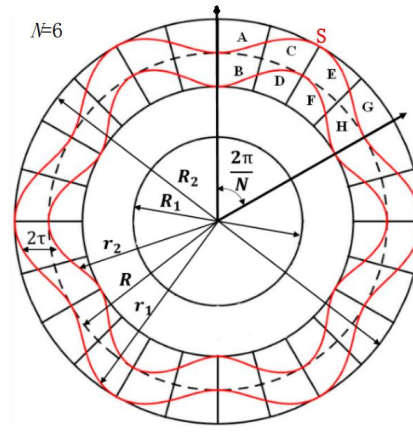
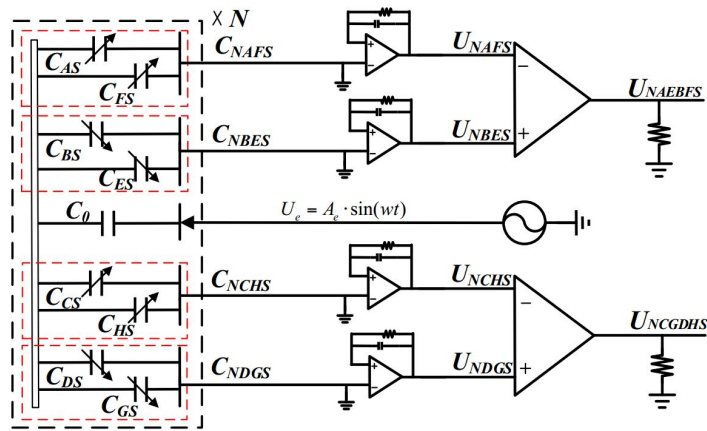


**Figure 1.7 Structure model of capacitive angular encoder**

Two of these groups are connected to a differential amplifier resulting in two pair outputs. These outputs are further processed using specific signal processing electronics. The final output is the average value obtained from these six segments which make this encoder less sensitive to mechanical non-idealities.



(a)



(b)

**Figure 1.8 Schematic view of the capacitive angular position sensor and corresponding equivalent circuit model**

Capacitive encoders provide better resolution and accuracy comparing with resistive and some magnetic encoders. They are also low cost and more robust than optical encoders when working in harsh environment. The permittivity of the dielectric material of the electrodes is affected however by the surrounding environments such as water and oil and electrodes require specific electric shielding which restrict their usage.

### 1.2.3 Magnetic encoders

Magnetic encoders are quite robust for harsh environment, compared with optical and capacitive encoders. They are immune to dust, oil or water and, as such, do not

require special shielding. Based on the material of the scale, the magnetic encoders can be divided into two groups.

In the first group, the scale is usually a magnetic strip with periodically placed permanent magnets whole width records the position information. Such encoders also have one or more magnetic sensor as the read head, which is usually a Hall effect sensor [11,12], a magnetoresistive sensor or a magnetostrictive sensor, with the Hall effect and magnetoresistive sensors being the more common [4]. The basic structure of an incremental magnetoresistive encoder is shown below in Figure 1.9.

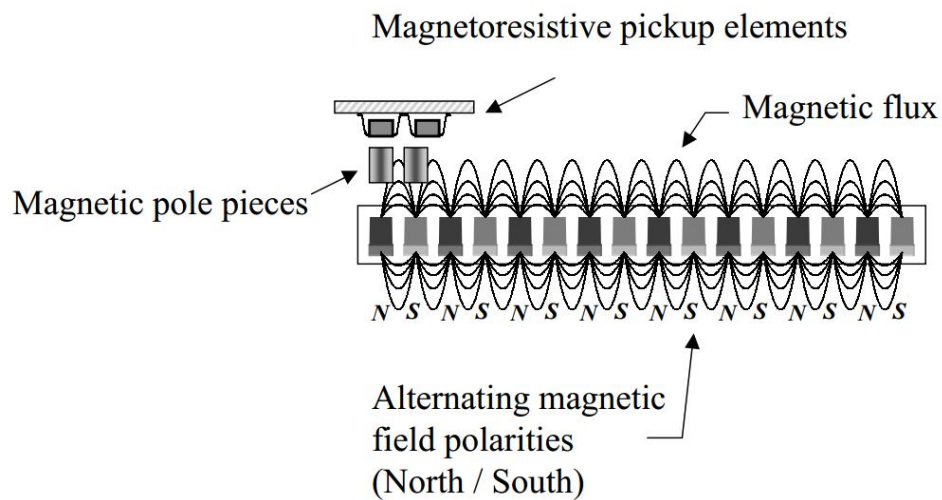


**Figure 1.9 Incremental magnetic encoder [4]**

The scale is a magnetic tape having periodical reversals of polarization along its length and these magnetic field variations are detected by the magnetoresistive pickup sensors above the scale. For incremental encoders, there are usually two pickup sensors with certain displacement to yield a 90° phase shift between the two outputs, resulting in a quadrature output which can be further interpolated to displacement.

The read head can be replaced by other magnetic sensors such as a Hall effect sensor or a magnetostrictive sensor. For this kind of magnetic encoders, the pickup elements can be any magnetic sensor mentioned above, but commonly used sensors are Hall effect and magnetoresistive sensors. They have relative simple signal processing circuit. As the scale is made of magnets, it is quite easy to attract ferromagnetic particles, which will affect the distribution of the magnetic field. It is also not suitable for high temperature environments which will demagnetise the



scale. The read head is also sensitive to any magnetic field so the encoders might be affected by surrounding magnetic fields.

To increase the robustness, the second group of encoders has scales made of conductive or ferromagnetic materials [13-17]. The read head is made of coils (inductors). One example is described in patent [18] with the structure shown in Figure 1.10. The scale is made of conductive material placed periodically along the scale, and the sensor head is composed of planar coils, where one emitter coil is labelled as  $V_r$  and two receiver coil pairs are labelled as  $V_{os}$  and  $V_{oc}$ ,

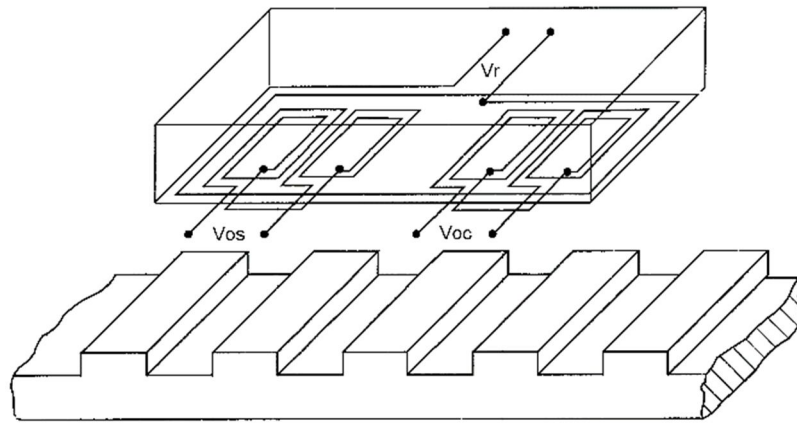


**Figure 1.10 Eddy currents based magnetic encoder**

The working principle is similar to that of a LVDT (Linear Variable Differential Transformer) where the emitter coil together with two receiver coil pairs form two differential transformers. An AC current is applied on the emitter coil  $V_r$  and generates an alternating magnetic field, which, in turn, induces eddy currents in the scale. The position of the scale will affect the coupling between emitter and receiver pairs and an amplitude modulated signal is generated in the receiver pair. With two secondary pairs placed together with a quarter period length offset, two quadrature signals are generated and further interpolated to displacement. Due to this principle, this encoder is insensitive to particles, dust, liquids and so on.

Different encoder structures based on this principle were proposed by many researchers, and will be discussed in Chapter 3. As the sensing part of this kind of encoder is in the form of differential transformer, they are less sensitive to the ambient magnetic field or temperature change. This thesis will explore specific configurations of this type of magnetic encoders.

#### 1.2.4 Optical encoders

An optical encoder uses optoelectronic devices as a transmitter and receiver pair [4], which convert mechanical displacement to an optical signal. Most of the optical encoders are implemented based on the Moiré pattern, as shown in Figure 1.11, which is generated by superimposing two optical gratings of similar pitch offset by a certain displacement or angle [19]. When one grating moves relative to the other along the lateral direction an oscillating signal is generated, which is detected by the corresponding photo-detector [20]. Compared with the other encoders mentioned above, optical encoders can provide higher resolution while maintaining a simple electronic interface.

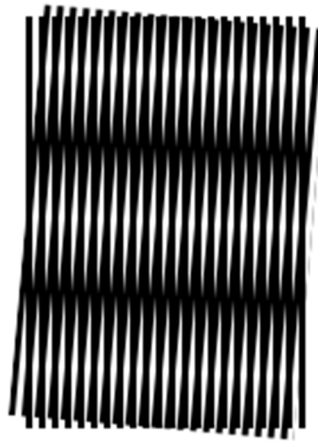


**Figure 1.11 Example of a Moiré pattern**

Based on the different configurations, the encoders can be divided as transmission type [21, 22] and reflection type [23-25]. The implementation is shown in Figure 1.12 for most optical encoders. A light emitted from the light source passes through (transmission method) or reflects off (reflection method) a periodic or specially patterned graduation, commonly known as a scale grating, and onto a series of photo-detectors that generate electric currents corresponding to variations in light intensity as the scale moves.

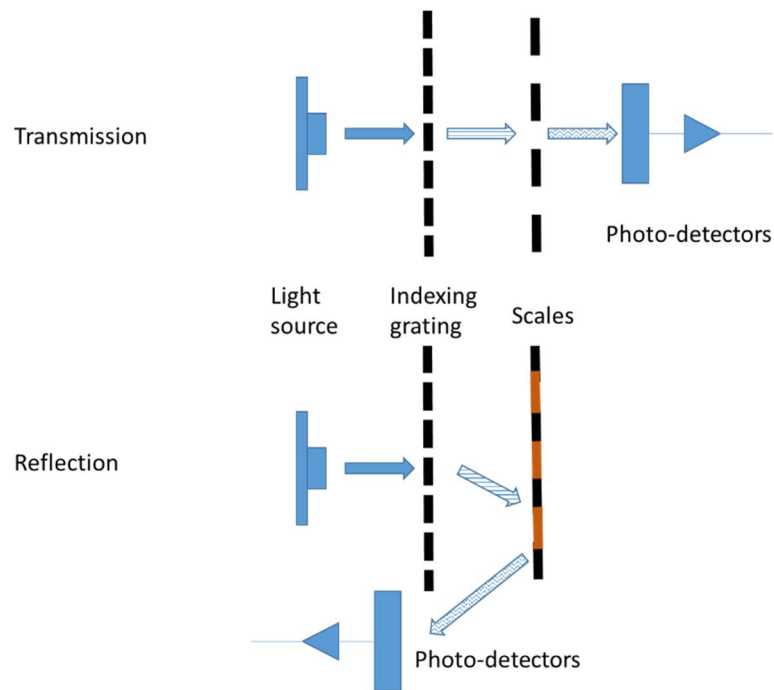


**Figure 1.12 Optical encoder working schematic: Transmission mode, top, where light passes straight from the source to the detector and below, reflection mode, where light reflects from the scale onto the detector.**

Usually the light source, indexing grating and photo-detectors compose the read head that also include analyser grating and some additional electronics. Depending on the geometry of the scale, they can be divided as linear and rotary encoders. As for the incremental encoders, there are usually two or more photo-detectors to determine the moving directions.

A comparison of the advantages and disadvantages of all the encoders discussed above is summarised in Table 1.1 below:

**Table 1.1 Different principle encoder comparison**

Encoder types	Advantage	Disadvantage
Resistive	low cost, simple wiring and easy understanding	Wear out and mechanical backlash
Capacitive	Better resolution and accuracy Low cost	Not robust, require specific electric shielding
Magnetic sensor hall effect magnetoresistive or magnetostrictive	Better resolution and accuracy	Not suitable for high temperature environments, affected by surrounding magnetic fields
Magnetic inductive	Better resolution and accuracy Robust to dust, water or oil	Require extra demodulation and amplification circuit
Optical	High resolution and accuracy	Expensive, not immune to dust, water or oil.

### 1.3 Motivation and thesis layout

Different sensing physical principles and corresponding encoder implementations and configurations were discussed in Section 1.2 of this chapter. From this discussion, we can see that the optical encoders are capable of providing the highest resolution but it is easily contaminated by water, oil and dust in some industry environment, while the eddy currents based encoder has better tolerance for high temperature and harsh industrial environments.

In this thesis, we study incremental magnetic position encoders. The aim of this thesis is to design, manufacture and test an eddy current-based magnetic encoder, which has the benefits of low cost and high robustness and immune to harsh industry environment.

To carry out this research work, the detailed layout of the thesis is as follows:

**Chapter 1**, this chapter, provides an overview of encoders and layout the motivation and plan of the thesis document. A brief introduction about the different kinds of encoders is introduced. Absolute and incremental encoders are discussed and compared. Different physical principles and implementations of the encoders are also discussed and compared. The advantage of eddy currents based magnetic encoder is highlighted comparing with other kind of encoders.

**Chapter 2** describes the specifications of the magnetic encoders with emphasis on the two main specifications, which are resolution and accuracy, together with other important characteristics and specifications of incremental encoders. As described in Chapter 1, the output of incremental encoder is usually composed of two quadrature signals. A representation of these signals, the Lissajous curve, is used to study the quality of the encoder output signals and sensitivity to operational and manufacturing parameters. The method used to convert the two signals to displacement is discussed and possible reasons for nonlinearity effects are discussed.

**Chapter 3** provide a more specific literature review on eddy currents based magnetic encoders. Different magnetic encoder mechanical structures and implementations are discussed in this chapter. An analytical modelling procedure was carried out to model such kind of encoders. An analytical model that calculates the coupling between rectangular planer coils with varying physical displacement in different direction is derived and calculated using Mathematica™ software. The results are verified using Finite Element Modelling (FEM) simulation software ANSYS Maxwell™ and physical measurement. The influence of the rectangular metal plate on the coupling between rectangular planer coils is also simulated and the results agreed well with measurement results.

**Chapter 4** presents an implementation of the proposed magnetic encoder using single layer PCB and presents the corresponding measurement results and improvement. Different encoder structures are studied in this chapter. The initial prototype is presented and studied following by different improved structures. All these different structures are fabricated using a standard PCB manufacturing

process and their properties and performances are measured and compared with simulation results. Influence of misalignment and rotation of the scale on the performance of the encoder is study in this chapter.

**Chapter 5** provides an alternative manufacturing process of the magnetic encoder based on multilayer Low Temperature Co-fired Ceramic (LTCC) technology. The LTCC encoder fabrication process is presented with detailed description on each fabrication step. The measurement results of the final device are described in this chapter.

**Chapter 6** is the final chapter for the thesis. It summarises all the analytical modelling, FEM simulation and measurements results achieved in the project and provides conclusions and guideline for future design improvement. Possible future work and challenges are also discussed in this chapter.

A graphic layout of the thesis structure is presented below in Figure 1.13:

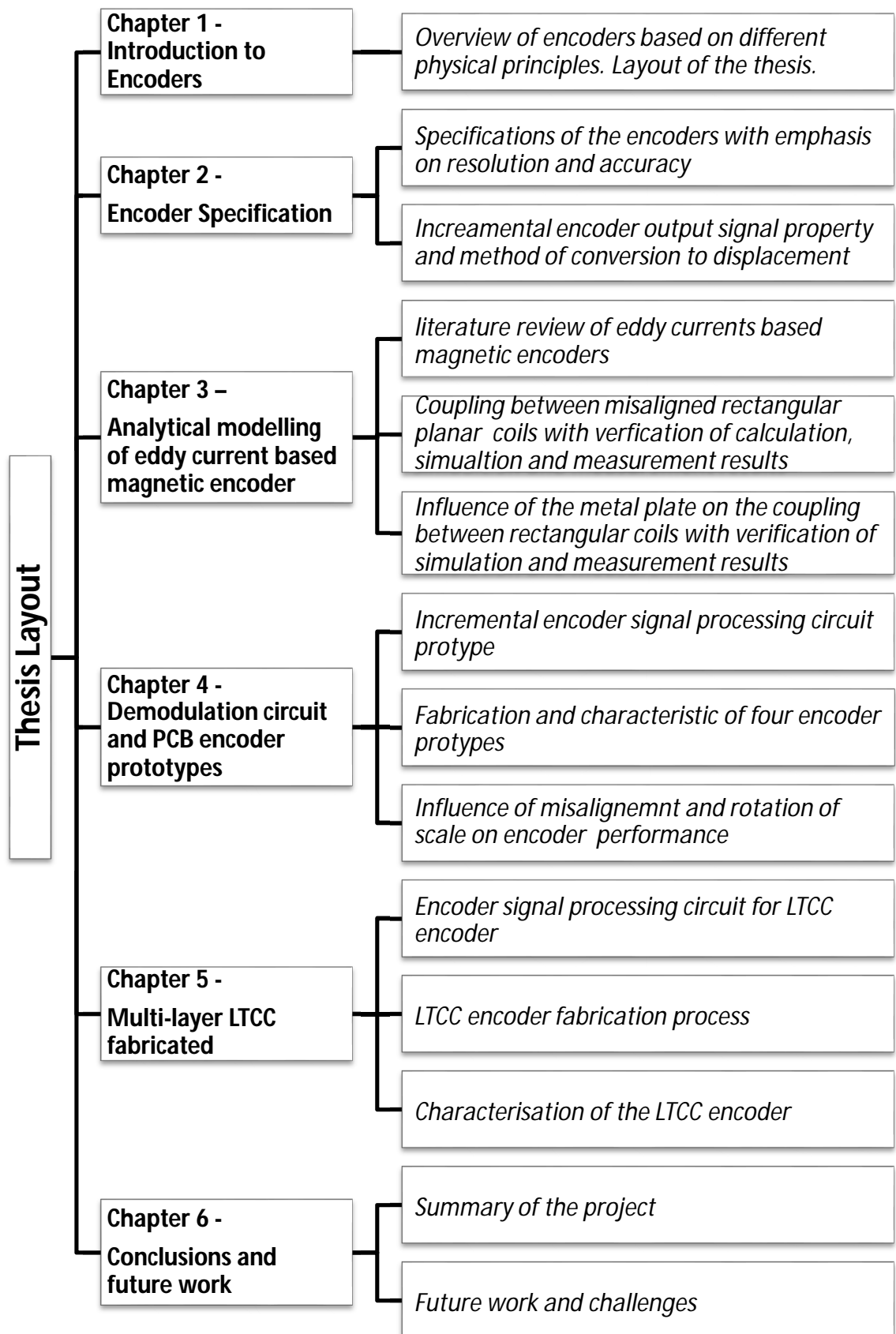


Figure 1.13 Thesis layout

## References

- [1] H. Walcher, "1 - Introduction," in Position Sensing, ed: Butterworth-Heinemann, pp. 1-4, 1994.
- [2] K. Engelhardt and P. Seitz, "Absolute, high-resolution optical position encoder," Applied Optics, vol. 35, pp. 201-208, 1996/01/01, 1996.
- [3] D. S. Nyce, "Resistive Sensing," in Linear Position Sensors, ed: John Wiley & Sons, Inc., pp. 47-61, 2004.
- [4] D. S. Nyce, "Encoders," in Linear Position Sensors, ed: John Wiley & Sons, Inc., pp. 151-161, 2004.
- [5] H. N. Norton, Handbook of transducers. Englewood Cliffs (New Jersey): Prentice-Hall, 1989.
- [6] M. Korntheuer. (2013, 5 May). Rotary encoder with absolute readout offers high resolution and low cost Available: <http://www.edn.com/design/components-and-packaging/4405828/Rotary-encoder-with-absolute-readout-offers-high-resolution-and-low-cost>
- [7] D. S. Nyce, "Capacitive Sensing," in Linear Position Sensors, ed: John Wiley & Sons, Inc., pp. 62-77, 2004.
- [8] L. K. Baxter, Capacitive Sensors: Design and Applications: Wiley-IEEE Press, 1996.
- [9] F. Kimura, M. Gondo, N. Yamashita, A. Yamamoto, and T. Higuchi, "Capacitive-Type Flexible Linear Encoder With Untethered Slider Using Electrostatic Induction," IEEE Sensors Journal, vol. 10, pp. 972-978, 2010.
- [10] B. Hou, B. Zhou, M. Song, Z. Lin, and R. Zhang, "A Novel Single-Excitation Capacitive Angular Position Sensor Design," Sensors (Basel), vol. 16, 2016.
- [11] J. Hu, J. Zou, F. Xu, Y. Li, and Y. Fu, "An Improved PMSM Rotor Position Sensor Based on Linear Hall Sensors," IEEE Trans. Magn., vol. 48, no. 11, pp. 3591–3594, Nov. 2012.
- [12] F. Caricchi, F. G. Capponi, F. Crescimbeni, and L. Solero, "Sinusoidal brushless drive with low-cost linear Hall effect position sensors," in 2001 IEEE 32nd Annual Power Electronics Specialists Conference (IEEE Cat. No.01CH37230), vol. 2, pp. 799–804.



- [13] W. W. Liu, H. Zhao, W. Tao, and C. F. Lv, "Research on combinatorial-code grating eddy-current absolute-position sensor," *Ieee Transactions on Instrumentation and Measurement*, vol. 61, pp. 1113-1124, Apr 2012.
- [14] W. W. Liu, H. Zhao, and H. L. Qi, "Research on Novel Grating Eddy-Current Absolute-Position Sensor," *Ieee Transactions on Instrumentation and Measurement*, vol. 58, pp. 3678-3683, Oct 2009.
- [15] M. Kamon, A.-M. Nguyen, and J. R. Gilbert, "A Design Tool for Inductive Position and Speed Sensors via a Fast Integral Equation Based Method," in *Technical Proceedings of the 1999 International Conference on Modeling and Simulation of Microsystems*, 1999, pp. 313 - 317.
- [16] M. Podhraski and J. Trontelj, "A Differential Monolithically Integrated Inductive Linear Displacement Measurement Microsystem," *Sensors (Basel)*, vol. 16, Mar 17 2016.
- [17] M. Podhraski and J. Trontelj, "An Integrated Microtransformer System for Displacement Measurement," *Informacije Midem-Journal of Microelectronics Electronic Components and Materials*, vol. 46, pp. 29-35, Mar 2016.
- [18] V. Vasiloiu and H. Eisschiel, "Inductive measuring device for detecting lengths and angles," *US Patent 20120223724*, issued September 6, 2012.
- [19] M. G. L. Gustafsson, "Surpassing the lateral resolution limit by a factor of two using structured illumination microscopy," *Journal of Microscopy*, vol. 198, pp. 82-87, 2000.
- [20] H. Miyajima, E. Yamamoto, and K. Yanagisawa, "Optical micro encoder with sub-micron resolution using a VCSEL," *Sensors and Actuators A: Physical*, vol. 71, pp. 213-218, 1998/12/01, 1998.
- [21] J. Rozman and A. Pletersek, "Linear Optical Encoder System With Sinusoidal Signal Distortion Below 60 dB," *IEEE Transactions on Instrumentation and Measurement*, vol. 59, pp. 1544-1549, 2010.
- [22] S. Merino, A. Retolaza, and I. Lizuain, "Linear optical encoders manufactured by imprint lithography," *Microelectronic Engineering*, vol. 83, pp. 897-901, 2006.
- [23] C.-F. Kao and M.-H. Lu, "Optical encoder based on the fractional Talbot effect," *Optics Communications*, vol. 250, pp. 16-23, 6/1/, 2005.

- [24] Y. Guoyong, L. Hongzhong, S. Yongsheng, Y. Lei, L. Bingheng, H. Xiangyuan, et al., "Optimizing design of an optical encoder based on generalized grating imaging," *Measurement Science and Technology*, vol. 27, p. 115005, 2016.
- [25] K. Hane, T. Endo, Y. Ito, and M. Sasaki, "A compact optical encoder with micromachined photodetector," *Journal of Optics A: Pure and Applied Optics*, vol. 3, p. 191, 2001.

## **Chapter 2 - Encoder Specification**

### **2.1 Introduction**

Incremental encoders whose sensing mechanisms are based on different physical principles were discussed in Chapter 1. The majority of them generate however two quadrature digital or analogue signals. In this chapter, the specifications that are important to describe the performance capability of encoders are explained. These include measurement range, repeatability, accuracy (nonlinearity), resolution, hysteresis and response time [1]. Detailed explanations of these specifications are first provided with special emphasis on resolution and accuracy. The process of converting these two signals to position information is then discussed. The influence of the various signal parameters on the performance of the encoders are also discussed.

### **2.2 Encoder specifications**

#### **2.2.1 Measurement range**

Measurement range defines the longest distance range that an encoder can measure. The measurement range can be specified from zero to full scale. It can also be specified as  $\pm$  full scale with zero located on the centre of the scale [1]. For example, most of the LVDT (Linear Variable Differential Transformer) sensors specify bipolar ranges[2-4].

#### **2.2.2 Repeatability**

Repeatability is specified as the readout deviation of the encoder that can be expected in consecutive measurements under the same conditions for the same

position or displacement. It is usually measured at fixed environmental conditions such as constant humidity and temperature [1].

Repeatability can be the most important characteristic of the encoder if the receiving equipment is able to compensate for nonlinearity, temperature effects, calibration error, and other errors [1], as the repeatability cannot be compensated. In many control systems, repeatability is more important than accuracy and resolution because the system are often programmed to provide the desired output in response to a given input from the encoder, as long as the signal received from the encoder is always the same for a given set of conditions.

### 2.2.3 Accuracy (Encoder output nonlinearity)

For an ideal encoder, the measured displacement should be a linear function of the real displacement. Due to non-linear effects affecting the real encoder output, there is a difference between the measured displacement and the real displacement. Encoder output nonlinearity, also commonly known as inaccuracy, refers to how accurate the encoder measurement is. It is the difference between the measured displacement and the ideal displacement, as shown Figure 2.1.

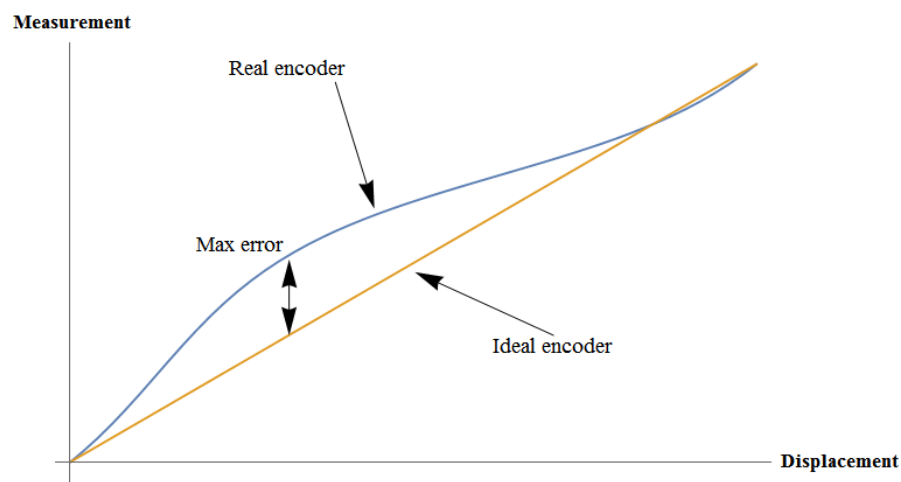


Figure 2.1 Comparison of ideal and real encoder displacement measurement

The maximum amount of difference between real displacement and the ideal encoder displacement measurements is defined as the maximum error.

There are usually two ways to reduce the nonlinearity: one method is to optimize the design of the encoder to reduce the nonlinearity error in the measurement

output [5]; the other method is to calibrate the error using software algorithms implemented in the signal processing electronics placed after the sensor. Software algorithms for error compensation are widely studied by researchers [6-17]; more details will be discussed later in this chapter.

#### **2.2.4 Resolution**

Resolution is the smallest valid readout measurement of the encoder. It defines the smallest displacement that the encoder can measure. It is usually determined together by the scale width, which determines the raw measurement displacement in one period and the signal processing circuitry [1], which determines the interpolation factor. The resolution is usually the ratio between the width of the scale and the interpolation factor. It is one of the most important parameters of the encoder when used in precision machining.

#### **2.2.5 Hysteresis**

Hysteresis is defined as the variation of encoder readings between upscale and downscale approaches to the same original position. More specifically, when an encoder is steadily indicating an increasing output, crossing through a specific position of the scale, then reverses direction, and steadily indicates a decreasing reading, again passing through the same specific position, there usually will be a slight difference in the reading recorded [1]. Hysteresis can be caused by mechanical backlash or magnetic remanence in the sensing element of the encoder.

#### **2.2.6 Drift**

Drift encompasses the changes in encoder output that occur over time even though there are no changes to the environmental conditions or in the relative position between read head and scale [1]. The only variable when measuring drift is the elapsed time. For the encoder, this means that there is no position and measurement conditions change. The read head is normally locked into a stationary position when testing to determine the amount of encoder drift. The test is run at constant temperature, constant humidity, constant power supply voltage, constant load

impedance, and so on, while the encoder output is recorded. The drift error could be caused by interference, condition change or electronic noise in the signal processing circuitry.

### 2.2.7 Response time

Response time is the amount of time elapsed between the application of a change in the relative position between encoder read head and scale at the encoder input, and the resulting indication of that change in the output. It is an important parameter in control systems when immediate feedback is required.

## 2.3 Incremental encoder displacement calculation

As discussed in Chapter 1, two quadrature signals are generated by incremental encoders. The signals can be either digital or analogue, as shown in Figure 2.2, depending on the configuration of the encoder.

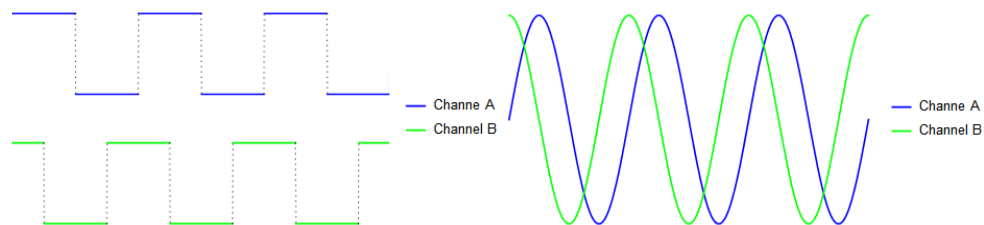


**Figure 2.2 Digital and analogue output of incremental encoder: left is the digital output signal of an encoder, right is the analogue output signal of an encoder**

These signals are further processed and interpolated by the electronic circuits to get the information of the movement, such as displacement, speed and moving directions.

### 2.3.1 Digital output interpolation

As shown in Figure 2.2, the digital output of the encoder consists of two quadrature square waveforms with alternative 1 and 0 indicating changes of position. The

frequency of the signal is proportional to the relative moving speed between the read head and the scale. The lead-lag phase relationship between the signals yields the moving direction of read head [18]. If the phase of channel A signal is leading channel B, then the read head is moving forward. If phase of channel A signal is behind channel B then the read head is moving in the opposite direction.

The two quadrature signals can be decoded to yield the relative displacement between read head and scale. Different decoding circuits can provide three different resolutions [18], as shown in Figure 2.3.

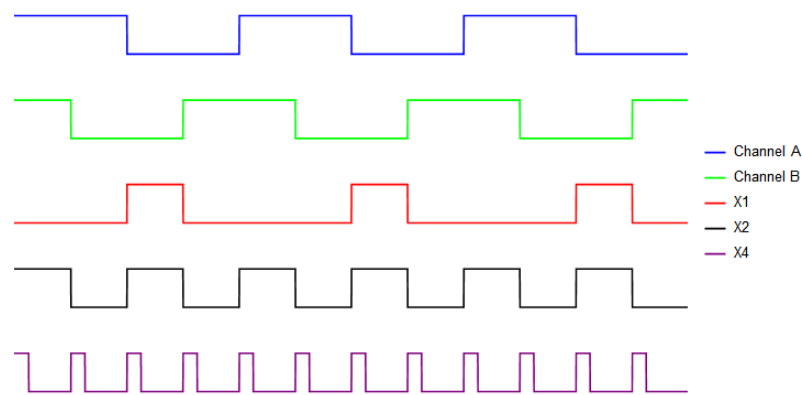


**Figure 2.3 Encoder digital output interpolator: X1 resolution in red square wave; X2 resolution in black square wave; X4 resolution in purple square wave.**

The output signal X1 provides one pulse at every negative edge of channel A or channel B signals. The negative edge of channel A signal is used here in Figure 2.3 to get the X1 output signal. The resolution is thus one pitch of the scale. The X2 resolution provides a pulse at every negative and positive edges of channel A or B signals. In Figure 2.3 the negative and positive edges of channel A signal are used. This results in twice the number of pulses of X1 output signal and the resolution is half pitch of the scale. The output signal X4 provides a pulse at every positive and negative edges of channel A and channel B signal. Figure 2.3 shows an example where negative and positive edge of channel A and channel B signals are used. This results in four times the number of output pulses and the corresponding resolution is a quarter of scale pitch. By counting the number of pulses in the signal, the moving displacement can be calculated. When channel A signal is leading channel B signal, the count is increased at each pulse while when channel B signal is leading channel

A signal, the count is decreased at each pulse. The actual displacement can be determined from the total count number multiplied by the resolution of the encoder.

### 2.3.2 Analogue output interpolation

The implementation of the digital output of encoder is relatively easy compared with the analogue output solution. Such encoders are however gradually replaced by their analogue output counterparts because the analogue encoders can offer much higher position and speed resolution. As shown in Figure 2.2 the analogue output from the encoders usually are two quadrature sine and cosine signals. The signals from the encoder are conditioned and processed using electronic circuitry and digital signal processing platform. The conversion of the signals to displacement have been studied extensively by many researchers [19-22]. One signal processing diagram is shown in Figure 2.4 [22]. The encoder output signals are amplified and filtered and then converted to digital signals using Analogue-to-Digital Conversion (ADC) circuits and further processed using digital signal processing algorithm implemented on a Digital Signal Processing (DSP) platform. The details of the calculations and possible nonlinearity errors are described in the following section.

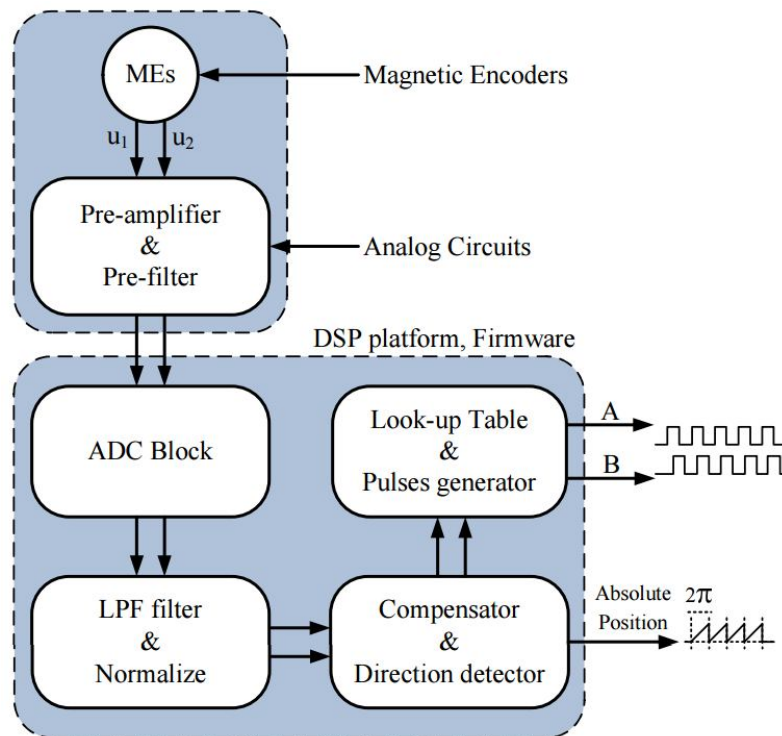


Figure 2.4 Encoder signal processing and conversion diagram [22]



### 2.3.3 Lissajous curve

As described above, the accuracy (output nonlinearity) is a very important specification for encoders. For the analogue output version encoder, the Lissajous curve is used to get a qualitative view of the signal integrity. It is commonly used by analogue electronic engineers to analyse the frequency ratio or phase difference of two signals [22-24]. To get a Lissajous curve, two analogue signals are plotted against each other with one signal on X axis while the other signal on Y axis, as shown in Figure 2.5 two quadrature sinusoidal signals are plotted against each other resulting in a circular Lissajous curve.

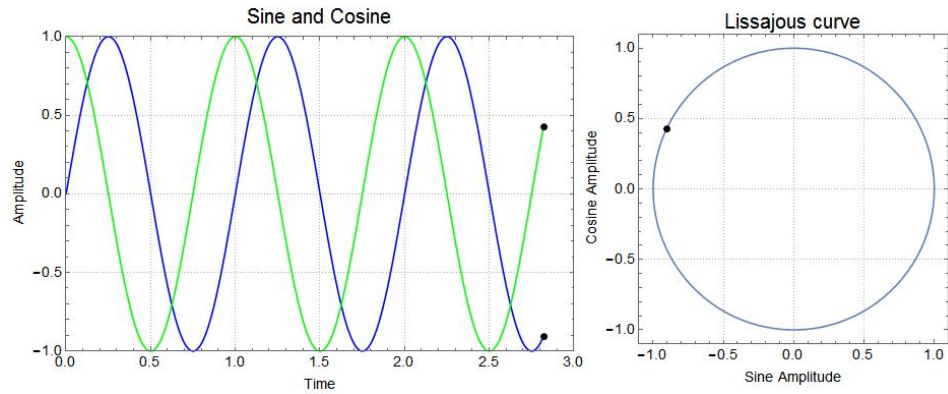


Figure 2.5 Quadrature sinusoidal signals (left) and resulting Lissajous curve (right)

At any moment, the phase of the point on a Lissajous curve represents the displacement while the rotation direction of the point on Lissajous curve determines the moving direction of the encoder. If channel A is leading channel B in phase, the encoder is moving in one direction, correspondingly the point on the Lissajous curve rotates in a clockwise direction, and vice-versa. The relative displacement is linear to the phase of the Lissajous curve. Assuming that the resulting signals have maximum unit voltage amplitude, the two quadrature sinusoidal signals can be written as:

$$\begin{aligned} V_a &= \sin(\theta) \\ V_b &= \cos(\theta) \end{aligned} \quad (2.1)$$

Here  $V_a$  is the channel A signal while  $V_b$  is the channel B signal. The displacement measured by the encoder is linear to the phase which can be calculated as the arctangent value of the two signals:

$$\theta = \arctan \frac{V_a}{V_b} \quad (2.2)$$

The corresponding calculated phase is plotted against displacement as shown in Figure 2.6. If the two signals are ideal, i.e. are perfect quadrature sinusoids, the phase displacement curve should be periodical straight lines with phase ranges from  $-\pi$  to  $\pi$ . The period of the phase displacement lines is related to the physical pitch period on the scale. In Figure 2.6 for example the pitch width is 0.5 unit and there is 0.5 unit gap between the pitches, so pitch period is 1 unit, the encoder phase output changes from  $\pi$  to  $-\pi$  as the measured displacement changes by 1 unit.

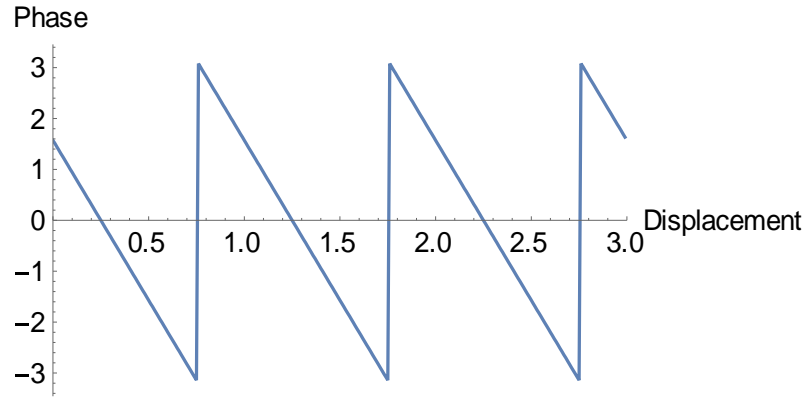


Figure 2.6 Calculated phase against displacement

In real situations, due to noise in the signal and imperfections of the encoder during manufacturing, the signal differs from a perfect quadrature sinusoid resulting in nonlinearity errors. There are mainly four types of nonlinearity errors [25-27]:

1. Amplitude imbalance errors,
2. DC offset errors,
3. Phase shift errors, and
4. Higher harmonic distortion errors.

The influence of each error is discussed here.

Let assume that these errors only happen in channel A. The signals can be written as:

$$V_a^{error} = U_1 + A_1 * \sin(\theta + S_1) + \sum_{n=2}^{\infty} A_n \sin(n * \theta) \quad (2.3)$$

$$V_b = \cos(\theta)$$

Here  $V_a^{error}$  is the real signal of channel A,  $U_1$  is the DC offset in the signal,  $A_n$  is the amplitude error of the signal which in an ideal situation should be 1, and  $S_1$  is the phase shift difference of the signal which in ideal situation should be 0,  $\sum_{n=2}^{\infty} \sin(n * \theta)$  are the harmonic terms in the signal. The various Lissajous curves obtained with errors taken separately are provided in Figure 2.7.

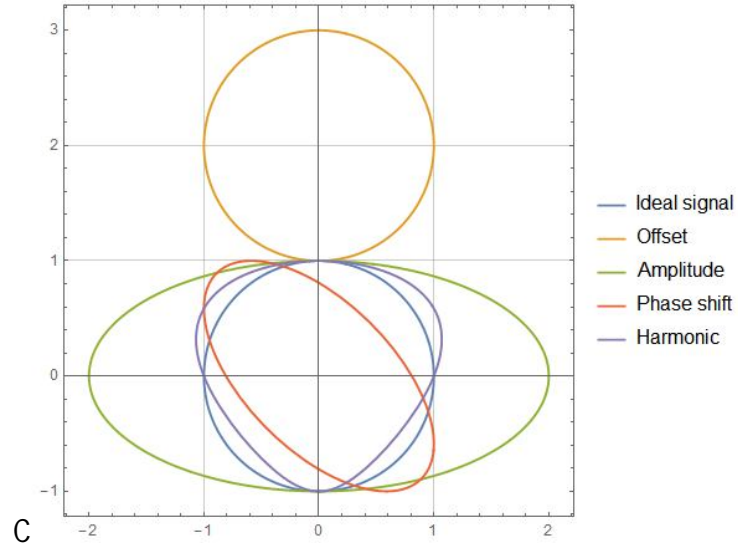


**Figure 2.7 Lissajous curve comparison for different errors**

The DC offset,  $U_1$ , in the signal moves the position of the circle, upwards in this case, as  $U_1$  is positive. The amplitude error  $A_1$  changes the shape of circle to a horizontal ellipse. The phase shift,  $S_1$ , generates a rotated ellipse and the harmonics change the shape of the Lissajous curve to a curve that is neither a circle nor an ellipse.

The Lissajous cannot generally give direct quantitative information of the accuracy (nonlinearity error). A more accurate way to determine the error is to calculate the phase and compare it with ideal encoder output. The real encoder output phase difference can be calculated using:

$$\Delta\theta = \arctan \frac{V_a^{error}}{V_b} - \theta \quad (2.4)$$

The calculation of the errors is discussed below in details.

### 2.3.4 DC offset

Assuming there is only DC offset error in the channel A signal, the corresponding signals can be represented as:

$$\begin{aligned} V_{ao} &= U_1 + \sin(\theta) \\ V_{bo} &= \cos(\theta) \end{aligned} \quad (2.5)$$

The resulting signal compared with the perfect signal is plotted in Figure 2.8.  $V_{ao}$  is the real output signal in channel A, the letter o in subscript stands for DC offset error and  $V_{bo}$  is the real output signal in channel B;  $U_1$  is the amount of DC offset taken here as 10% of the original unit.

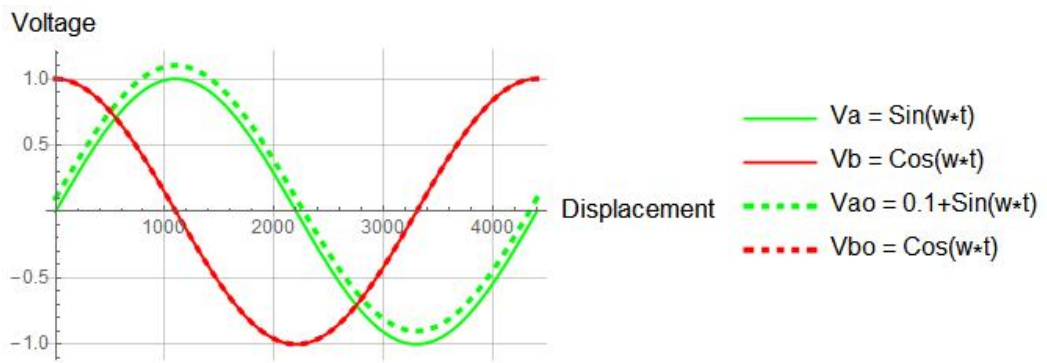


Figure 2.8 Comparison of ideal signal and signal with DC offset

The corresponding Lissajous curve is shown in Figure 2.9, where the offset will affect the central position of the Lissajous curve, with a shift, in this case, along the horizontal axis.

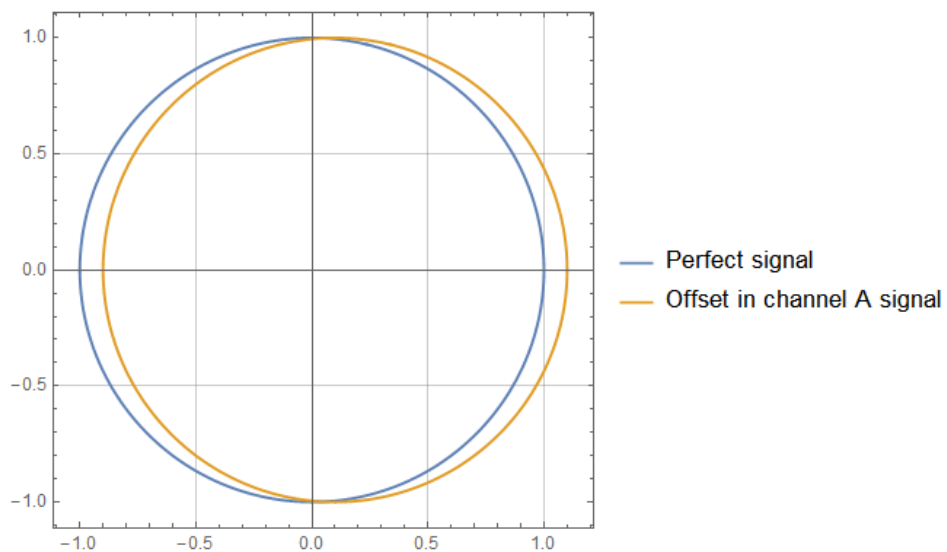


Figure 2.9 Lissajous curve of ideal signal and offset signal

The corresponding phase can be calculated using the arctangent function

$$\theta_o = \arctan \frac{V_{ao}}{V_{bo}} \quad (2.6)$$

The calculated phases of perfect signal and real signal are plotted together in Figure 2.10. The phase is linear with displacement for the perfect signal, while the phase of the real signal is not linear with displacement.

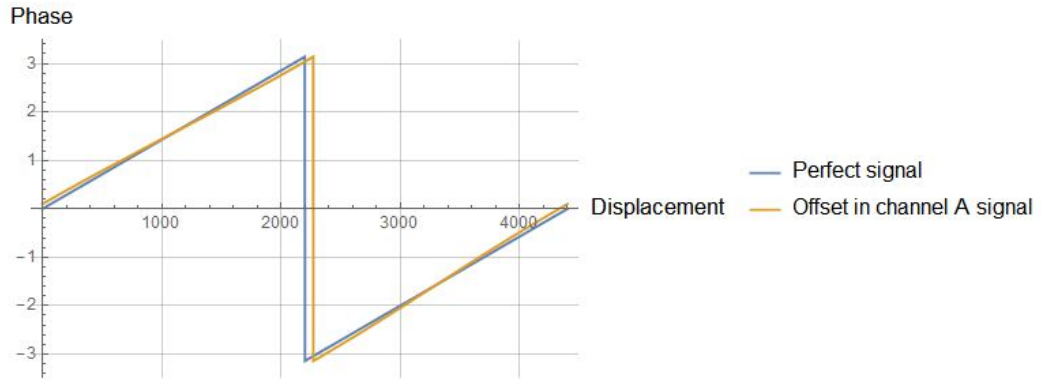


Figure 2.10 Phase of perfect signal and error signal against displacement

To further compare the nonlinearity of the real encoder signal, the difference of the phase between ideal signal and real signal is calculated using Equation 2.4 and plotted in Figure 2.11.

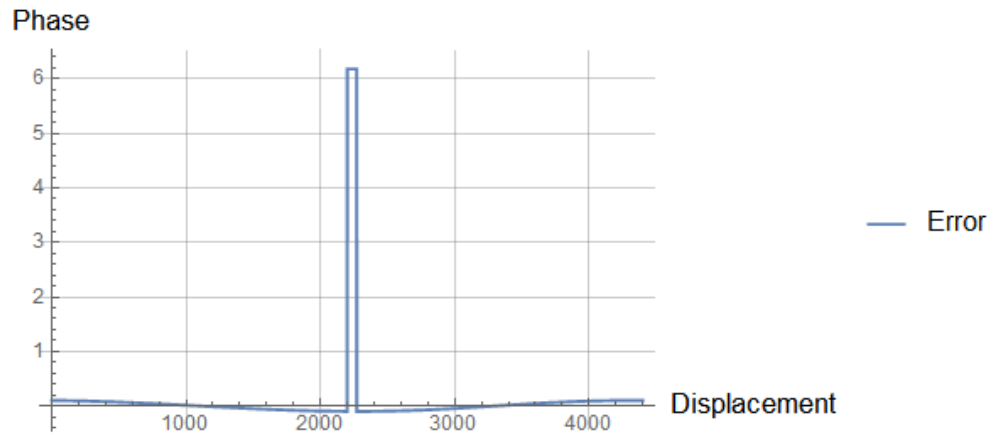


Figure 2.11 Error against displacement

From Figure 2.10, the offset in the encoder quadrature signals will cause nonlinearity in the calculated phase displacement line and offset the maximum position to the left, resulting in  $2 * \pi$  error in the calculated displacement, as shown in Figure 2.11.

### 2.3.5 Amplitude imbalance

Assuming that the error in amplitude occurs only in channel A, the corresponding real signals can be represented as:

$$\begin{aligned} V_{aa} &= A_1 * \sin(\theta) \\ V_{ba} &= \cos(\theta) \end{aligned} \quad (2.7)$$

Here  $V_{aa}$  and  $V_{ba}$  are the real signals from encoder with amplitude imbalance, the first letter a in the subscript stands for signal of channel 'a' of the encoder while the second letter a in the subscript stands for the amplitude imbalance.  $A_1$  is the amplitude of the channel A signal and equal to 110% of the original signal of unit amplitude. The corresponding signals are plotted in Figure 2.12.

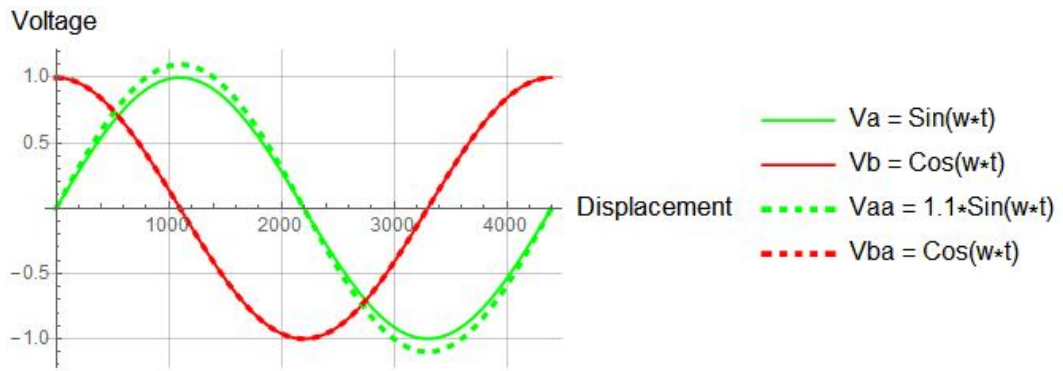


Figure 2.12 Comparison of ideal signal and real signal with amplitude imbalance

The corresponding Lissajous curve is shown in Figure 2.13. The amplitude imbalance stretches the Lissajous curve along the horizontal axis and renders the circle an ellipse.

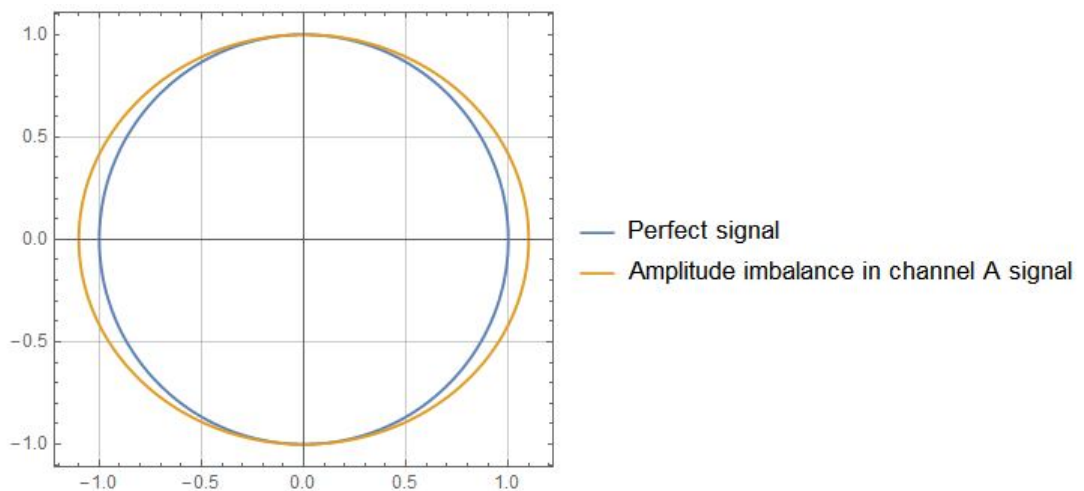
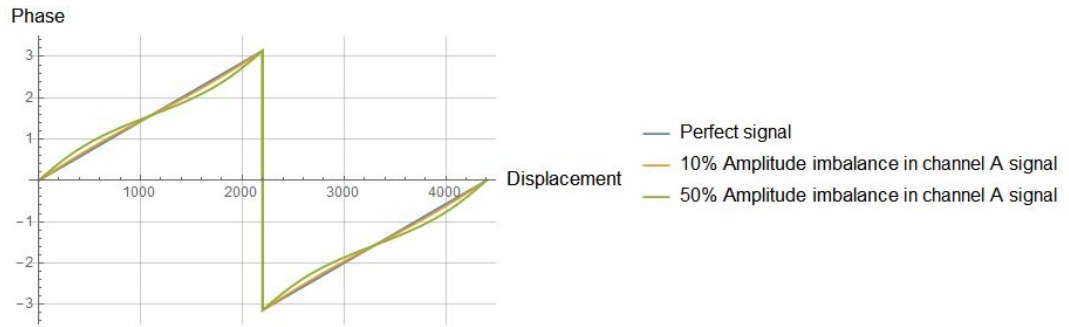


Figure 2.13 Lissajous curve of ideal signal and amplitude imbalance signal

The corresponding phase can be calculated using the arctangent function. The calculated phases of perfect signal and real signal are plotted together in Figure 2.14. The phase of the real signal is not linear with displacement.



**Figure 2.14 Phase of perfect signal and error signal against displacement**

The nonlinearity inaccuracy of 10% amplitude imbalance error is not quite obvious as it is overlapping with the ideal signal. Here 50% amplitude imbalance was added in Figure 2.14. To further compare the nonlinearity of the real signal, the difference of the phase between ideal signal and real signal is calculated using Equation 2.4 and plotted in Figure 2.15.

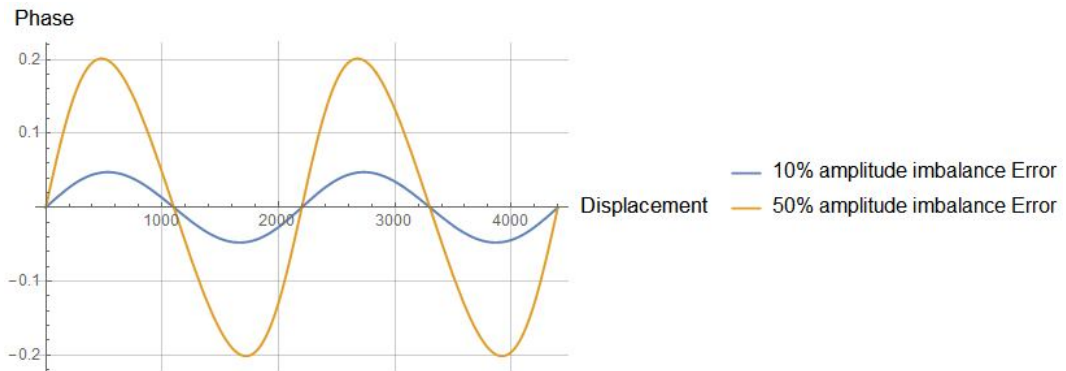


**Figure 2.15 Error against displacement**

The amplitude imbalance in the real signal makes the nonlinearity error periodic with the displacement. The larger the amplitude imbalance, the larger error in the encoder output.

### 2.3.6 Phase error

Assuming there is only phase error in the real signal of channel A, the corresponding real signals can be presented as:

$$\begin{aligned} V_{ap} &= \sin(\theta + S1) \\ V_{bp} &= \cos(\theta) \end{aligned} \quad (2.8)$$

Here  $V_{ap}$  and  $V_{bp}$  are the real signals from encoder, the p letter in the subscript stands for phase error and  $S1$  is the phase shift of channel A signal and equals to 0.2 rad. The corresponding signals can be plotted as below in Figure 2.16.

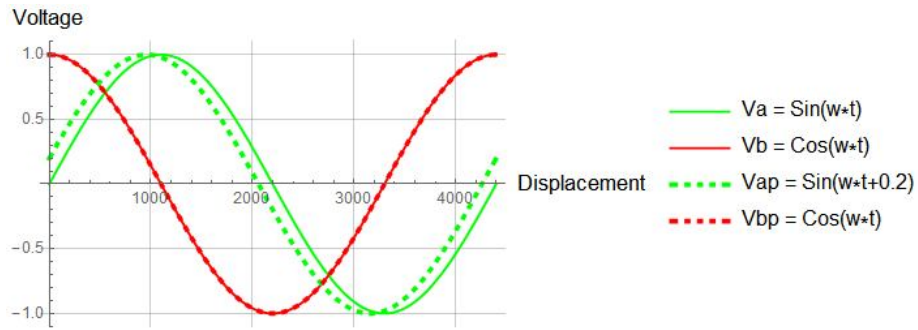


**Figure 2.16 Comparison of ideal signal and real signal with amplitude imbalance**

The corresponding Lissajous curve is shown in Figure 2.17. The phase shift in the signal makes the Lissajous curve a rotated ellipse.

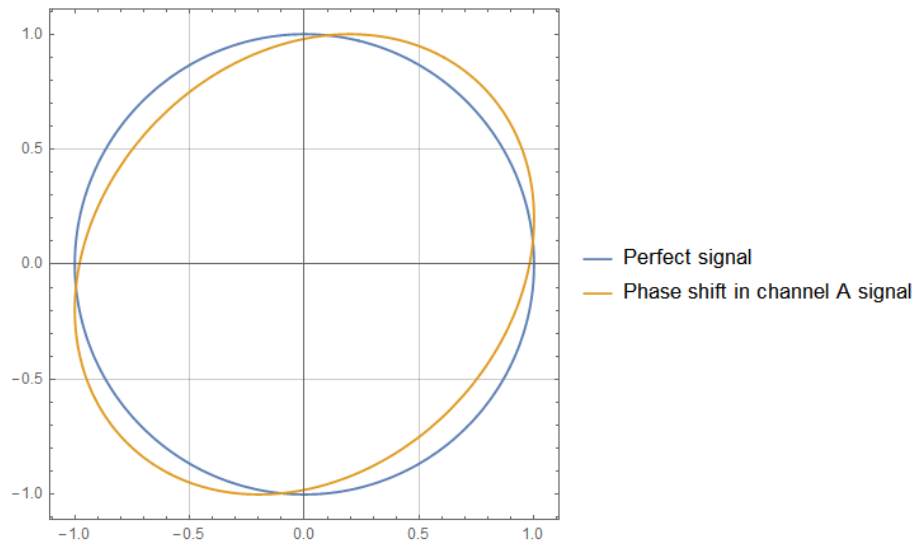


**Figure 2.17 Lissajous curve of ideal signal and amplitude imbalance signal**

The corresponding phase can be calculated using the arctangent function. The calculated phases of perfect signal and real signal are plotted together in Figure 2.18. The phase of the real signal is not linear with displacement.





Figure 2.18 Phase of perfect signal and error signal against displacement

To further compare the nonlinearity of the real signal, the difference of the phase between ideal signal and real signal is calculated and plotted in Figure 2.19.

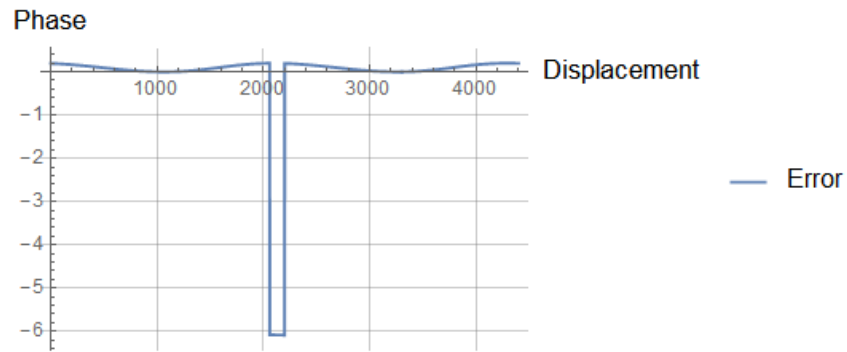


Figure 2.19 Error against displacement

Compared with the ideal phase displacement curve of the encoder, the phase shift error in the encoder signal will induce a  $-2 * \pi$  error in the encoder output.

### 2.3.7 Harmonic distortion

Assuming there is only second order harmonic distortion in the real signal of channel A, the corresponding real signals can be presented as:

$$\begin{aligned} V_{ah} &= \sin(\theta + S_1) + A_2 * \sin(2 * \theta) \\ V_{bh} &= \cos(\theta) \end{aligned} \quad (2.9)$$

Here  $V_{ah}$  and  $V_{bh}$  are the real signals from encoder and the letter h in the subscript stands for harmonics error in the signal. The  $\sin(2 * \theta)$  is the second order harmonics in channel A signal and its amplitude  $A_2$  equals to 0.1. The corresponding signals can be plotted as below in Figure 2.20.

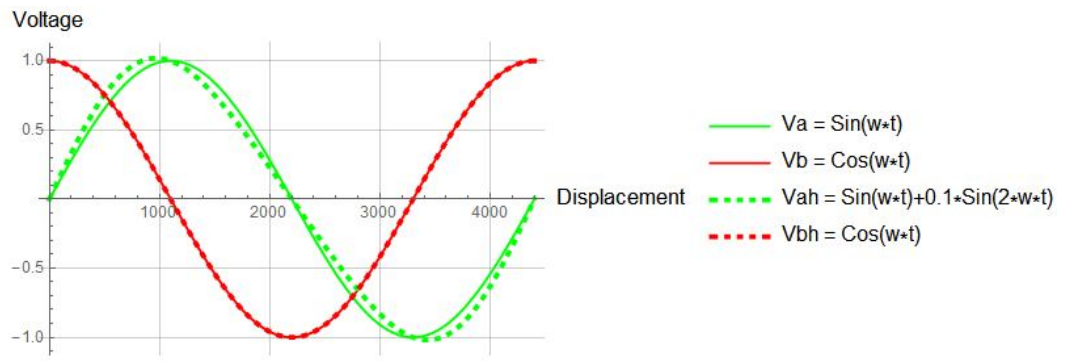


**Figure 2.20 Comparison of ideal signal and real signal with second order harmonics**

The corresponding Lissajous curve is shown in Figure 2.21. The harmonic in the signal changes the Lissajous curve from circle to a different nonregular shape.

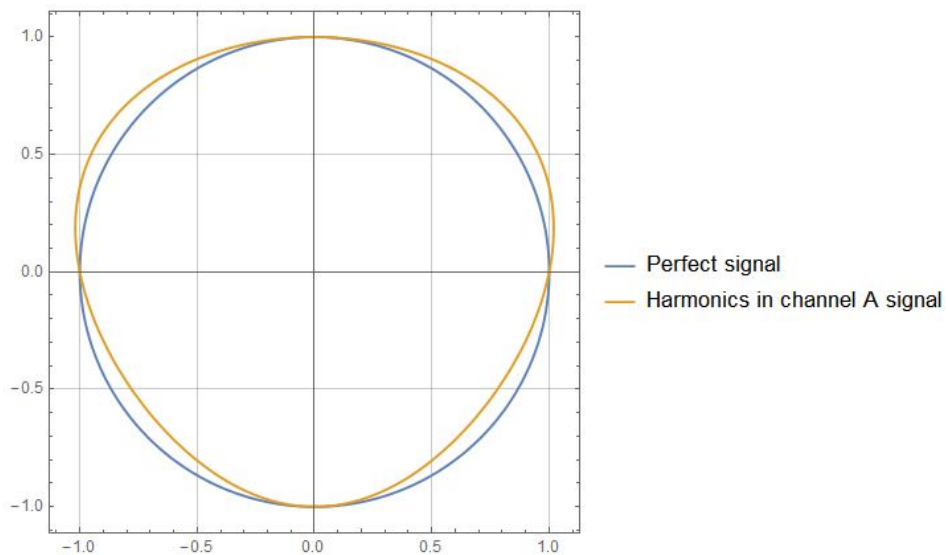


**Figure 2.21 Lissajous curve of ideal signal and real signal with second order harmonics**

The corresponding phase displacement output of the encoder can be calculated using arctangent function. The calculated phases of perfect signal and real signal are plotted together in Figure 2.22. Again, the phase of the real signal is not linear with displacement. As the nonlinearity inaccuracy of 10% harmonics amplitude imbalance error is not quite obvious as it is overlapping with the ideal signal. A 50% harmonics amplitude imbalance was added in Figure 2.22.

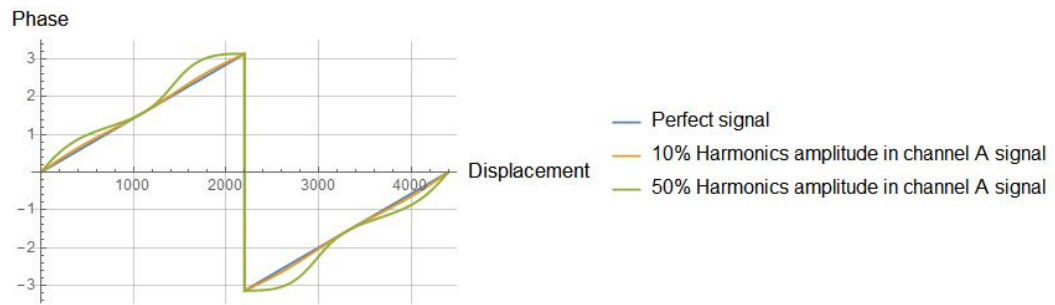


**Figure 2.22 Phase of perfect signal and real signal against displacement**

To further compare the nonlinearity of the real signal, the difference of the phase between ideal signal and real signal is calculated and plotted in Figure 2.23. The phase difference is anti-symmetric and change polarities every half period.

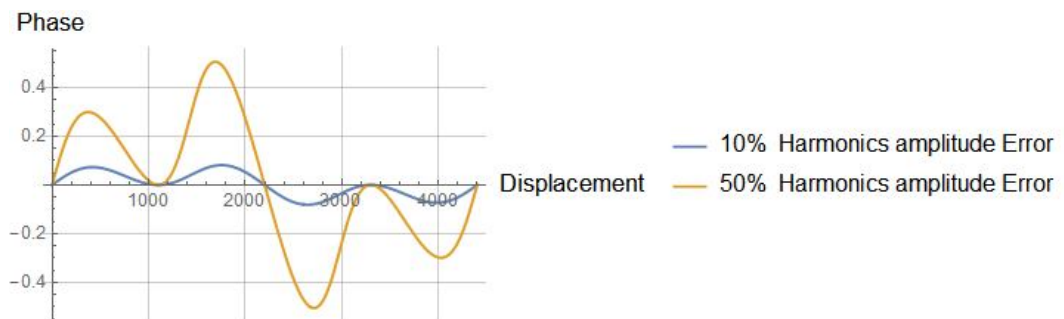


**Figure 2.23 Error against displacement**

## 2.4 Summary

The specifications of the encoder, such as measurement range, repeatability, accuracy (output nonlinearity), resolution, hysteresis and response time, have been defined and explained in this chapter, among which the accuracy and resolution are the most important parameters. The signal processing methods of the digital and analogue signal of the encoder have also been described. The digital output of the encoder is easier to implement with simpler encoder structure design and electronics while the analogue output type encoders are capable of providing higher position and speed resolution.

The common errors in the analogue output type encoders have been individually studied and discussed. The signal quality has been qualitatively assessed using the

Lissajous curve and corresponding phase displacement curves. The phase of the corrupted signal has been compared with the ideal signal. The influence of the different error types on the Lissajous curve and error form have been plotted, and will provide useful information for characterising encoders, as listed below in

Table 2.1:

**Table 2.1 Encoder output error and corresponding Lissajous curve and error form**

<b>Error signal type</b>	<b>Lissajous curve</b>	<b>Displacement measurement error</b>
DC offset	Shifted circle	Maximum $2 * \pi$
Amplitude imbalance	Ellipse	Two cycles of periodic error within one scale period
Phase shift	Rotated ellipse	Maximum $-2 * \pi$
Harmonics	Nonregular shape(neither circle or ellipse)	Anti-symmetric and change polarities every half period

## Reference

- [1] D. S. Nyce, "Encoders," in *Linear Position Sensors*, ed: John Wiley & Sons, Inc., 2004, pp. 151-161.
- [2] P. H. Sydenham, V. Taing, D. J. Mounsey, and Y. Wen-Xin, "Low-cost, precision, flat inductive sensor," *Measurement*, vol. 15, no. 3, pp. 179–188, 1995.
- [3] M. Martino, G. Golluccio, R. Losito, and A. Masi, "An analytical model of the effect of external DC magnetic fields on the AC voltages of an LVDT," in *2010 IEEE Instrumentation & Measurement Technology Conference Proceedings*, 2010, pp. 213–218.
- [4] A. Masi, A. Danisi, R. Losito, M. Martino, and G. Spiezia, "Study of Magnetic Interference on an LVDT: FEM Modeling and Experimental Measurements," *J. Sensors*, vol. 2011, pp. 1–9, 2011.
- [5] L. Weiwen, Z. Hui, T. Wei, and L. Chunfeng, "Research on Combinatorial-Code Grating Eddy-Current Absolute-Position Sensor," *IEEE Trans. Instrum. Meas.*, vol. 61, no. 4, pp. 1113–1124, Apr. 2012.
- [6] R. Merry, R. van de Molengraft, and M. Steinbuch, "Error modeling and improved position estimation for optical incremental encoders by means of time stamping," in *2007 American Control Conference*, 2007, pp. 3570–3575.
- [7] M. S. Wang, Y. S. Kung, Y. M. Tu, and T. T. Lin, "Novel interpolation method for quadrature encoder square signals," in *IEEE International Symposium on Industrial Electronics*, 2009, pp. 333–338.
- [8] K. K. Tan, H. X. Zhou, and T. H. Lee, "New interpolation method for quadrature encoder signals," *IEEE Trans. Instrum. Meas.*, vol. 51, no. 5, pp. 1073–1079, Oct. 2002.
- [9] K. K. Tan and K. Z. Tang, "Adaptive online correction and interpolation of quadrature encoder signals using radial basis functions," *IEEE Trans. Control Syst. Technol.*, vol. 13, no. 3, pp. 370–377, May 2005.
- [10] N. Hagiwara, Y. Suzuki, and H. Murase, "A Method of Improving the Resolution and Accuracy of Rotary Encoders Using a Code Compensation Technique," *IEEE Trans. Instrum. Meas.*, vol. 41, no. 1, pp. 98–101, 1992.
- [11] Y. Matsuzoe, "Error dispersion algorithms to improve angle precision for an encoder," *Opt. Eng.*, vol. 41, no. 9, p. 2282, Sep. 2002.

- [12] Y. Zimmerman, Y. Oshman, and A. Brandes, "Improving the accuracy of analog encoders via Kalman filtering," *Control Eng. Pract.*, vol. 14, no. 4, pp. 337–350, Apr. 2006.
- [13] S. H. Hwang, D. Y. Kim, J. M. Kim, and D. H. Jang, "Signal compensation for analog rotor position errors due to nonideal sinusoidal encoder signals," *J. Power Electron.*, vol. 14, no. 1, pp. 82–91, Jan. 2014.
- [14] N. K. Boggapu and R. C. Kavanagh, "New Learning Algorithm for High-Quality Velocity Measurement and Control When Using Low-Cost Optical Encoders," *IEEE Trans. Instrum. Meas.*, vol. 59, no. 3, pp. 565–574, Mar. 2010.
- [15] D. E. Denk, "A method for estimating the accuracy of quadrature output sensors," *Optoelectron. Instrum. Data Process.*, vol. 44, no. 2, pp. 105–110, Apr. 2008.
- [16] S. K. Kaul, R. Koul, C. L. Bhat, I. K. Kaul, and A. K. Tickoo, "Use of a look-up table improves the accuracy of a low-cost resolver-based absolute shaft encoder," *Meas. Sci. Technol.*, vol. 8, no. 3, pp. 329–331, Mar. 1997.
- [17] H. Van Hoang and J. W. Jeon, "Signal compensation and extraction of high resolution position for sinusoidal magnetic encoders," in *ICCAS 2007 - International Conference on Control, Automation and Systems*, 2007, pp. 1368–1373.
- [18] D. G. Alciatore and M. B. Hestand, *Introduction to Mechatronics and Measurement Systems*: McGraw-Hill, 2003.
- [19] J. Burke, J. F. Moynihan, and K. Unterkofler, "Extraction of high resolution position information from sinusoidal encoders," in *Proceedings of The International Intelligent Motion Conference*, 2000, pp. 217–222.
- [20] N. C. Cheung, "An innovative method to increase the resolution of optical encoders in motion servo systems," in *Power Electronics and Drive Systems, 1999. PEDS '99. Proceedings of the IEEE 1999 International Conference on*, 1999, pp. 797–802 vol.2.
- [21] K. K. Tan, H. X. Zhou, and L. Tong Heng, "New interpolation method for quadrature encoder signals," *IEEE Transactions on Instrumentation and Measurement*, vol. 51, pp. 1073–1079, 2002.
- [22] T. Hong and F. de Leon, "Lissajous Curve Methods for the Identification of Nonlinear Circuits: Calculation of a Physical Consistent Reactive Power,"

- IEEE Trans. Circuits Syst. I Regul. Pap., vol. 62, no. 12, pp. 2874–2885, Dec. 2015.
- [23] L. Balado, E. Lupon, L. Garcia, R. Rodriguez-Montanes, and J. Figueras, "Lissajous Based Mixed-Signal Testing for N-Observable Signals," in 2006 IEEE Design and Diagnostics of Electronic Circuits and systems, pp. 123–128.
  - [24] L. Balado, E. Lupon, J. Figueras, M. Roca, E. Isern, and R. Picos, "Verifying Functional Specifications by Regression Techniques on Lissajous Test Signatures," IEEE Trans. Circuits Syst. I Regul. Pap., vol. 56, no. 4, pp. 754–762, Apr. 2009.
  - [25] J. Lara and A. Chandra, "Position error compensation in quadrature analog magnetic encoders through an iterative optimization algorithm," in IECON 2014 - 40th Annual Conference of the IEEE Industrial Electronics Society, 2014, pp. 3043–3048.
  - [26] H. X. Nguyen, T. N.-C. Tran, J. W. Park, and J. W. Jeon, "Auto-calibration and noise reduction for the sinusoidal signals of magnetic encoders," in IECON 2017 - 43rd Annual Conference of the IEEE Industrial Electronics Society, 2017, pp. 3286–3291.
  - [27] S.-H. Hwang, D.-Y. Kim, J.-M. Kim, and D.-H. Jang, "Signal Compensation for Analog Rotor Position Errors due to Nonideal Sinusoidal Encoder Signals," J. Power Electron., vol. 14, no. 1, pp. 82–91, Jan. 2014.

## **Chapter 3 - Analytical modelling of eddy current based magnetic encoder**

### **3.1 Introduction**

The configuration of new an eddy current based magnetic position encoder is proposed and studied both analytically and numerically in this chapter. The concept of eddy currents is first introduced and followed by literature review of position sensors and encoders using this effect. The structure and working principle of the proposed encoder is studied using an analytical modelling method. The encoder structure was simplified as a coil system. Coupling between planar rectangular spiral coils was studied both analytically and numerically; both results were verified by the measurements and good agreement was achieved. The behaviour of electrical outputs of the proposed encoder were also studied providing guidelines for the design of the subsequent signal processing circuit.

### **3.2 Eddy currents and eddy currents sensors**

Eddy currents occur in any conductive materials that are subjected to a time-varying magnetic field as a result of Faraday's law of induction. Eddy currents, first discovered by François Arago, flow in closed loops lying on planes perpendicular to the magnetic field. Such currents can be induced within conductors by the relative movement of a nearby magnet or by a magnetic field created by an AC current. The magnitude of the induced current in a given loop is proportional to the strength of the magnetic field, the rate of changing flux and the areas of the loop. The current is also inversely proportional to the conductor resistivity.

By Lenz's law, eddy currents create a magnetic field that opposes the field that created them. Eddy currents react therefore to the source of the magnetic field. This effect is employed for example in eddy currents brakes [1-3]. The currents flowing through the resistance of the conductor also dissipates energy as heat in the material.



This effect is used in induction heating equipment [4-6]. The reaction of the induced eddy currents will also affect the source impedance if the magnetic field is generated by AC currents in inductors. This change in the impedance can be detected using the specified electronic circuit. This effect is used in non-destructive testing for the detection of flaws and cracks in metal [7, 8], and for proximity or displacement sensors used in control systems [9-14].

### 3.3 Eddy currents based magnetic encoder review

As described in Chapter 1, eddy currents-based magnetic encoders have been studied extensively in the past few years. Different encoder structures have been proposed in scientific articles or patents [10, 11, 15-19, 20-24]. A typical working principle of this kind of encoder is described in patent [24] whose structure is shown in Figure 3.1. The encoder read head is made of inductor coils and the scale is made of conductive plates placed periodically on a substrate. In Figure 1.10 the sensor head is composed of planar coils: one emitter coil delivering a voltage  $V_r$  and two receiver coil pairs producing the voltages  $V_{os}$  and  $V_{oc}$ .

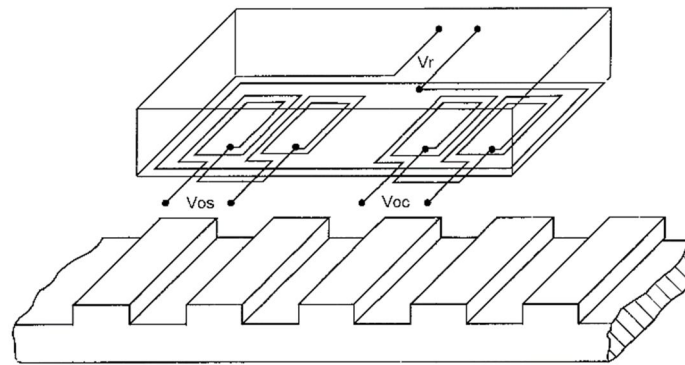


**Figure 3.1 Eddy currents based magnetic encoder**

The working principle of the encoder is similar to that of a LVDT (Linear Variable Differential Transformer). The emitter coil together with two receiver coil pairs form two differential transformers. An AC signal, applied to the emitter coil  $V_r$ , generates an alternating magnetic field, which, in turn, induces eddy currents in conductive plates on the scale. The position of the scale will affect the coupling between the emitter coil and the receiver coil pairs. An amplitude modulated signal is generated in the receiver pairs as the relative position between the scale and coils

changes. With two secondary pairs placed together with a quarter period length offset, two quadrature signals are generated and further interpolated to provide a measurement of the displacement.

Podhraski implemented a different encoder structure on an application-specific integrated circuit, both the sensor element and the signal conditioning circuit are monolithically integrated together [16]. In his configuration, for each receiver coil there is one emitter coil forming a transformer as shown in Figure 3.2(a). The system is composed of two transformers whose secondary windings are connected differently, so that the induced voltage in them are cancelling each other. The quadrature signals are generated from the two transformer pairs which have a lateral offset of a quarter of a period. The device is measured to have 20  $\mu\text{m}$  resolution and 18.75  $\mu\text{m}$  maximum nonlinearity error for a copper scale, 30.55  $\mu\text{m}$  maximum nonlinearity error for a steel scale.

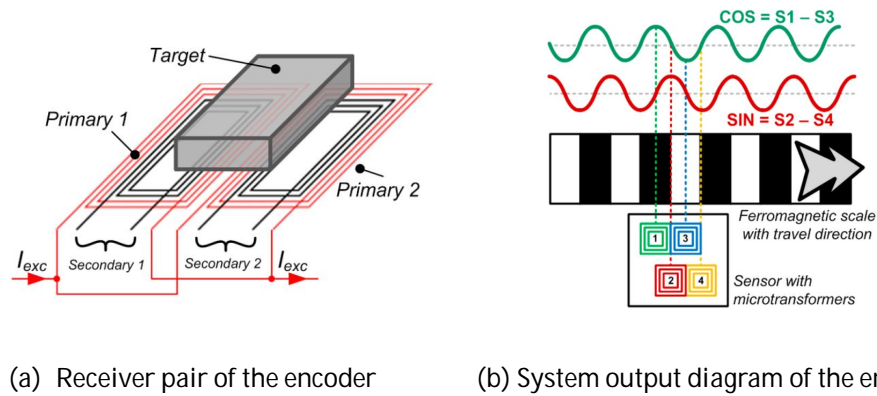


**Figure 3.2 Encoder structure implemented by Podhraski [16].**

A different structure was patented by Irle as shown in Figure 3.3 [20]. The working principle is similar to the previous one, although the configuration of the receiver coils in the read head is different. The two receivers are evenly placed inside the emitter coil and are overlapped vertically on different layers of a multi-layer structure. The geometry of the receivers is designed to have zero induced voltage when there is no scale, so the voltages in the receivers are only induced by the eddy currents in the scale.

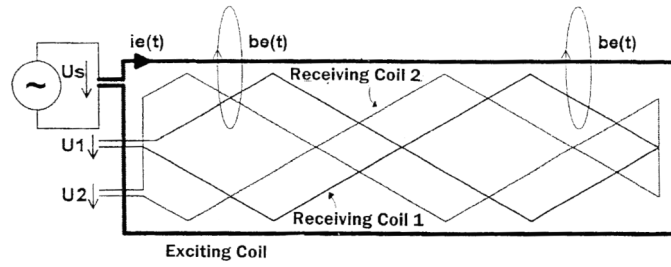


Figure 3.3 Eddy currents based magnetic encoder read head diagram [20].

Another improved structure, described in patent by the Mituyoto corporation [22], the structure is shown in Figure 3.4 below. The receiver starts at one end near the emitter coil and follows a sinusoidal-like path until it reaches the other end, where it turns back to the beginning, the second pair is a quarter of a period offset generating thereby quadrature signals.

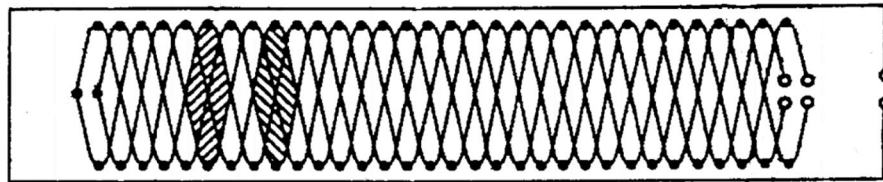


Figure 3.4 Patented encoder structure by Mituyoto corporation

Mattan [15] studied a similar encoder structure as used by Posic technology [17]. The structure of the encoder is shown in Figure 3.5; the read head is composed of circular coils, which have a similar working principle as in the previous encoders. The newest encoder product from Posic technology has  $0.02 \mu\text{m}$  resolution and  $38 \mu\text{m}$  nonlinearity error before error corrections.

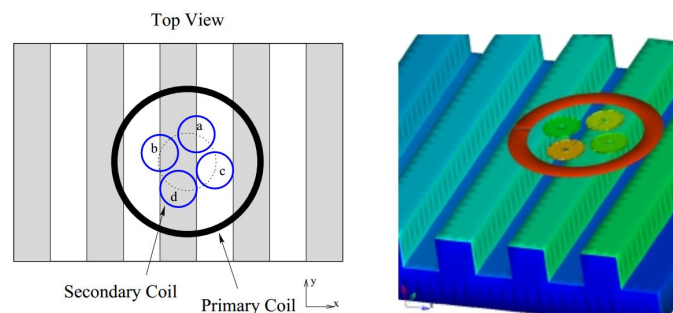


Figure 3.5 Magnetic encoder structure proposed by Posic technology [17].

### 3.4 Proposed Structure and working principle

An eddy currents based encoder structure is proposed in this section. The working principle is described alongside the analytical modelling.

#### 3.4.1 Structure and working principle

The proposed encoder structure is composed of a read head and a scale, as shown in Figure 3.6. The read head is composed of an emitter (primary) coil, two receiver (secondary) coil pairs, while the scale is composed of periodically placed rectangular copper plates on a non-conductive substrate.

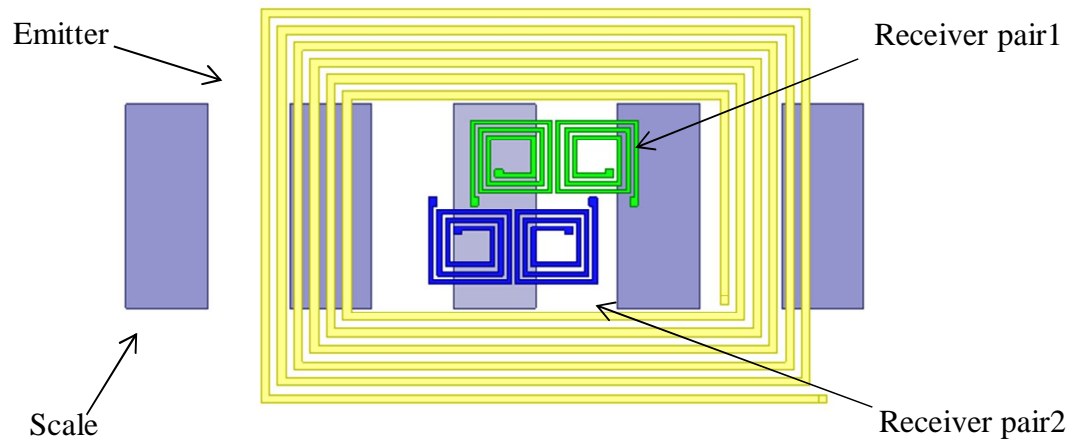
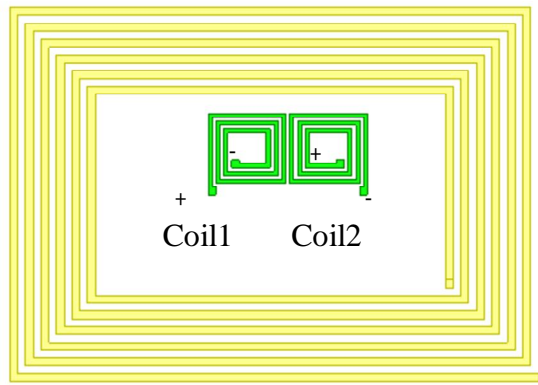


Figure 3.6 Simplified encoder structure and diagram

The operation of the system is described here. An AC current is applied to the emitter coil, which generates an alternating magnetic field. This field induces eddy currents in the metal plates on the scale. The induced eddy currents generate themselves another alternating magnetic field. Both fields induce a voltage in the receiver coils. We will now study the induced voltage in one receiver pair by the emitter coil. The structure is simplified and shown as in Figure 3.7.



**Figure 3.7 Emitter coil with one receiver pair**

The coil windings for coil1 and coil2 are set up in opposite directions providing thereby different voltage polarities as shown in Figure 3.7. Here the positive terminals of coil1 and coil2 are connected with each other so that the voltages induced by the emitter coil in the receiver pairs are neutralized. When the scale is far away from the read head, the output voltage of the receiver pair should be zero, assuming the magnetic field generated by the emitter is uniform. So the structure can be further simplified as in Figure 3.8 (a).

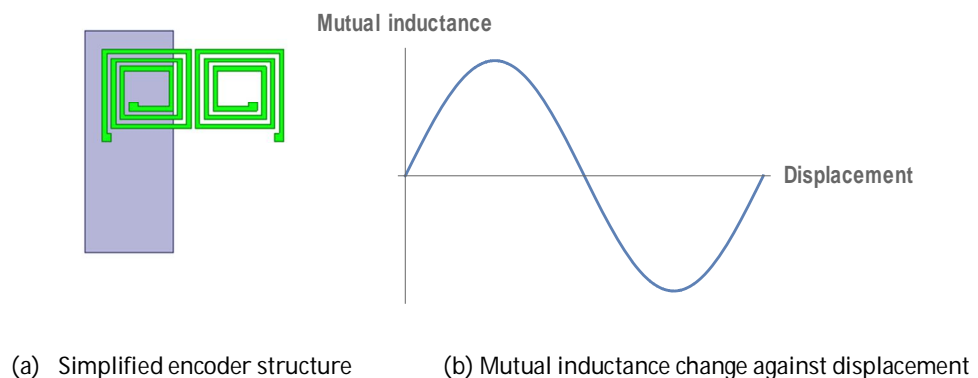


**Figure 3.8 Receiver and plate coupling**

As the magnetic field of the emitter coil is assumed to be uniform, the magnitude of the induced currents in the conductive plates is constant when they move beneath the emitter. As the scales move near the receiver coils along the x-axis, the coupling changes between eddy currents in the plate and the receiver coils. This coupling depends on the position of the scale position. One example is shown in Figure 3.8 (b). When the scale is beneath coil1 in the receiver pair, the coupling reaches maximum value and when it moves beneath coil2 in the receiver pair, the coupling reaches the minimum value. As the metal plates in the scale are placed periodically,

the mutual inductance between the receiver and the eddy currents in the plate changes periodically as well. The other receiver pair is offset by a quarter of a period (period length equals to the receiver pair width), resulting in a 90° phase shift in the coupling signal. The output coupling signals are then processed by an amplification and demodulation electric circuit. Two quadrature signals are generated, as shown in Figure 3.9, which are to be converted to displacement information by an interpolation electronics circuit.

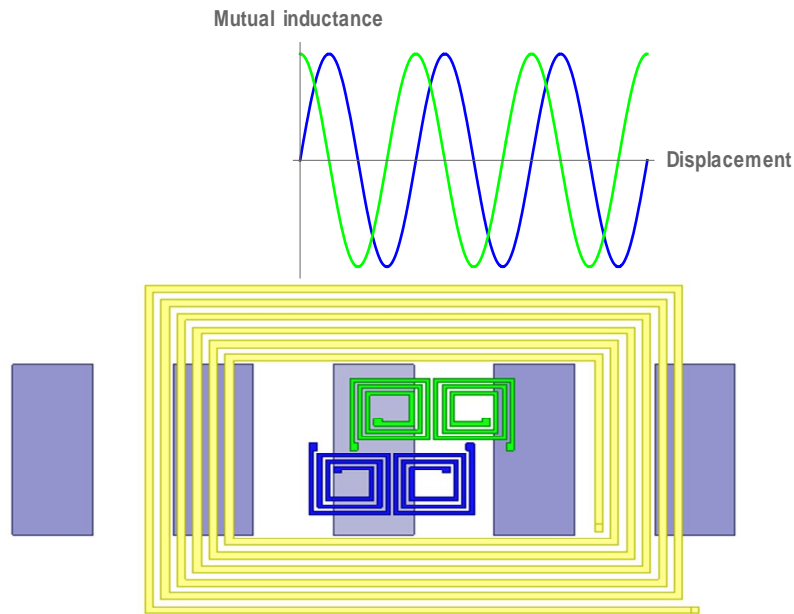


**Figure 3.9 Mutual inductance change of the two receiver pairs as the scale moves: (top) mutual inductance; (bottom) encoder structure.**

### **3.5 Modeling of the proposed eddy currents based magnetic encoder**

As described previously, there are two types of induced voltages in the receiver pairs: one voltage induced by the emitter coil, the other voltage induced by the eddy currents in the conductive plates on the scale. To model the encoder, the magnetic couplings between planar coils, and between planar coils and the planar conductive plate are studied.

### 3.5.1 Eddy currents in scale

The distribution of eddy currents in the conductors has been studied by many researchers [25-32]. Smith proposed a coupled circuit method to analyse the distribution of the induced eddy currents on a circular conductive plate [28]. In his method, the circular plate is simplified as multi-turn coaxial coils. The induced currents in the coils were calculated and used to represent the eddy currents in the plate. Simulation of the eddy current were carried out using the ANSYS Maxwell™ simulation software in order to assess their distribution in the rectangular copper plate. The configuration of the structure and result are shown in Figure 3.10. An AC current with 0.1 Amp amplitude and 1 MHz frequency is applied to the rectangular emitter coil and the density of the induced eddy currents is plotted for copper plates placed 0.5mm beneath the emitter coil. It can be seen that eddy currents are mainly flowing on the edge of the copper plate. As the thickness of the copper plate used in the simulation is 35  $\mu\text{m}$ , which is about half of the skin depth of the eddy currents at 1MHz for copper, the difference of the induced currents density in the Z axis direction is ignored. It can be seen that due to the proximity effect, the eddy currents are mainly distributing near the edge of the rectangular plates.

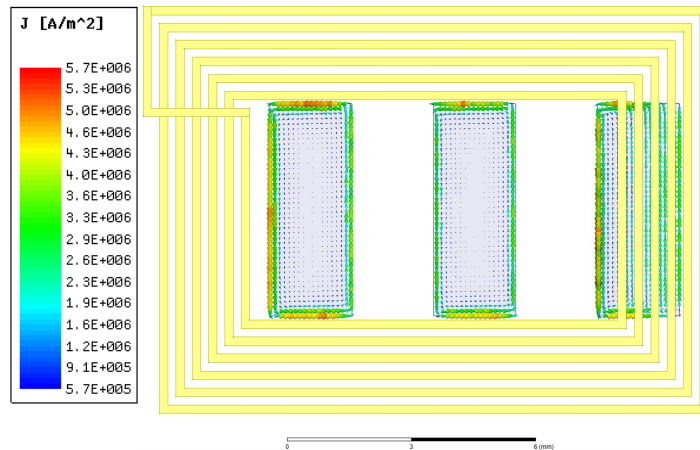
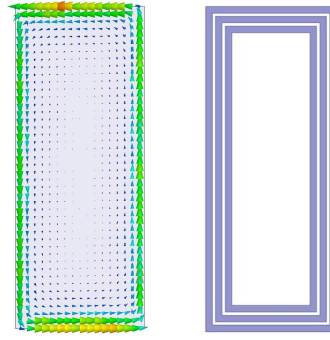


Figure 3.10 Representation of the eddy current density on the copper plates

Based on the simulation results obtained, the scale is simplified as a multi-turn coaxial rectangular coils, an example of which is shown in Figure 3.11.



**Figure 3.11** Scale simplified as a multi-turn coaxial coil: on the left are represented the induced eddy currents in the scale; on the right is the equivalent 3-turns coil.

### 3.5.2 Encoder structure simplification

After modelling the metal scales as coils, the proposed encoder structure is shown in Figure 3.12. The problem now becomes one of calculation of the mutual inductance between multi-turn rectangular coils with different relative displacement.

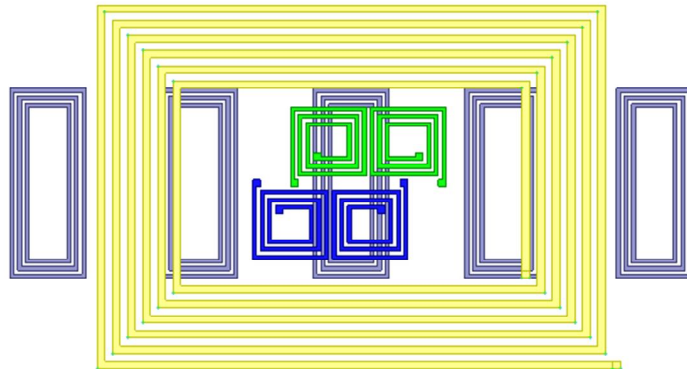


**Figure 3.12** Encoder structure after modelling scales as coils

Due to the symmetry of the encoder system, for analytical modelling purposes, we only need to calculate the coupling between receiver pair one and the emitter and scales. The simplified model structure is shown in Figure 3.13.



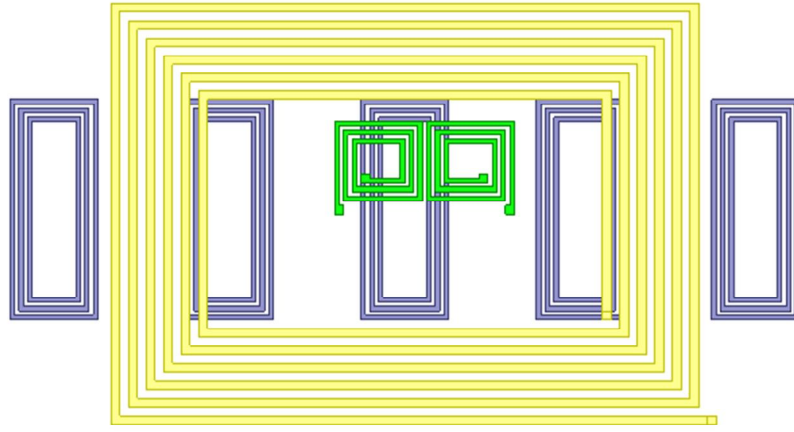


**Figure 3.13 Encoder equivalent structure for one receiver pair**

Only the coupling of coil one in the receiver pair needs to be calculated. The configuration of the equivalent structure is further simplified as shown in Figure 3.14.

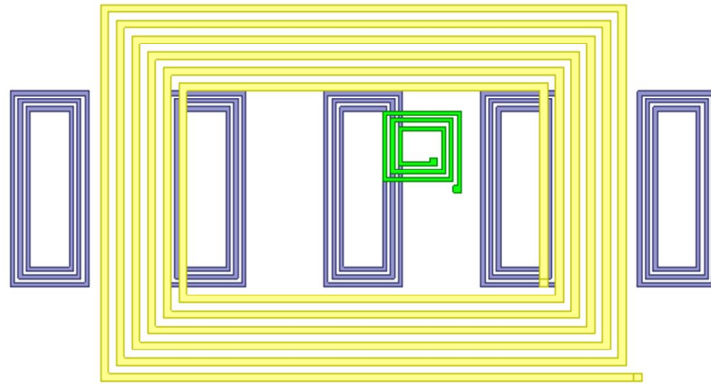


**Figure 3.14 Encoder equivalent structure for one receiver coil**

### **3.5.3 Mutual inductance between rectangular planar coils**

The problem has therefore been simplified to the calculation of the coupling between planar rectangular coils. A top level flowchart for calculating the mutual inductance between two rectangular coils with  $M$  and  $N$  turns is provided here in Figure 3.15 . Details of the calculation are presented in this part.

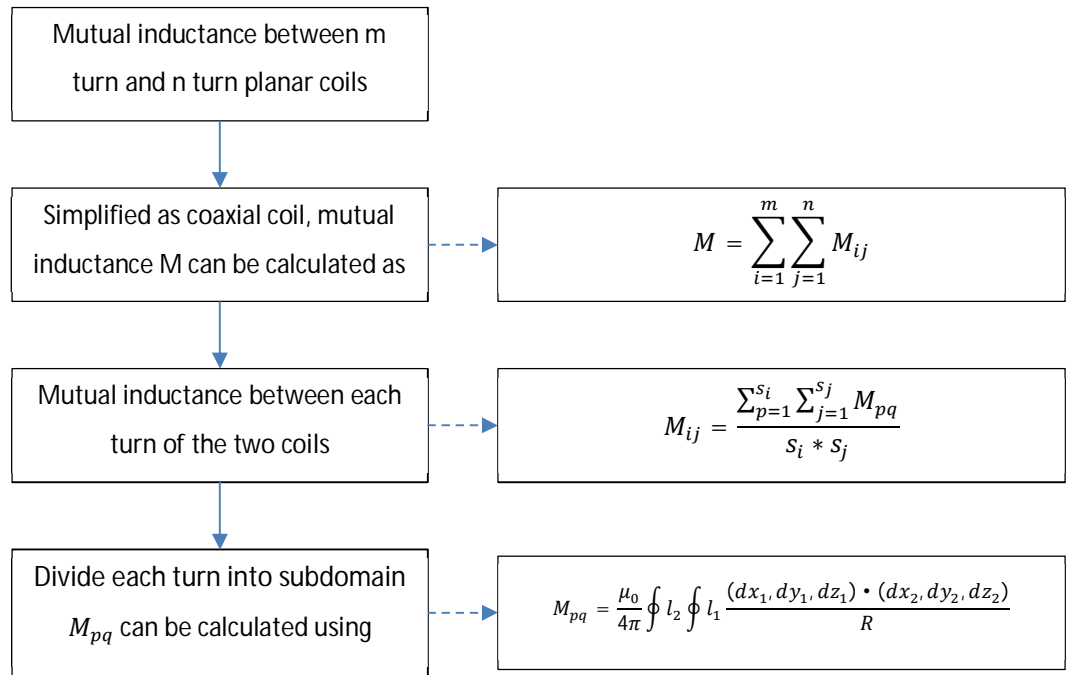


Figure 3.15 Flow chart of mutual inductance calculation

### 3.5.3.1 Analytical calculation

Calculating the coupling between planar rectangular coils with different offsets or misalignments in the X, Y and Z directions. The multi-turn spiral coil is further simplified as a multi-turn coaxial rectangle coil, as shown in Figure 3.16 below.

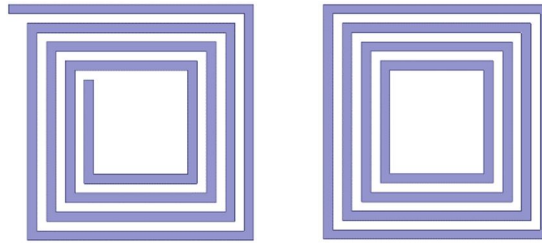
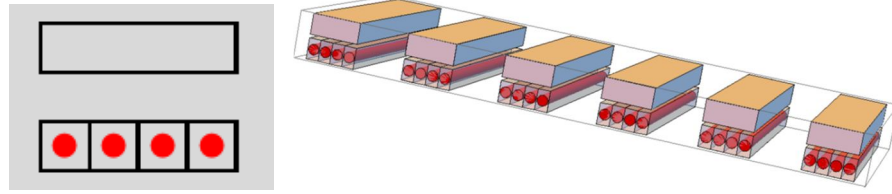


Figure 3.16 Rectangular spiral coil (left) simplified as a set of concentric squares (right)

The mutual inductance between turn  $i$  in the emitter coil and turn  $j$  in the equivalent scale plate coil is defined as  $M_{ij}$ . Assuming there are  $m$  turns in the emitter coil and  $n$  turns in the equivalent scale coil, the total mutual inductance between the emitter coil and the equivalent scale coil is calculated as:

$$M = \sum_{i=1}^m \sum_{j=1}^n M_{ij} \quad (3.1)$$

To calculate the mutual inductance  $M_{ij}$ , each turn in the multi-turn coil is divided into subdomains. If the dimensions of the subdomains are small enough they can be simplified as filaments in the geometry centre of the subdomains as shown in Figure 3.17.



**Figure 3.17** Coil track simplified as subdomains and filaments: 2D (left) and 3D (right) view, in the 2D and 3D view the top part is the coil tracks while the bottom part is the simplified subdomains and corresponding filaments.

The mutual inductance between turn  $i$  in emitter coil and turn  $j$  in equivalent scale plate coil  $M_{ij}$  can be calculated as:

$$M_{ij} = \frac{\sum_{p=1}^{s_i} \sum_{q=1}^{s_j} M_{pq}}{s_i * s_j} \quad (3.2)$$

$M_{pq}$  is the mutual inductance between two filaments in turn  $i$  and turn  $j$ , respectively.  $M_{pq}$  can be calculated using the Neumann formula, as discussed in the next section. The  $s_i$  and  $s_j$  are the total numbers to subdomains of the two single turn coils, for example in Figure 3.17 the track is divided to 4 subdomains. Substituting Equation 3.2 into Equation 3.1, the mutual inductance can be calculated between two multi-turn rectangular coils for any relative position.

### **3.5.3.2 Mutual inductance between rectangular coils composed of filaments**

To calculate the mutual inductance  $M_{pq}$ , a coordinate system is built as shown in Figure 3.18.  $L_1$  represents one subdomain in the equivalent scale plate coil and is located at the origin of the coordinate system.  $L_2$  represents one subdomain in the emitter coil at position  $(T_x, T_y, T_z)$ . Let  $P_1(x_1, y_1, z_1)$  be a point on  $L_1$ , and  $P_2(x_2, y_2, z_2)$  a point on  $L_2$ , as illustrated in Figure 3.18.

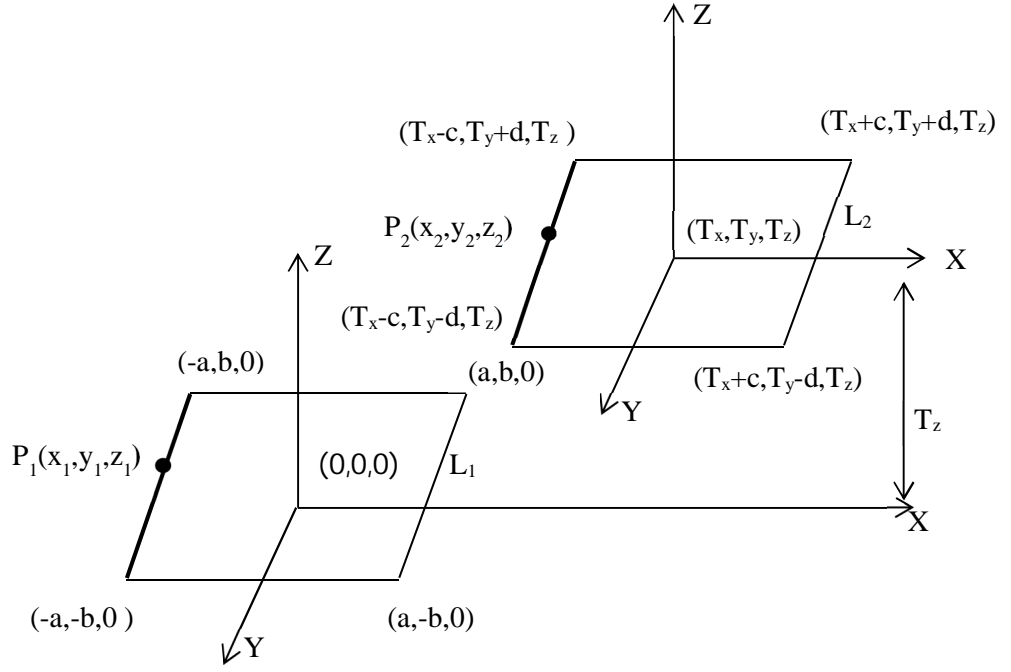


Figure 3.18 Coordinate system of two coils with X, Y and Z direction displacement

The mutual inductance between the left side of  $L_1$  and  $L_2$  can be calculated using the Neumann formula:

$$M = \frac{\mu_0}{4\pi} \oint l_2 \oint l_1 \frac{(dx_1, dy_1, dz_1) \cdot (dx_2, dy_2, dz_2)}{R} \quad (3.3)$$

Here,  $R$  is the distance between  $P_1$  and  $P_2$  and equals:

$$R = \sqrt{(x_1 - x_2)^2 + (y_1 - y_2)^2 + (z_1 - z_2)^2} \quad (3.4)$$

Thus,

$$M = \frac{\mu_0}{4\pi} \oint l_2 \oint l_1 \frac{dx_1 dx_2 + dy_1 dy_2 + dz_1 dz_2}{\sqrt{(x_1 - x_2)^2 + (y_1 - y_2)^2 + (z_1 - z_2)^2}} \quad (3.5)$$

Let  $x_1 = c$ ,  $-b \leq y_1 \leq b$ ,  $z_1 = 0$ ,  $x_2 = T_x + c$ ,  $T_y - d \leq y_2 \leq T_y + d$ ,  $z_2 = T_z$ . Taking these values into Equation 3.5 the mutual inductance between the left sides of the two rectangular filaments can be calculated.

$$M = \frac{\mu_0}{4\pi} \oint_{-b}^b dy_1 \oint_{T_y-d}^{T_y+d} dy_2 \frac{1}{\sqrt{(T_x+c-a)^2 + (y_1 - y_2)^2 + (T_z)^2}} \quad (3.6)$$

Let  $L^2 = (T_x + c - a)^2 + (T_z)^2$ ,

$$M = \frac{\mu_0}{4\pi} \oint_{-b}^b dy_1 \oint_{T_y-d}^{T_y+d} dy_2 \frac{1}{\sqrt{(y_1 - y_2)^2 + L^2}} \quad (3.7)$$

Finishing the first integration:

$$M = \frac{\mu_0}{4\pi} \phi_{-b}^b dy_1 [\ln(k + \sqrt{k^2 + L^2})]_{T_y-d-y_1}^{T_y+d-y_1} \quad (3.8)$$

After simplification:

$$M = \frac{\mu_0}{4\pi} \phi_{-b}^b dy_1 \ln \left( (T_y + d - y_1) + \sqrt{(T_y + d - y_1)^2 + L^2} \right) - \frac{\mu_0}{4\pi} \phi_{-b}^b dy_1 \ln \left( (T_y - d - y_1) + \sqrt{(T_y - d - y_1)^2 + L^2} \right) \quad (3.9)$$

such that:

$$M = \frac{\mu_0}{4\pi} [n \ln(n + \sqrt{n^2 + L^2}) - \sqrt{n^2 + L^2}]_{T_y-d+b}^{T_y-d-b} - \frac{\mu_0}{4\pi} [m \ln(m + \sqrt{m^2 + L^2}) - \sqrt{m^2 + L^2}]_{T_y+d+b}^{T_y+d-b} \quad (3.10)$$

The total mutual inductance of the two one-turn filaments coils is the sum of the mutual inductance between their four sides which can be calculated using Equation 3.10. To verify this analytical expression, simulation was carried out using ANSYS Maxwell™ software. Figure 3.15 shows the configuration of the simulated system as well as the simulated and calculated results. In the simulation, one rectangular coil with 2 mm width and length was placed above five rectangular coils of 2 mm width and 4 mm length. The mutual inductance was calculated and simulated at different relative displacements. The simulation and calculation result agree well. The width of the tracks is assigned small enough (100 μm) in the simulation to simplify them as filaments.

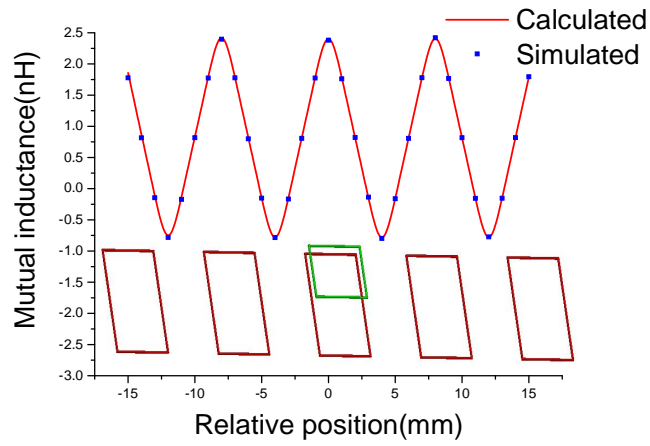


**Figure 3.15 Configuration of simulation and calculation results of mutual inductance between rectangular filament coils**

### 3.5.3.3 Calculation

The mutual inductance between two multi-turn coils was calculated using the software package Mathematica™. The dimensions of the coils used in the calculation are listed in Table 3.2. The rectangular spiral coils are simplified as rectangular coaxial coils and the structure used in the calculation is plotted as in Figure 3.20.

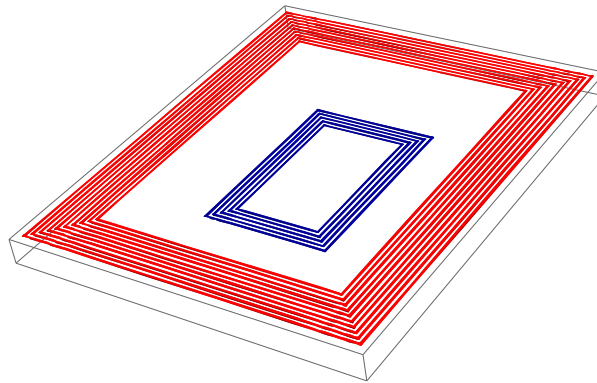


**Figure 3.20 3D coil geometry used in Mathematica calculation**

As the track width and thickness of the coils are relatively small compared with the geometry of the coils, the tracks are divided into four small domains in its width direction and each domain is replaced by the filaments, an example of which is shown in Figure 3.21.

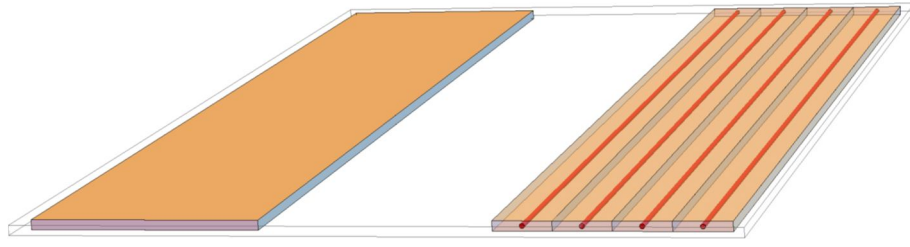


Figure 3.21 Example of divide one turn coil track(left) as subdomains and equivalent filaments(right)

The mutual inductance,  $M_{ij}$ , between different turns of the coils is then calculated as the average of the coupling between the equivalent filaments  $M_{pq}$  as calculated using Equation 3.2.

#### 3.5.3.4 Simulation

To verify the calculation method proposed in the previous part, two rectangular spiral coils were simulated using ANSYS Maxwell™; the configuration to be simulated is shown in Figure 3.16.

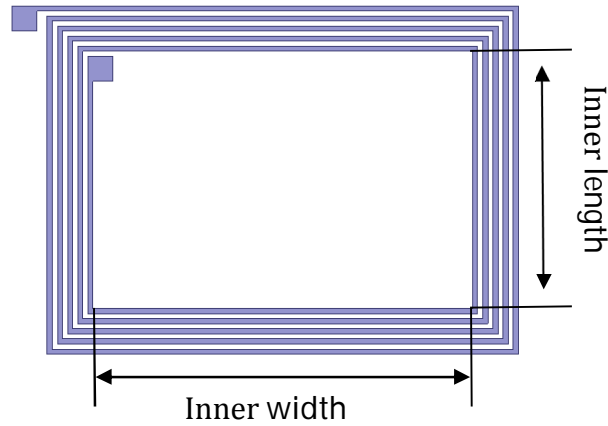


Figure 3.162 Coil geometry illustration

Table 3.2 Geometry of emitter and receiver coil

	Turn	Track width (mm)	Track gap (mm)	Track thickness (mm)	Inner length (mm)	Inner width (mm)
Emitter	10	0.2	0.2	0.017	15	26
Receiver	5	0.2	0.2	0.017	10.2	20.2

The corresponding configuration is shown in Figure 3.23. A 1 MHz AC current was applied to the emitter coil in the simulation setting. The values of the mutual inductance between the two coils were acquired for different Y and Z direction misalignments.

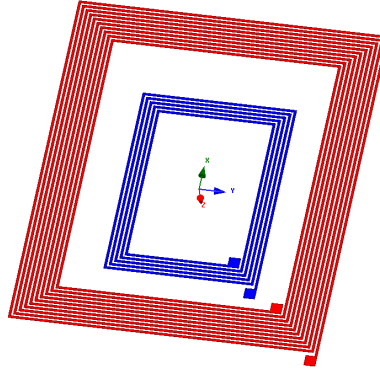


Figure 3.23 Geometry of the coils used in simulation

#### 3.5.3.5 Measurement

Two spiral coils with the same dimensions as in the simulation were fabricated using Printed Circuit Board (PCB) technology. The mutual inductance between coils was measured using the platform shown on the left of Figure 3.17. The emitter coil is attached to a PT3/M stage, which is a manual 3-axis translation (Thorlabs Inc., USA) stage with 10  $\mu\text{m}$  resolution and 25 mm travel range in all directions. The receiver coil was fixed and the mutual inductance at different relative misalignment was measured by using the 3-axis stage.

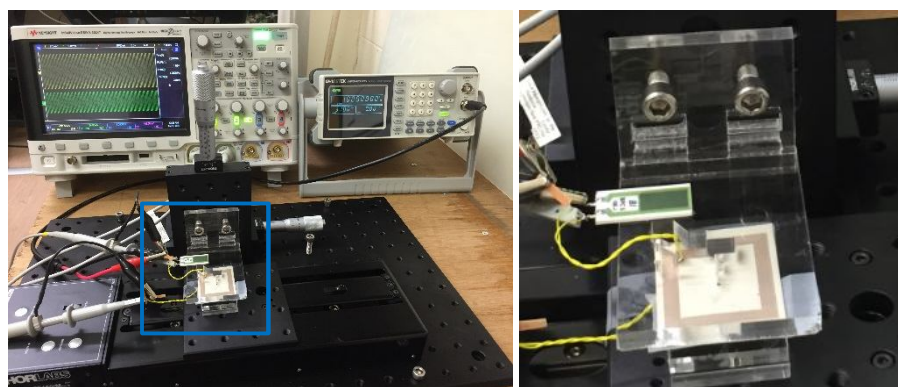
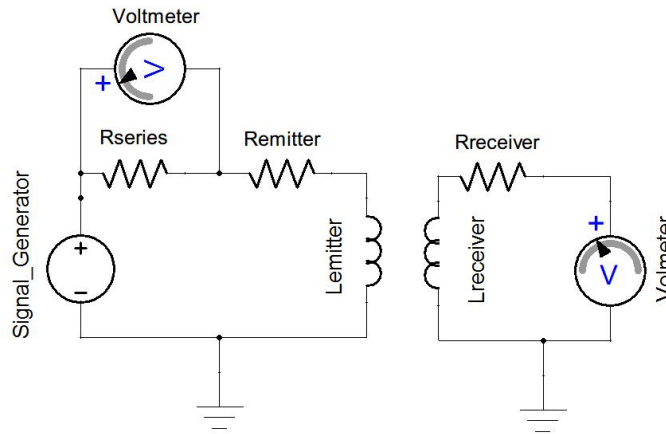


Figure 3.17 Misaligned coil coupling measurement setup: left measurement setup; right zoom in on the coils.

The corresponding equivalent electrical measurement diagram is shown in Figure 3.18.





**Figure 3.18 Coil coupling measurement equivalent circuit**

An AC signal from the GW INSTEK AFG-2125 function generator was applied to the emitter. A  $10\ \Omega$  resistor was connected in series with the emitter coil. The voltage amplitude across the resistor and the induced voltage in the receiver coil were measured directly using a Keysight DSOX3024T oscilloscope.

The mutual inductance between the emitter and receiver coils was then calculated based on Faraday's law of induction using the equations:

$$I_R = \frac{V_R}{R_{series}} \quad (3.11)$$

$$M = \frac{dI_R}{V_r dt} \quad (3.12)$$

Here,  $V_R$  is the voltage across the  $10\ \Omega$  resistor  $R_{series}$ .  $V_r$  is the voltage induced in the receiver coil.  $M$  is the calculated mutual induced between emitter and receiver coil.

### **3.5.3.6 Comparison of the results**

The calculated, simulated and measured mutual inductance between the two multi-turn coils against vertical displacement are listed in Table 3.3 and plotted in Figure 3.196. Good agreement exists between the three sets of results.

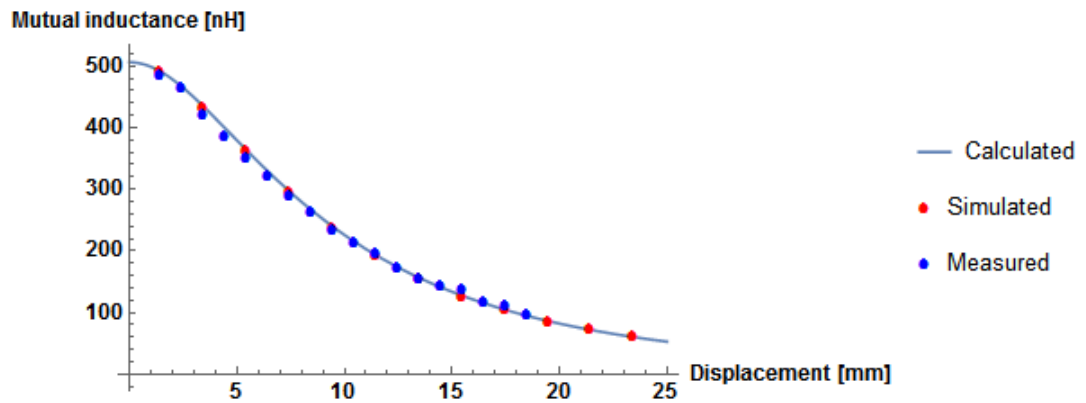


Figure 3.196 Comparison of measured, simulated and calculated mutual inductance values with vertical (Z) displacement

Table 3.3 Mutual inductance between coils with different Z direction displacement

Displacement (mm)	1.5	3.5	5.5	7.5	9.5	11.5	13.5	15.5	17.5
Mutual Inductance (nH)									
Simulation	488.2	430.3	359.2	292.4	236.0	190.1	153.7	124.9	102.1
Measured	483.8	418.1	347.7	286.8	232.3	193.9	153.8	134.6	108.9
Calculated	490.2	432.7	361.6	294.9	238.4	192.5	155.9	127.0	104.1

The difference of the measured and calculated mutual inductance between the two coils are compared with the simulation results, the difference are listed in Table 3.4. Results agree very well for all displacements with maximum error of 7.7% and average absolute error of 2.97% between measurements and simulation results. The analytical results agree well also with the simulation, with maximum error difference of 2% and average error of 1.09%.

Table 3.4 Mutual inductance error compared with simulation results

Displacement (mm)	1.5	3.5	5.5	7.5	9.5	11.5	13.5	15.5	17.5	AVG. Abs. Error
Error compared with Simulation(%)										
Measured	-0.9	-2.8	-3.2	-1.9	-1.6	1.9	0.0	7.7	6.7	2.97
Calculated	0.4	0.5	0.7	0.9	1.0	1.2	1.4	1.7	2.0	1.09

The calculated, simulated and measured mutual inductance between the two multi-turn coils against lateral displacement at a specific vertical distance ( $z = 5.5$  mm) are plotted in Figure 3.20. The negative mutual inductance indicates a change of the direction of the induced current, and therefore a change of sign of the induced voltage, as the relative position of the two coils changes.

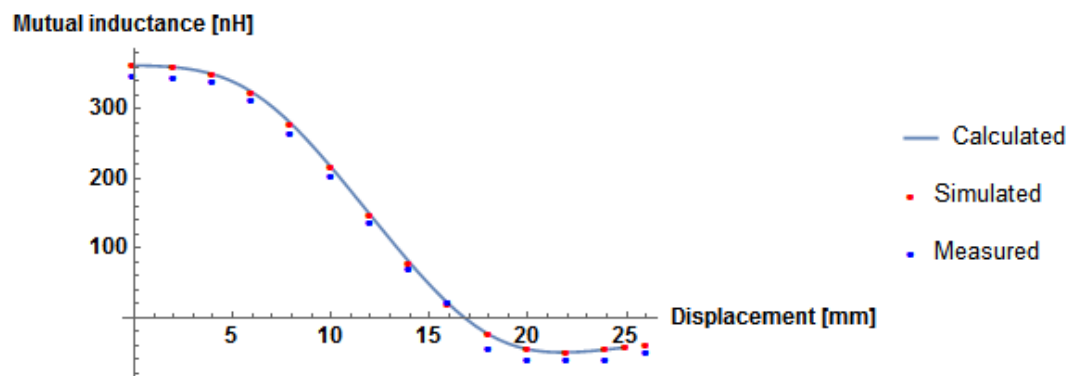


Figure 3.20 Comparison of measured, simulated and calculated mutual inductance values with lateral (Y) displacement

Table 3.5 Mutual inductance between coils with different Y direction displacements

Displacement (mm)	0	2	4	6	8	10	12	14	16	18	20	22	24	26
Mutual Inductance (nH)														
Simulation	359.3	357.0	346.9	320.7	274.8	213.4	144.6	76.5	16.8	-25.9	-47.1	-51.5	-47.4	-40.8
Measured	345.4	342.1	336.5	308.3	261.6	199.6	134.4	66.8	19.3	-46.7	-62.0	-64.4	-62.0	-53.1
Calculated	361.6	359.4	349.1	323.2	277.3	215.6	146.8	78.5	18.7	-24.0	-45.4	-49.8	-45.7	-39.1

The difference of the measured and calculated mutual inductance between the two coils are compared with the simulation results and listed in Table 3.6. The average mutual inductance difference between the calculated and simulated results is about 3% with a maximum difference of 11.3%. The average mutual inductance difference between the measured and simulated results is 18.5% with maximum difference value of 80.3%. The mutual inductance values at 18 mm to 26 mm of displacement were larger than at other positions. As the misalignment increases, the induced voltage in the receiver coil becomes smaller and is similar to the amplitude of the noise picked up by the probe, resulting in a large inaccuracy in the measurement.

**Table 3.6 Mutual inductance error compared with simulation results**

Displacement (mm) Error compared with Simulation (%)	0	2	4	6	8	10	12	14	16	18	20	22	24	26	AVG. Abs Error
Measured	-3.9	-4.2	-3.0	-3.9	-4.8	-6.5	-7.1	-12.7	14.9	80.3	31.6	25.0	30.8	30.1	18.5
Calculated	0.6	0.7	0.6	0.8	0.9	1.0	1.5	2.6	11.3	-7.3	-3.6	-3.3	-3.6	-4.2	3.0

### 3.5.4 Coupling between coil plates

#### 3.5.4.1 Simulation

Simulation was carried out in ANSYS Maxwell™ to study the influence of the conductive plate on the coupling between coils. The simulated configuration is shown in Figure 3.21, whereby two rectangular coils are placed on a same substrate and one copper plate is placed beneath them. The mutual inductance between the two coils is simulated at different plate positions.

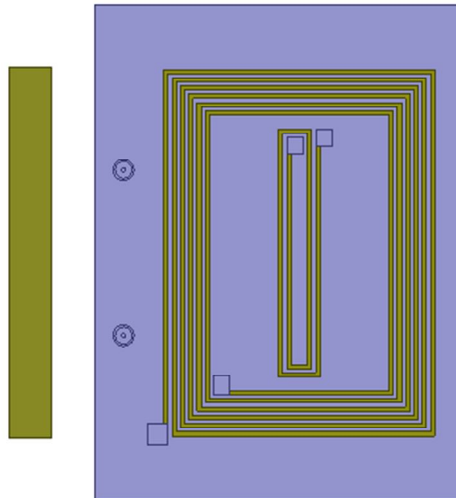


**Figure 3.21 Coil plate structure used in simulation. The length of the scale is 10 mm; width is 2 mm and the thickness is 0.035 mm.**

The dimensions of the coils in the simulation are listed in Table 3.7 below.

**Table 3.7 Dimensions of the coils**

	Turns	Track width ( $\mu\text{m}$ )	Track gap ( $\mu\text{m}$ )	Track thickness ( $\mu\text{m}$ )	Inner length (mm)	Inner width (mm)
<b>Emitter</b>	6	200	200	35	13.2	8.7
<b>Receiver</b>	2	200	200	35	10	0.8

The simulation results of the mutual inductance between emitter and receiver at different relative scale plate positions are shown in Figure 3.22. The induced eddy currents affect the coupling between the emitter and the receiver coil when the scale is strictly beneath the receiver coil. In that position, the coupling between emitter and receiver reaches the smallest value. In the graph, the gap is defined as the vertical separation between the scale plate and the two coils: the closer the scale to the coils, the larger the influence on the coupling is.

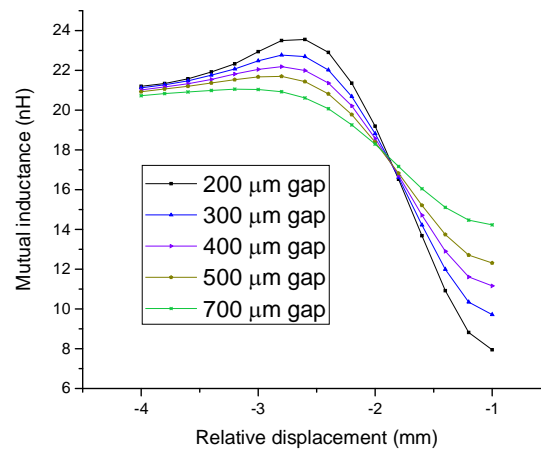


**Figure 3.22 Simulated mutual inductance change against vertical and horizontal displacements**

#### **3.5.4.2 Measurement**

The coils and the plate were fabricated using PCB technology to verify the simulation results. Both emitter and receiver coils were fabricated on the same board, while the rectangular plate was fabricated on a separate PCB. The influence of the scale on the coupling between emitter and receiver coils was measured with the measurement setup shown in Figure 3.30 .

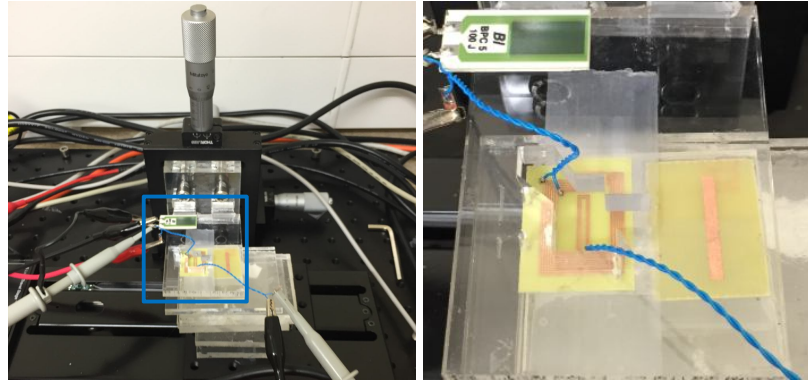


**Figure 3.30** Coil plate coupling measurement setup: left measurement setup; right zoom in on the coils and plate.

The equivalent circuit of the measurement setup is shown in Figure 3.31.

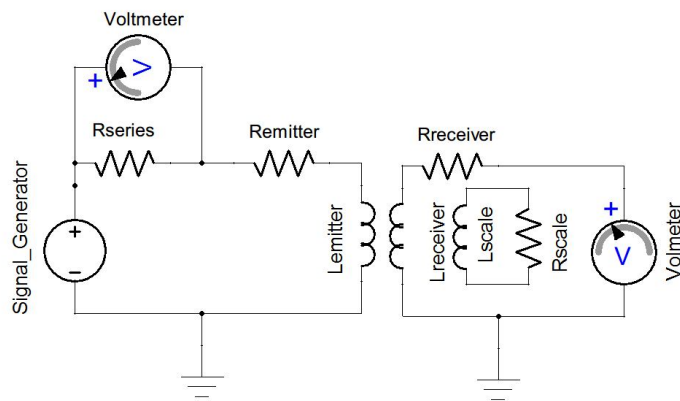


**Figure 3.31** Coil plate coupling measurement equivalent circuit

The planar coils are fixed on the same 3-axis manual stage described in the previous section. The copper scale is attached to a motorized stage from Thorlab beneath them, via holes drilled on both the coil and plate substrates for alignment purpose. The corresponding electrical measurement diagram is shown in Figure 3.31. The emitter and receiver coils are modelled as a resistor in series with an inductor. The copper plate, modelled as a multi-turn coil is also represented as a resistor,  $R_{scale}$ , connected in series with an inductor,  $L_{scale}$ . A  $10\ \Omega$  resistor,  $R_{series}$ , is connected in series with the emitter coil. The voltage developed across it was measured using an Keysight oscilloscope from which the current across the emitter coil was calculated. The induced voltage in the receiver coil, and therefore the mutual inductance, was also measured at different displacements of the scale plate.

The mutual inductance is calculated using Equation 3.13 for a frequency  $f$  of 1 MHz. The peak-peak value of the voltage across the resistor  $V_R$  and induced voltages in the two receiver pairs  $V_{ind}$  were measured using the same oscilloscope.

$$V_{ind} = 2\pi f * M * I_{emitter} \cos(2\pi f t) \quad (3.13)$$

$$M = \frac{V_{ind}}{2\pi f * I_{emitter}} \quad (3.14)$$

Mutual inductance values for relative displacement in the Y and Z directions are shown in Figure 3.32. Note that the relative displacement -1mm is where the plate was right beneath the receiver coil.

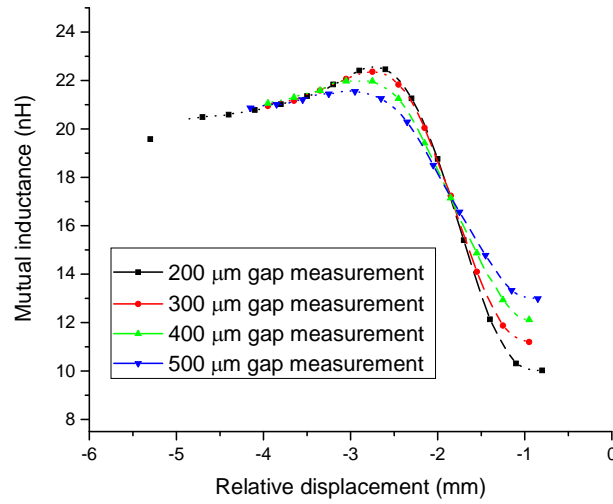
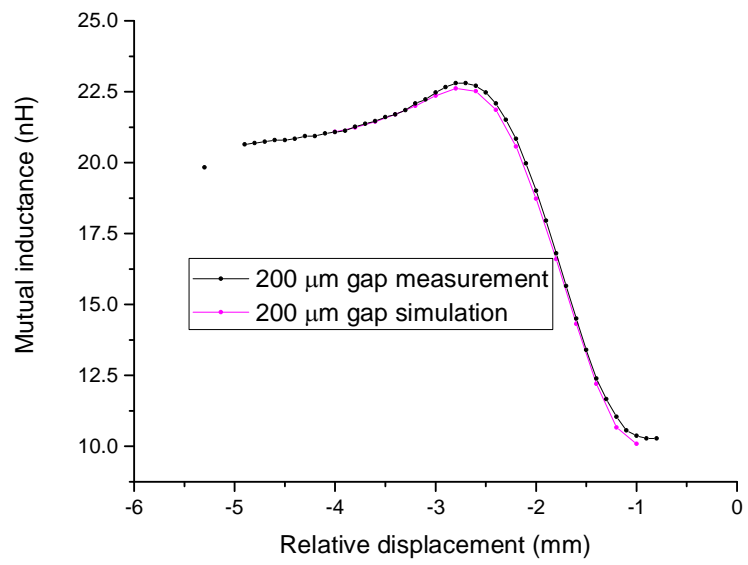
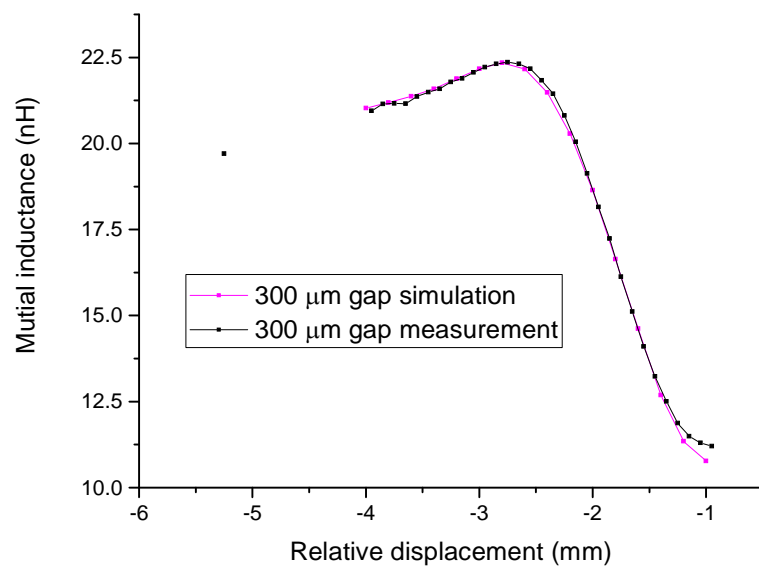


**Figure 3.32 Measured mutual inductance affected by the copper plate**

The simulation and measurement results have been compared in Figure 3.33 at different gaps (Z-direction). The simulated and measured results agreed well except for 500 μm gap, this could be because of the inaccurate alignment during the measurement.

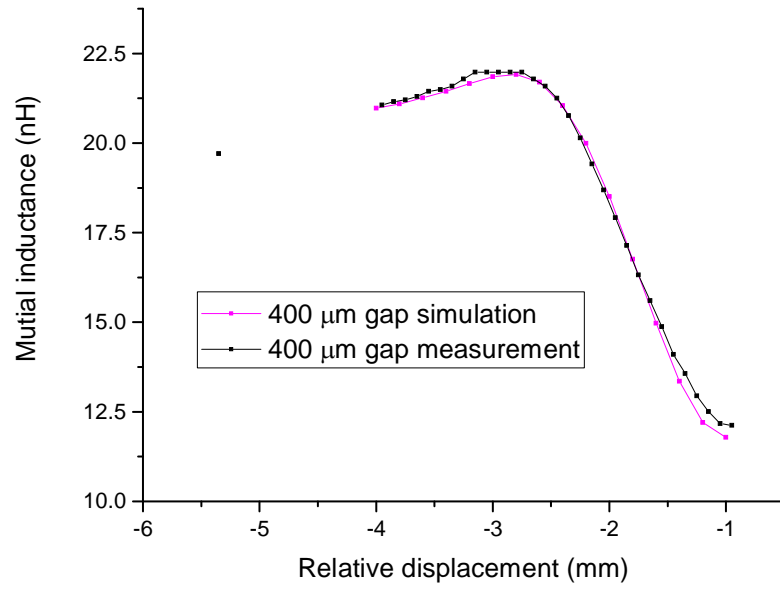


(a)

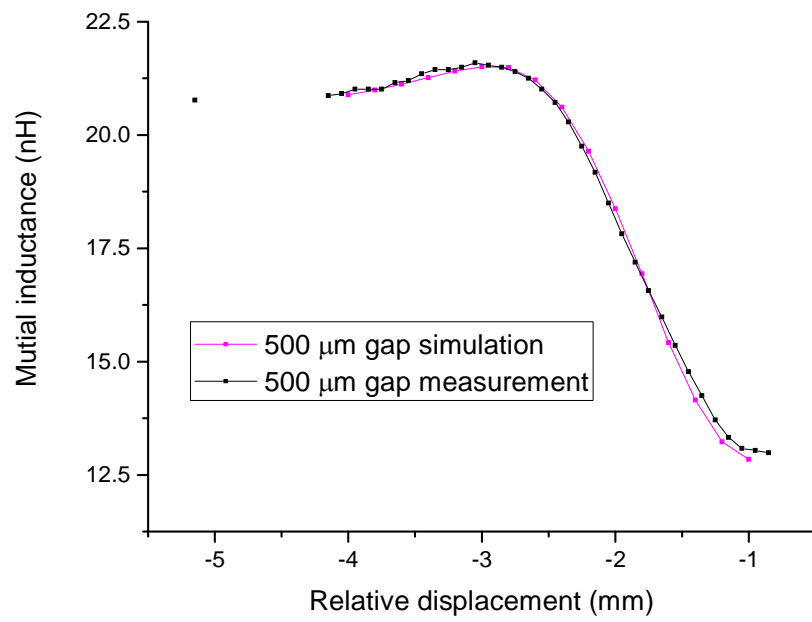


(b)





(c)



(d)

**Figure 3.33 Simulation mutual inductance compared with measured values.**

The simulated and measured results are also listed in Table 3.8

**Table 3.8 Mutual inductance difference between simulation and measurement with different vertical gaps**

	<b>Mutual inductance with different vertical gaps (nH)</b>											
	<b>200 <math>\mu\text{m}</math></b>			<b>300 <math>\mu\text{m}</math></b>			<b>400 <math>\mu\text{m}</math></b>			<b>500 <math>\mu\text{m}</math></b>		
Dis. (mm)	Sim.	Mea.	Er. %	Sim.	Mea.	Er. %	Sim.	Mea.	Er. %	Sim.	Mea.	Er. %
-4	21.1	21.1	0.0	21.0	21.0	-0.4	21.0	21.1	0.4	20.9	21.0	0.6
-3.8	21.2	21.3	0.2	21.2	21.2	-0.1	21.1	21.2	0.5	21.0	21.2	0.8
-3.6	21.4	21.5	0.1	21.4	21.4	0.0	21.3	21.4	0.9	21.1	21.3	1.1
-3.4	21.7	21.7	0.0	21.6	21.6	0.0	21.4	21.6	0.7	21.3	21.4	0.8
-3.2	22.0	22.1	0.4	21.9	21.9	0.1	21.7	22.0	1.5	21.4	21.6	0.8
-3	22.4	22.5	0.5	22.2	22.2	0.2	21.8	22.0	0.6	21.5	21.5	-0.1
-2.8	22.6	22.8	0.8	22.3	22.4	0.1	21.9	22.0	0.3	21.5	21.3	-1.1
-2.6	22.5	22.7	0.9	22.2	22.2	0.0	21.7	21.6	-0.5	21.2	20.7	-2.3
-2.4	21.9	22.1	1.1	21.5	21.4	-0.2	21.0	20.8	-1.3	20.6	19.8	-4.2
-2.2	20.6	20.8	1.3	20.3	20.0	-1.2	20.0	19.4	-2.9	19.6	18.5	-5.8
-2	18.7	19.0	1.5	18.6	18.2	-2.6	18.5	17.9	-3.2	18.4	17.2	-6.4
-1.8	16.6	16.8	1.2	16.6	16.1	-3.1	16.8	16.3	-2.6	16.9	16.0	-5.6
-1.6	14.3	14.5	1.3	14.6	14.1	-3.5	15.0	14.9	-0.6	15.4	14.8	-4.1
-1.4	12.2	12.4	1.5	12.7	12.5	-1.5	13.3	13.6	1.6	14.1	13.7	-3.1
-1.2	10.7	11.0	3.6	11.4	11.5	1.2	12.2	12.5	2.5	13.2	13.1	-1.1
-1	10.1	10.4	2.7	10.8	11.2	3.9	11.8	12.1	2.8	12.8	13.0	1.1
ER. AVG.			1.06			1.13			1.43			2.44

The average error for 200  $\mu\text{m}$ , 300  $\mu\text{m}$ , 400  $\mu\text{m}$  and 500  $\mu\text{m}$  gaps are 1.06%, 1.13%, 1.43% and 2.44%, respectively. The error at 500  $\mu\text{m}$  gap is larger than with the other gaps, due to the possible misalignment during the measurement. Indeed, by shifting the data by 0.15mm to the right along the X-axis, the agreement of the measurement and the simulation data will be much better, the average error is about 1.2%, as shown in Figure 3.234.

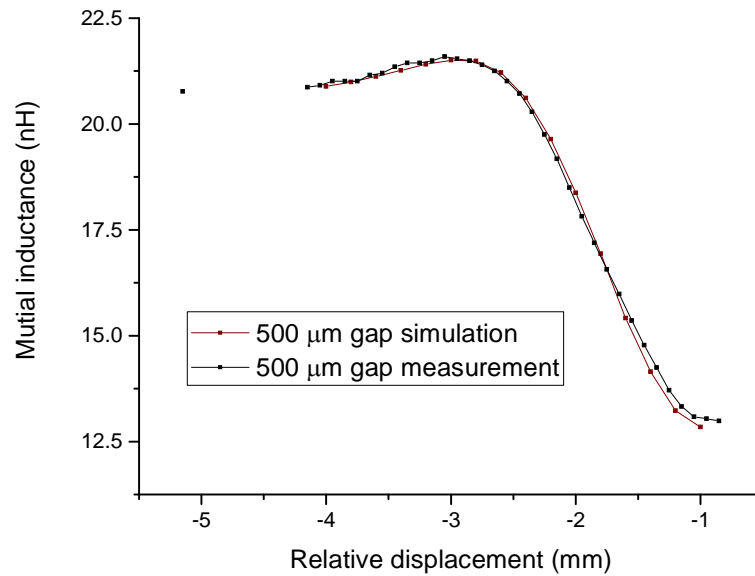


Figure 3.234 Comparison of simulated and measured mutual inductance with the measured data shifted 0.15mm to right.

## 3.6 System output

Different encoder outputs are described in this section. As described previously, the scale has been simplified as a rectangular coil. Possible reason for the encoder output nonlinearity error is also proposed.

### 3.6.1 System output

With the simplification of the scale as a multi-turn coil, the whole system can be considered as being made of coils. The encoder output can then be studied by calculating the coupling between the coils, an example of which is shown in Figure 3.24.

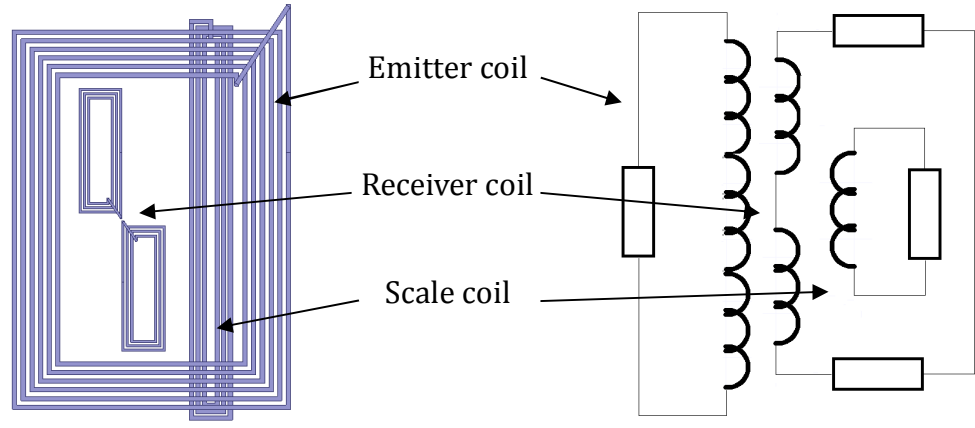


Figure 3.24 Encoder equivalent coil system, left: emitter, receiver pair and scale coils; right: equivalent circuit model.

Let the excitation current in the equivalent emitter coil be  $j\omega * I_{emitter}$ , with  $\omega$  the angular frequency of the exciting current and  $I_{emitter}$  amplitude of the current. There will be two induced voltages in the receiver pair: one induced by the emitter coil and the other by the eddy currents in the scale coil. The induced voltage in the receiver by the emitter is:

$$V_{emitter12}^{Ind} = j\omega * (M_{offset1} - M_{offset2}) * I_{emitter} = j\omega * M_{offset} * I_{emitter} \quad (3.15)$$

Here  $M_{offset1}$  and  $M_{offset2}$  are the mutual inductances between the emitter coil and the two receiver coils in the receiver pair.  $M_{offset}$  is the total mutual inductance between the emitter and the receiver pair.

Eddy currents should be calculated to determine the voltage in the receiver pair induced by the scale coil. The induced current in the scale coil by the emitter is:

$$I_{eddy} = \frac{j\omega * M_{emisca} * I_{emitter}}{Z_{scale}} = j\omega * M_{esr} * I_{emitter} \quad (3.16)$$

Here  $M_{emisca}$  is the mutual inductance between the emitter coil and the scale coil.  $Z_{scale}$  is the impedance of the scale coil and can be calculated using the method proposed in [28].

The induced voltage in the receiver pair by the eddy currents is:

$$V_{eddy12}^{Ind} = j\omega * M_{coil} * I_{eddy} \quad (3.17)$$

Here  $M_{coil}$  is the mutual inductance between the receiver pair and the scale coil so that:

$$V_{eddy12}^{Ind} = j\omega * M_{esr} * M_{coil} * I_{emitter} \quad (3.18)$$

The total induced voltage in the receiver pair by both the emitter coil and the scale coil is therefore:

$$V_{receiver}^{Ind} = V_{emitter12}^{Ind} + V_{eddy12}^{Ind} = (M_{offset} + M_{esr} * M_{coil}) * j\omega * I_{emitter} \quad (3.19)$$

As the relative position of the emitter coil and the receiver pair is constant, so is  $M_{offset}$ .  $M_{esr}$  and  $M_{coil}$  are position related with  $M_{coil}$  changing periodically with the scale position. We assume here that the change of  $M_{esr}$  is small enough and can be treated as constant value. This assumption will be discussed in the next subsection. We also assume that  $M_{coil}$  is sinusoidal of the form:

$$M_{coil} = M_{coil}^{Amp} * \sin(2 * \pi * x) , \quad (3.20)$$

Where  $x$  is the relative displacement between the receiver pair and the scale coil.  $M_{coil}^{Amp}$  is the amplitude of the mutual inductance. The induced voltage in the receiver pair can be written as:

$$V_{receiver}^{Ind} = (M_{offset} + M_{esr} * M_{coil}^{Amp} * \sin(2 * \pi * x)) * j\omega * I_{emitter} \quad (3.21)$$

If  $U_1 = M_{offset}$ ,  $A_1 = M_{esr} * M_{coil}^{Amp}$ , Equation 3.21 can be simplified as:

$$V_{receiver}^{Ind} = (U_1 + A_1 * \sin(2 * \pi * x)) * j\omega * I_{emitter} \quad (3.22)$$

In the time domain:

$$V_{receiver}^{Ind} = (U_1 + A_1 * \sin(2 * \pi * x)) * I_{emitter} * \sin(\omega * t) \quad (3.23)$$

Based on the value of  $U_1$  and  $A_1$ , three different waveforms of the induced voltage can be generated.

If  $U_1$  is zero, the induced voltage is an AM signal with 100% modulation depth as shown in Figure 3.25

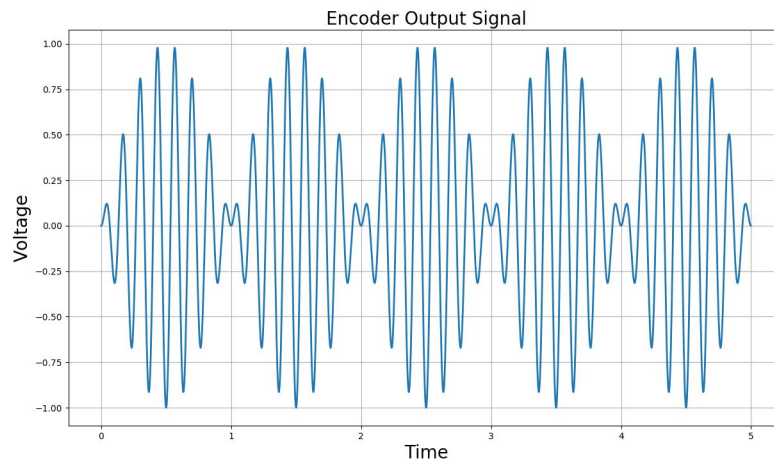


**Figure 3.25 Induced voltage in the receiver pair when  $U_1$  is zero**

If  $U_1$  is not zero and smaller than  $A_1$ , the induced voltage will be in the form of an over modulated AM signal with an interval big and small amplitude as shown in Figure 3.26

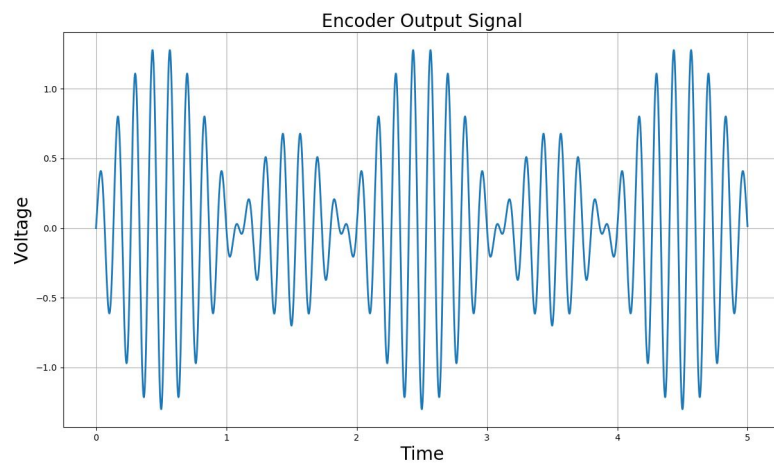


**Figure 3.26 Induced voltage in the receiver pair when  $U_1$  is not zero and smaller than  $A_1$**

If  $U_1$  is larger than  $A_1$ , the induced voltage will be in the form of AM signal with modulation depth less than 100% and is represented as shown in Figure 3.27.

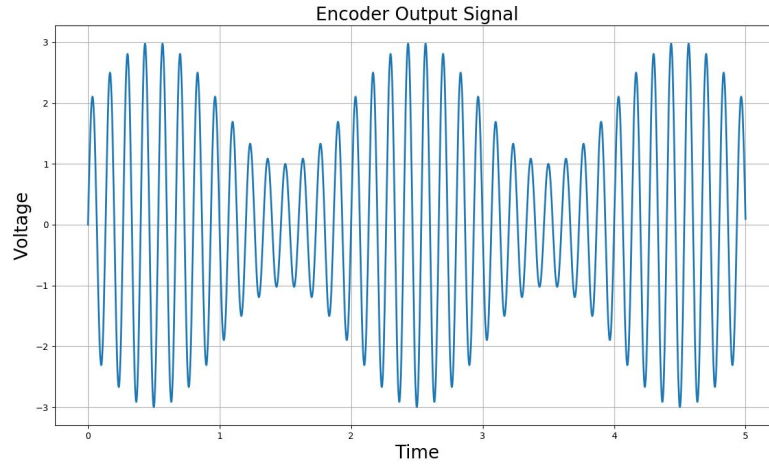
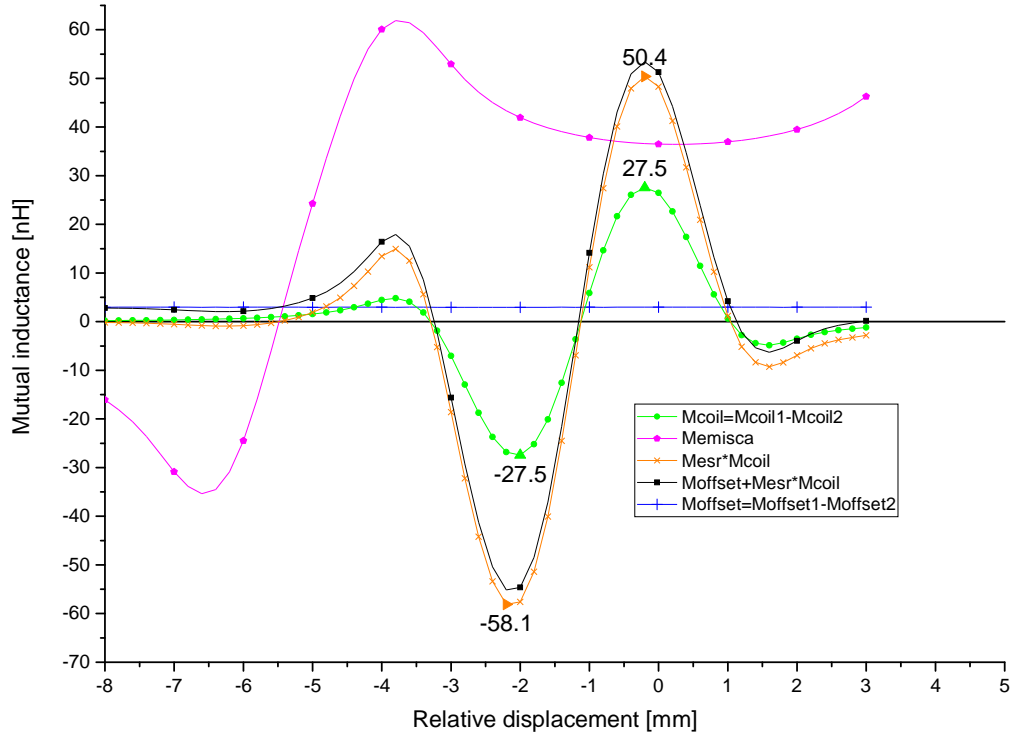


Figure 3.27 Induced voltage in the receiver pair when  $U_1$  is larger than  $A_1$

### 3.6.2 Possible reason for the encoder output nonlinearity error

The results obtained in the previous subsection are based on the assumption that the mutual inductance between the scale coil and the emitter coil is constant. This assumption is discussed here.

The mutual inductances between the coils are simulated using ANSYS Maxwell™ and plotted in Figure 3.289.  $M_{offset}$  only provides a constant small level shift on the final mutual inductance. It does not affect the coupling between the emitter coil and scale coil thus the coupling between emitter coil and the receiver pairs does not affect the encoder output nonlinearity error. As for the coupling between the receiver pair and the scale coil,  $M_{coil}$ , the absolute maximum and minimum values are the same and equal to 27.5 nH. However the mutual inductance value between the emitter coil and the scale coil  $M_{emisca}$  is not constant as assumed. So the maximum and minimum value of  $M_{esr} * M_{coil}$  becomes 50.4 nH and -58.1 nH. This could be the main reason for the encoder output nonlinearity error.



**Figure 3.289 Simulated mutual inductances of the coil structure**

To increase the accuracy of the encoder, the change of  $M_{emisca}$  should be reduced. This could be achieved by making the field of the emitter coil more uniform by changing the shape and dimensions of the emitter coil.

### 3.7 Summary

Literature review on eddy currents based magnetic encoder has been presented in this chapter. A new encoder structure composed of one emitter coil and two receiver coil pairs working with a conductive metal scale has been proposed.

Neumann formula was used to calculate the mutual inductance between multi turn coils with different relative positions. The measured and calculated results were compared with the simulated results. Good agreements were achieved with absolute values of the average errors for Z-axis displacements of 2.97% and 1.09%. The values of the average errors for the Y-axis displacements were 18.5% and 3.0%.



The influence of the metal scale on the coupling between emitter coil and receiver coil was also simulated. The influence on the mutual inductance at different gaps were simulated and measured. The simulated results and the measured results were compared with absolute value of the average errors are 1.06%, 1.13%, 1.43% and 2.44% for 200  $\mu\text{m}$ , 300  $\mu\text{m}$ , 400  $\mu\text{m}$  and 500  $\mu\text{m}$  respectively.

Three different encoder output signals are generated by treating the scale as a multi turn coil. The main reason for the encoder output nonlinearity error is because the coupling between the emitter coil and the scale coil is not constant as the relative displacement changes. This could be reduced by making the field of the emitter coil more uniform through changing the emitter coil shape or geometries such as coil turns, track width and gaps.

## Reference

- [1] J. D. Edwards, B. V. Jayawant, W. R. C. Dawson, and D. T. Wright, "Permanent-magnet linear eddy-current brake with a non-magnetic reaction plate," *IEEE Proceedings-Electric Power Applications*, vol. 146, pp. 627-631, Nov 1999.
- [2] C. Holtmann, F. Rinderknecht, and H. E. Friedrich, "Simplified model of eddy current brakes and its use for optimization," *2015 Tenth International Conference on Ecological Vehicles and Renewable Energies (Ever)*, 2015.
- [3] H. J. Shin, J. Y. Choi, H. W. Cho, and S. M. Jang, "Analytical Torque Calculations and Experimental Testing of Permanent Magnet Axial Eddy Current Brake," *IEEE Transactions on Magnetics*, vol. 49, pp. 4152-4155, Jul 2013.
- [4] H. Sarnago, O. Lucia, A. Mediano, and J. M. Burdio, "Design and implementation of a high-efficiency multiple-output resonant converter for induction heating applications featuring wide bandgap devices," *IEEE Transactions on Power Electronics*, vol. 29, pp. 2539-2549, 2014.
- [5] S. Semiatin, *Elements of induction heating: design, control, and applications*: ASM International, 1988.
- [6] O. Lucía, P. Maussion, E. J. Dede, and J. M. Burdío, "Induction heating technology and its applications: past developments, current technology, and future challenges," *IEEE Transactions on Industrial Electronics*, vol. 61, pp. 2509-2520, 2014.
- [7] N. Yusa, H. Hashizume, R. Urayama, T. Uchimoto, T. Takagi, and K. Sato, "An arrayed uniform eddy current probe design for crack monitoring and sizing of surface breaking cracks with the aid of a computational inversion technique," *NDT & E International*, vol. 61, pp. 29-34, 2014.
- [8] R. Hamia, C. Cordier, and C. Dolabdjian, "Eddy-current non-destructive testing system for the determination of crack orientation," *NDT & E International*, vol. 61, pp. 24-28, 2014.
- [9] H. L. Qi, H. Zhao, and W. W. Liu, "Multi-parameters Optimization and Nonlinearity Analysis of the Grating Eddy Current Displacement Sensor," *2008 IEEE Conference on Robotics, Automation, and Mechatronics, Vols 1 and 2*, pp. 511-516, 2008.

- [10] W. W. Liu, H. Zhao, W. Tao, and C. F. Lv, "Research on combinatorial-code grating eddy-current absolute-position sensor," *Ieee Transactions on Instrumentation and Measurement*, vol. 61, pp. 1113-1124, Apr 2012.
- [11] W. W. Liu, H. Zhao, and H. L. Qi, "Research on Novel Grating Eddy-Current Absolute-Position Sensor," *Ieee Transactions on Instrumentation and Measurement*, vol. 58, pp. 3678-3683, Oct 2009.
- [12] H. L. Qi, T. Li, and J. Lin, "Parameters Optimization for GECDS Using Response Surface Methodology and Genetic Algorithms," *Proceedings of 2015 Ieee 5th International Conference on Electronics Information and Emergency Communication*, pp. 198-202, 2015.
- [13] H. L. Qi, H. Zhao, W. W. Liu, and H. B. Zhang, "parameters optimization and nonlinearity analysis of grating eddy current displacement sensor using neural network and genetic algorithm," *Journal of Zhejiang University-Science A*, vol. 10, pp. 1205-1212, Aug 2009.
- [14] H. L. Qi, H. Zhao, and W. W. Liu, "characteristic analysis and parameters optimization for the grating eddy current displacement sensor," *Journal of Zhejiang University-Science A*, vol. 10, pp. 1029-1037, Jul 2009.
- [15] M. Kamon, A.-M. Nguyen, and J. R. Gilbert, "A Design Tool for Inductive Position and Speed Sensors via a Fast Integral Equation Based Method," in *Technical Proceedings of the 1999 International Conference on Modeling and Simulation of Microsystems*, 1999, pp. 313 - 317.
- [16] M. Podhraski and J. Trontelj, "A Differential Monolithically Integrated Inductive Linear Displacement Measurement Microsystem," *Sensors (Basel)*, vol. 16, Mar 17 2016.
- [17] T. Posic. (2017, 17, 2). *Technology - Posic*. Available at : [www.posic.com](http://www.posic.com).
- [18] M. Podhraski and J. Trontelj, "An Integrated Microtransformer System for Displacement Measurement," *Informacije Midem-Journal of Microelectronics Electronic Components and Materials*, vol. 46, pp. 29-35, Mar 2016.
- [19] M. Podhraski and J. Trontelj, "Linear Incremental Displacement Measurement System with Microtransformers," *Informacije Midem-Journal of Microelectronics Electronic Components and Materials*, vol. 46, pp. 149-153, Sep 2016.

- [20] H. Irle, N. Kost, and F. J. Schmidt, "Inductive linear position sensor including exciting and receiving coils and a movable induction coupling element," ed: Google Patents, 2002.
- [21] V. Vasiloiu, "Inductive measuring device for detecting relative position and/or movement," ed: Google Patents, 2003.
- [22] A. N. Dames, "Position detection using a spaced apart array of magnetic field generators and plural sensing loop circuits offset from one another in the measurement direction," ed: Google Patents, 2000.
- [23] D. T. F. Ely and A. N. Dames, "Position sensor having compact arrangement of coils," ed: Google Patents, 2003.
- [24] V. Vasiloiu and H. Eisschiel, "Inductive measuring device for detecting lengths and angles," ed: Google Patents, 2015.
- [25] A. M. Niknejad and R. G. Meyer, "Analysis of eddy-current losses over conductive substrates with applications to monolithic inductors and transformers," *IEEE Transactions on Microwave Theory and Techniques*, vol. 49, pp. 166-176, 2001.
- [26] C. V. Dodd and W. E. Deeds, "Analytical Solutions to Eddy - Current Probe - Coil Problems," *Journal of Applied Physics*, vol. 39, pp. 2829-2838, 1968.
- [27] W. G. Hurley and M. C. Duffy, "Calculation of self and mutual impedances in planar sandwich inductors," *IEEE Transactions on Magnetics*, vol. 33, pp. 2282-2290, 1997.
- [28] R. T. Smith, "Circuit Analysis of Eddy Currents," *IEEE Transactions on Aerospace and Electronic Systems*, vol. AES-11, pp. 495-498, 1975.
- [29] M. S. H. Akram, Y. Terada, I. Keiichiro, and K. Kose, "Coupled circuit numerical analysis of eddy currents in an open MRI system," *Journal of Magnetic Resonance*, vol. 245, pp. 1-11, 8, 2014.
- [30] M. Krakowski, "Eddy-current losses in thin circular and rectangular plates," *Archiv für Elektrotechnik*, vol. 64, pp. 307-311, 1982.
- [31] D. Flynn, A. Toon, L. Allen, R. Dhariwal, and M. P. Y. Desmulliez, "Characterization of Core Materials for Microscale Magnetic Components Operating in the Megahertz Frequency Range," *IEEE Trans. Magn.*, vol. 43, no. 7, pp. 3171–3180, Jul. 2007.

- [32] D. Flynn and M. P. Y. Desmulliez, "Design methodology and fabrication process of a microinductor for the next generation of DC–DC power converters," *Microsyst. Technol.*, vol. 15, no. 8, pp. 1233–1243, Aug. 2009.

## Chapter 4 - Demodulation circuit and PCB encoder prototypes

### 4.1 Introduction

Four new different encoder structures were simulated, fabricated and measured in this chapter. The output AM signals of these encoders were amplified and demodulated using the signal processing circuits designed and presented in this chapter. The accuracy (encoder output nonlinearity error) of the different versions were compared. Guidelines for future designs were deduced in the light of the results obtained.

### 4.2 Signal processing circuit

As analyzed in Chapter 3, the output signals of the encoders are amplitude modulated (AM) signals with different modulation depths. The most generic form of the obtained signals can be written as:

$$x(t) = (C + m(t)) * \cos(\omega * t) \quad (4.1)$$

In the equation above,  $\omega$  is the angular frequency of the excitation signal applied to the emitter coil;  $m(t)$  is the mutual inductance change. Synchronous demodulation method is used to demodulate the AM signal with different modulation depths such that:

$$y(t) = (C + m(t)) * \cos(\omega * t) * \cos(\omega * t) \quad (4.2)$$

After simplification, Equation 4-2 can be written as:

$$y(t) = \frac{1}{2} (C + m(t)) (1 + \cos(2 * \omega * t)) \quad (4.3)$$

The signal is then filtered using a low pass filter leaving only the DC signal  $m(t)$ . As the encoder works in a principle similar to a differential transformer, the amplitude of the signal can be quite small, so signal amplification is required at the source. The

signal processing flowchart is shown in Figure 4.1. The signal of the encoder is amplified first and then demodulated using synchronous demodulator, passed through the low pass filter. The envelope of the amplitude modulated signal is thereby extracted and fed into the interpolator or other signal processing circuit that will convert the signal into displacement information.

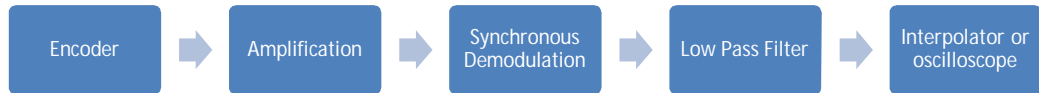


Figure 4.1 Signal processing flowchart

#### 4.2.1 Amplification circuit

As described in the previous chapter the encoder has the similar configuration as a differential transformer. It is therefore represented as a differential transformer in the circuit diagram shown in Figure 4.2. Two resistors,  $R_1$  and  $R_3$ , are connected in series to the pair of receivers, forming a bridge detection circuit which is sensitive to the impedance change of the pair. The signal is then amplified using the amplifier INA103 from Texas Instrument, which is a very low noise, low distortion instrumentation amplifier and has 100MHz gain-bandwidth product. The circuit connection is shown in Figure 4.2.

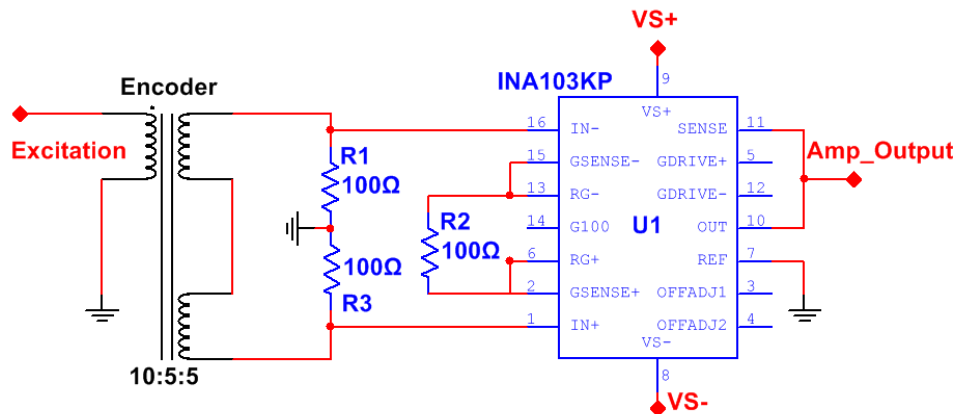


Figure 4.2 Amplification circuit configuration using INA103

#### 4.2.2 Demodulation circuit

The output signal, *Amp\_Output* in Figure 4.2, of the amplifier is fed into the AD630 demodulator circuit which is a high precision demodulator from Analog Devices. The device has 2 MHz channel width which is suitable for the encoder whose working frequency is 1 MHz. As shown in Figure 4.3, the amplified signal is demodulated by the excitation signal, *Trig*, connected to the Excitation pin. The output of the demodulator, *pin 13*, is connected to a RC low pass filter. The filter is composed of a 10 K $\Omega$  resistor and a 0.002  $\mu$ F capacitor, providing a cut-off frequency at about 8 KHZ, which is sufficient to filter out the 1 MHz excitation signal. The wiring of the demodulator and low pass filter is shown in Figure 4.3.

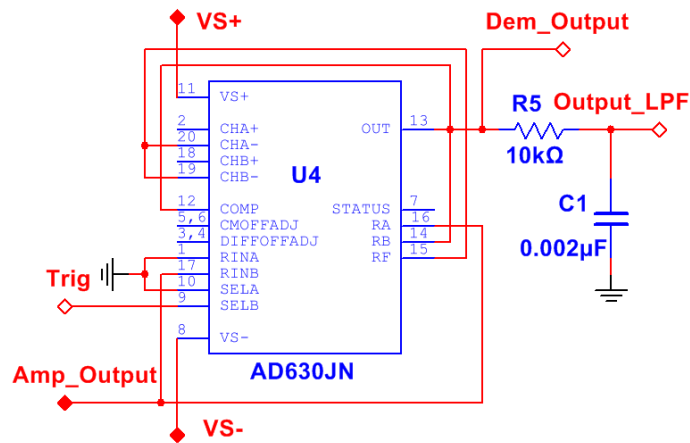
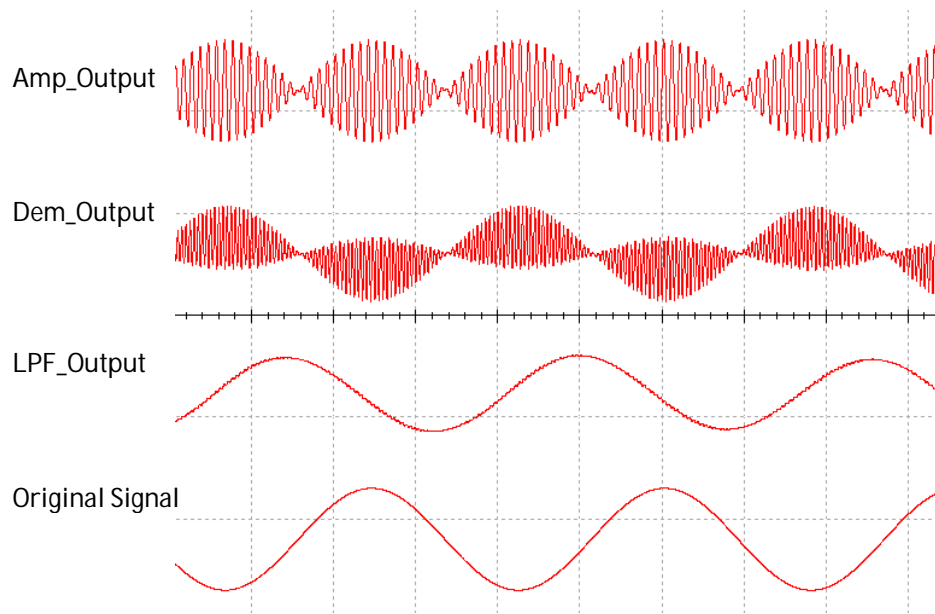


Figure 4.3 Demodulation and low pass filter circuit configuration using AD630

The amplification and demodulation circuits were simulated using Multisim software from National Instruments. Results are shown in Figure 4. 4. Looking at the various waveforms from top to bottom, the AM signal is amplified by amplifier INA103 and demodulated by AD630. The signal is then further processed by the RC low pass filter and the final output signal is then converted to displacement by corresponding circuit such as interpolator. The original signal is given on the bottom row.





**Figure 4. 4 Simulation result of the demodulation circuit. From top to bottom: AM signal; after demodulation; after low pass filter; original signal.**

A breadboard circuit embodying the circuit layout was used to process the output signal of the encoder, the measured waveform is shown in Figure 4.5. It can be seen that the demodulation circuit can recover the signal from the large noise.

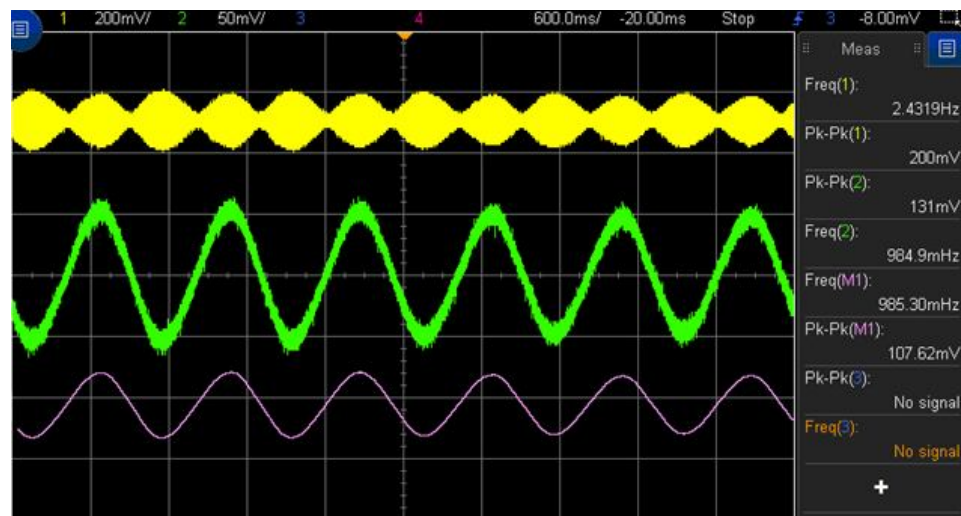


**Figure 4.5 Demodulation output: yellow channel is signal before demodulation and green channel is the signal after demodulation; pink channel is signal further filtered by the oscilloscope built-in low pass filter.**

### 4.3 Prototypes of encoders using PCB technology

Different encoder structures were fabricated using typical PCB technology. This section presents the different encoder structures and corresponding simulation and measurement results.

### 4.3.1 Prototype One

#### 4.3.1.1 Simulation

As discussed in Chapter 3, the proposed encoder structure is composed of rectangular coils. One single layer encoder prototype was simulated using the software package ANSYS Maxwell™; the structure of the single layer device is shown in Figure 4.6.

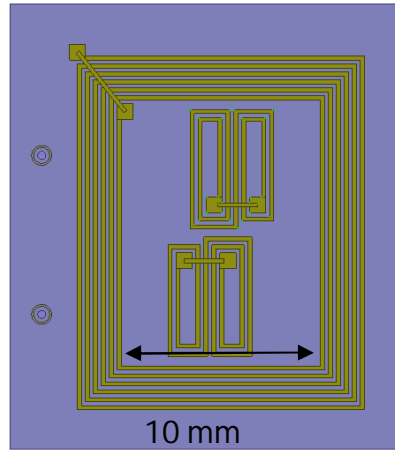


Figure 4.6 Prototype of single layer encoder structure. Dimensions listed in Table 4.1

The prototype consists of one rectangular emitter coil and two receiver pairs which are composed of four rectangular coils. The dimensions of the coils are listed in Table 4.1.

Table 4.1 Dimensions of the emitter and receiver pairs coils (in mm)

Emitter				Receiver			
Inner length	Inner width	Track gap	Track width	Outer length	Outer width	Track gap	Track gap
13.4	10	0.2	0.2	6	2	0.2	0.2

The width of the receiver coil is 2 mm with a 0.2 mm gap between the two coils in the same receiver pair, so the average width of the coils is 2.2mm. The width of one receiver pair is therefore 4.4 mm. The bottom receivers pair is placed at a 1.1 mm ( $\lambda/4$ ) offset to top receivers pair in the horizontal direction, resulting in a 90° phase shift between the two signals in the two receiver pairs. As the width of the pair of receivers determines the period of the copper plates on the scale, the width and gap of the copper plates on the scale are also 2.2 mm, as shown in Figure 4.7.

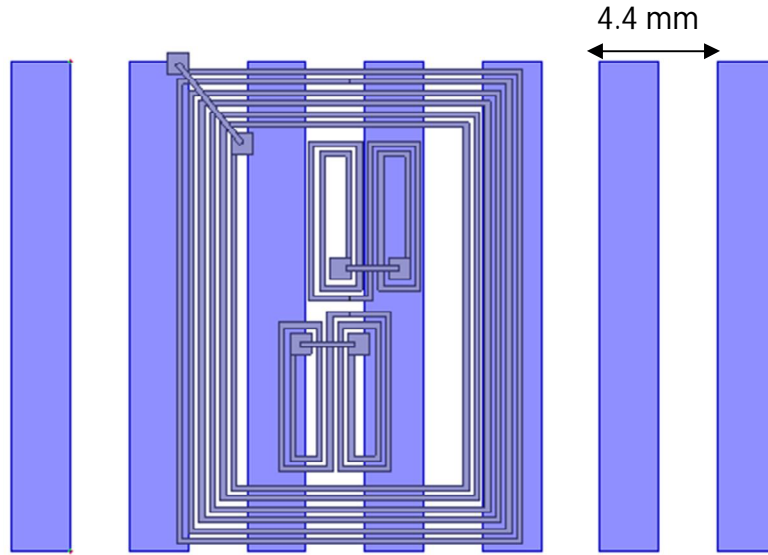


**Figure 4.7 Encoder structure of prototype one together with scale.**

This whole structure was simulated using the software package ANSYS Maxwell™. Changes of the emitter-receiver pair mutual inductance values were measured as a function of the relative position of the scale with respect to the encoder. The resulting simulation data were imported into OriginLab™ software and plotted in Figure 4.8. Please note that the negative displacement is relative to the central position of the encoder.

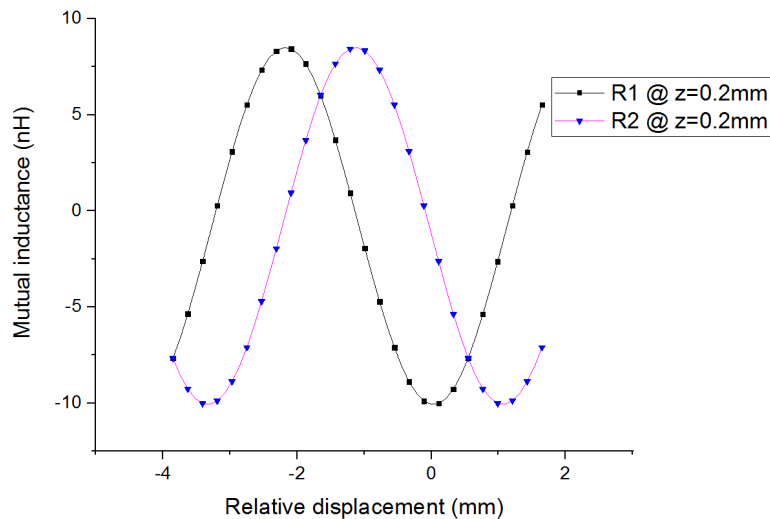


**Figure 4.8 Mutual inductance between emitter and receiver pairs (R1, R2) against different scale position. The separation between the encoder and the scale is 0.2 mm.**

The Lissajous curve of the mutual inductance, plotted in Figure 4.9, was compared to a perfect circle. The adjusted R-squared value of the circular fitting is excellent and equal to 0.99913.

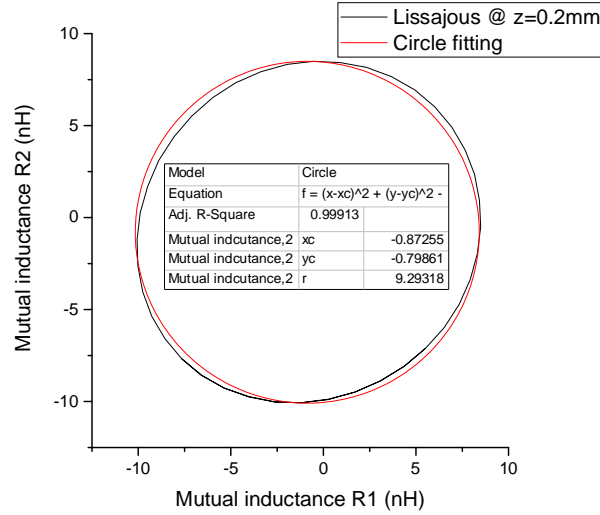


**Figure 4.9 Lissajous curve of the mutual inductance at z=0.2mm**

In the figure above, the Lissajous curve resembles a rotated ellipse. From the analysis carried out in Chapter 2, this geometrical shape indicates a phase shift different from 90° between the output signals of the two receiver pairs. The position of the center of the Lissajous curve and the amplitude of signals also imply that there are DC offset and amplitude imbalance in the two signals. As it is difficult to calculate the DC offset, amplitude imbalance and phase shift separately, the output nonlinearity of the encoder is first calculated. Assuming the encoder output signals are sinusoidal and an ideal 90° phase difference between the two signals:

$$V_a = U_1 + A_1 * \sin(\theta) \quad (4.4)$$

$$V_b = U_2 + A_2 * \cos(\theta) \quad (4.5)$$

Where  $U_1$  and  $U_2$  are the DC offsets of signals  $V_a$  and  $V_b$ , respectively, and  $A_1$  and  $A_2$  are the maximum amplitudes of the AC components of the signals. The tangent value can be written as:

$$\tan(\theta) = \frac{\sin(\theta)}{\cos(\theta)} = \frac{(V_a - U_1)/A_1}{(V_b - U_2)/A_2} \quad (4.6)$$

Thus the corresponding phase difference at different positions can be calculated:

$$\theta = \text{Arctan}(\theta) = \text{arctan}\left(\frac{\frac{V_a - U_1}{A_1}}{\frac{V_b - U_2}{A_2}}\right) \quad (4.7)$$

The arctangent value was plotted as a function of the displacement of the scale as shown in Figure 4.10. As the calculated phase covers more than one period, it is unwrapped for future linear fitting.

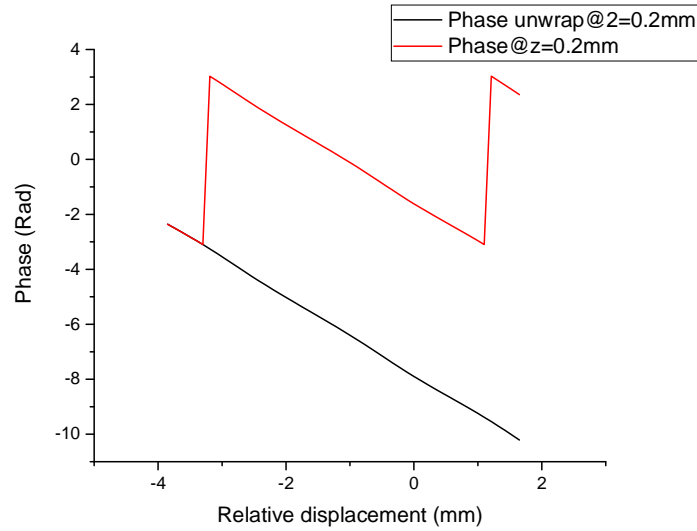


**Figure 4.10 Phase and unwrapped phase plotted as a function of the relative displacement of the scale with respect to the encoder.**

A linear fitting is carried out on the unwrapped phase-displacement curve to analysis the encoder output nonlinearity. The fitting result is plotted in Figure 4.11. The adjusted R-squared value of the linear fitting is 0.99987.

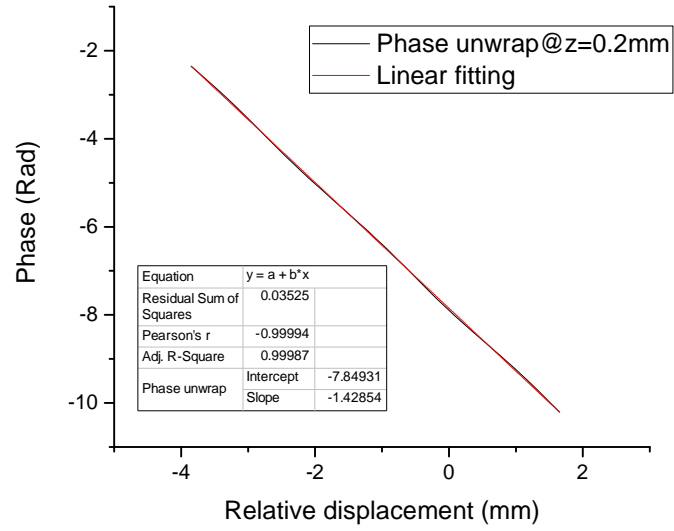


**Figure 4.11 Linearity of phase displacement**

The residual of the linear fitting, plotted in Figure 4.12, varies from -0.04 to 0.04 Rad, which corresponds to a displacement of  $\pm 30 \mu\text{m}$  according to the following calculation.

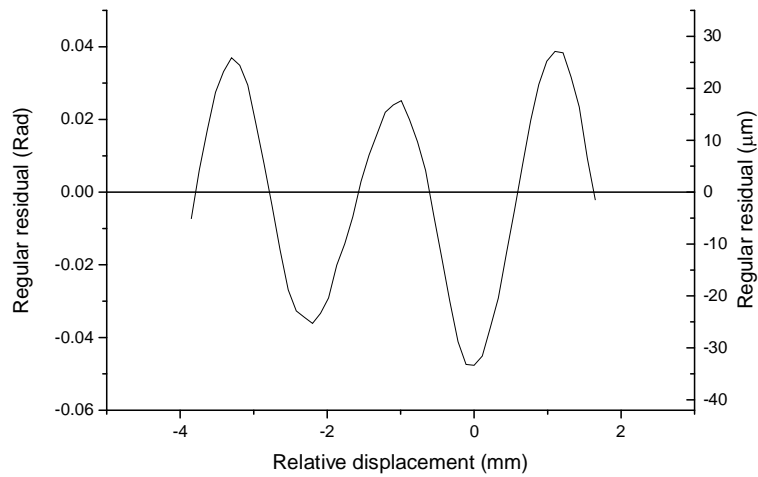


**Figure 4.12 Linearity fitting residual of the phase displacement**

The calculated phase should vary from  $-\pi$  to  $\pi$  which corresponds to the period of the plates on the scale. The residual of the linear fitting can therefore be converted to the corresponding displacement using the equation:

$$\frac{R_{rad}}{R_{dis}} = \frac{2*\pi}{\lambda} \quad (4.8)$$

Here  $R_{rad}$  is the residual expressed in radians and  $R_{dis}$  is the corresponding displacement residual.  $\lambda$  is the period length of the plates on the scale which equals to the width of one receiver pair. Using Equation 4.8 the residual was converted to displacement which ranges from -30  $\mu\text{m}$  to 30  $\mu\text{m}$  ( $\text{Rad}/2/\text{Pi}*4400$ ), as plotted on the axis on the right hand-side in Figure 4.12.

#### 4.3.1.2 Experimental results

The device was fabricated using PCB technology as shown in Figure 4.13; the geometrical dimensions of the coils are the same as listed in Table 4.1, as etching method was used, the real dimensions of the coils may have about 5-10  $\mu\text{m}$  difference from the designed values, this influence is believe to be neglectable as discussed later in the chapter. The thickness of the coil tracks is 35  $\mu\text{m}$  and the thickness of the substrate is 0.2 mm.

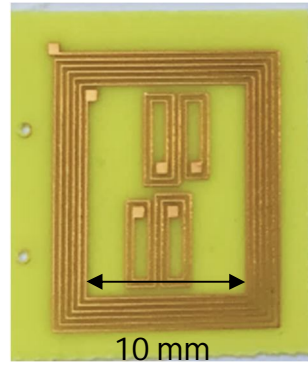


Figure 4.13 PCB device prototype

The corresponding scale was also fabricated using PCB technology as shown in Figure 4.14. Rectangular copper plates were fabricated on a FR4 substrate with 2.2 mm width and 2.2 mm gap.

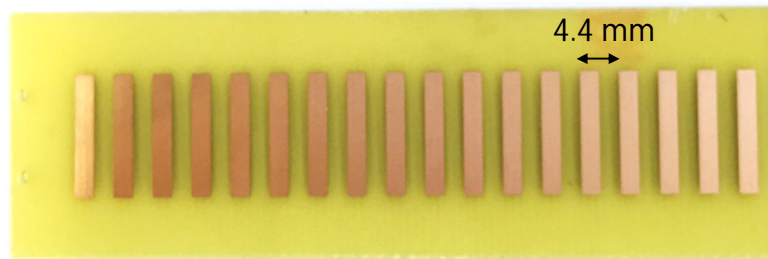
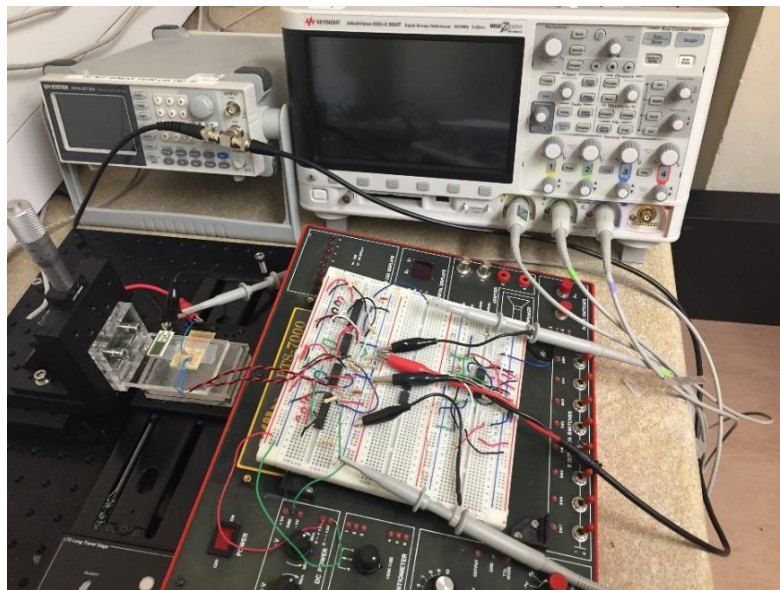


Figure 4.14 PCB scale: 0.8 mm FR4 thickness and 35  $\mu\text{m}$  copper thickness

The measurement setup, shown in Figure 4.15, is similar to the one described in Chapter 3. The setup was used to measure the influence of the scale on the coupling between emitter and receivers. Twisted wires were soldered onto the terminals of the coils to reduce the influence of the electromagnetic noise. The fabricated PCB encoder head was attached to a PT3/M stage (Thorlabs Inc.) , which is a 3-axis translation stage with 10  $\mu\text{m}$  resolution and 25 mm travel range in all 3 directions. The PCB scale was attached to a LTS150/M stage (Thorlabs Inc.) which is a motorized stage with 150 mm linear travelling range and 0.1  $\mu\text{m}$  resolution, placed beneath the encoder read head. An AC signal from the GW INSTEK AFG-2125 function generator was applied to the emitter coil. A 10  $\Omega$  resistor was connected in series with the emitter coil, with the voltage amplitude across the resistor measured directly using Keysight DSOX3024T oscilloscope. The current in the emitter coil could then be calculated. The output signals of the receiver coils were connected to the amplification and demodulation circuit assembled on the bread board. After amplification and demodulation, the signals were also measured using Keysight DSOX3024T oscilloscope.



**Figure 4.15 Encoder measurement setup**

The measured direct output of the encoder receiver coils before amplification is shown in Figure 4.16. The output signals of the two receiver pairs behave as over modulated AM signals as discussed in Chapter 3. In order to make the signal obvious in the measurement set up, the frequency of the excitation current was set to 5 MHz



which increases the amplitude of the induced voltages by increasing the strength of the eddy currents. The scale itself was attached to a motorized stage and moved at a constant speed.

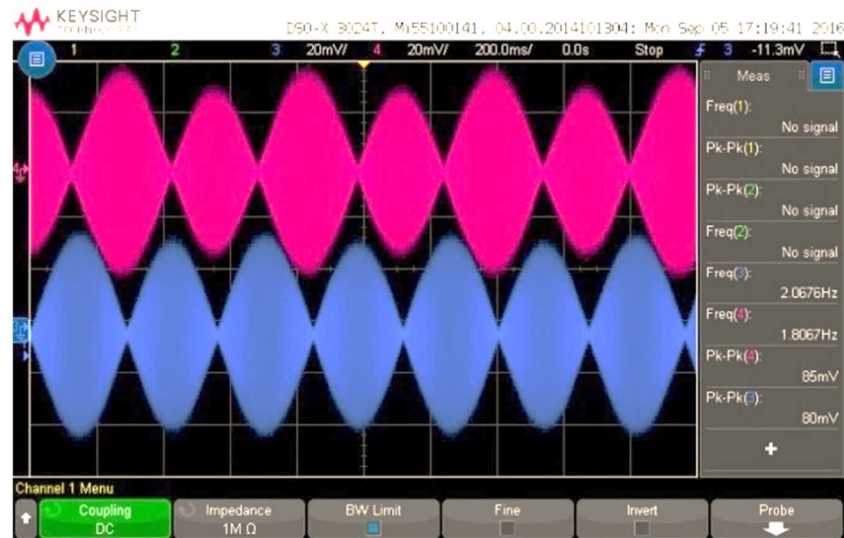


**Figure 4.16 Induced voltage in the receiver pairs. 5 MHz 10 Vpp signal generator output, 3.06 Vpp across a 10  $\Omega$  resistor.**

#### 4.3.1.2.1 Static scale measurement

To get the envelope of the induced voltage signal, a scale measurement method was performed whereby the scale was moved in increments of 0.1 mm and the amplitudes of the induced voltages recorded. The measured amplitudes of the voltages were plotted against the displacement as shown in Figure 4.17.

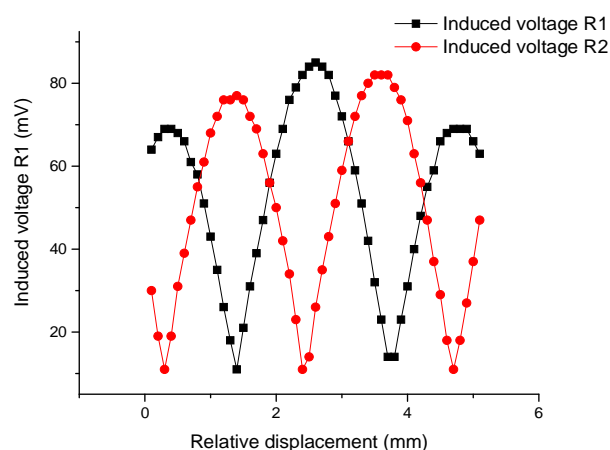


**Figure 4.17 Induced voltage in the receiver pairs with different scale displacements**

As seen in Figure 4.17, the minimum values of the two voltage signals are around 10 mV, due to the noise picked up by the oscilloscope when there is no input in the emitter coils. After subtracting the noise from the signals, the minimum value of the two voltages were nearly zero as shown in figure 4.18.

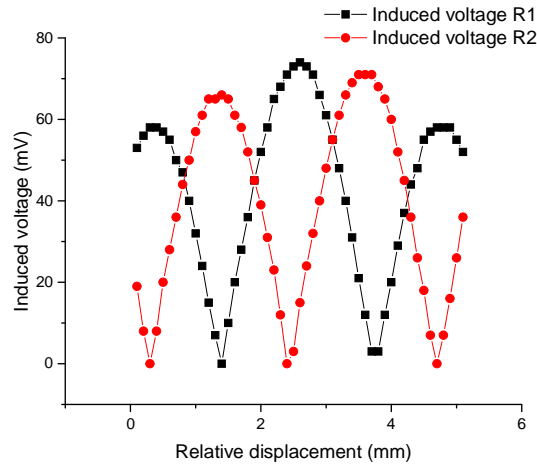


**Figure 4.18 Induced voltages in receiver pairs with noise subtracted from measurements.**

In the measurement, only the positive half of the envelope of the AM signals could be measured. To get the full envelope, the sign of the half period of the measured voltage values was changed where the amplitude should have been negative as shown in Figure 4.19. These values were compared with the simulation results after converting the simulated mutual inductances to voltages using Equation 3-13 in Chapter 3, and plotted in Figure 4.20.

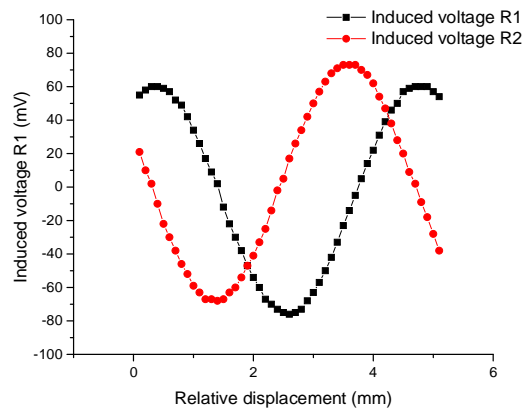


**Figure 4.19 Induced voltages in the receiver pairs after conversion**

The average amplitude difference (AAD) was defined as the induced voltage amplitude difference between the simulated and measured induced signals divided by the amplitude of the simulated signal. The AAD values for the two receiver pairs,  $R_1$  and  $R_2$ , were 8.8% and 13.1%, respectively. This difference could be due to the misalignment of the coils with the scale in one or three directions during the measurement and the electromagnetic noise during the measurement. More details on this matter will be discussed later in this chapter.

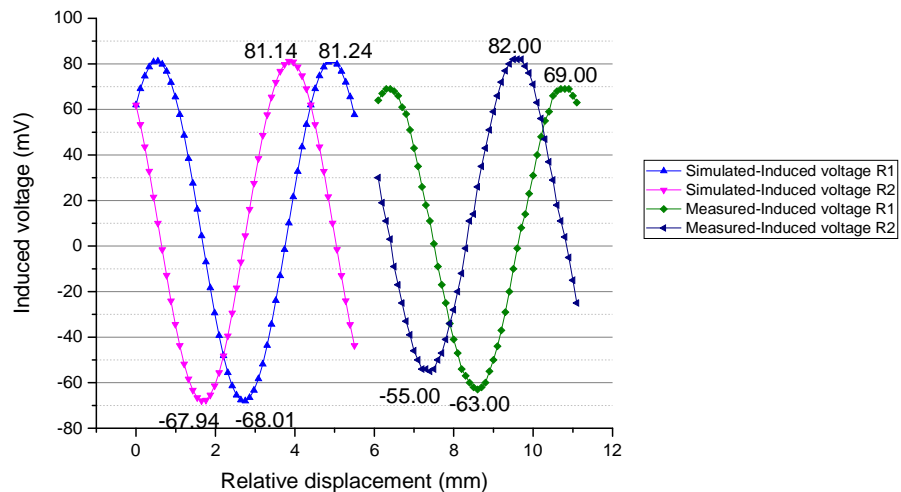


Figure 4.20 Comparison between simulated and measured voltages.

The Lissajous curves and curve fitting of the measured induced voltages are plotted in Figure 4.21. The adjusted R-square value of the fitting is 0.99719.

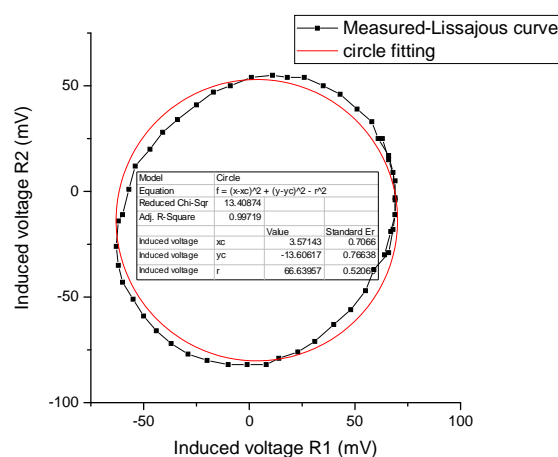
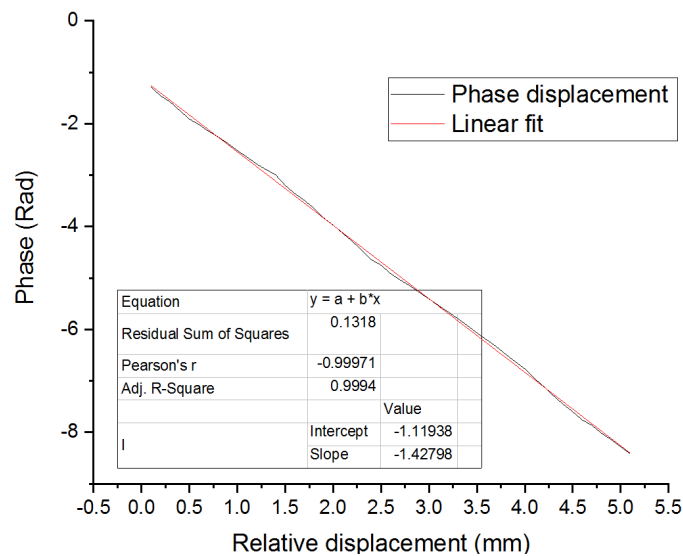


Figure 4.21 Lissajous curve of the measured induced voltage

The phases were calculated using Equation 4-7 and plotted against displacement as shown in Figure 4.22, together with the corresponding linear fitting. The adjusted R-square value of the fitting is 0.9994.



**Figure 4.22 Linear fitting of the calculated phase-displacement curve of the measured result**

The residual of the linear fitting is plotted below in Figure 4.23. The residual ranges from -0.1 to 0.125 radian, which corresponds to a displacement of about 70 to 80  $\mu\text{m}$ .

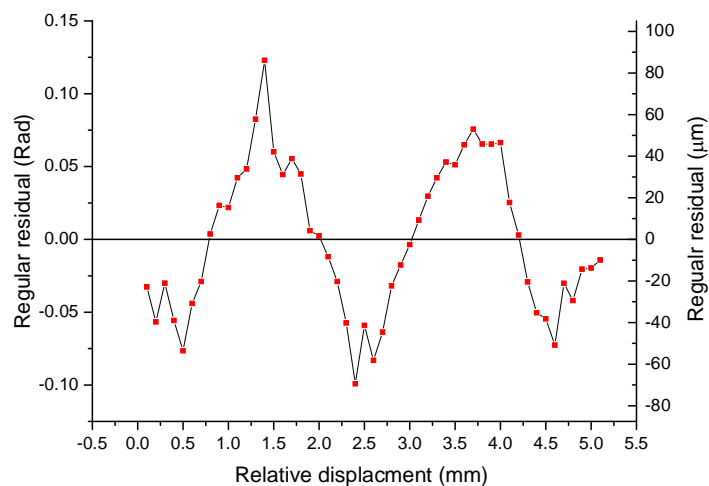


**Figure 4.23 Residual of linear fitting**

#### 4.3.1.2.2 Demodulation circuit measurement

The scale measurement method is only employed for comparing the measured and simulated voltages before the demodulation circuit was built. An easier

measurement method is to use the demodulation circuit. The AM signals of the two receiver pairs were amplified and demodulated using the breadboard circuit with the outputs of the circuit measured using the oscilloscope as shown in Figure 4.24. The peak-to-peak amplitude of the two signals,  $R_1$  and  $R_2$ , are 504.27 mV and 495.23 mV, respectively.

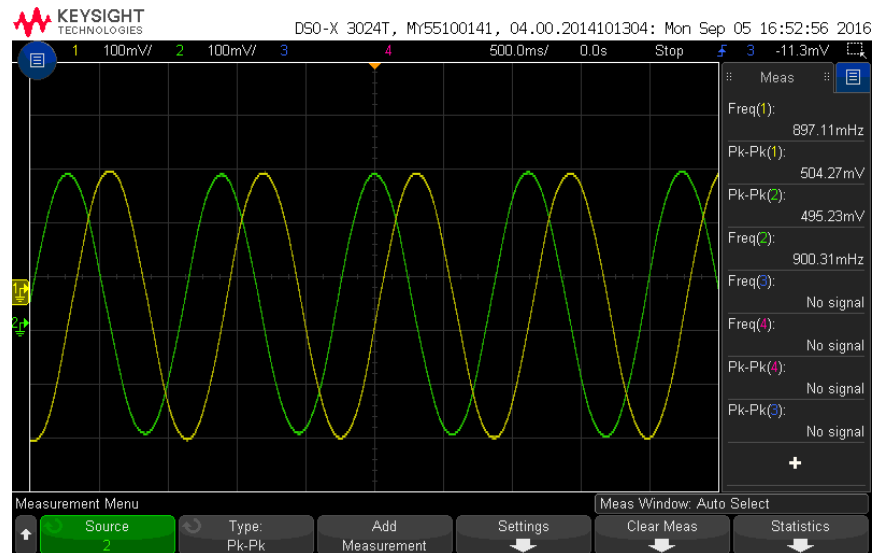


**Figure 4.24 Demodulation circuit output**

Data over slightly more than one period was imported into the OriginLab™ software package as shown in Figure 4.25. The x-axis in the plot is the time is assumed to be linear with displacement as the scale is moving at constant speed. Please note that the time here is relative, negative time means the data is sampled before the central position on the oscilloscope screen.

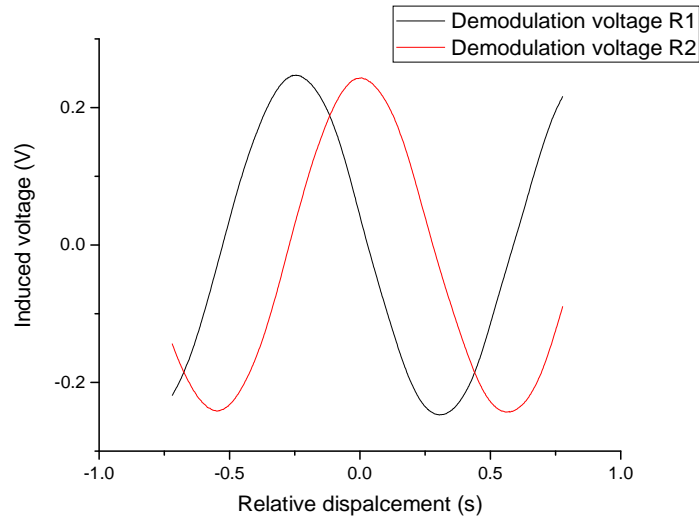


**Figure 4.25 Signals output from the demodulation circuit.**

The Lissajous curve of the signal is plotted in Figure 4.26 together with a circular fitting; the adjust R-square value for the fitting is 0.99744.

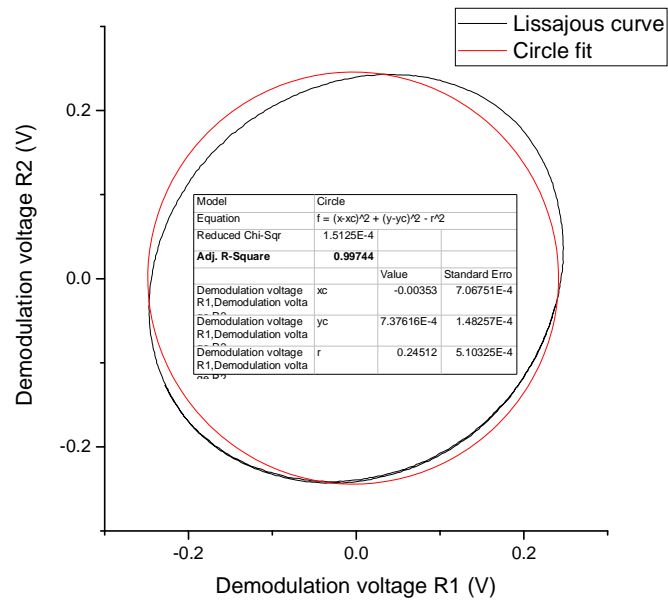


**Figure 4.26 Lissajous curve and circle fitting of the demodulated signal.**

The phase for the corresponding displacement was calculated using Equation 4-7 and plotted in Figure 4.27 together with linear fitting. The adjusted R-square value of the fitting is 0.99996.

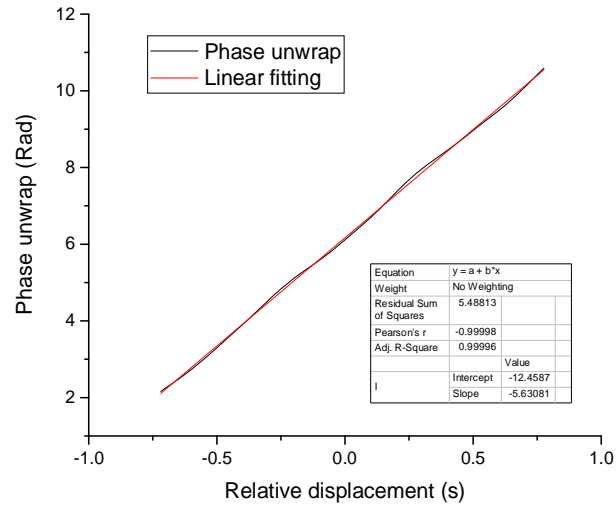


**Figure 4.27 Linear fitting of the calculated phase displacement curve of the demodulation signal.**

The residual of the fitting is shown in Figure 4.28. The residual ranges from -0.1 to 0.75 Rad which corresponds to a displacement of about -80 to 60  $\mu\text{m}$ .

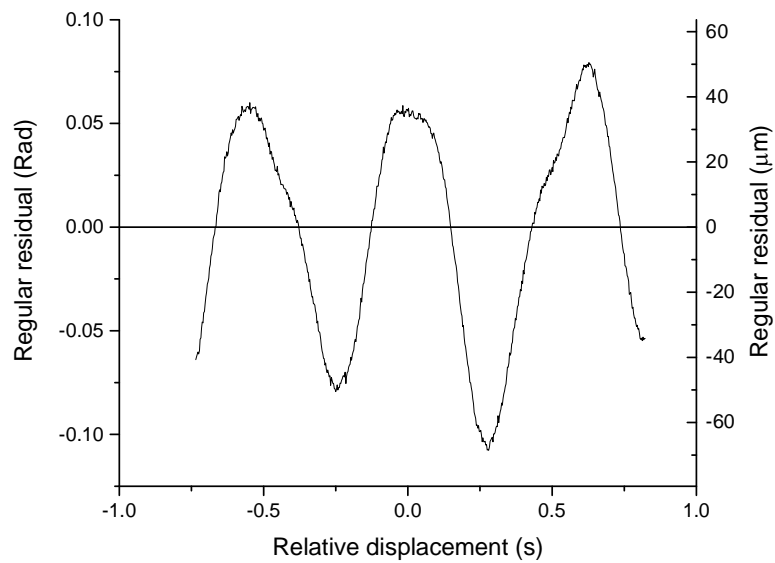


**Figure 4.28 Fitting residual of the linear fitting**

#### **4.3.1.3 Improvement of Prototype one**

From the Lissajous curves of the simulated and measured results, there is a phase shift error between the outputs of the two receiver pairs, as discussed in Chapter 2. The simulated mutual inductances of the two receiver pairs were further analyzed using FFT (Fast Fourier Transform) to get the phase difference between them. The

detailed implementation Mathematica script is listed in Appendix A. Assuming that the two signals are sinusoidal and of same frequency, the calculated phase shift between the two channels is about  $85.44^\circ$  instead of  $90^\circ$ . The phase difference corresponds then to  $4.56/360 \times 4400$  which equals to  $56 \mu\text{m}$  using Equation 4-8.

The second receiver pair was therefore moved  $50 \mu\text{m}$  closer to the first receiver pair to compensate for the phase shift calculated above. The offset between the two receiver pairs is now  $1.05 \text{ mm}$ . Using the software package ANSYS Maxwell™, the simulation results of the new configuration are shown in Figure 4.29.

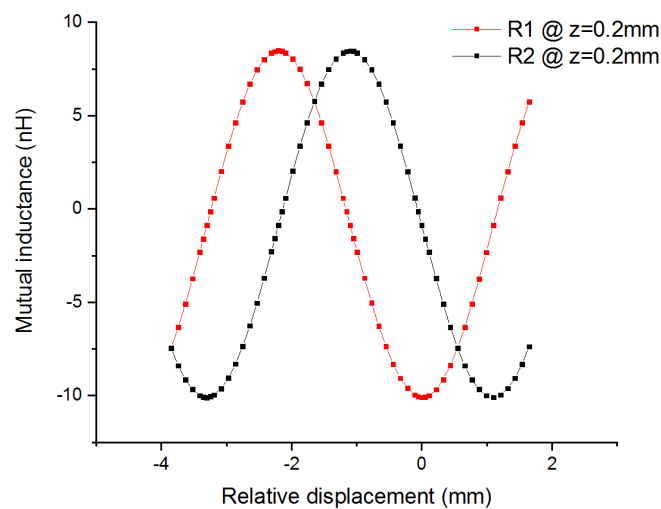


**Figure 4.29 Simulated mutual inductance.**

The Lissajous curve of the simulated mutual inductance is plotted in Figure 4.30 together with a circular fitting; the R-square value of the fitting is about 0.99999.

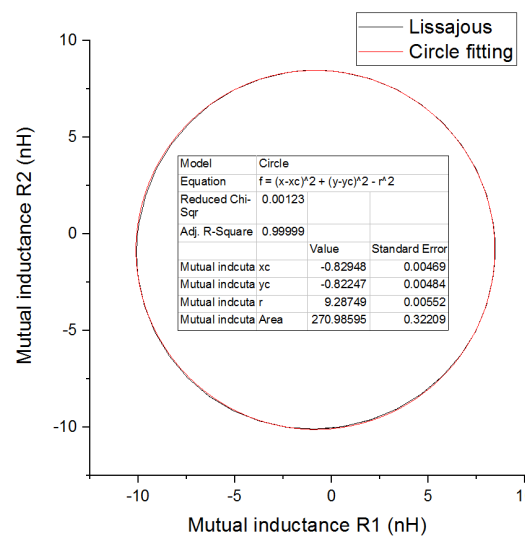


**Figure 4.30 Lissajous curve of the simulated mutual inductance.**



The phase displacement curve of the updated structure was calculated using Equation 4-7 and plotted together with a linear fitting as in Figure 4.31. The adjusted R-square value of the fitting is 1, which implies the phase is almost linear with displacement.

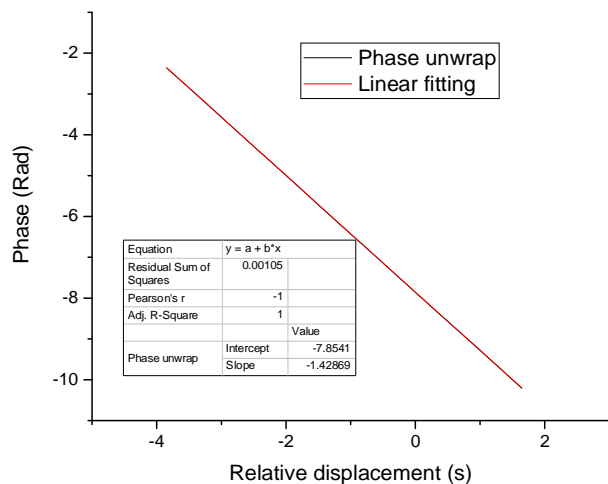


**Figure 4.31 Linear fitting of the phase displacement curve.**

The residual of the linear fitting, plotted in Figure 4.32, results in residual ranges from -0.075 to 0.075 radians, which correspond to -5 to 5  $\mu\text{m}$  virtual displacement.

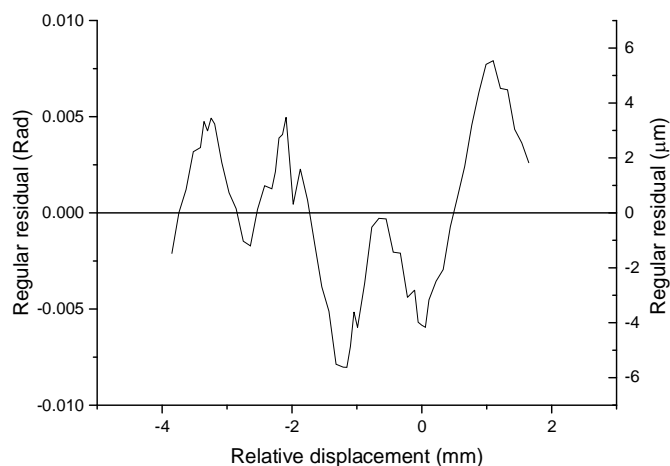


**Figure 4.32 Linear fitting residual**

The above results confirm that the width of the receiver pair should be 4.2 mm (4 x 1.05 mm). The period of the plates on the scale should also be adjusted to 4.2 mm in the simulation with width and gap at 2.1 mm. The Lissajous curve of the simulation results were plotted below together with circular fitting in Figure 4.33; the adjusted

R-square value of the fitting is 0.9986. The Lissajous curve is not a circle, which implies that the plate width and gap should stay at 2.2 mm. A possible reason is that the two coils in the same receiver pair have not been placed symmetrically. To verify this, the two coils in one receiver were placed symmetrically, and the characteristic of this encoder structure after this change is studied in the next section.

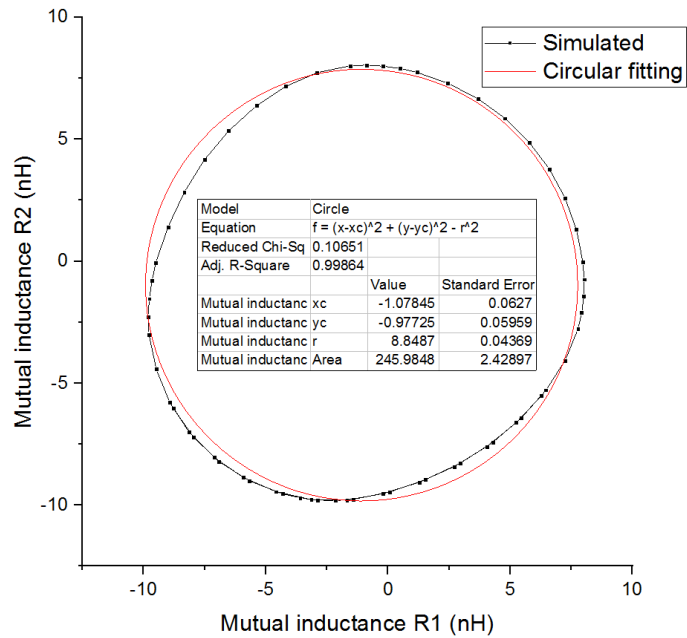


Figure 4.33 Lissajous curve with circular curve fitting.

### 4.3.2 Prototype Two

In the previous prototype, the two coils in one receivers pair were not identical and symmetric. The electrical connection might have provided the wrong value of the width of the receivers pairs. A new prototype was therefore designed, whose structure is shown in Figure 4.34. The dimensions of the emitter and receiver coils are the same as those in the previous structure listed in Table 4.1. The main difference is that one of the receiver coils is flipped, making the average receiver coil width 2.2mm. The width of one receiver pair is therefore 4.4 mm, which provides a value of 2.2 mm for the width of the plates and the gap.

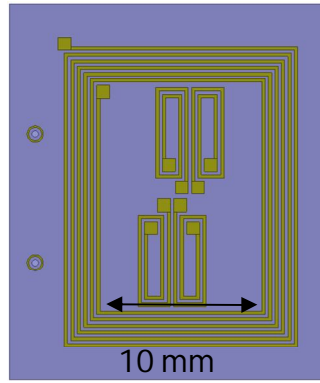


Figure 4.34 Encoder structure with new receiver coil configuration.

#### 4.3.2.1 Simulation results

This structure was simulated using the ANSYS Maxwell™ software package. Simulated measurements of the mutual inductance change between emitter and receiver pairs at different relative scale displacements were carried out and imported into the OriginLab™ software for analysis. Results are plotted in Figure 4.35.

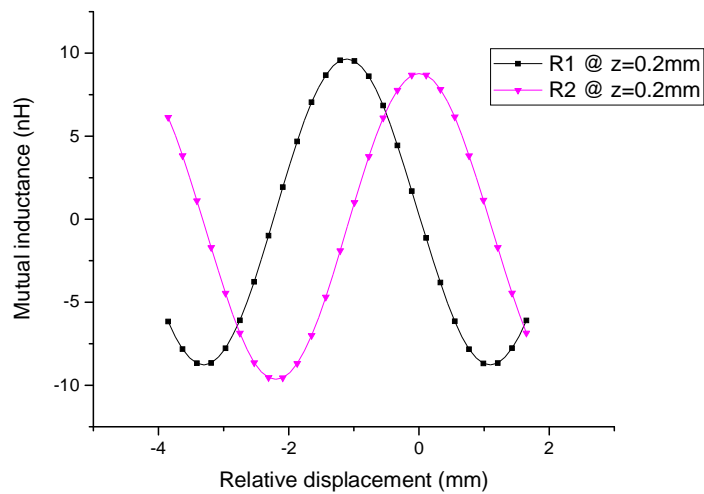
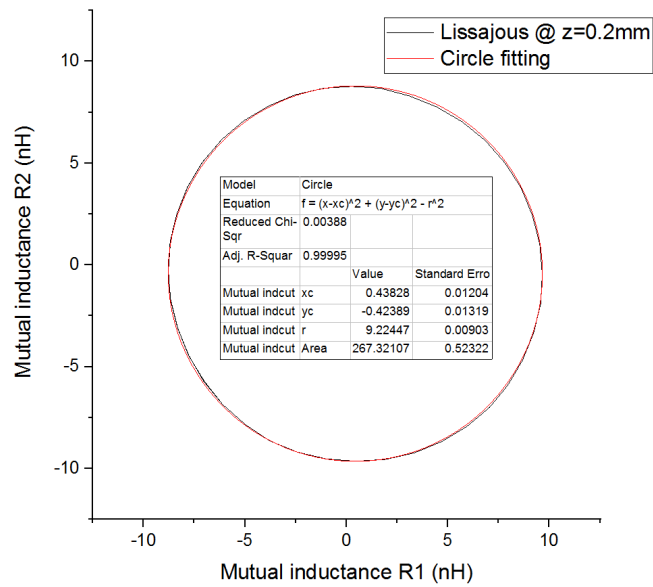


Figure 4.35 Simulated mutual inductance

The corresponding Lissajous curve of the simulated mutual inductance was plotted together with a circular curve fitting. The adjusted R-square value of the fitting is 0.9999 as shown in Figure 4.36.



**Figure 4.36 Lissajous curve with circular curve fitting.**

The corresponding phase at difference displacements was calculated for the scale set up at a distance of 0.2 mm and the phase-displacement curve was plotted in Figure 4.37.

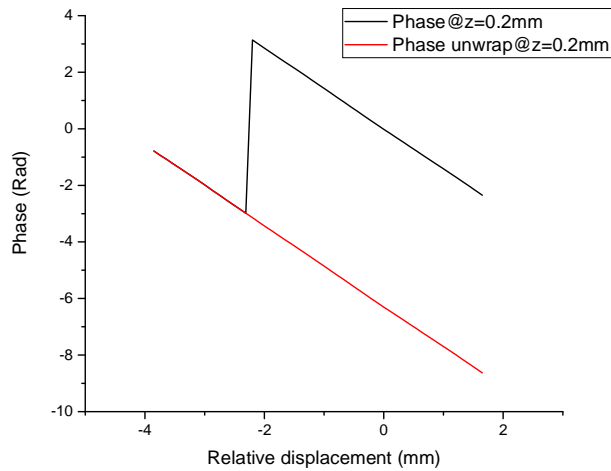


**Figure 4.37 Phase displacement curve**

The linear fitting was carried out on the phase-displacement curve; the adjusted R-square value of the fitting is 0.99998 as shown in Figure 4.38.

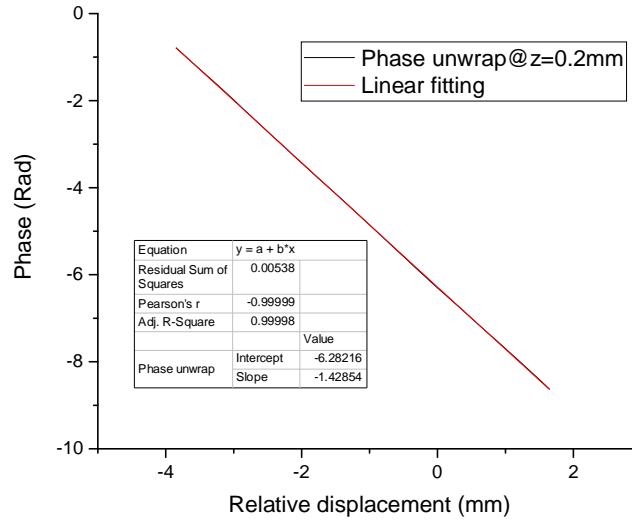


**Figure 4.38 Phase displacement curve together with linear curve fitting**

The fitting residual is plotted in Figure 4.39 and the residual ranges from -0.02 to 0.02 radians corresponding to a virtual displacement of about -15 to 15  $\mu\text{m}$ .

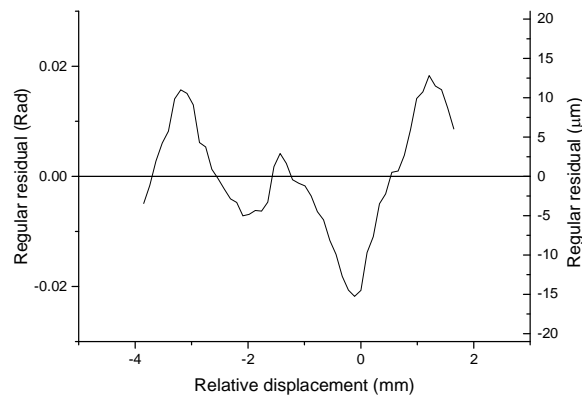


**Figure 4.39 Linear fitting residual.**

#### **4.3.2.2 Measurement**

The structure of the encoder was fabricated using PCB technology as shown in Figure 4.40. The thickness of the coil tracks is 35  $\mu\text{m}$  and the thickness of the substrate is 0.2 mm.

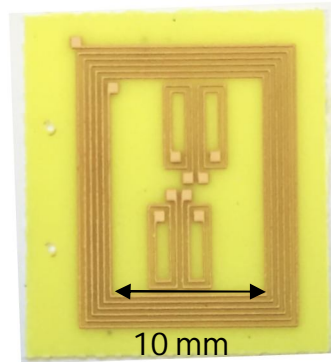


**Figure 4.40 Fabricated PCB encoder**

The same measurement setup as for prototype 1 was used. The direct output from the encoder is shown in Figure 4.41. The outputs waveforms of the two channels are not identical, due to the extra coupling between the soldered twisted wire on the receivers and the emitter coil. As discussed in Chapter 3 this coupling would mainly affect the waveforms but has limited effect on the coupling between the receivers and the scale.

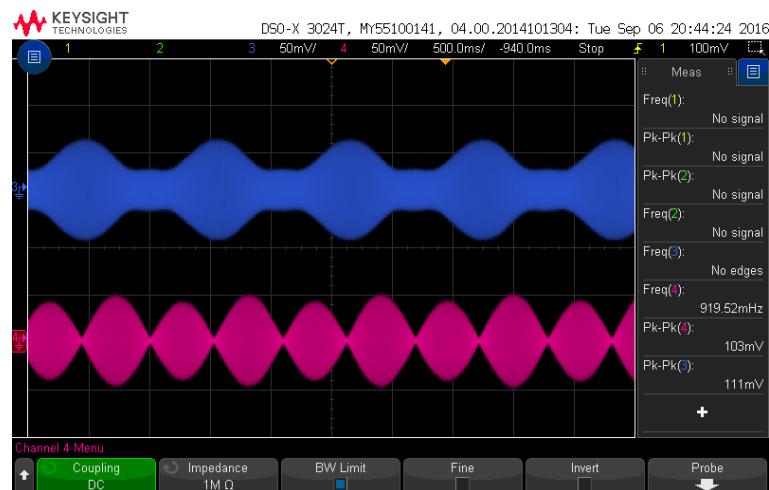


**Figure 4.41 Outputs of the encoder for a 5 MHz emitter signal.**

The output signals were demodulated using breadboard circuit as shown in Figure 4.42. Due to the extra coupling, the amplitudes of the two signals are not equal with peak-to-peak amplitudes of 647.24 mV and 838.19 mV.

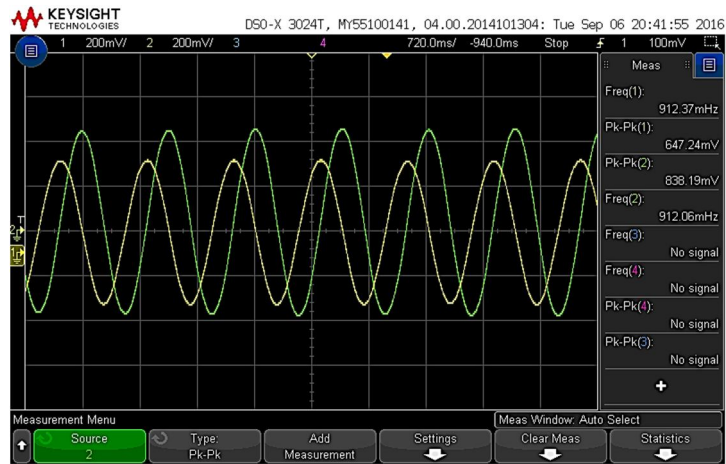


**Figure 4.42 Demodulated signals**

As in the previous prototypes the variation of the voltage was plotted against time assuming that the scale was moving at constant speed. Results are displayed in Figure 4.43.

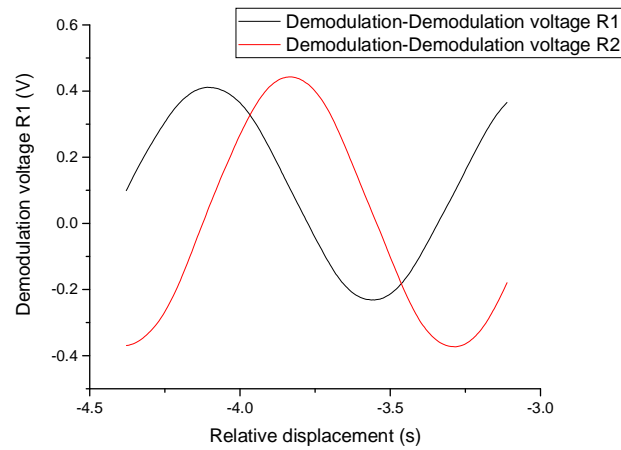


**Figure 4.43 Demodulated voltages**

The unequal signals can be written in the form of Equation 4-4 and Equation 4-5. The DC offset, which is calculated as the average value of the maximum and minimum value of the voltages, was removed from the signals and then normalized to their amplitudes respectively. The results are plotted against displacement as in Figure 4.44.

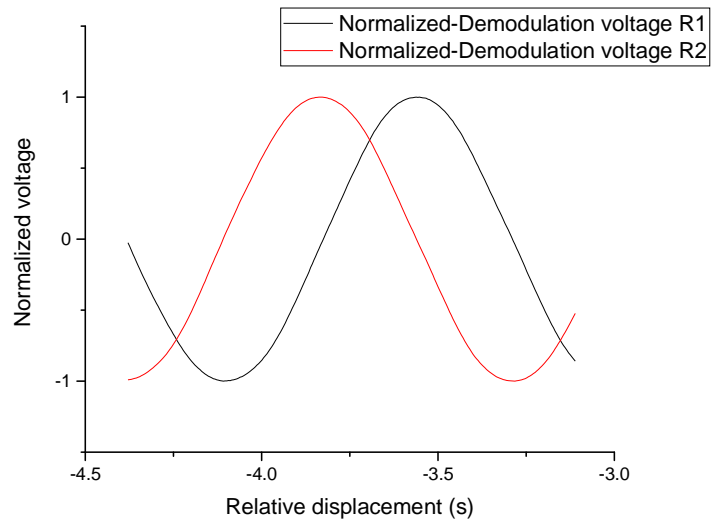


**Figure 4.44 Normalized voltages**

The Lissajous curve of the normalized signal was plotted in Figure 4.45 together with a circular curve fitting. The adjusted R-square value for the fitting is 0.99991.

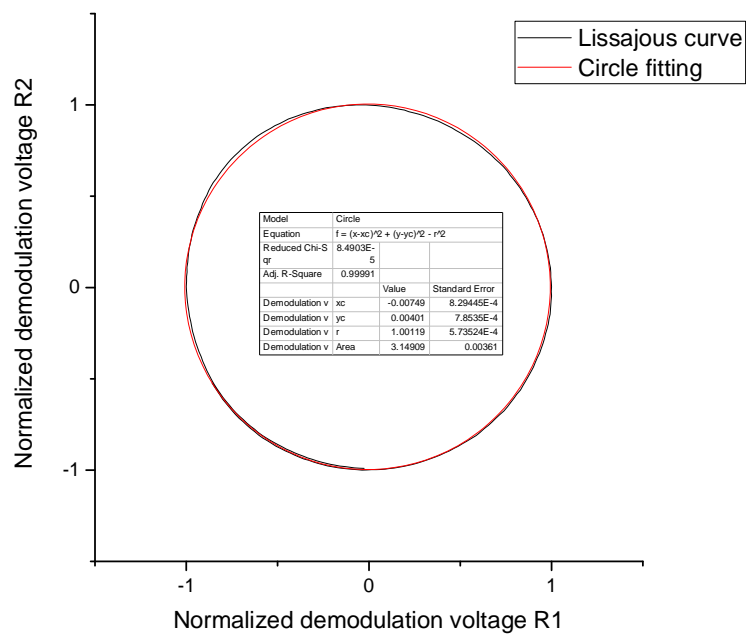


**Figure 4.45 Lissajous curve with circular curve fitting.**

The phase for the corresponding displacement was calculated using Equation 4-7 and plotted in Figure 4.46 together with the result of linear fitting. The adjusted R-square value of the fitting is 0.99989.



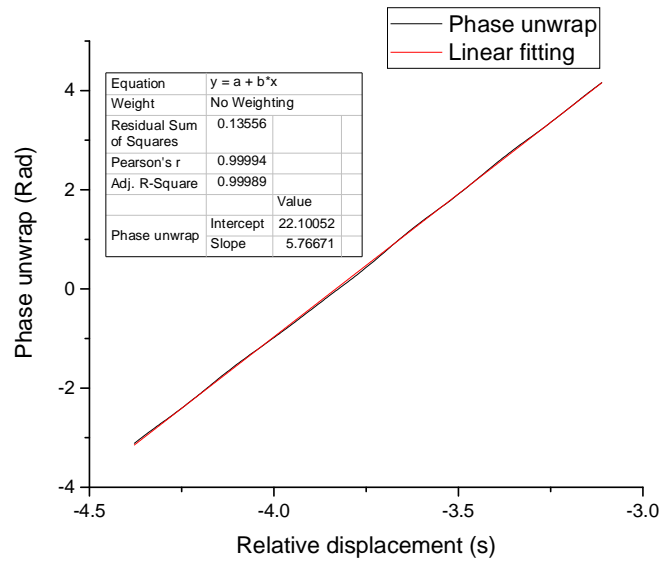


**Figure 4.46 Unwrapped phase measurement and linear curve fitting**

The regular residual of the linear fitting is plotted below in Figure 4.47. The residual varies from -0.05 to 0.03 radians which correspond to a virtual displacement of -35  $\mu\text{m}$  to 25  $\mu\text{m}$ .

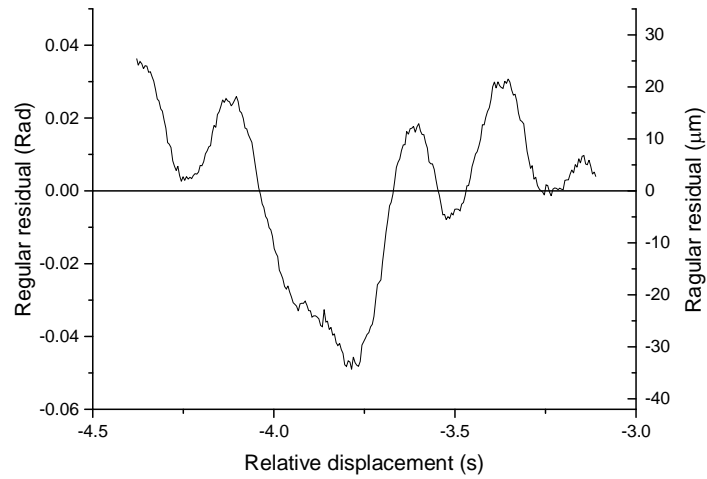


**Figure 4.47 Residual of linear curve fitting**

### 4.3.3 Prototype Three

Another structure, shown in Figure 4.48, was designed whereby the two coils in one receiver pair are placed differently on one side.

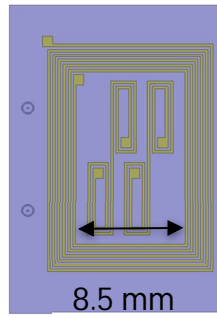


**Figure 4.48 Encoder structure used in simulation**

The geometrical configuration of the coils is listed in Table 4.2. The width of the receiver coil is 2 mm. One track is overlapping between the two receiver coils making the width of the pair of receivers 4 mm. A corresponding scale width of 2 mm plate width and gap was used and simulated using the ANSYS Maxwell™ software.

**Table 4.2 Dimensions of the emitter and receiver pairs coils (in mm)**

Emitter				Receiver			
Inner length	Inner width	Track gap	Track width	Outer length	Outer width	Track gap	Track gap
13.4	8.5	0.2	0.2	6	2	0.2	0.2

#### **4.3.3.1 Simulation results**

The change of the mutual inductance between emitter and receiver pairs was simulated against different relative scale positions and is plotted in Figure 4.49.

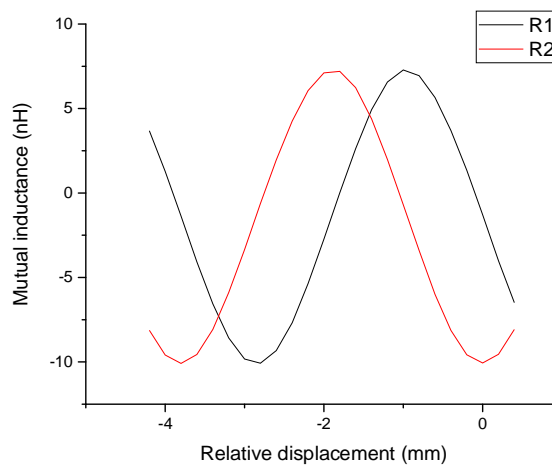


**Figure 4.49 Simulated mutual inductance change against displacement of the scale**

The Lissajous curve of the mutual inductance is plotted in Figure 4.50 compared to a circular curve fitting. The adjusted R-squared value of the circular fitting is 0.99985.

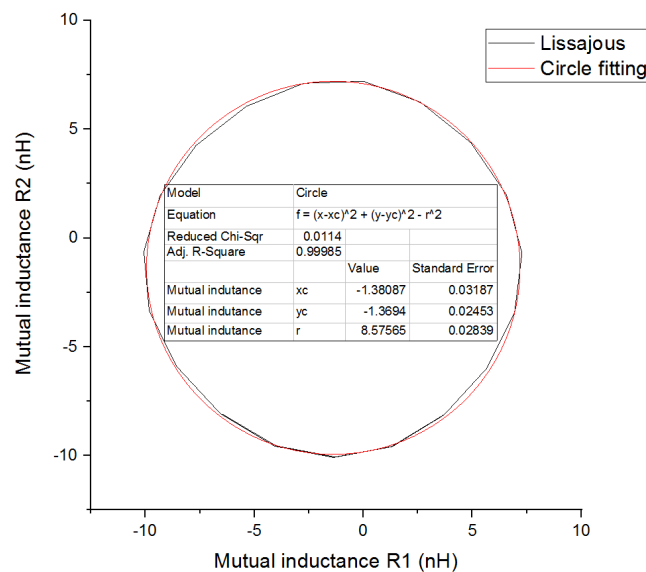


**Figure 4.50 Lissajous curve and circular curve fitting.**

The corresponding phase at difference displacements was calculated and the phase-displacement curve was unwrapped and plotted in Figure 4.51 together with the linear curve fitting. The adjusted R-square value of the fitting is 0.99998.

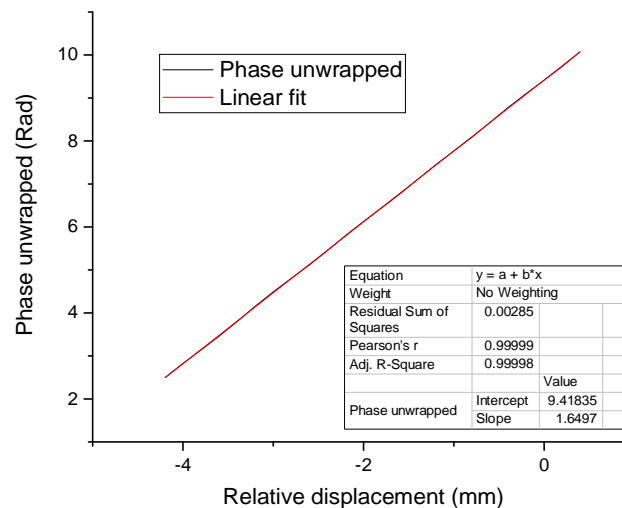


**Figure 4.51 Linear fitting of the phase displacement curve.**

The fitting residual was again plotted in Figure 4.52; the residual ranges from -0.02 to 0.02 radians which corresponds to a virtual displacement of about  $\pm 13 \mu\text{m}$ .

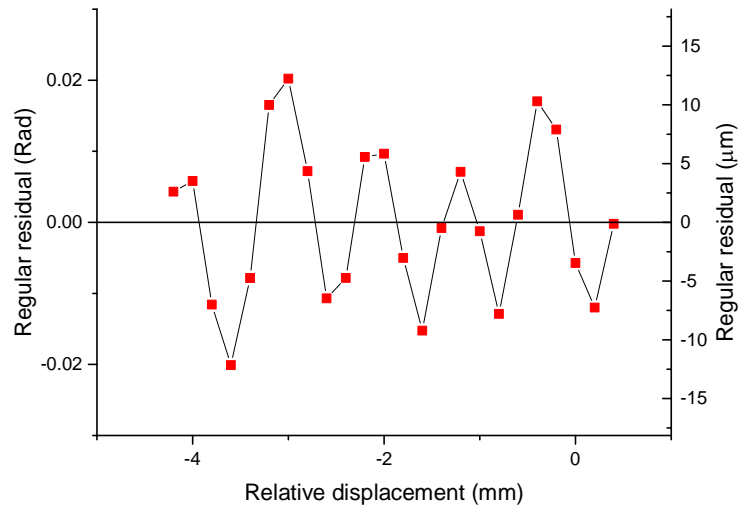


**Figure 4.52 Residual of the linear fitting.**

#### **4.3.3.2 Measurement**

The encoder was fabricated using PCB technology shown in Figure 4.53.

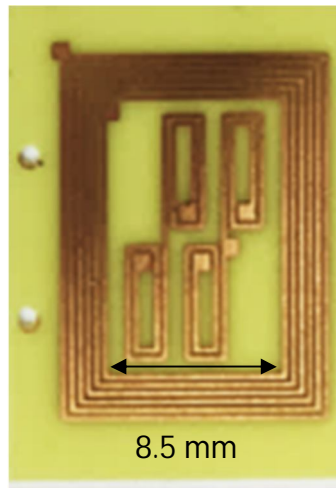


**Figure 4.53 PCB device used for measurement**

The direct outputs from the encoder were measured, as shown in Figure 4.54. A  $10\ \Omega$  resistor was connected in series with the emitter and the voltage across it was measured as shown in channel 3 in blue with channels 1 and 2 connected to the two receivers. The scale was attached to the motorized stage and moved at a constant speed.

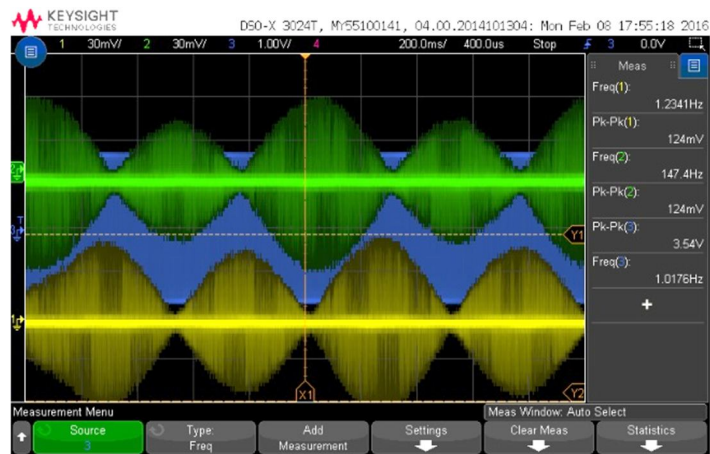


**Figure 4.54 Outputs of the encoder**

The output signals were demodulated as shown in Figure 4.55. The peak-to-peak amplitudes are 208.4 and 202.26 mV.

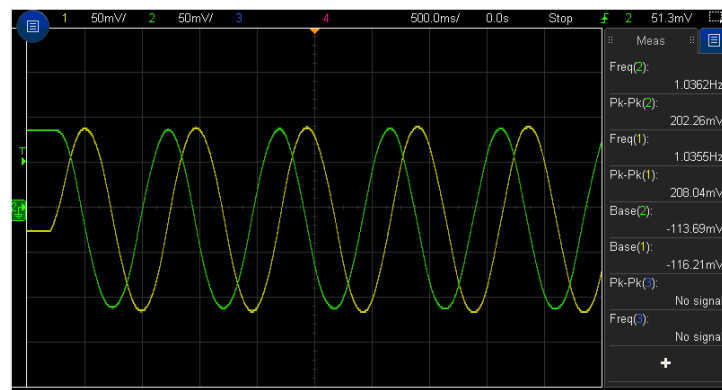


**Figure 4.55 Demodulation measurement results**

The corresponding Lissajous curve was measured directly using an oscilloscope as shown in Figure 4.56.

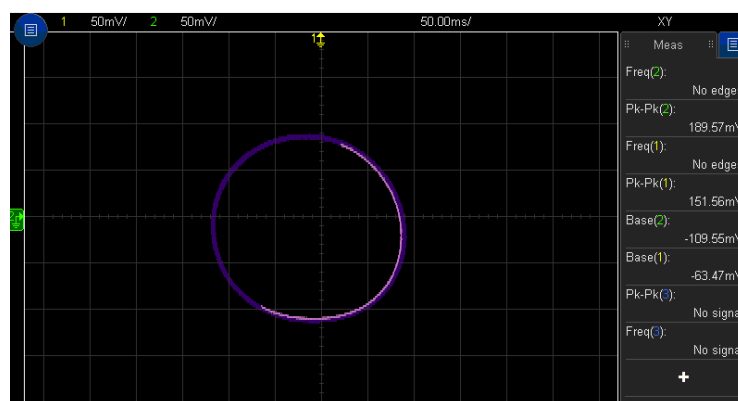


**Figure 4.56 Lissajous curve measured using oscilloscope**

After removal of the DC offset and normalization of the amplitudes, the Lissajous curve for about five scale periods is shown below in Figure 4.57 together with circular curve fitting. The adjusted R-square value of the fitting is 0.9999.

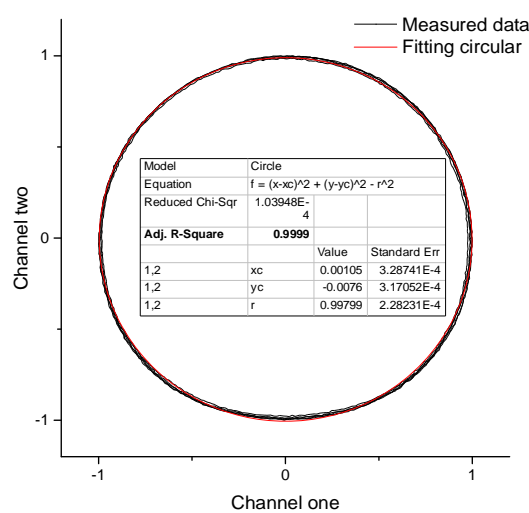


Figure 4.57 Lissajous curve of the measured data

The phase was calculated using the arctangent function and plotted against scale displacement in Figure 4.58.

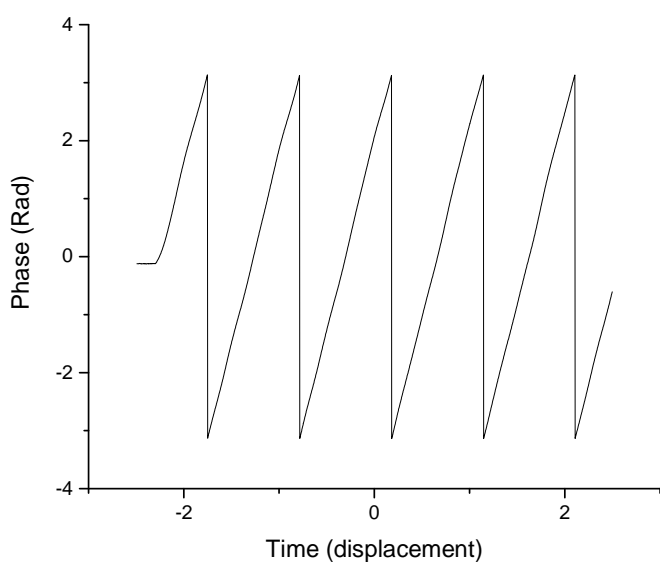
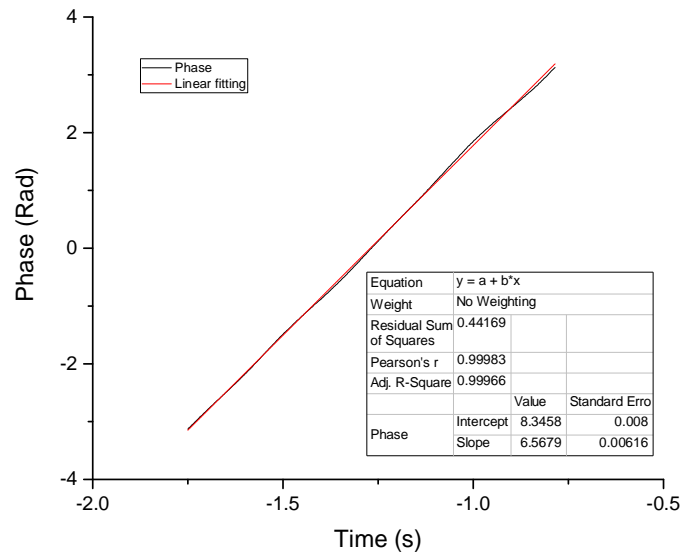


Figure 4.58 Phase displacement curve

Result of linear curve fitting is shown in Figure 4.59. The adjusted R-square value of the fitting is 0.99966.



**Figure 4.59 Phase and displacement**

The regular residual of the fitting is shown Figure 4.60 with a residual range from -0.75 to 0.75 radians corresponding to a virtual displacement of  $\pm 50 \mu\text{m}$ .

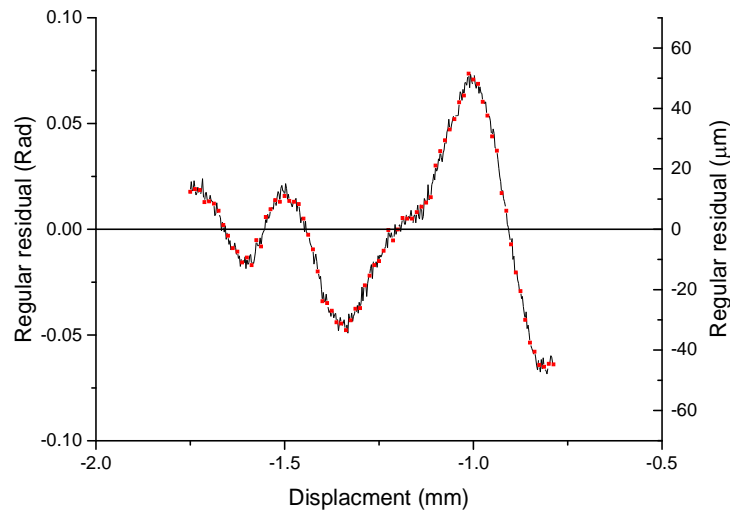


**Figure 4.60 Regular residual**

#### 4.3.4 Prototype Four

From Equation 4-8, the nonlinearity output of the encoder is defined as the ratio to the period length of the plates on the scale, which equals to the width of one receiver pair. Thus reducing the width of the receiver pair could reduce the encoder output nonlinearity. The prototype three structure was therefore changed as shown in Figure 4.61. The distance between the two coils in the same receiver pair was

reduced to 1.2 mm which makes the receiver pair width equals to 3.2 mm. The other receiver pair is placed with a 2.4 mm offset to the left of this receiver coil pair on the horizontal direction.

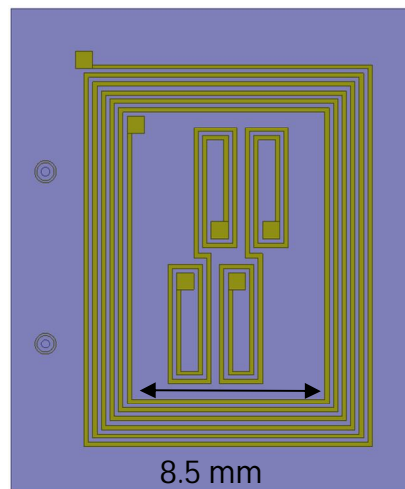


**Figure 4.61** Encoder structure of prototype four.

As the width of the receiver coils is still 2 mm, the width of the plates on the scale is set at 2 mm while the gap between them is set at 1.2 mm making the period of the plates as 3.2 mm as shown in Figure 4.62.

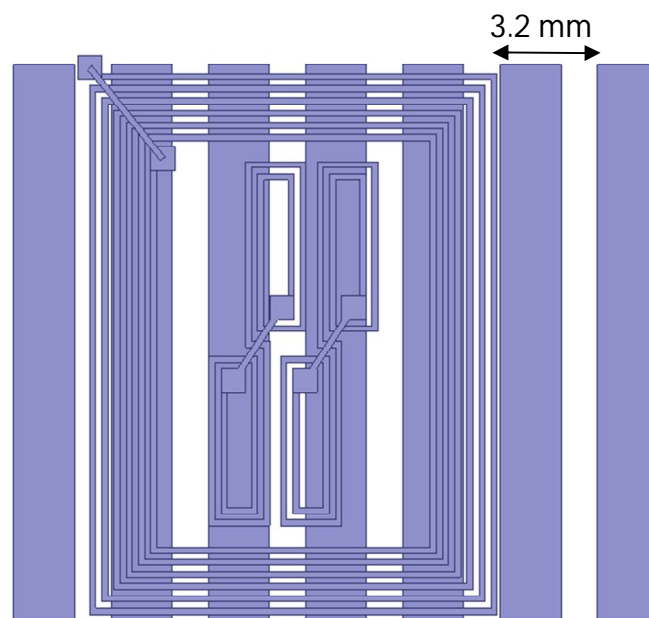


**Figure 4.62** Encoder prototype four with scale



#### 4.3.4.1 Simulation results

This structure in Figure 4.62 was simulated as before. The mutual inductance change between emitter and receiver pairs against different relative scale displacements was calculated and plotted as shown in Figure 4.63.

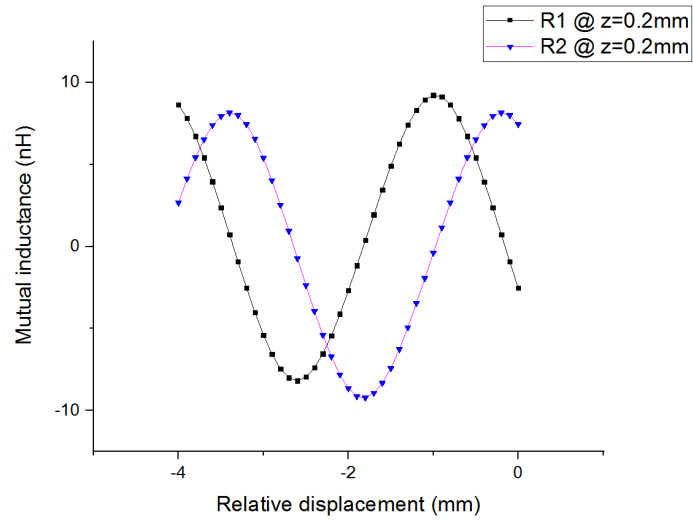


Figure 4.63 Mutual inductance change against displacement

The Lissajous curve of the mutual inductance was again plotted alongside a circular curve fitting. The adjusted R-squared value of the circular fitting is 0.99965.

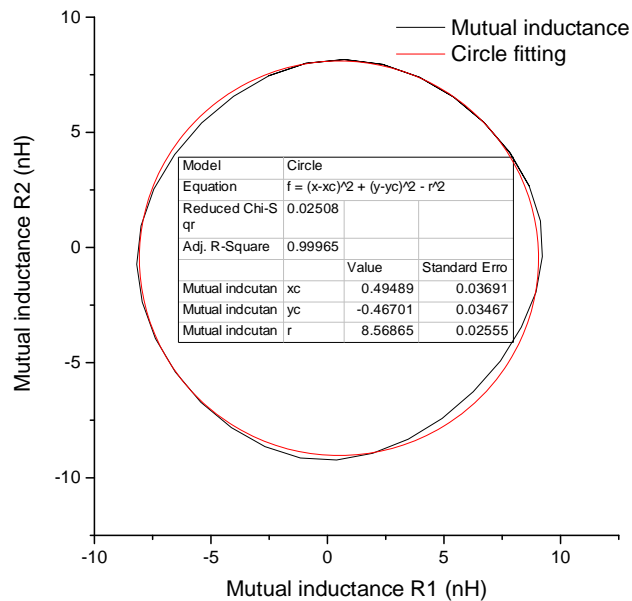
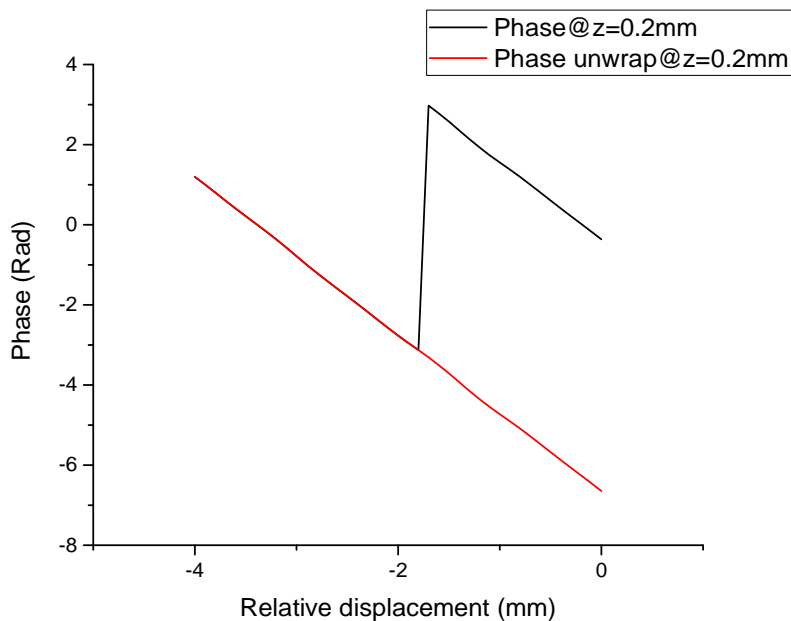


Figure 4.64 Lissajous curve and circular curve fitting of prototype four.

The corresponding phase at different displacements was calculated and plotted in figure 4.65.



**Figure 4.65 Phase displacement curve of prototype four**

Linear curve fitting was carried out on the phase-displacement curve as shown in Figure 4.66 and, the adjusted R-square value of the fitting is 0.99992.

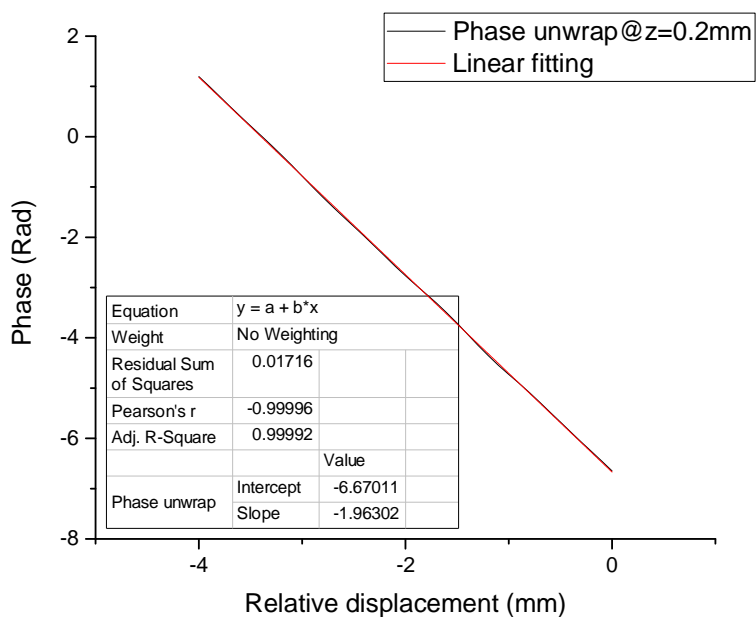


**Figure 4.66 Linear curve fitting of prototype four**

The fitting residual is plotted in Figure 4.67 with the residual ranging from -0.04 to 0.02 radians which a virtual displacement of about about -20  $\mu\text{m}$  to 15  $\mu\text{m}$ .

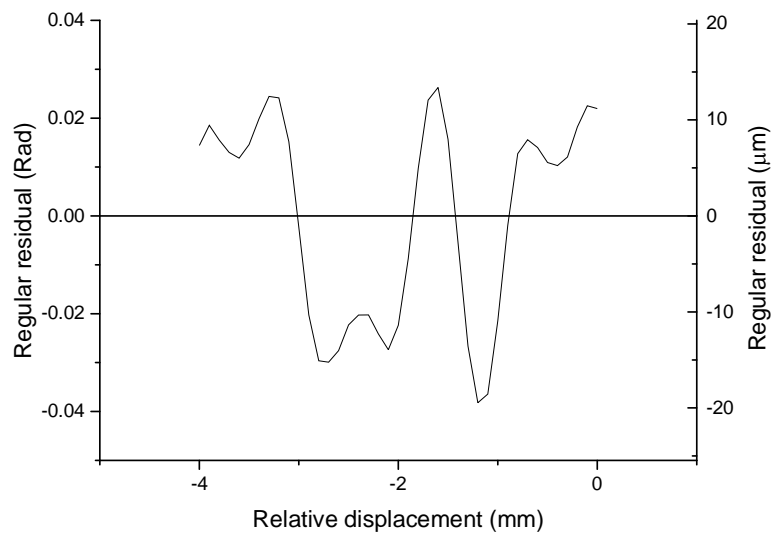


**Figure 4.67 Fitting residual of prototype four**

#### **4.3.4.2 Measurement results**

The structure of the encoder was fabricated using PCB technology as shown in Figure 4.68.

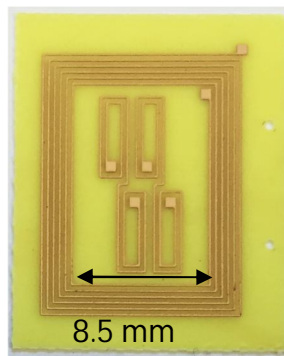


**Figure 4.68 PCB device of prototype four**

The direct output from the encoder is shown in Figure 4.69. The two signals are amplitude modulated with similar modulation depth.

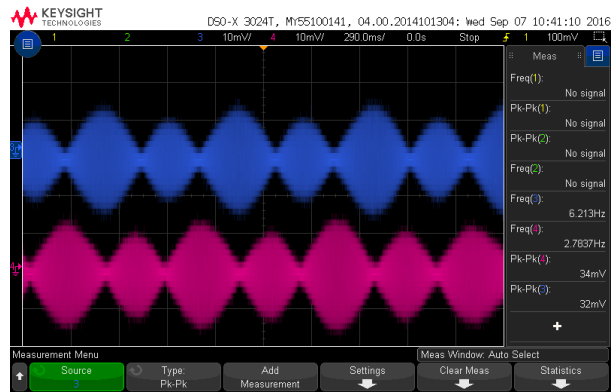


**Figure 4.69 Encoder direct outputs for a 5MHz excitation frequency**

The output signals were demodulated and measured as shown in Figure 4.70.

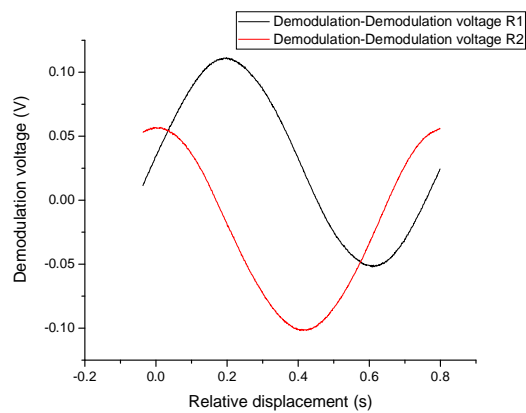


**Figure 4.70 Measured demodulation voltages of Prototype four.**

The DC offset was removed from the signals and then normalized to their amplitudes. The results were plotted against displacement as in Figure 4.71.

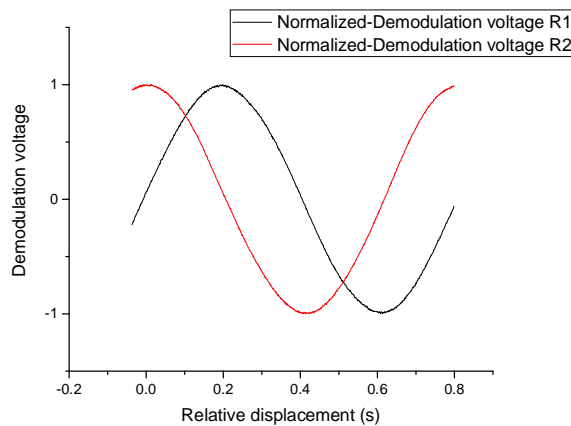


**Figure 4.71 Normalized voltages against displacement**

The Lissajous curve of the normalized signal was plotted in Figure 4.72 alongside the corresponding circular curve fitting. The adjust R-square value for the fitting is 0.99927.

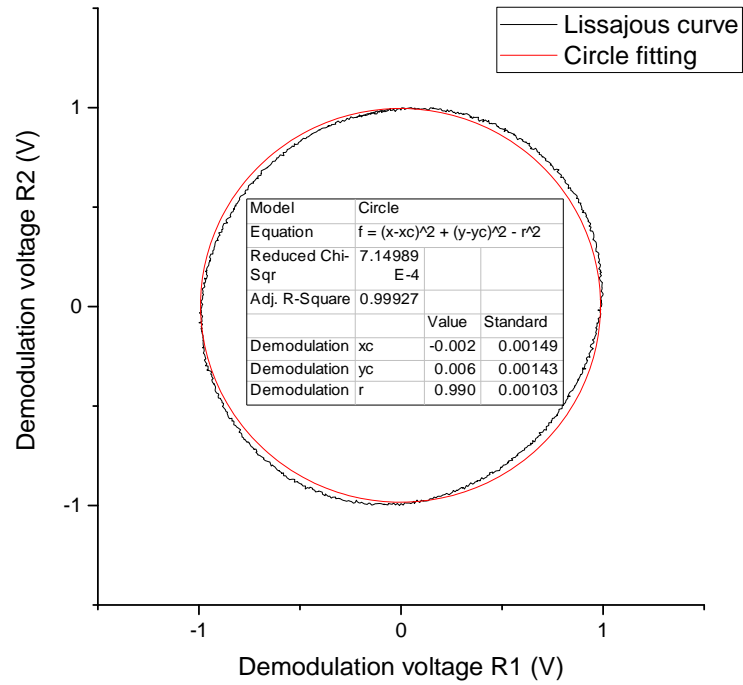


Figure 4.72 Lissajous curve of the normalized voltages of prototype four

The corresponding phase at different displacements was calculated and plotted in Figure 4.73.

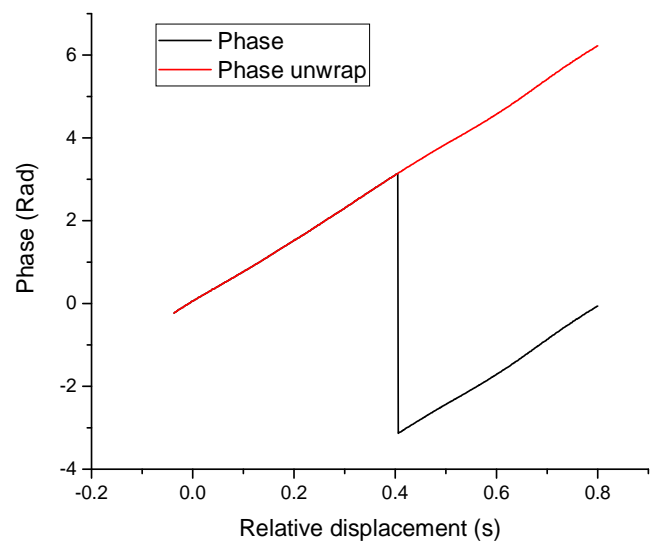
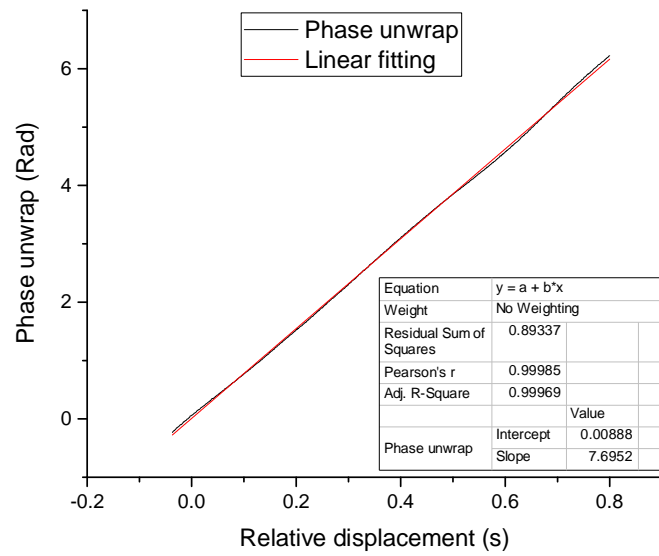


Figure 4.73 Phase displacement of encoder prototype four

The linear curve fitting was carried out on the phase-displacement curve. The adjusted R-square value of the fitting is 0.99969 as can be seen in Figure 4.74.



**Figure 4.74 Linear fitting of measured data of prototype four**

The fitting residual, plotted in Figure 4.75 shown a residual range from -0.05 to 0.05 radians which corresponds to a virtual displacement of about +/- 30  $\mu\text{m}$ .

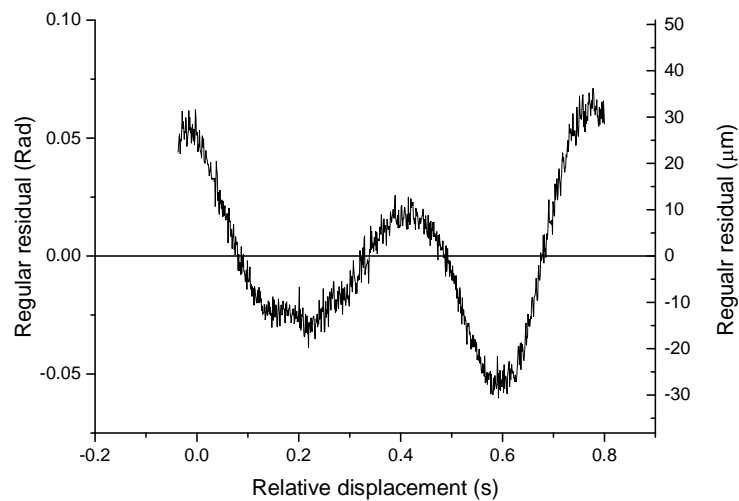


**Figure 4.75 Fitting residual**

## 4.4 Discussion

The nonlinearity properties of the four encoder prototypes from both simulation and measurement are summarized in Table 4.3. The performance improved prototype 1 was not measured, only simulated.

**Table 4.3 Simulated and measured nonlinearity of the four encoder prototypes**

<b>Prototype</b>	<b>One</b>	<b>One Improved</b>	<b>Two</b>	<b>Three</b>	<b>Four</b>
<b>Nonlinearity</b>					
<b>Simulation (<math>\mu\text{m}</math>)</b>	+/- 28	+/- 5	+/- 15	+/- 13	-20 / +15
<b>Measurement (<math>\mu\text{m}</math>)</b>	-80 / +60	N/A	-35/+ 25	+/- 30	+/- 30

From Table 4.3, encoder prototype two and three offer better accuracy than prototype one, because the coils in receiver pairs in these two prototypes are more symmetric. The accuracy of prototype four is also better than prototype but not worse than prototype three, which indicates the improvement is not very good.

The difference between the simulation and measurement is believed to be due to the misalignment between the read head and the scale during the measurement. The alignment is indeed adjusted manually with no feedback information relaying only on the eye observation.

The structure of prototype two was used to simulate the influence of misalignment between the read head and the scale using the ANSYS Maxwell™ software package. Two misalignment effects were studied: (1) the influence of the distance separating the read head and the scale and (2) the influence of the read head rotation around X, Y and Z axis on the encoder output signals. One example is shown in Figure 4.76 where the read head coils are rotated around Z axis by 2.5 degrees.

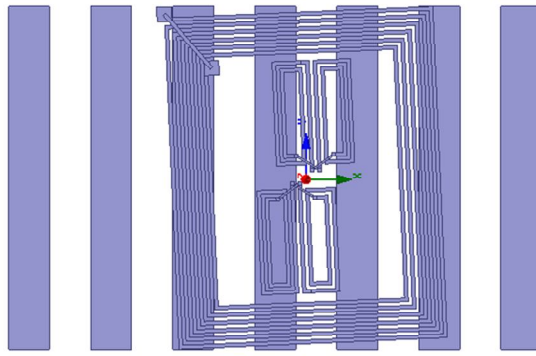


**Figure 4.76** Read head rotated around the Z-axis.

#### 4.4.1 Vertical gap

The distance between the read head and the scale was determined by eye observation. To study the influence of the gap, different values of the gaps (0.2 mm, 0.5 mm and 0.8 mm) were set in the simulation. The simulation results were processed using OriginLab™ software with the respective Lissajous curves plotted in Figure 4.77. The vertical gap affects the signal strength: the smaller the gap, the bigger the mutual inductance changes.

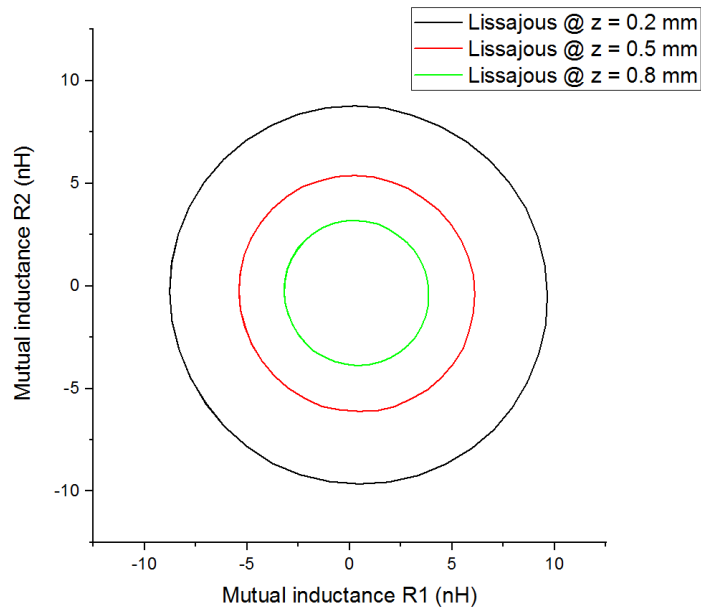


**Figure 4.77** Lissajous curves of the mutual inductance at different gaps

The linear curve fitting residual of the calculated phase displacement curve was plotted in Figure 4.78. The influence of the vertical gap on the linearity is negligible for this structure.



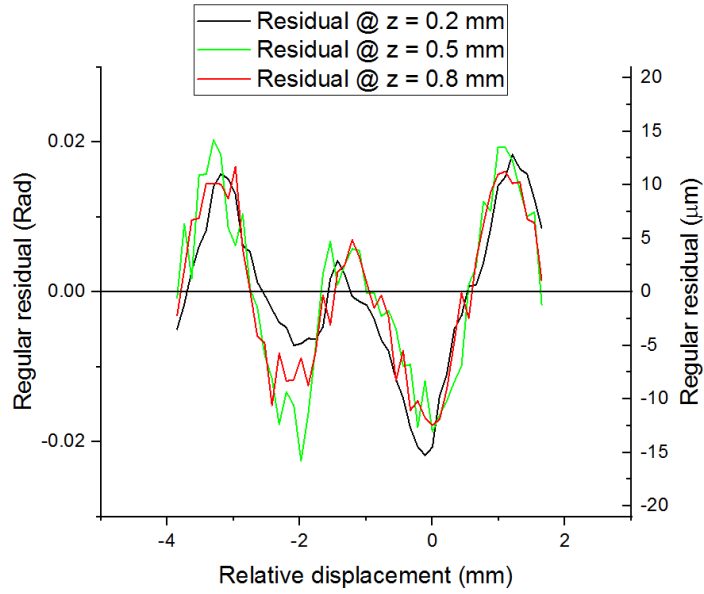


**Figure 4.78 Residual of the linear fitting for different gaps.**

#### **4.4.2 Rotation around the X-axis**

The read head was simulated for a rotation of around the X-axis at  $\pm 2.5^\circ$ . The calculation of the mutual inductance between emitter and receiver at different relative scale positions was carried out and processed using the OriginLab™ software. The Lissajous curve of the simulated mutual inductance is plotted in figure 4.79. The relative rotation around the X-axis affects the DC offset and amplitude of the two signals, which makes the Lissajous curve more like an ellipse. Here the vertical gap between the coils and the scale is 0.5 mm.

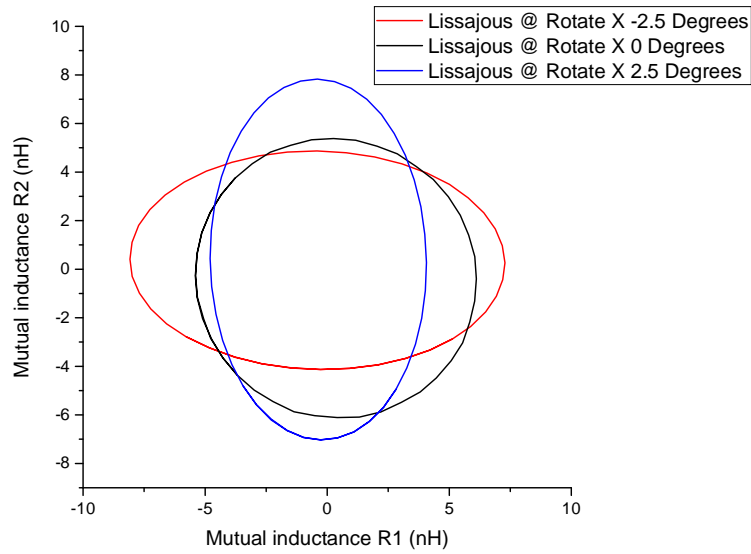


**Figure 4.79 Lissajous curves of the mutual inductance at different X-axis rotations**

The regular residuals of the linear fitting on the calculated phase displacement curves are plotted in Figure 4.80. Here the residuals are nearly equal, which implies that the influence of the rotation around X axis on the nonlinearity of the encoder is small.

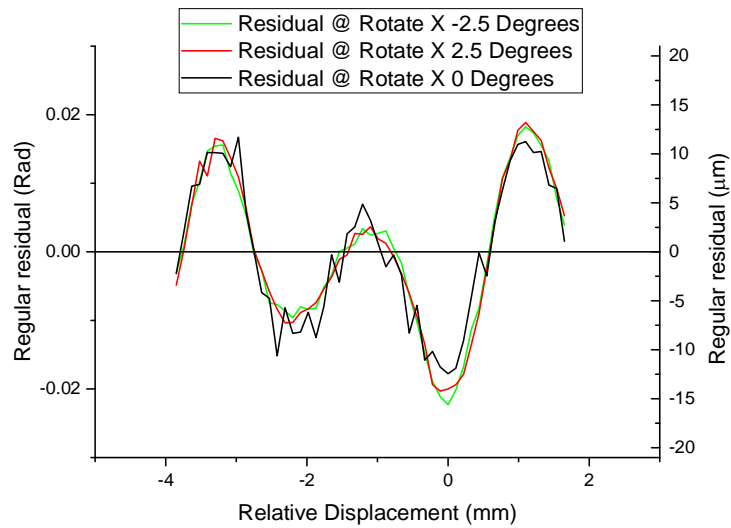


**Figure 4.80 Residuals of the linear fitting at different X-axis rotations.**

#### 4.4.3 Rotation around Y-axis

The read head was rotated around the Y-axis at  $\pm 2.5^\circ$ . The mutual inductance between emitter and receiver was simulated at different relative scale positions. The Lissajous curves of the simulated mutual inductance, plotted in Figure 4.81 indicate

that the rotation affects mainly the DC offset of the two signals, as the position of the difference centers of the Lissajous curves are shifted.

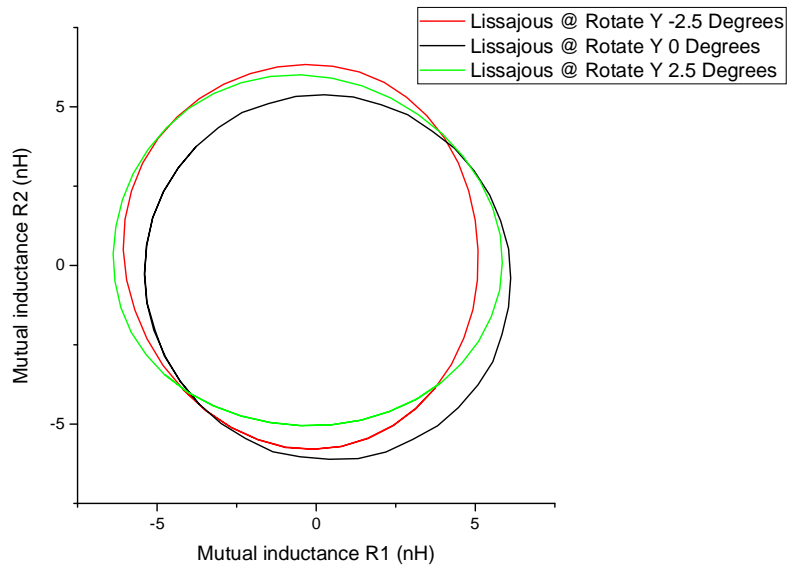


**Figure 4.81 Lissajous curves of the mutual inductance at different Y-axis rotations**

The residuals of the linear fitting on the calculated phase displacement curves are plotted in Figure 4.82 and shown an increase after rotation. The residuals for  $2.5^\circ$  and  $-2.5^\circ$  are of a similar form but rotated.

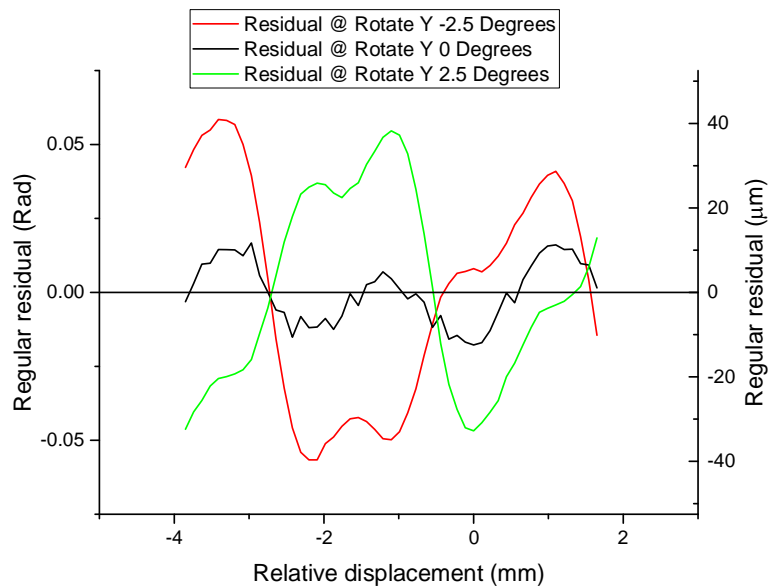


**Figure 4.82 Residuals of the linear fitting at different Y-axis rotations.**

#### 4.4.4 Rotation around the Z-axis

The read head was rotated around the Z-axis for  $2.5^\circ$  and  $-2.5^\circ$ . The mutual inductance between emitter and receiver was simulated at different relative scale positions. The Lissajous curves are plotted in Figure 4.83. The relative rotation around Z axis affects mainly the phase shift between the two signals, resulting in rotated ellipses.

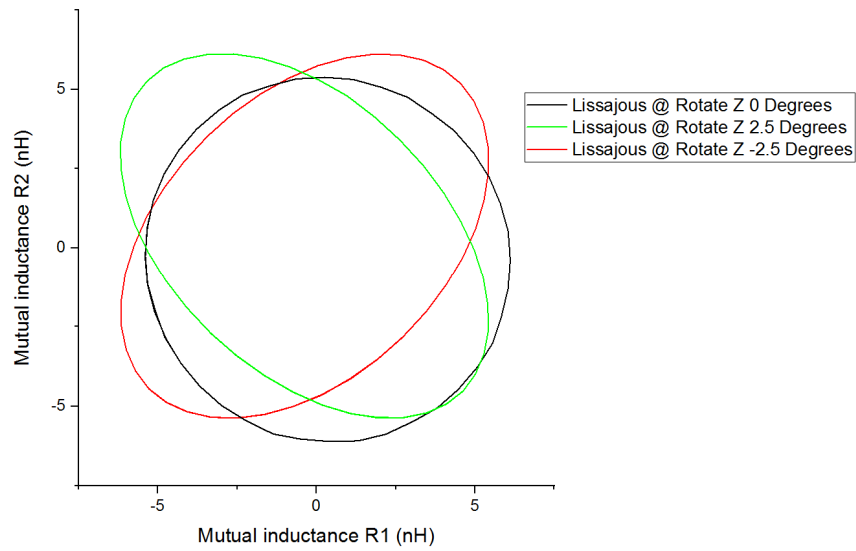


**Figure 4.83** Lissajous curves of the mutual inductance at different Z-axis rotations.

The corresponding residuals of the linear fitting are plotted in Figure 4.84. The rotation around the Z-axis increases the nonlinearity. The form of the residuals implies that the signals of the encoder structure before rotation have a phase shift as well. This could be due to the offset between the two receiver pairs as discussed in the improvement part of prototype one.

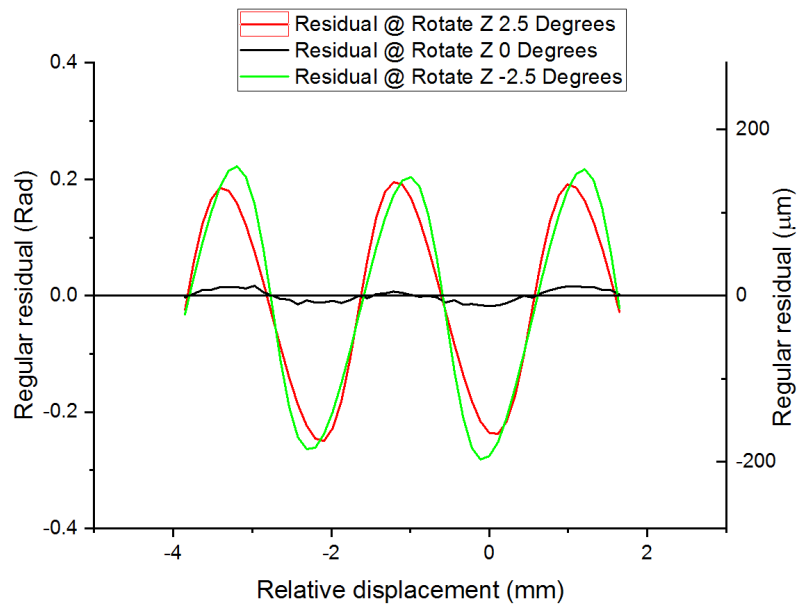


**Figure 4.84 Residuals of the linear fitting at different Z-axis rotations**

#### 4.4.5 Coil Track width

As described previously, there could be 5-10  $\mu\text{m}$  difference between the manufactured and the designed coil width. The influence of the unideal manufacture was studied here. The track width of the emitter coil was changed to 0.21mm and 0.19 mm in the simulation. The mutual inductance between emitter and receiver was simulated at different relative scale positions. The Lissajous curves are plotted in Figure 4.85.

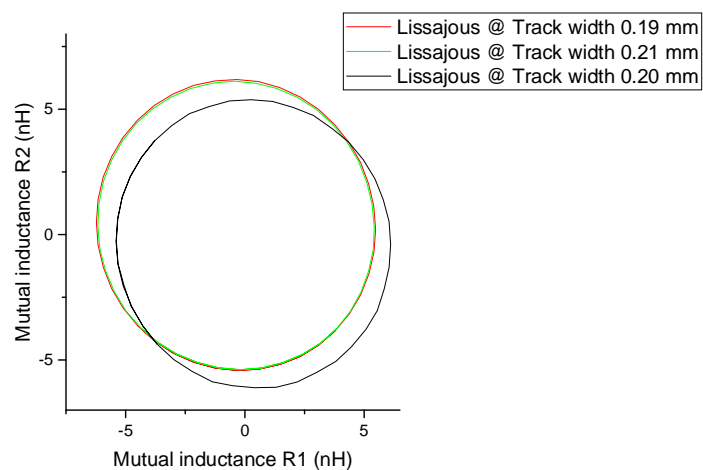


**Figure 4.85 Lissajous curve of the mutual inductance with different coil track width**

The corresponding residuals of the linear fitting are plotted in Figure 4.86. It can be seen that the different track widths cause DC offset in the final signal but do not significantly affect the output linearity.

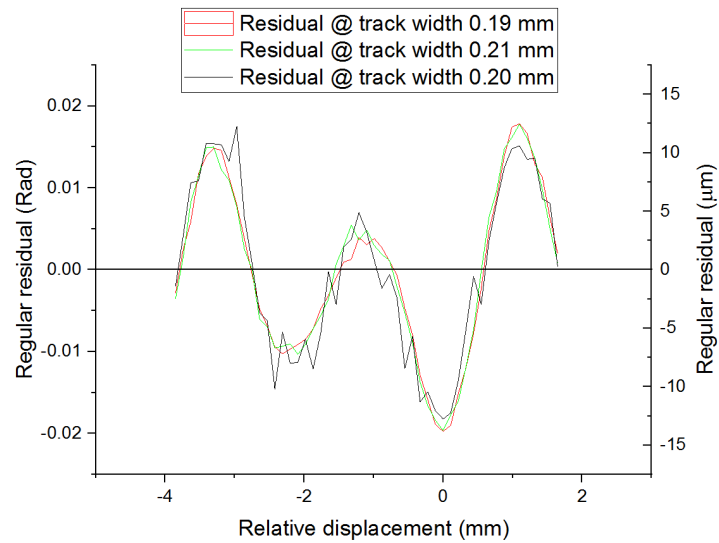


**Figure 4.86 Residual of linearity fitting with different track width**

#### **4.4.6 Scale plate width**

The scale is also manufactured using the same PCB technology as the coils. So the manufacture could also affecting the actual scale plate width. The scale plate width was changed to 2.21mm and 2.19 mm in the simulation. The mutual inductance between emitter and receiver was simulated at different relative scale positions. The Lissajous curves are plotted in Figure 4.87

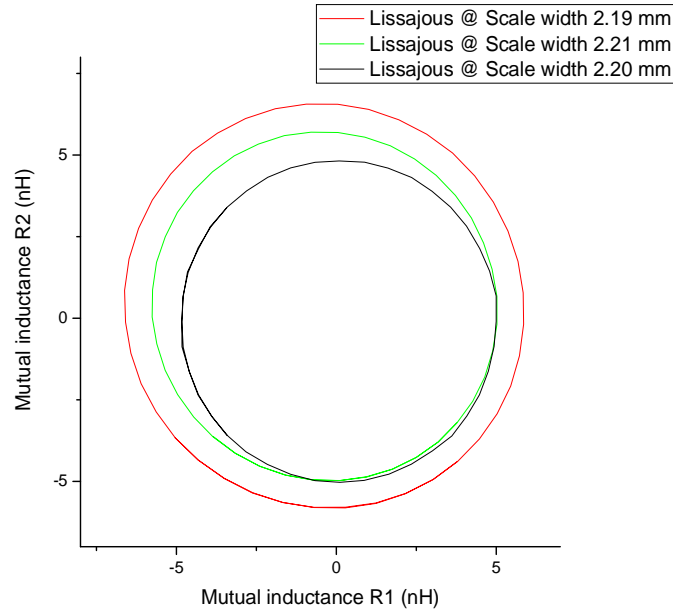


**Figure 4.87 Lissajous curve of the mutual inductance with different scale plated width**

The corresponding residuals of the linear fitting are plotted in Figure 4.88. It can be seen that the difference of the scale plated width affects the signal amplitude but do not affect the output linearity.

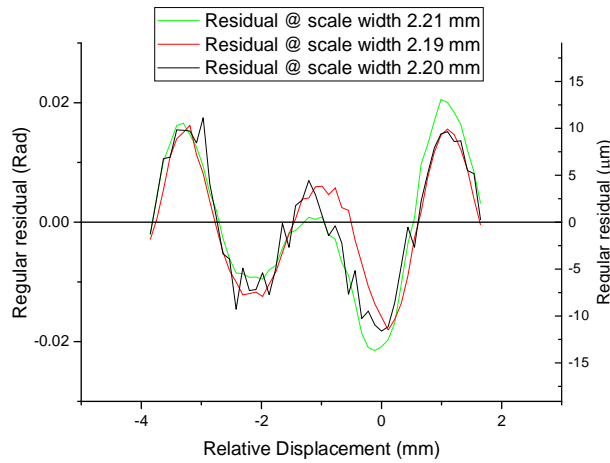


**Figure 4.88 Residuals of the linearity fitting with different scale plate width**

## 4.5 Conclusions

This chapter presented the design of a signal processing circuit and assembled its construction on a breadboard. As the synchronize demodulation method is used, the circuit is able to recover the signal from a high noise environment. The

demodulation circuit was used successfully to measure the electric signals of different encoder prototypes.

Four new different encoder structure prototypes were studied in this Chapter. The mutual inductance changes between emitter and receiver pairs as a function of the scale displacement were simulated using the ANSYS Maxwell™ software package and measured. The Lissajous and phase displacement curves were plotted and analyzed using the OriginLab™ software package. The circular fitting and linear fitting were used to studied the nonlinearity of the encoders.

The possible misalignment configurations during measurement were simulated. The vertical gap between the read head and scale affects the signal strength as expected: the smaller the gap, the stronger the signal will be. For encoder prototype two, the vertical gap and rotation around the X-axis have a negligible influence on the nonlinearity. The rotation around the Y-axis increases the nonlinearity while rotation around the Z-axis causes a phase shift between the two signals. The influence of the coil track width difference between the designed and manufacture encoders were studied using simulation, which proves the influence of difference caused by manufacture on the encoder output nonlinearity performance is negligible.

In conclusion, four signal layer PCB encoder prototypes were studied using simulation and the signal outputs were measured, structure of prototype two and three have better accuracy comparing with the other two prototypes.



## Chapter 5 - Multi-layer LTCC based encoders

### 5.1 Introduction

Multi-layer encoder structures have been fabricated using Low Temperature Co-fired Ceramics (LTCC) technology in order to achieve structures more compact than their PCB-based counterparts. The fabrication process of the encoders and their performance characterisation are summarised in this chapter.

A demodulation PCB circuit board, which has better anti-electromagnetic interference property than breadboard circuit, was designed, fabricated and used to measure the LTCC encoders. The circuit uses microchips INA217 from Texas Instruments and AD630 from Analog Devices for amplifying and demodulating the modulated signals of the LTCC encoder. The schematic of the signal processing circuit and the layout of the PCB board are presented in this chapter.

In the second part, an introduction is given about the LTCC encoder fabrication process. The fabrication steps of the LTCC encoder are also described in this section. The impedance of the LTCC encoder coils was measured and compared with finite element simulation results achieved using the Ansoft Maxwell™ simulation software.

The multilayer LTCC encoder outputs were measured using Keysight oscilloscope and Renishaw REE4000 interpolator circuits, the measurement displacement results are compared with displacement measured using Renishaw T1000-10A optical encoders; good accuracy agreement was achieved. The reasons for the nonlinearity error of the LTCC-based encoder are discussed in the last part of the chapter.

## 5.2 Multi-layer LTCC encoder structure

The 3D structure of the multi-layer LTCC encoder is shown in Figure 5.1. There are four layers in this encoder structure with three layers to accommodate the coils and a top electrical interconnection layer to connect the encoder with the excitation signal and corresponding signal processing circuit. The emitter and receivers coils are connected separately using inner vertical interconnection accesses(VIAs) to form 3D multi-layer structures. The coils lying on odd-numbered layers are wound in the opposite direction to those laid out on even-numbered layers, so that the total magnetic field can be added together. An example of this can be seen in Figure 5.1. In this example, the current follows the coils in all layers in the counter clockwise direction producing thereby a greater magnetic field.

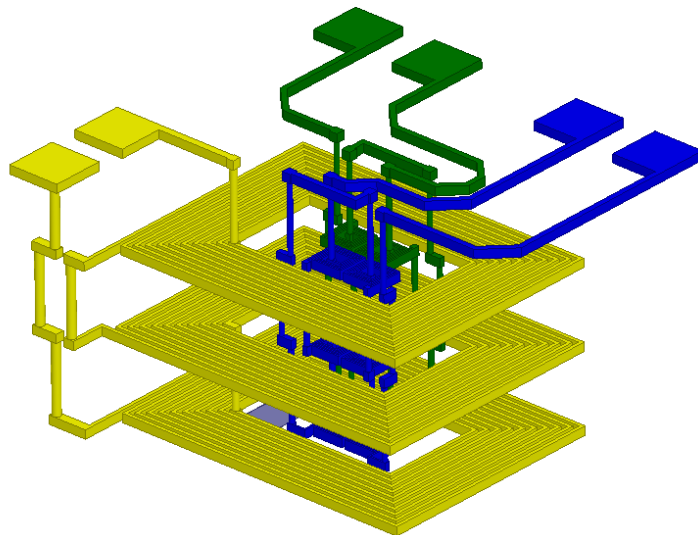


**Figure 5.1 3D structure example of the LTCC encoder in ANSYS Maxwell™ software showing emitter coil (yellow), receiver coil pair one (green) and receiver coil pair two (blue). Vertical connections between layers are achieved through vias, which are holes filled in with conductive paste. The space between layers has been exaggerated for clarity.**

The 2D view of the bottom layer of the encoder is shown in Figure 5.2.

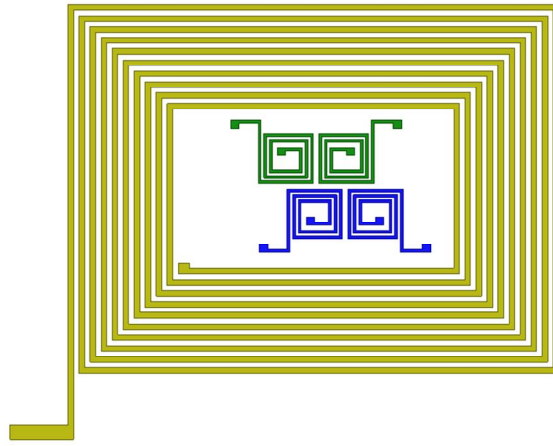


**Figure 5.2 2D view of the bottom layer of the encoder**

There are 10 turns for the emitter coil and 3 turns for the receiver coils. The dimensions of the four coils for the two receiver pairs are the same. Details of the coil dimensions are listed in Table 5.1. The track width and track gap of the receiver coils are 0.1 mm which is the limit of resolution of the LTCC fabrication equipment used. The width of the coil in the receiver is 2 mm and the distance between the two coils in one receiver pair is 0.2 mm, which makes the total width of the receiver pair is 4.4 mm.

**Table 5.1 Coils dimensions in mm of the LTCC encoder**

Emitter				Receiver			
Outer (mm)		Track (mm)		Outer (mm)		Track (mm)	
Length	Width	Gap	Width	Length	Width	Gap	Width
17.8	13.8	0.2	0.2	2	2	0.1	0.1

### 5.3 LTCC encoder fabrication

In this part of the chapter, the fabrication process of the encoder using Low Temperature Co-fired Ceramic (LTCC) is presented. The details of each fabrication step using equipment at Heriot Watt University is described.

### 5.3.1 Definition of LTCC technology

LTCC, which means Low Temperature Co-Fired Ceramic, is a multilayer ceramic packaging technology. It is derived from the high temperature co-fired ceramic technology (abbreviated HTCC). The main difference is the sintering temperature of LTCC technology of around 850°C to 900°C compared to sintering temperature for 1050°C to 1200°C for HTCC. The main advantage of the LTCC technology for packaging is that conductive wires and structures can be manufactured on each individual layer and by stacking those layers together, 3D structures can be achieved, resulting in a compact structure.

The basic material in LTCC technology is the green tape which is a soft, highly flexible and easy to handle thin film. The green tape is made from slurry of several raw materials: aluminium oxide, glass power and some other organic materials. Those raw materials are mixed together, cast onto a carrier film conveyor, which usually is PET foil, and dried. During the sintering process, the organic material sublimates and the glass melts encapsulating the alumina particles, resulting in a loss of porosity and a densification of the material.

The shrinkage of the layers during sintering is a special character of LTCC green tape. This shrinkage effect must be taken into consideration during the design and manufacture of LTCC-based systems. The melting of glass particles in green tape eliminates the space between particles, leading to the shrinkage of the structure in all x, y and z directions. The reduction in dimensions is significant and varies depending on the composition of the different tapes. Customizing the composition parameters will modify the shrinkage as reported in [1,2]. However the shrinkage can be prevented by constraining the tape between porous ceramic release tapes [3,4]. Certain tapes do have zero shrinkage in the x and y directions, at the expense of a higher shrinkage in the z direction [5]. For example, the HeraLock 2000 green tape from Heraeus, has a 0.2% shrinkage in the x and y directions but has about 39% shrinkage in z direction.

### 5.3.2 Fabrication process

The fabrication process of the encoder using LTCC technology is shown in Figure 5. The green tape is preconditioned and then cut to form vias or cavities using subtractive manufacturing processes such as laser ablation as provided by the Epilog™ machine. Following the etching process, the vias are filled with conductive paste and conductive tracks are printed, if relevant, on the tape using screen printing technology. Different layers of tapes are stacked together and then fired in the furnaces forming a hard ceramic structure. The pieces of equipment used are shown in Figure 5.3. The details of each fabrication step are presented in the following sections.

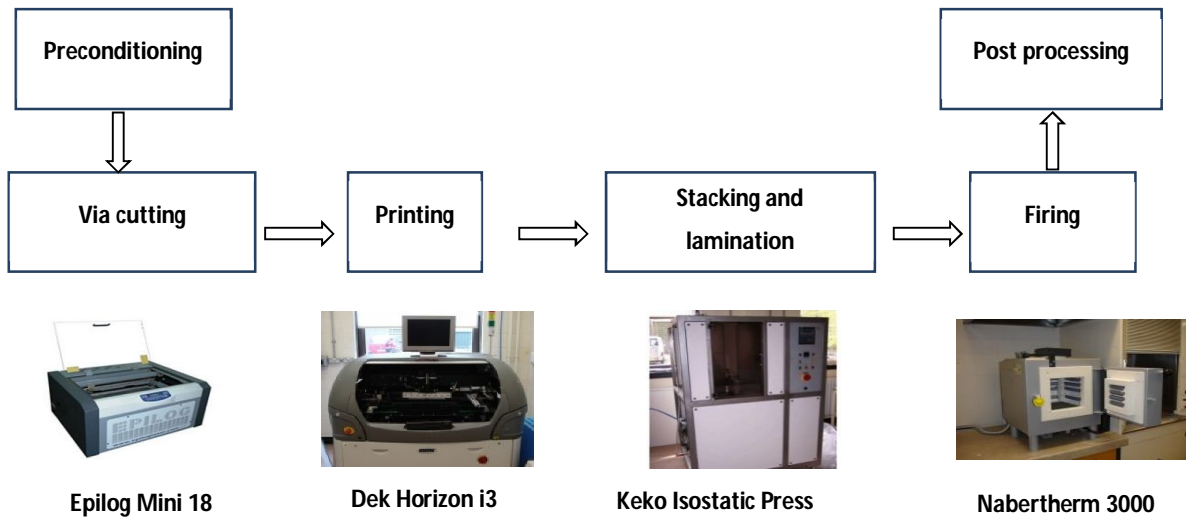


Figure 5.3 Fabrication process of LTCC based magnetic encoder and main equipment used.

#### 5.3.2.1 Green tape cutting

The HeraLock 2000 LTCC tape from Heraeus was used in this project because of its excellent shrinkage property in the x and y directions. The HeraLock 2000 tape shrinks mainly in the z direction, with nearly zero shrinkage in the x and y directions, so the fabricated device would have the same dimensions as designed. The green tape comes in a roll of 15 cm width. The roll was cut out into suitable size (16x15 cm) to fit into the laser cutting machine, where the fiducial holes for alignment and vias were cut.

### 5.3.2.2 Via and cavity forming

In this step of the LTCC fabrication process vias for interlayer connection, fiducial markings and cavity for 3D structuring are cut on each individual layer. There are mainly four ways to machine the green tapes: mechanical punching [6-9], laser cutting [10-14], embossing [15-19] and powder blasting [20,21].

The laser cutting method was used in this project to fabricate the vias for inter layer connection and the fiducial markings for alignment of the LTCC encoder device. The Epilog™ mini 18 laser machine was used for laser cutting. Three different parameters determine the cutting characteristics of the Epilog™ laser cutting machine: frequency, power and speed. The frequency parameter is the switching frequency of the laser beam. The range of frequency is from 1 Hz to 5,000 Hz. The power of the laser beam can be regulated using a gradator and is expressed in percentage of maximum power achievable, which is 30 Watts. The speed parameter relates to the moving speed of the laser head. The speed parameter is expressed as a percentage of the maximum speed that can be achieved. These parameters have been adjusted into order to achieve a diameter of the vias that roughly matches the designed diameter. The holes with 0.15 mm radius in design were cut on the green tape using different parameter values. Results are shown in Figure 5.4.

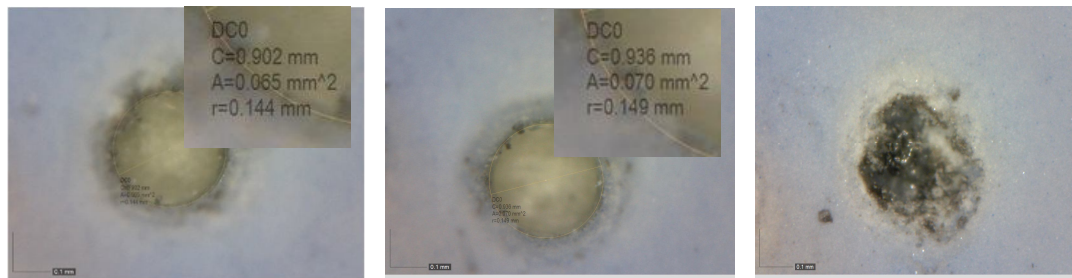


**Figure 5.4 Laser cut vias results: (left) speed: 8%, power: 3%, frequency:100Hz, for a measured radius of 0.144mm; (middle) speed: 8%, power: 3%, frequency: 200Hz for a measured radius:0.149mm. (right) speed: 8%, power: 3%, frequency: 400Hz. The last result is a failure.**

The second set of parameters, as indicated in Figure 5.4, was used and the green tape after cutting is shown in Figure 5.5. The four holes in the outer four corners of the tape are used for stacking alignment, while the four smaller holes next to them

are used as fiducials for aligning the tape with the mask during the screen printing step. The smaller holes (vias) are for inter layer connections.

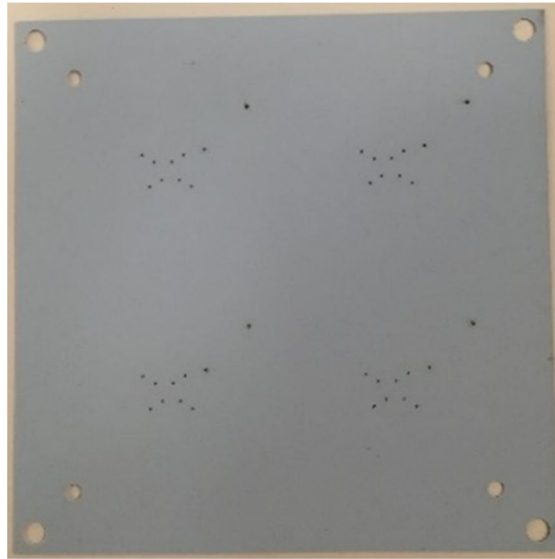


**Figure 5.5 LTCC green sheet with laser cut vias for connection and fiducials markings for alignment**

#### **5.3.2.3 Screen printing**

Screen printing technology is used for the filling of vias with conductive paste and the printing of metal tracks on the green ceramic tapes. During this process the paste is squeezed through apertures defined on a mask. The resulting paste is deposited onto the tape. Fiducial markings on both the mask and the tape are used for alignment [22-25].

Stencils and emulsion screens have both been used for the patterning of the LTCC tapes. The stencil screen is used to fill the vias on the tape. This stencil is often a stainless-steel mask with apertures which are usually laser-cut. The emulsion screen is made of an exposed photo-imageable emulsion laid on a fine metallic or polymeric wire mesh [25]. The emulsion is acting as a mask to define the large patterns that require to be developed and used as apertures. The tracks or pads are defined using emulsion screen printing. The wire mesh allows also the printing of complex structures such as concentric circles, which could not be possible using a stencil [25]. As the masks are different, the pastes used are also different. The paste used for an emulsion screen is usually less viscous than the paste for stencil printing such that it can be squeezed easily through the wire mesh of the emulsion mask.

Two different masks were used in this project to manufacture the LTCC encoder: a stainless steel stencil mask for filling vias and printing the top layer tracks of the encoder; a wire mesh emulsion screen mask for printing the coil tracks on the inner layer of the encoder, as shown in Figure 5.6.



**Figure 5.6 Different masks used for screen printing**

Before printing, the green tapes are preconditioned on a hot plate at around 80°C for 10 minutes in the air atmosphere, as recommended by the tape manufacturer. This step ensures dimensional accuracy during firing shrinkage and relieves the tape from the stress generated if the backing foil is removed.

During printing, the masks are fitted into DEK Horizon i3 screen printer as shown in Figure 5.7, The minimum track width can be achieved by the machine is 100  $\mu\text{m}$  in the lab.



**Figure 5.7 DEK Horizon i3 screen printer used for fabricating the LTCC encoder**

Different silver pastes were used for the different parts of the LTCC encoder as suggested by the paste manufacturer Heraeus. The TC0308 silver paste was used for filling vias. The TC0307 silver paste was used for printing the inner layer tracks while the TC0307 silver paste that is solderable was used for the top layer tracks.



The vias were filled in first using the stainless-steel mask. The tracks were then printed. An example of the tape after printing is shown in Figure 5.8.

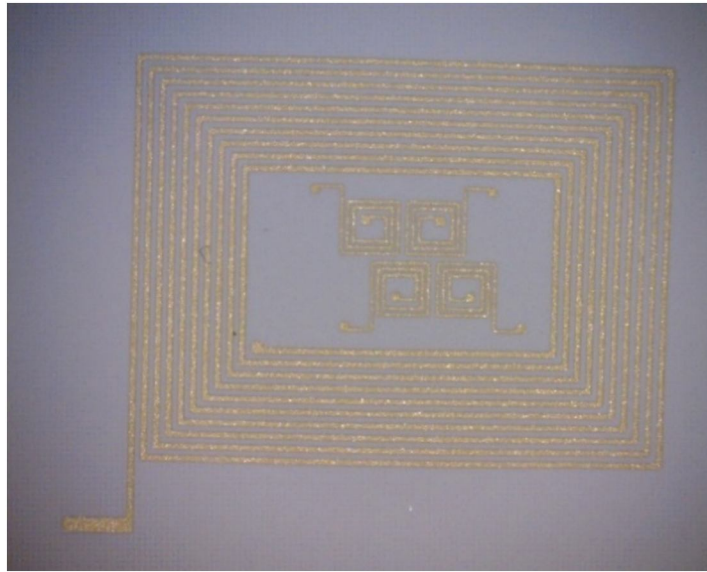


**Figure 5.8 Example of tape after tracks were printed. Vias are under the tracks**

After screen printing the tapes were soft baked on a hot plate for about 10 minutes at 80°C to evaporate solvents from ink. The baked tapes were then stacked together on a rig and vacuum packed in a bag, which is laminated later using the Keko Isostatic Press machine.

#### **5.3.2.4 Stacking and lamination**

In this step, the PET foil on the backside of the tape is removed and different layers were aligned and stacked one by one on an aluminium jig using stacking pins. This step can be done manually or by using an automatic stacker. Extra care has to be taken during the removal of the foils and the stacking of the tapes in order to avoid the substrates from stretching which may destroy the printed track patterns. After stacking, the tapes and the jig are vacuum packaged into a vacuum sealable bag. It is important that the air in the bag is fully evacuated. The sealed bag is then heated up in the Keko isostatic press machine at about 70°C for 10 minutes under a pressure between 10 to 20 MPa. The lamination process creates a soft bonding of the layers due to the material interpenetration at the boundary of the tapes.

### 5.3.2.5 Firing

After the lamination of the tapes, the bag and the jig are removed. The resulting composite structure is then fired using the Nabertherm 3000 furnace following a precise temperature profile.

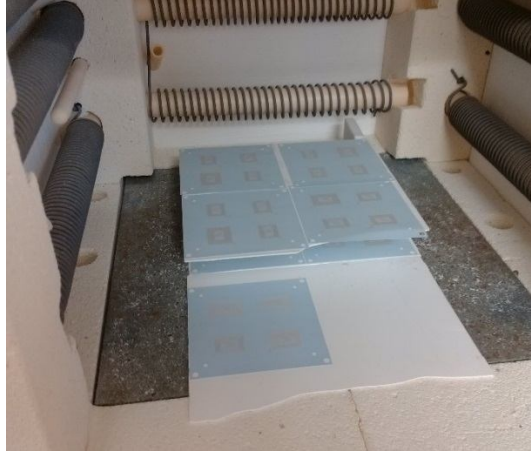


**Figure 5.9 Firing of the LTCC encoder device**

The firing profile for the HL 2000 LTCC tape as shown in Figure 5.10 can be described as follows:

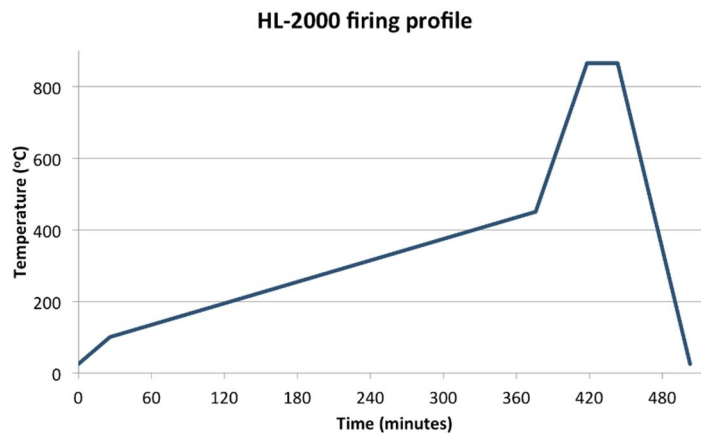


**Figure 5.10 HL2000 firing profile**

The temperature of the furnace is increasing by 3°C/min from room temperature to 100°C in order to start the burnout of the organic compounds forming part of the green tape. The temperature is then raised to 450°C by 1°C /min during which the LTCC tape continues the burnout and the organic binder is driven off. After reaching 450°C, the temperature is increased by 10°C/min to 865°C and dwells for 25

minutes to achieve glass densification. The furnace is then cooled at 10°C/min to room temperature. The whole process takes about 8 hours.

#### **5.3.2.6 Post processing**

After firing, electronic components or connection wires can be attached to the LTCC device by soldering, wire bonding, thermo-compression bonding or flip-chip bonding. The fired structure, which in this case is made of four individual encoders, can then be singulated into individual devices using laser machining or diamond sawing. An example of a singulated LTCC encoder is shown in Figure 5.11. Twisted wires were soldered onto the terminals of the LTCC encoders later. Properties of the encoders were later measured using an oscilloscope and interpolator as discussed in the later part of this chapter.

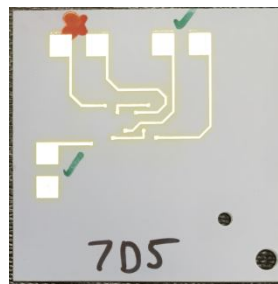


**Figure 5.11 LTCC encoder after slicing**

#### **5.3.2.7 Trouble shooting**

Electrical continuity tests were carried out on the sliced LTCC encoders using a Fluke 70 series digital multimeter. Short circuit between the emitter and the receiver pairs was observed on some of the devices. From the SEM investigations, the cause was the inter-layer connections, most likely due to the large amount of silver deposited on the top layer. This is shown in Figure 5.12. This issue can be mitigated in future designs by having smaller top layer tracks and redesigning their geometry.

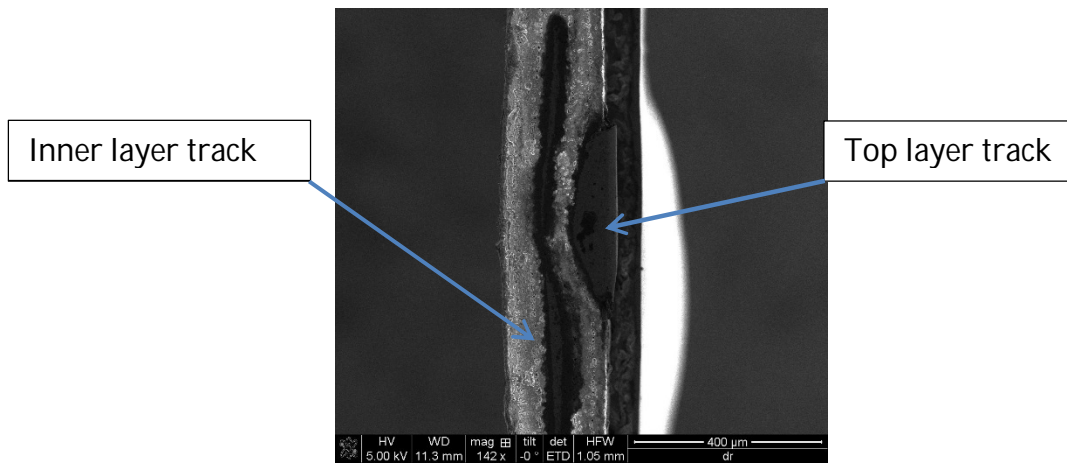


**Figure 5.12 SEM cross section showing the thickness of the top layer tracks comparing with the thickness of the inner layer track.**

Devices with and without top layer tracks, as shown in Figure 5.13, were fabricated and tested. The emitter and receivers were found to be short circuited for the one with the top layer tracks. The other device without top layer tracks was electrically good.



**Figure 5.13 LTCC encoders with and without top layer tracks**

To solve the problem, extra layers with only vias were added to the encoders structures to increase the distance between the tracks on different layers.

### **5.3.3 Measurement of the dimensions of the fabricated LTCC encoder**

The fabricated LTCC encoder device was sliced using wafer dicing saw machine and the cross section was observed using the Dino-lite microscope from Anmo Electronics™. The magnified cross-section is shown in Figure 5.14. Three coils track layers and one top layer within the ceramic layers can be seen in the cross-section.

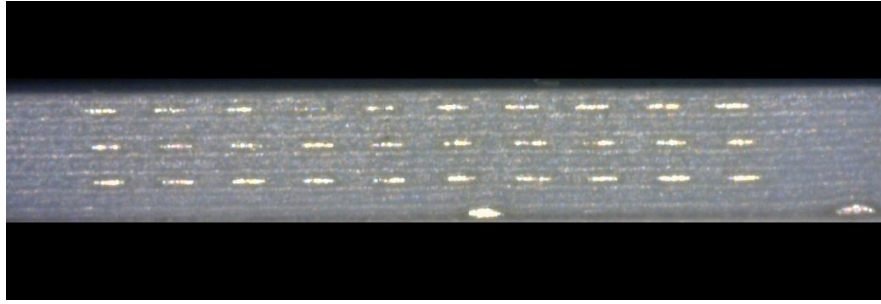


**Figure 5.14 Cross section of the LTCC encoder device**

To further measure the actual dimensions of the fabricated device, a higher magnification Dino-lite microscope was used and the measured results for the emitter coil are shown in Figure 5.15.

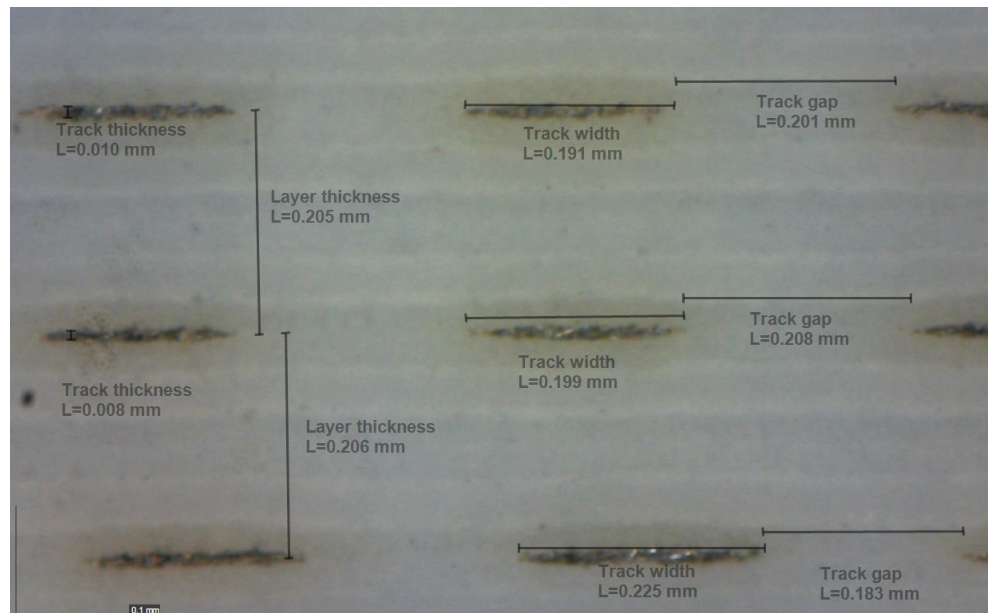


**Figure 5.15 Tracks of the emitter coil as part of the cross section**

The measurement results for the receiver coil are shown in Figure 5.16.

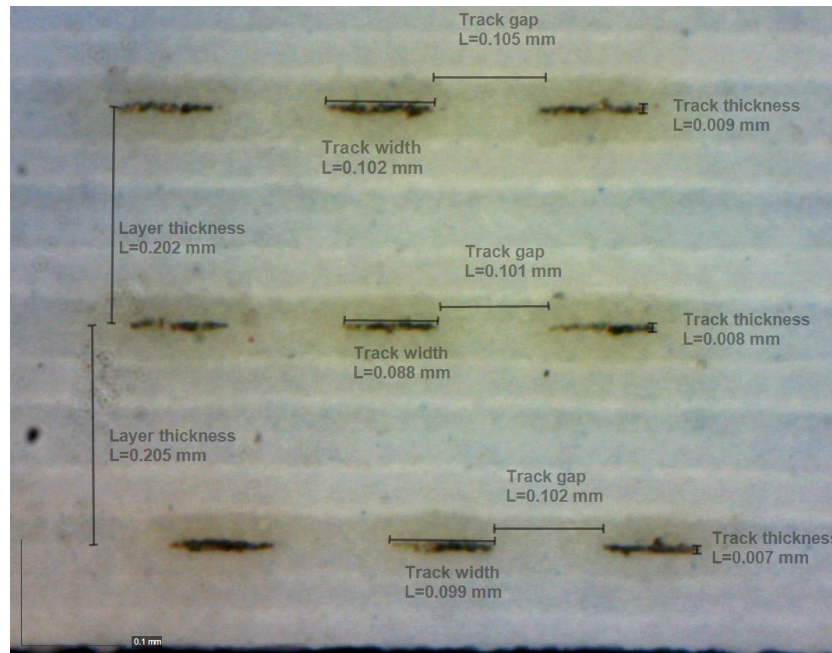


**Figure 5.16 Tracks of the receiver coil as part of the cross section**

The average dimensions of both emitter and receiver coils are summarised in Table 5.2. The average layer thickness of the tape was 205  $\mu\text{m}$  and the thickness of the track was 8  $\mu\text{m}$ .

**Table 5.2 Designed and measured dimensions of the LTCC-based encoder**

Emitter Track				Receiver Track			
Designed ( $\mu\text{m}$ )		Measured ( $\mu\text{m}$ )		Designed ( $\mu\text{m}$ )		Measured ( $\mu\text{m}$ )	
Width	Gap	Width	Gap	Width	Gap	Width	Gap
200	200	205	197	100	100	96	103

### 5.3.4 Impedance measurement

The impedance of the fabricated device was measured using an HP4192A impedance analyser from Keysight™. The impedance analyser is capable of measuring the impedance of the device from 5 Hz to 13 MHz. The measurement setup is shown in Figure 5.17. The HP16095A probe fixture is attached to the impedance analyser to measure the impedance of the LTCC encoder at 1 MHz. As the impedance was measured at low frequency, the equivalent circuit of which is a resistor connected in series with inductor, so the R and L parameters were measured. Calibration was carried out before the measurement. The two tips of the test fixture were connected to a copper plate which will short circuit the test fixture



and zero offset adjustment was carried out by following the instructions from the impedance manual.

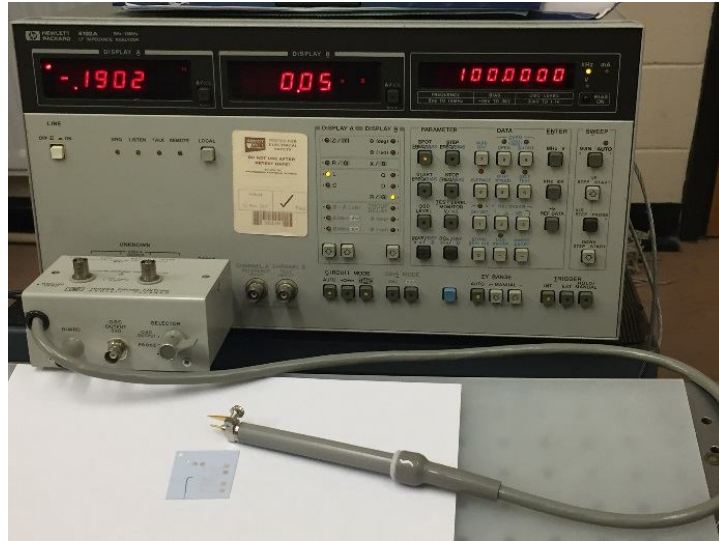


**Figure 5.17 Impedance measurement using HP 4192A impedance analyser**

The self-inductance and resistance values of the emitter and receiver pair coils were measured. Results are summarised and compared in Table 5.3 with the results simulated using the Ansys Maxwell™ software. The difference of impedance values between the measured and simulated results might be due to the misalignment of the coils in the different layers.

**Table 5.3 Simulated and measured impedance of the LTCC encoder at 1MHz**

	Inductance ( $\mu\text{H}$ )			Resistance ( $\Omega$ )		
	Emitter	Receiver pair one	Receiver pair two	Emitter	Receiver pair one	Receiver pair two
Measured	14.9	0.12	0.11	16	3.6	3.3
Simulated	15.5	0.16	0.14	17.5	4.1	3.8
% Difference	3.9	25.0	21.4	8.6	12.2	13.1

To further characterise the encoder, a PCB circuit board was designed and used to process the output signals of the encoders. The positional accuracy of the LTCC-based encoder was compared with Renishaw RGSZ20-S optical encoders, details of which are included in the following section.

#### 5.4 PCB board of the amplification and demodulation circuits

A breadboard amplification and demodulation circuit was assembled and used to measure the PCB encoder prototypes developed in Chapter 4. The connection wires on the breadboard picked up noise from the environment. An amplification and demodulation PCB circuit was therefore designed and fabricated to measure the LTCC encoders.

The signal processing steps of the circuit are the same as the one described in Chapter 4 which was illustrated in Figure 4-1. The circuit is composed of an amplifier, a band pass filter, a demodulator and a low pass filter with an offset shift component. The details of the circuit schematic of the components are described here.

The amplifier of the circuit is implemented using INA217, which is a low noise and low distortion instrumental amplifier from Texas Instruments. The schematic connection of the amplifier is shown in Figure 5.18. Here SK4 and SK5 are the differential signals from the encoders receiver coil outputs.

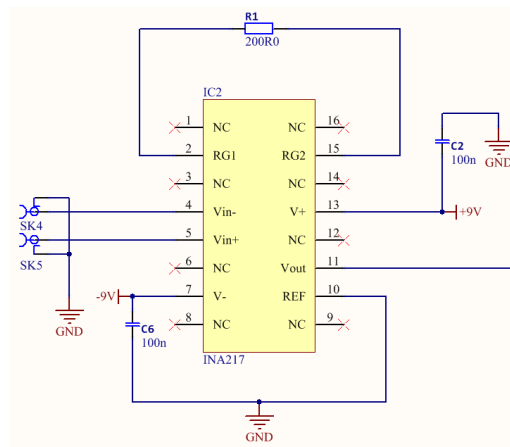
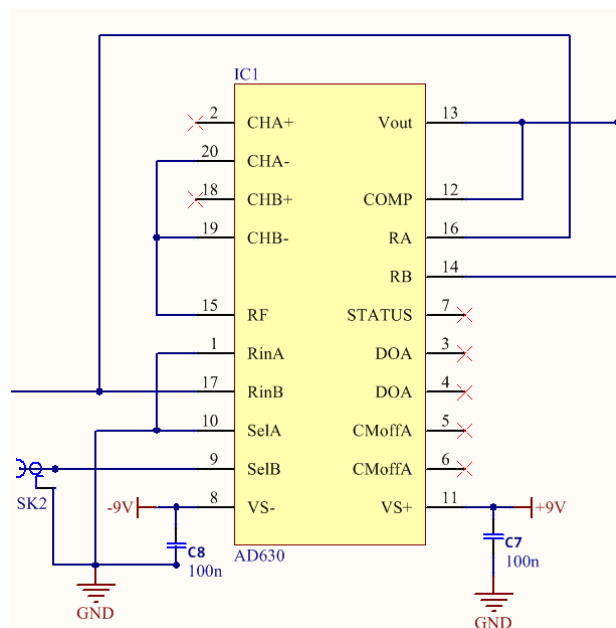


**Figure 5.18 Circuit connection of the amplifier**

After amplification, the signals were processed using a low pass filter and a band pass filter, the implementation of which is shown in Figure 5.19. The purpose of the band pass filter is to limit the signal frequency to the carrier frequency which will reduce both the higher and lower frequency noise. In the physical measurement, the



The demodulator is implemented using AD630 from Analog Device which was described in Chapter 4. The connection of the circuit is shown in Figure 5.20, here the SK2 is the demodulation signal which was connected to the excitation signal of the emitter coil.



The demodulated signal was further processed to extract the envelop of the signal after demodulation. To make the output signals suitable for the Renishaw interpolator, a sum circuit was implement to shift the demodulated signal to the required DC level, as shown in Figure 5.21, since the Renishaw interpolator requires 1.5V DC offset in the signal. Here SK9 is the connector for the final output signal

which can be measured using an oscilloscope or processed by the interpolator circuit.

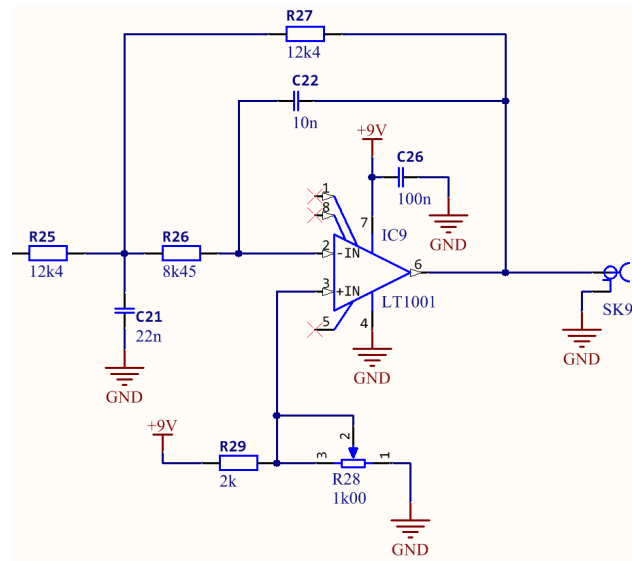


**Figure 5.21 Circuit connection of the low pass filter and offset shift circuit**

The layout of the circuit for the two layers PCB board is shown Figure 5.22. The paths of the signals were placed on the top layer of the board while the power supply connections were placed on the bottom layer.

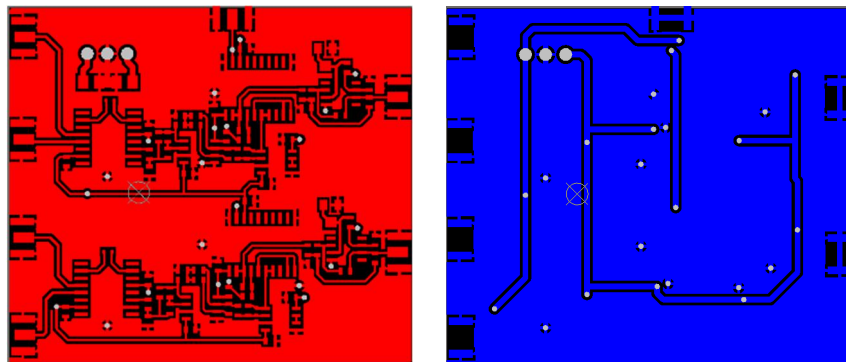


**Figure 5.22 Top (left) and bottom (right) layer of the PCB circuit layout**

The 3D layout of the PCB board and the fabricated physical board are shown in Figure 5.23. SMA connectors were used to reduce the noise. As the noise in the real measurement is small, the low pass filters were removed from the physical board and the red wires were soldered for connection as can be seen on the right of Figure 5.23.

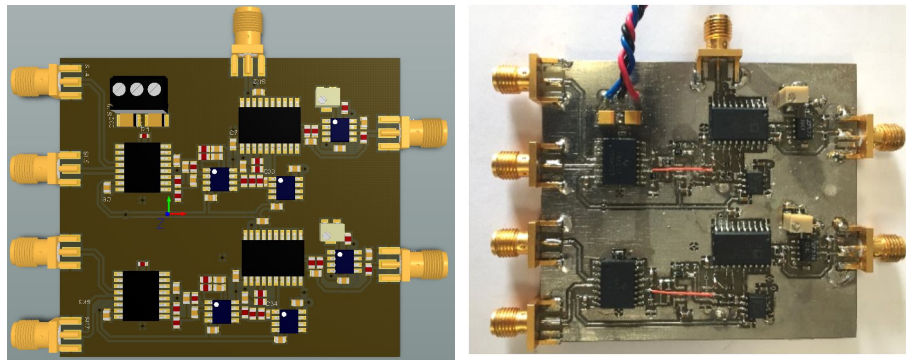


**Figure 5.23 3D PCB layout (left) and fabricated physical PCB board (right)**

This circuit board is used for measuring the LTCC encoders outputs as discussed later.

## **5.5 Characterisation of the LTCC encoder**

Two different methods were used to measure the performance of the LTCC encoders. One method is to measure the demodulated sine and cosine output signals of the two pairs using an oscilloscope. The phase from the measured signals is then calculated and compared with the ideal result which is a straight line in ideal situation as discussed in Chapter 2. The other method is to use an interpolator circuit to convert directly the demodulated sine cosine signals to displacement information. This displacement is then compared with optical encoders that have better resolution and accuracy. Both methods have been used to measure the output nonlinearity (accuracy) performance of the LTCC encoder. Measurement results using the oscilloscope and interpolator are described separately and the results are compared.

### **5.5.1 Measurement setup**

The direct output signals of the LTCC encoders are amplitude modulated signals. The PCB circuit board described above is used to amplify and demodulate these signals. After demodulation, the two signals from the two receiver pairs of the

encoder are acquired using an oscilloscope and also processed using Renishaw REE4000E40A interpolator. The measurement setup is shown in Figure 5.24 below.

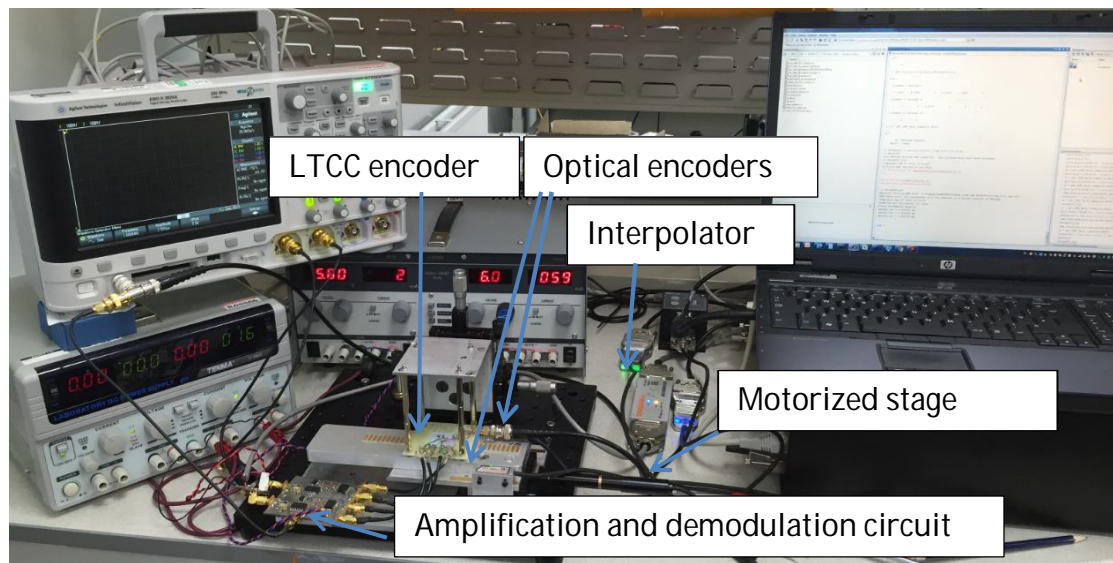


**Figure 5.24 LTCC encoder test setup**

The LTCC encoder is mounted onto a PT3/M stage which is a 3-axis manual stage from Thorlab that has 10  $\mu\text{m}$  resolution. The PCB scale for the LTCC magnetic encoder and two RGSZ20-S optical encoder scales from Renishaw are mounted onto a motorized translation stage MT1-Z8 from Thorlab. The motorized translation stage has 0.1  $\mu\text{m}$  minimum incremental movement and 12 mm travel range. Two Renishaw T1000-10A optical encoders were mounted on the base plate to measure the real displacement for comparison with the measurement of the LTCC magnetic encoder. The optical encoders were mounted on the two edges of the plate on the motorized stage along the travelling direction and were calibrated before the measurement.

The measured displacement by the optical encoders is calculated by the average value of the two optical encoders to counteract the offset movement of the plate during the measurement. The outputs of the LTCC magnetic encoder were connected to the PCB circuit board for amplification and demodulation. The demodulated signals were connected to the Keysight™ oscilloscope and Renishaw REE4000E40A interpolator, which were processed separately to get displacement information. One laptop running MATLAB software is used to provide signals to drive the motorized stage to move at a constant speed. The MATLAB software is also used to acquire the output information from both the optical encoders and the LTCC

magnetic encoder. The measured displacement of the LTCC encoder was compared to that recorded by the optical encoders.

### 5.5.2 Measurement results using the Renishaw interpolator

The stage was moved 9.8 mm forward and then moved back. The displacement was measured using both the optical encoders and the LTCC encoder. The vertical gap between the LTCC encoder and the scale was measured at 0.4mm.

#### 5.5.2.1 Measured displacement

The measured displacement measured by the three encoders was plotted as shown in Figure 5.25. The measured displacement from the three encoders are overlapping with each other and are in good agreement.

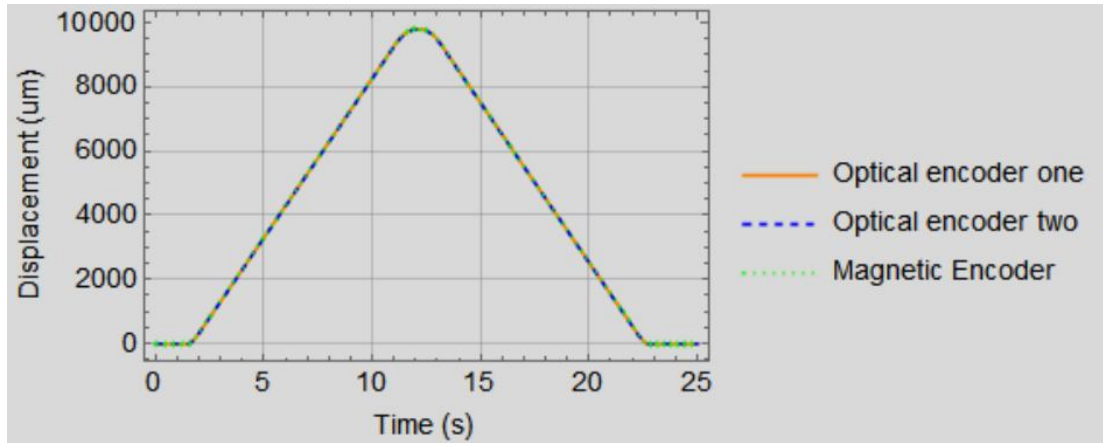


Figure 5.25 Measured displacement from optical encoder one, optical encoder two and magnetic encoder

#### 5.5.2.2 Measurement Error

The actual displacement of the stage was defined as the mean value of the more precise measurements obtained from the two optical encoders. The measurement error is defined as the difference between the encoder measurement value and the mean value. The corresponding measurement nonlinearity error of the three encoders were calculated and plotted against time as shown in Figure 5.26.

For this particular measurement, the error of the magnetic encoder was about  $[-35 \mu\text{m}, 10 \mu\text{m}]$  within one period. One period is defined when the displacement changes by 4.4mm which is from 0 second to about 6 seconds timewise.

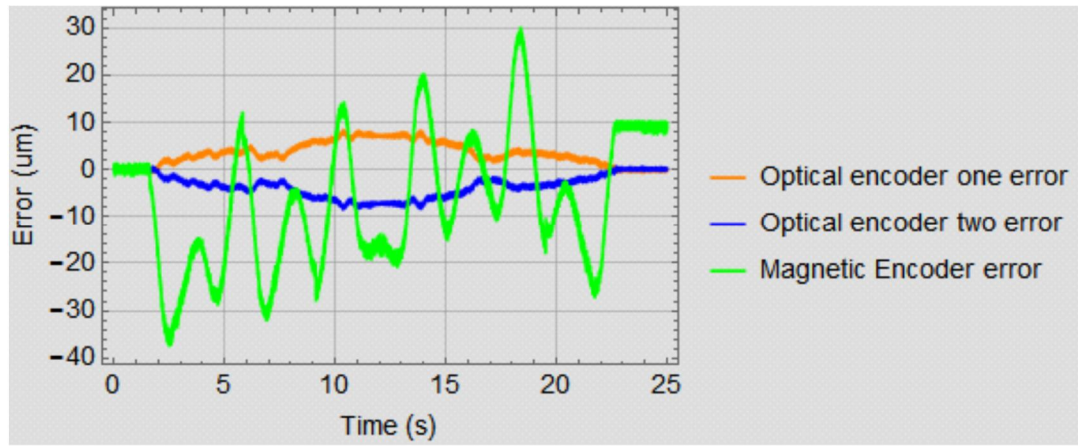


Figure 5.26 Measurement error of the encoders

### 5.5.3 Measurement results using the oscilloscope

The output signals of the LTCC encoder after demodulation were also measured using an oscilloscope and saved as CSV file at the same time. The measured signals data were calibrated to remove the DC offset and imbalanced amplitude. The phase shift between the two signals, if there are any, could also be corrected. The signal calibration process is shown in Figure 5.27.

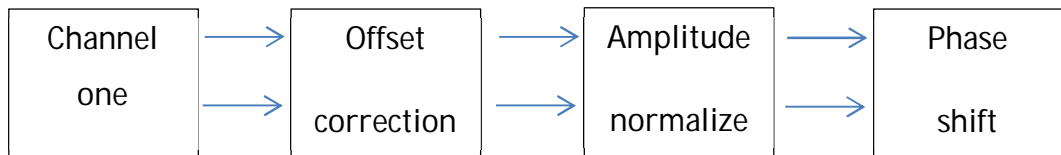
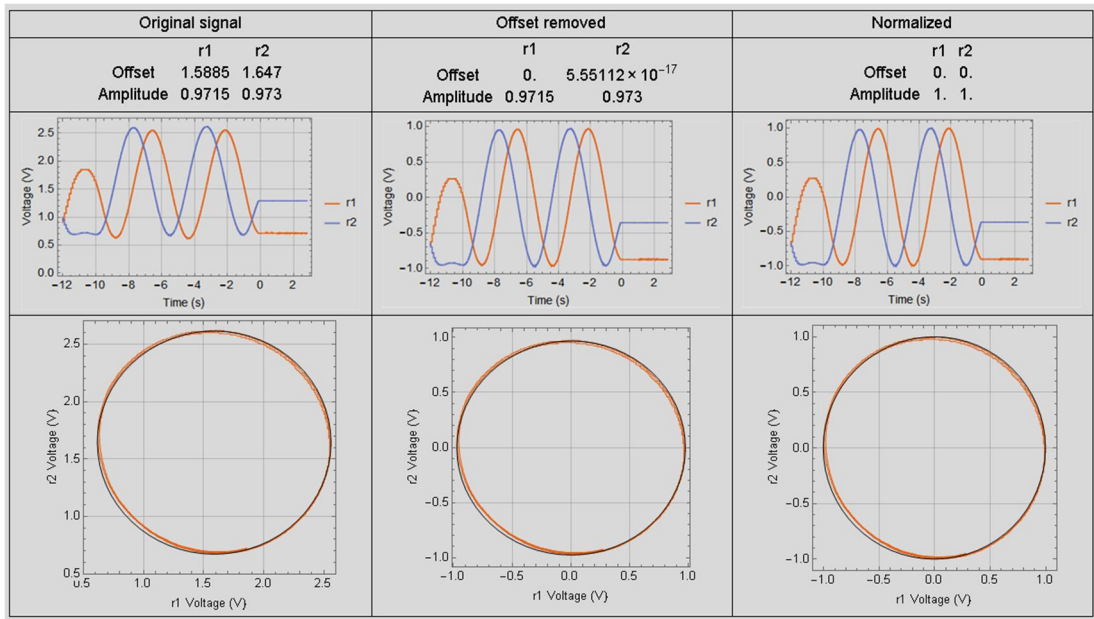


Figure 5.27 Signal calibration process

The offsets were first calculated and removed from the signals, and the signals were then normalized to their amplitude. The signals and corresponding Lissajous curve are summarised in Figure 5.28. In the first column of Figure 5.28, the DC offset of the two signals are 1.5885 V and 1.647 V, respectively. After removing the DC offset, the amplitude of the two signals are 0.9715 V and 0.9730 V.





**Figure 5.28** LTCC encoder output signals before and after calibration: the first column is the original signal, the second column is the data with DC offset removed, the third column is the data with normalized amplitude. The corresponding Lissajous curves are also plotted.

After removing the DC offset and normalizing the amplitude, the phase was calculated using arctangent function and plotted in Figure 5.29.

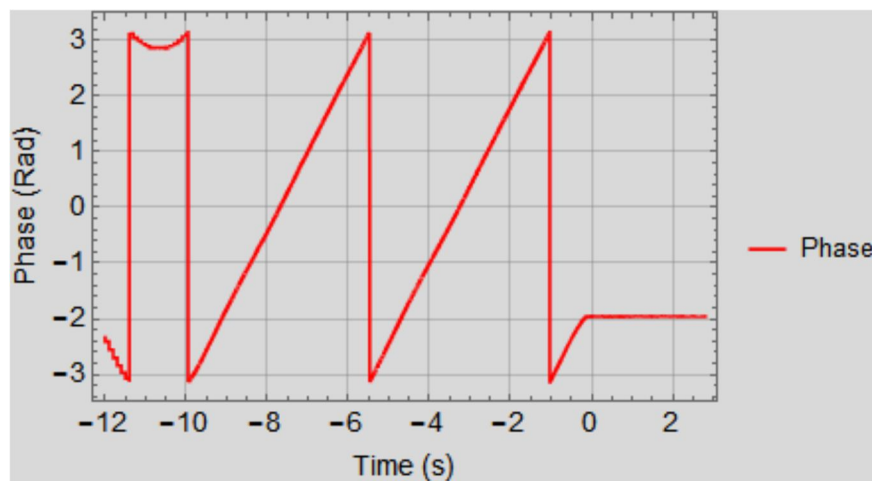


**Figure 5.29** Calculated phase displacement curve

From the phase, it can be seen that there are about two periods of signal. The phase was unwrapped and the result is shown in Figure 5.30 and compared with the phase before unwrap.

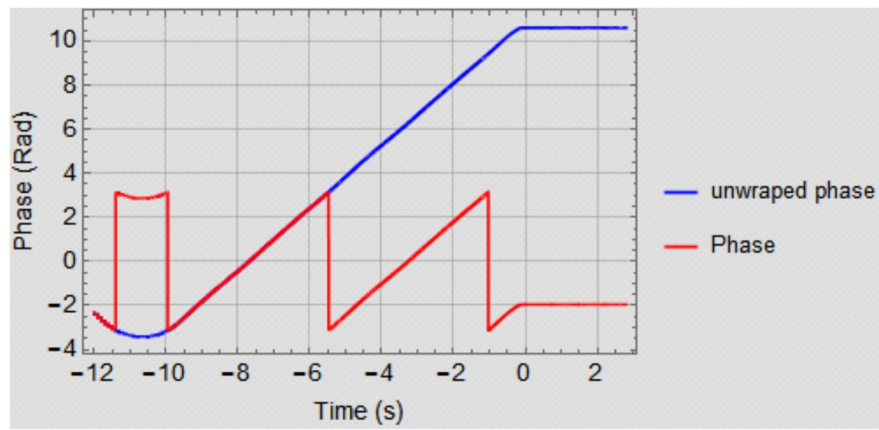


Figure 5.30 Comparison of the calculated phase and unwrap phase

Linear fitting was carried out on the unwrapped phase displacement curve and plotted in Figure 5.31. The adjusted R-square value of the fitting is 0.999976.

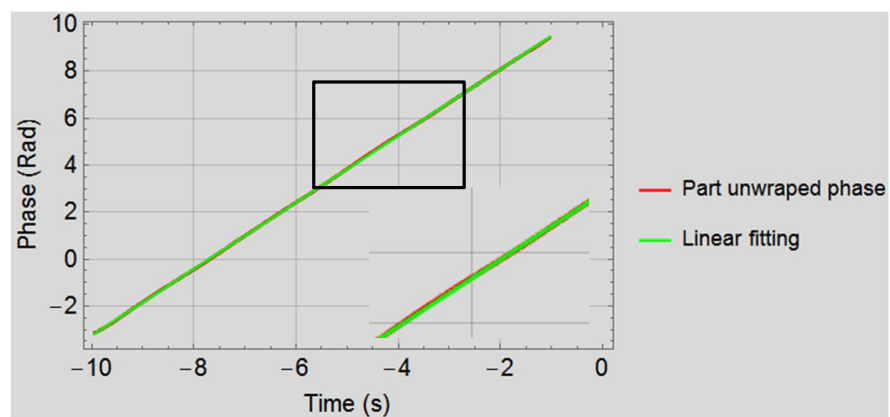
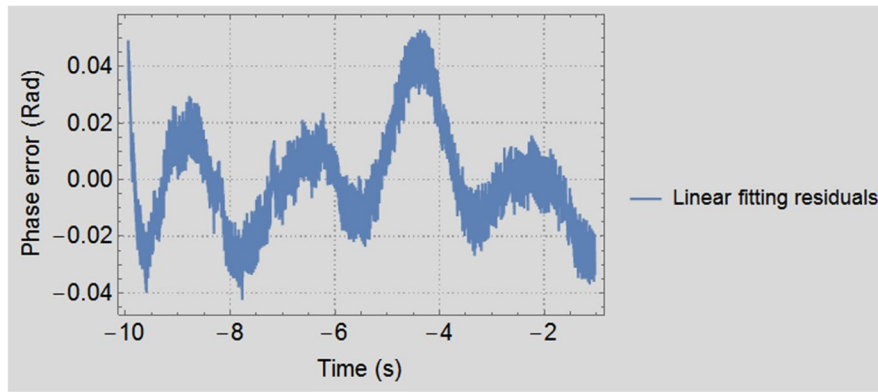


Figure 5.31 Phase displacement curve together with linear curve fitting

The residual of the linear fitting is shown in Figure 5.32





**Figure 5.32 Linear fitting residual**

The residual is converted to corresponding displacement according to the phase displacement relationship of the encoder, the result is shown in Figure 5.33.

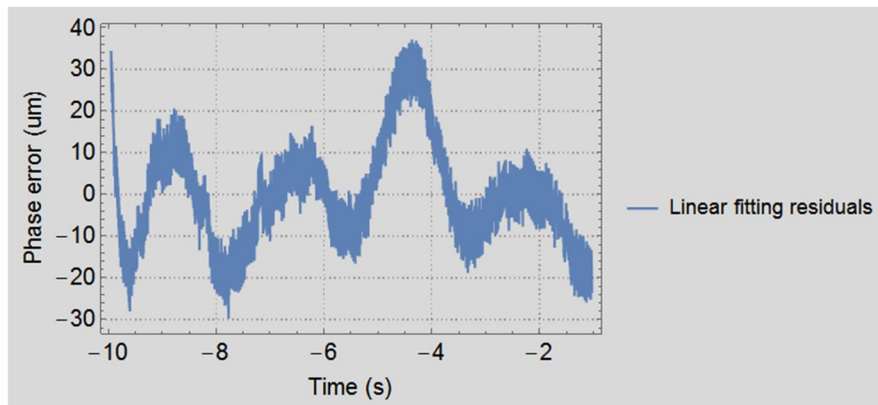


**Figure 5.33 Linear fitting residual**

#### **5.5.4 Comparison of the resulting errors with the two methods**

The error results in the two different measurement methods were shown in Figure 5.26 for the measurement error using the interpolator and in Figure 5.33 for the measurement error using the oscilloscope. Both errors are now plotted together in Figure 5.34. The error values agree well which proves that both methods can be used for characterising the encoder. The measuring method using the oscilloscope is very useful when a better resolution and accuracy encoder is not available for charactering the encoder.

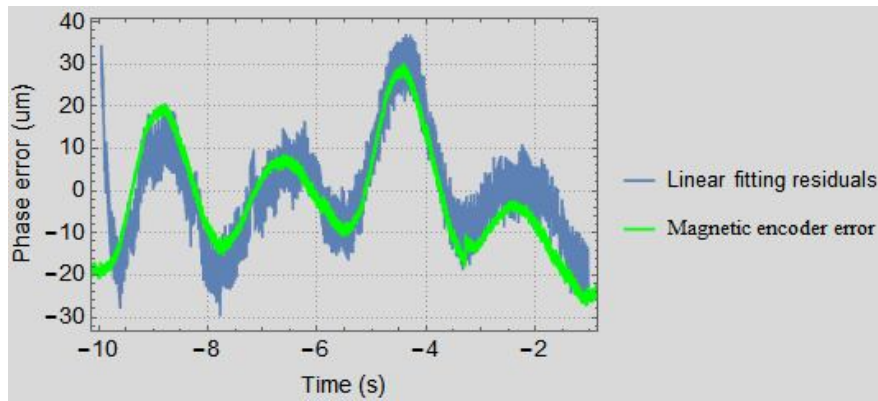


Figure 5.34 Comparison of measurement error and linear fitting residual

### 5.5.5 Correction to the encoder output nonlinearity (accuracy)

Correction using a lookup table used for further calibration was used to increase the accuracy of the encoder. To calibrate the encoder, one period of the signal was sliced and characterised using linearity fitting, the fitting result is shown in Figure 5.35. The adjusted R-square value of the fitting is 0.99919.

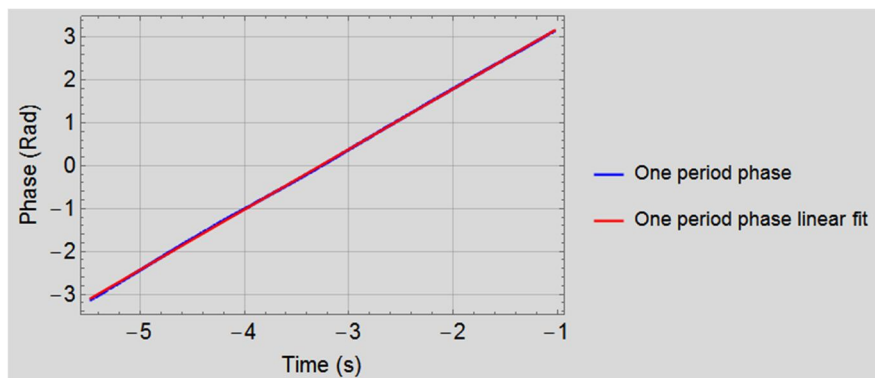
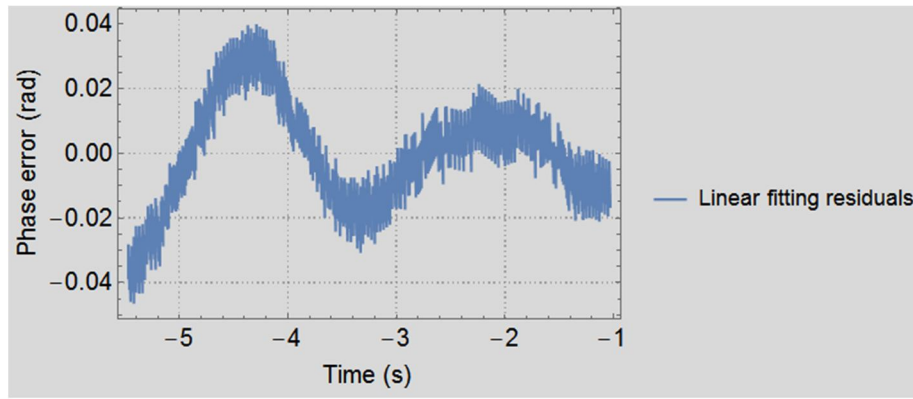


Figure 5.35 Phase displacement curve together with linear curve fitting

The linear fitting residuals were plotted in Figure 5.36.



**Figure 5.36 Linear fitting residual**

The residual is converted to corresponding displacement according to the phase displacement relationship of the encoder, the result is shown in Figure 5.37.

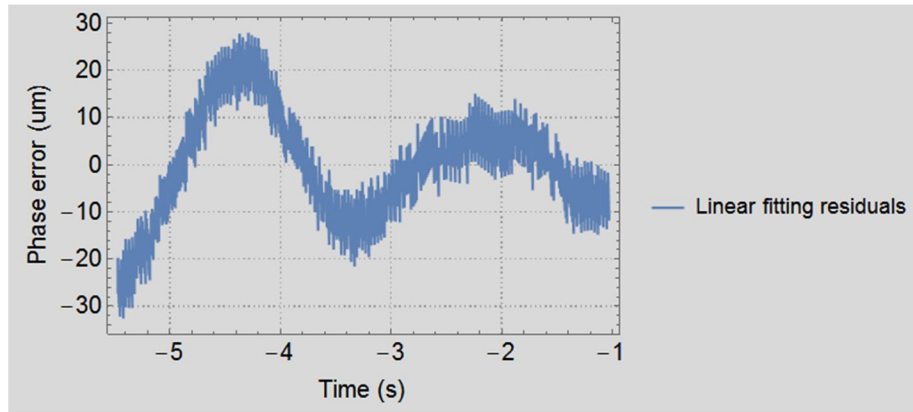


**Figure 5.37 Linear fitting residual**

A 64-bit lookup table was initialized based on the error and used to calibrate the encoder. The error before and after calibration are plotted in Figure 5.38. The residual, originally between -30  $\mu\text{m}$  to 25  $\mu\text{m}$ , reduces to -10  $\mu\text{m}$  to 10  $\mu\text{m}$  after look-up table correction.

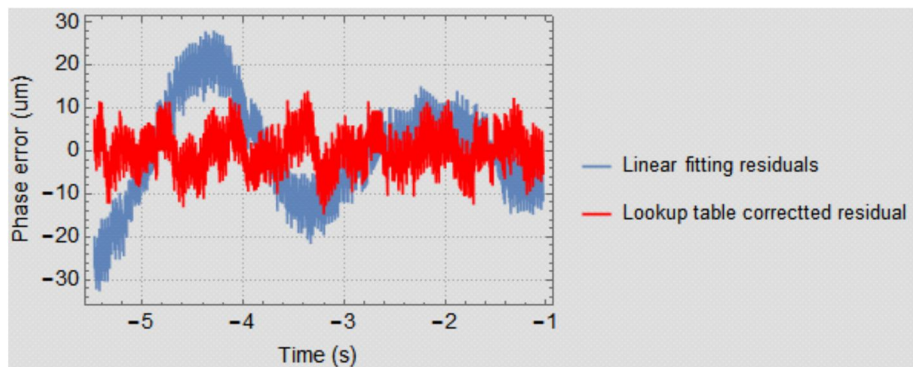


**Figure 5.38 Comparison of residuals before and after correction using a look-up table**

The signals of the two channels were fitted with a sinusoidal function. The results are shown in Figure 5.39. The adjusted R-square value for r1 and r2 are 0.999947 and 0.999952, respectively.

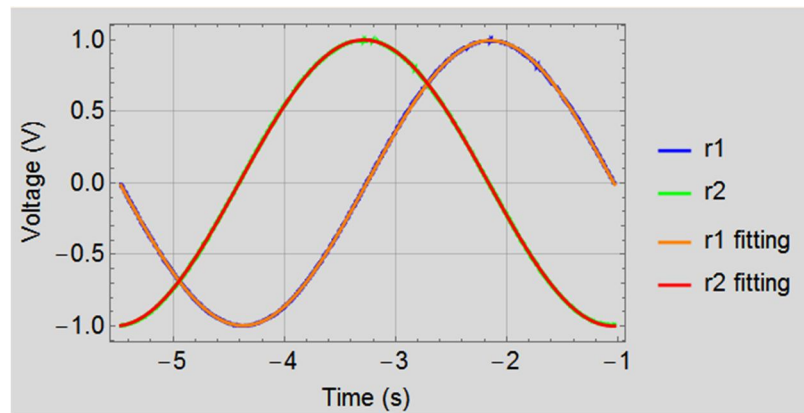


**Figure 5.39 Encoder signals with corresponding Sinusoid curve fitting**

The fitting residual is shown in Figure 5.40, it can be seen that the residuals ranges from -0.015 V to 0.015 V, which is relative small comparing with the amplitude.

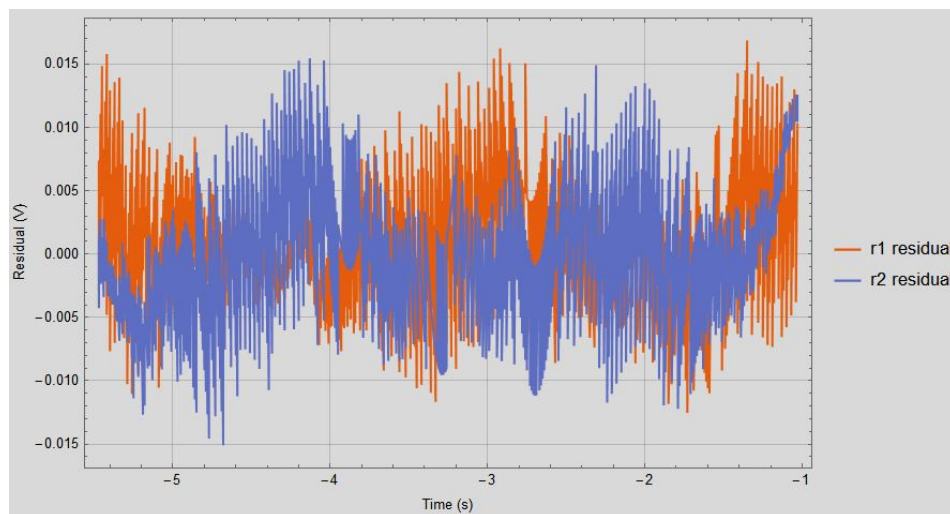


**Figure 5.40 Sinusoid curve fitting residuals**

From the fitting results, the signal is clearly of a sinusoidal form. The two signals were therefore analysed in the frequency domain using the same method described in Chapter 4. The phase difference between the two signals was about 2.14 degrees smaller than 90 degrees. There are 2,963 data points in one period in this

measurement, which corresponds to 360 degrees. As the 2.14 degrees difference represents about 17 data points, so the data in channels two was rotated to left to correct this phase difference. The phase displacement was calculated using the corrected data and fitted to a straight line. The residual was plotted in Figure 5.41 and compared with the residual before correction.

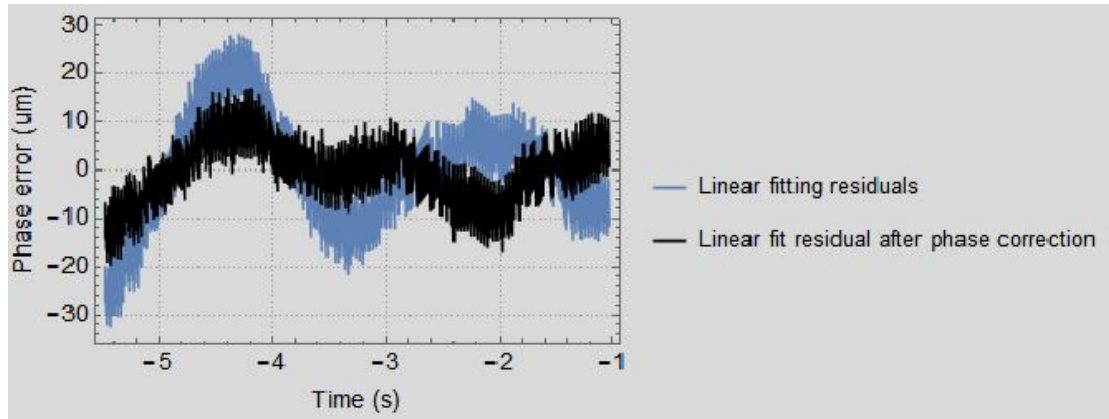


Figure 5.41 Comparison of residuals before and after phase correction.

After phase correction, the nonlinear error was reduced from  $[-30 \mu\text{m}, 25 \mu\text{m}]$  to  $[-20 \mu\text{m}, 15 \mu\text{m}]$ . A look-up table was used to further reduce the error, the result is shown in Figure 5.37. After the look-up table correction the residual reduced from  $[-20 \mu\text{m}, 15 \mu\text{m}]$  to  $[-10 \mu\text{m}, 10 \mu\text{m}]$ .

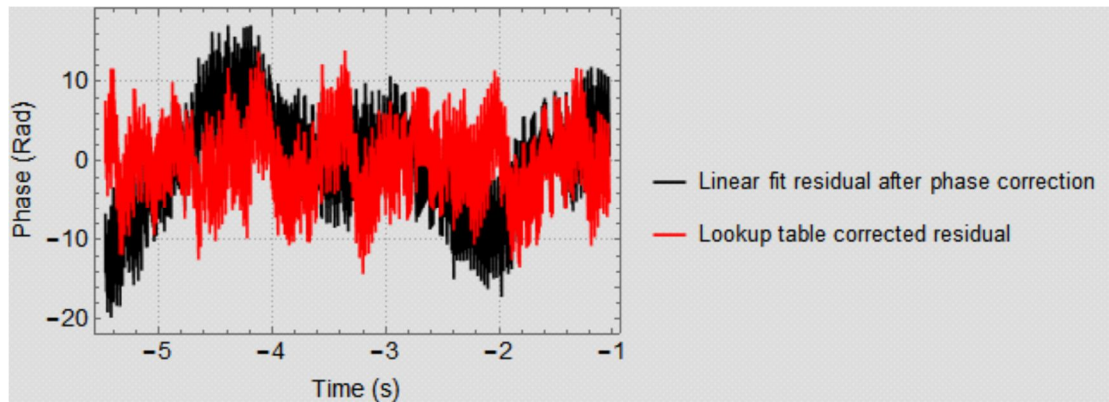


Figure 5.42 comparison of residuals before and after correction using lookup table

## 5.6 Conclusions

A multi-layer structured magnetic position encoder was fabricated using Low Temperature Co-fired Ceramic (LTCC) technology. The fabrication process of the encoder was described in details in this Chapter. A PCB circuit board was fabricated to amplify and demodulate the LTCC encoder output signals. The schematic and PCB layout of the circuit board were also presented. Two different methods were used to characterize the LTCC encoder, with good agreement between the measurement results of the two methods. The output nonlinearity of the LTCC encoder was about  $-30\text{ }\mu\text{m}$  to  $25\text{ }\mu\text{m}$  and after lookup table correction, this nonlinearity reduces to  $-10\text{ }\mu\text{m}$  to  $10\text{ }\mu\text{m}$ .

The output nonlinearity performance of the LTCC encoder is in general better than the PCB encoders, with the best results for the PCB encoders is  $-35\text{ }\mu\text{m}$  to  $25\text{ }\mu\text{m}$ . But the cost and the manufacture process of the PCB encoders is lower than that of the LTCC encoder.

## Reference

- [1] Y. Fournier, "3D Structuration Techniques of LTCC for Microsystems Applications": EPFL, 2010.
- [2] Y. Fournier, "Influence of lamination parameters on LTCC shrinkage under unconstrained sintering".
- [3] C. R. Needes, M. F. Barker, P. T. Ollivier, K. W. Hang, K. E. Souders, C. B. Wang, and M. A. Smith, "Constrained-sintered, low-temperature Co-fired ceramic for IC packaging applications," in Electronic Components and Technology Conference, 2003. Proceedings. 53rd, 2003, pp. 30-35.
- [4] K. M. D. S. RH Jensen, "Method for reducing shrinkage during firing of the green ceramic bodies," , 1992.
- [5] Lautzenhised, F. and E. Amaya HeraLockTM 2000 Self-constrained LTCC Tape.
- [6] J. C. Lin, W. S. Lin, K. S. Lee, and J. L. Tong, "The optimal clearance design of micro-punching die," Journal of Achievements in Materials and Manufacturing Engineering, vol. 29, pp. 79--82, 2008.
- [7] W. Gangqiang, E. C. Folk, F. Barlow, and A. Elshabini, "Fabrication of microvias for multilayer LTCC substrates," Electronics Packaging Manufacturing, IEEE Transactions on, vol. 29, pp. 32-41, 2006-01-01 2006.
- [8] Z. Tekiner, M. Nalbant and H. Gürün, "An experimental study for the effect of different clearances on burr, smooth-sheared and blanking force on aluminium sheet metal," Materials & Design, vol. 27, pp. 1134-1138, 2006-01-01 2006.
- [9] B. Joo, S. Rhim and S. Oh, "Micro-hole fabrication by mechanical punching process," Journal of Materials Processing Technology, vol. 170, pp. 593-601, 2005-12-30 2005.
- [10] M. F. Shafique and I. D. Robertson, "Rapid prototyping of LTCC microwave circuits using laser machining," in Microwave Symposium Digest, 2009. MTT '09. IEEE MTT-S International, Boston, MA, 2009, pp. 469-472.
- [11] K. M. Nowak, H. J. Baker and D. R. Hall, "A model for "cold" laser ablation of green state ceramic materials," APPLIED PHYSICS A-MATERIALS SCIENCE & PROCESSING, vol. 91, pp. 341-348, 2008.

- [12] H. Huang, J. He, C. Zuo, B. Zhang, X. Dong, S. Zhao, and Y. Wang, "Highly efficient and compact laser-diode end-pumped Q-switched Nd:YVO<sub>4</sub>/KTP red laser," *Optics Communications*, vol. 281, pp. 803-807, 2008-02-15 2008.
- [13] K. M. Nowak, H. J. Baker and D. R. Hall, "Cold processing of green state LTCC with a CO<sub>2</sub> laser," *APPLIED PHYSICS A-MATERIALS SCIENCE & PROCESSING*, vol. 84, pp. 267-270, 2006.
- [14] J. J. Zhu and W. Yung, "Studies on laser ablation of low temperature co-fired ceramics (LTCC)," *INTERNATIONAL JOURNAL OF ADVANCED MANUFACTURING TECHNOLOGY*, vol. 42, pp. 696-702, 2009.
- [15] S. Bredeau and J. Bancillon, "Opportunities and Challenges in Room Temperature Embossing/Punching for Ceramic Green Tapes," *PROCEEDINGS OF THE 8TH INTERNATIONAL CONFERENCE ON MULTI-MATERIAL MICRO MANUFACTURE (4M 2011)*, pp. 256-259, 2011.
- [16] X. C. Shan, S. H. Ling, H. P. Maw, C. W. Lu, and Y. C. Lam, "Micro Embossing of Ceramic Green Substrates for Micro Devices," *DTIP 2008: SYMPOSIUM ON DESIGN, TEST, INTEGRATION AND PACKAGING OF MEMS/MOEMS*, pp. 355-359, 2008.
- [17] X. C. Shan, H. P. Maw, R. T. Tjeung, S. H. Ling, C. W. Lu, and R. Jachowicz, "Microstructure formation on low temperature co-fired ceramic green substrates using micro embossing," *MICROSYSTEM TECHNOLOGIES-MICRO-AND NANOSYSTEMS-INFORMATION STORAGE AND PROCESSING SYSTEMS*, vol. 14, pp. 1405-1409, 2008.
- [18] H. P. Maw, S. C. Wai, R. T. T'Jeung, L. C. Wai, L. B. Keng, and X. C. Shan, "Micro embossing of LTCC (Low Temperature Co-fired Ceramic) green substrates," *2007 9TH ELECTRONICS PACKAGING TECHNOLOGY CONFERENCE, VOLS 1 AND 2*, pp. 510-513, 2007.
- [19] M. Hecke and W. K. Schomburg, "Review on micro molding of thermoplastic polymers," *JOURNAL OF MICROMECHANICS AND MICROENGINEERING*, vol. 14, pp. R1-R14, 2004.
- [20] Y. Lacrotte, J. P. Carr, R. W. Kay, and M. P. Y. Desmulliez, "LTCC package manufacturing using powder blasting technology," in *Design, Test, Integration and Packaging of MEMS/MOEMS (DTIP), 2012 Symposium on, Cannes, 2012*, pp. 186-191.



- [21] Y. Lacrotte, R. W. Kay and M. P. Y. Desmulliez, "Manufacture of a 3-D package using Low Temperature Co-fired Ceramic technology," in Microelectronics and Packaging Conference (EMPC), 2011 18th European, Brighton, 2011, pp. 1-8.
- [22] R. W. Kay, G. Cummins, M. P. Y. Desmulliez, J. Terry, and A. J. Walton, "Novel dual layer electroformed stencils for high resolution LTCC circuit manufacture," in 2011 IEEE 13th Electronics Packaging Technology Conference, 2011, pp. 507–512.
- [23] B. Synkiewicz, J. Kulawik, A. Skwarek, Y. Yashchyshyn, and P. Piasecki, "High resolution patterns on LTCC substrates for microwave applications obtained by screen printing and laser ablation," in 2016 39th International Spring Seminar on Electronics Technology (ISSE), 2016, pp. 17–21.
- [24] I. Ferrer and J. Svedin, "A 60 GHz image rejection filter manufactured using a high resolution LTCC screen printing process," in 33rd European Microwave Conference Proceedings (IEEE Cat. No.03EX723C), pp. 423–425.
- [25] Y. Lacrotte and Yves, "Novel patterning technology for the LTCC based packaging of an optical encoder," 2013.

## Chapter 6 - Conclusions and future work

### 6.1 Conclusions

In this thesis, several different new eddy currents based magnetic position encoder structures have been designed, fabricated using two different manufacturing technologies and the relative performance of each type of encoder has been assessed. The working principle of the encoders were described and the performance were studied both analytically using mathematical modelling and numerically using the Maxwell™ FEM simulation software package. Different types of encoders were fabricated using PCB and LTCC technology. The corresponding signal conditioning circuits were also fabricated and used to characterise the accuracy performance of the encoders.

A literature review of encoders was presented which was based on different physical sensing principles such as resistive encoder, capacitive encoder, magnetic and optical encoder. A more specific literature review on eddy currents based magnetic encoders was also provided. The specifications of the encoder, such as measurement range, repeatability, accuracy (output nonlinearity), resolution, hysteresis and response time, were described and revisited when performance characterization was implemented for each of the type of encoder.

An analytical model that calculates the coupling between rectangular planar coils with physical displacements occurring in different directions was derived and calculated using the Mathematica™ software package. The results were verified using the Finite Element Modelling (FEM) simulation software ANSYS Maxwell and experimentally validated. The measured and calculated results were compared with the simulated results. Good agreements were achieved with absolute values of the average errors for Z-axis displacements of 2.97% and 1.09%. The values of the average errors for the Y-axis displacements were 18.5% and 3.0%.

By simplifying the metal plate on the scale as a multi-turn planar coil, a system level analytical model of the encoder was presented. Three different AM (amplitude modulation) signal forms could be generated depending on the encoder structure. An amplification and demodulation circuit was designed and used to demodulated the AM signals. After demodulation, two sinusoidal signals should be generated in ideal situation. The two sinusoidal signals were qualitatively assessed using the Lissajous curve and the corresponding phase displacement curves. In an ideal situation, the phase calculated from the two receiver pair signals using arctangent function should be linear to the relative displacement between the read head and the scale. The phase of the corrupted signal has been compared with the ideal signal. Four errors in the signals were elucidated: DC offset error, amplitude imbalance error, phase shift error and higher harmonic distortion error. The influence of the four error types on the Lissajous curve and phase displacement curve were summarized.

Four different encoder structure prototypes were implemented using PCB technology. The mutual inductance changes between emitter and receiver pairs as a function of the scale displacement were simulated using the ANSYS Maxwell™ software package and measured. The simulated and measured results were compared and summarised in Table 4.3. Prototype four has the best accuracy performance which ranged from -35  $\mu\text{m}$  to 25  $\mu\text{m}$ .

An alternative manufacturing process of the magnetic encoder based on multilayer Low Temperature Co-fired Ceramic (LTCC) technology was also presented. The details of the fabrication process of the LTCC encoder and equipment used were described. The LTCC encoder was characterised using Keysight oscilloscope and Renishaw optical encoders with good agreement for all the measurements. The best accuracy performance of the LTCC encoder was -30  $\mu\text{m}$  to 25  $\mu\text{m}$ . A look up table correction method was used to reduce the error with nonlinearity error reducing to -10  $\mu\text{m}$  to 10  $\mu\text{m}$ .

## 6.2 Future work

An optimization on the encoder structure dimensions should be carried out. The main reason for the encoder output nonlinearity error is that the coupling between the emitter coil and the metal plates on the scale is not constant as the relative displacement changes as described in Chapter 3. This could be reduced by making the field of the emitter coil more uniform through changing the emitter coil shape or geometries such as coil turns, track width and gaps. An optimization should be carried on the emitter coil geometry to make its magnetic field more uniform.

Another way of doing the optimization is from the system level. Except for only changing the geometry of the emitter coil, the geometry of the receiver coils and the metal plates on the scale could also be changed. A design of experiments (DOE) based on these geometry variables could be carried out aiming at reducing the nonlinearity error of the encoder.

An investigation on other encoder performance specifications should be carried out in the future. The work in the thesis mainly focused on study the accuracy (encoder output nonlinearity) of the encoder which indeed is a very important specification. But in some control systems, when the accuracy or the nonlinearity measurement error is acceptable, hysteresis and repeatability become more important. So an investigation on these specifications of the encoder should also be expected.

## Appendix A – Mathematica script for data processing

### ***Import data acquired using Keysight oscilloscope***

```
data=Drop[Import["F:\\ secf4.csv"],2];  
posx=data[[All,1]];r1=data[[All,4]];r2=data[[All,5]];
```

### ***Import data acquired using Renishaw interpolator***

```
edata=Import["F:\\ secondfz4.xls"][[1]];  
time=edata[[All,1]]; opt1=edata[[All,2]]*103; opt2=edata[[All,3]]*103;  
mag=edata[[All,4]]*103;
```

### ***Calculate the average measured displacement from the two optical encoders***

```
optavg=(opt1+opt2)/2;
```

### ***Calculate the difference between the encoder measurements and the average value***

```
eopt1=opt1-optavg; eopt2=opt2-optavg; emag=mag+optavg;
```

### ***Set style for the plot***

```
ptErStyle={ImageSize->Medium,PlotTheme->{"Scientific"},{FrameLabel->{"Time  
(s)", "Error (um)"},LabelStyle->Directive[14,Black]},GridLines->Automatic};
```

### ***Plot the corresponding encoder measurement errors***

```
plotError=ListLinePlot[{Transpose@{time,eopt1},Transpose@{time,eopt2},Transpose@  
{time,emag}},PlotStyle->{Orange,Blue,Green},PlotLegends->{"Optical encoder one  
error", "Optical encoder two error", "Magnetic Encoder error"},ptErStyle//Rasterize;
```

### ***Plot the measured displacement of the two optical encoders and the LTCC encoder***

```
plotDis=plotError=ListLinePlot[{Transpose@{time,opt1},Transpose@{time,opt2},Trans  
pose@{time, - mag}},PlotStyle->{Orange,{Dashed,Blue},{Dotted,Green}},  
PlotLegends->{"Optical encoder one ", "Optical encoder two ", "Magnetic Encoder  
"},FrameLabel->{"Time (s)", "Displacement (um)"},LabelStyle->Directive[14,Black],  
PlotTheme->"Scientific",GridLines->Automatic,ImageSize->Medium]//Rasterize
```

### ***Get one segment of the measured displacement for analysis***

```
segPoint={{6000,17000},{20000,33000}}  
{ListPlot[(Transpose@{time,-mag})][[segPoint[[1,1]];;segPoint[[1,2]]]],  
PlotTheme->"Detailed"],ListPlot[(Transpose@{time,-  
mag})][[segPoint[[2,1]];;segPoint[[2,2]]]],PlotTheme->"Detailed"]}
```

### ***Linear fitting on the data***

```
{magLF=LinearModelFit[(Transpose@{time,-mag})][[segPoint[[1,1]];;  
segPoint[[1,2]]]],x,x],  
magLF2=LinearModelFit[(Transpose@{time,-mag})][[segPoint[[2,1]];;  
segPoint[[2,2]]]],x,x)}
```

### ***Plot the residual of the linear fitting***

```
magResidual=magLF["FitResiduals"]; magResidual2=magLF2["FitResiduals"];
{plotmagResidual=ListLinePlot[Transpose@{time[[segPoint[[1,1]];;segPoint[[1,2]]]],-
magResidual-
15},ImageSize->Medium,PlotRange->All,PlotTheme->"Detailed",PlotLegends->{"Linear
fitting residuals"},FrameLabel->{"Time (s)", "Phase error
(um)"},LabelStyle->Directive[{FontFamily->"Arial",FontSize->14,Black}],
plotmagResidual2=ListLinePlot[Transpose@{time[[segPoint[[2,1]];;segPoint[[2,2]]]],-
magResidual2-
20},ImageSize->Medium,PlotRange->All,PlotTheme->"Detailed",PlotLegends->{"Linear
fitting residuals"},FrameLabel->{"Time (s)", "Phase error
(um)"},LabelStyle->Directive[{FontFamily->"Arial",FontSize->14,Black}]}
```

### ***Processing the data acquired using oscilloscope,Set style for the plot***

```
ptSCStyle={PlotTheme->{"Scientific"},FrameLabel->{"Time (s)", "Voltage
(V)"},PlotLegends->{"r1", "r2"},GridLines->Automatic,LabelStyle->Directive[14,Black]};
ptLissaStyle={AspectRatio->1,PlotTheme->"Scientific",FrameLabel->{"r1 Voltage
(V)", "r2 Voltage (V)"},GridLines->Automatic,AspectRatio->1,
ImageSize->Medium,LabelStyle->Directive[14,Black]};
```

### ***Calculated the DC offset and amplitude***

```
r1Orgf=Mean[{Max[r1],Min[r1]}];r2Orgf=Mean[{Max[r2],Min[r2]}];
r1max=Max[r1]-r1Orgf;r2max=Max[r2]-r2Orgf;
pr12=ListLinePlot[{Transpose@{posx,r1},Transpose@{posx,r2}},ptSCStyle]//Rasteriz;
pqr12=Show[ListLinePlot[Transpose@{r1,r2},PlotRange->{{0.5,2.6},{0.5,2.7}},ptLissaSty
le],Graphics[Circle[{r1Orgf,r2Orgf},r1max]]];
```

### ***Remove the DC offset and plot***

```
r1o=r1-r1Orgf;r2o=r2-r2Orgf;
r1Offf=Mean[{Max[r1o],Min[r1o]}];r2Offf=Mean[{Max[r2o],Min[r2o]}];
r1offM=Max[r1o];r2offM=Max[r2o];
pr12o=ListLinePlot[{Transpose@{posx,r1o},Transpose@{posx,r2o}},ptSCStyle]//Rasteri
ze;pqr12o=Show[ListLinePlot[Transpose@{r1o,r2o},ptLissaStyle],Graphics[Circle[{r1Off
f,r2Offf},r1offM]]];
```

### ***Normalize the signals to its amplitude and plot***

```
r1n=r1o/Max[r1o];r2n=r2o/Max[r2o];
r1Norf=Mean[{Max[r1n],Min[r1n]}];r2Norf=Mean[{Max[r2n],Min[r2n]}];
r1Norm=Max[r1n];r2Norm=Max[r2n];
pr12n=ListLinePlot[{Transpose@{posx,r1n},Transpose@{posx,r2n}},ptSCStyle]//Rasteri
ze;pqr12n=Show[ListLinePlot[Transpose@{r1n,r2n},ptLissaStyle,PlotRange->{{-
1.1,1.1},{-1.1,1.1}},Graphics[Circle[{r1Norf,r2Norf},r1Norm]]];
```

### ***Set plot style***

```
ptPLStyle={ImageSize->Medium,PlotTheme->{"Scientific"},PlotStyle->Red,FrameLabel-
>{"Time (s)", "Phase
(Rad)"},GridLines->Automatic,LabelStyle->Directive[{FontFamily->"Arial",FontSize->14},
Black]};
```

### ***Calculate the phase using the arctangent function***

```
phase=ArcTan[r2n,r1n];  
plotPhase=ListLinePlot[{{Transpose@{posx,phase}}},ptPLStyle,PlotLegends->{"Phase"}]
```

### ***Get one period of the data***

```
di=Table[phase[[i]]-phase[[i-1]],{i,2,Length[phase]}; dii=Append[di,0];  
ListLinePlot[{{Transpose@{posx,dii}}},ImageSize->Medium,PlotTheme->"Detailed",Plot  
Range->All] peak=FindPeaks[Abs[dii],0,0,3]
```

### ***Unwrap the periodical data***

```
unwrapPeak={peak[[2]],peak[[4]]}; onepeak=peak[[3;4]];  
plotonePhase =  
ListLinePlot[Transpose@{posx[[onepeak[[1,1]]+1;;onepeak[[2,1]]]],phase[[onepeak[[1,  
1]]+1;;onepeak[[2,1]]]]},PlotStyle->Blue,ptPLStyle,PlotLegends->{"One period phase"}]  
plotNewphase=ListLinePlot[{{Transpose@{posx,newPhase}}},PlotLegends->{"unwrapped  
phase"},PlotStyle->Blue,ptPLStyle]  
plotunwrapPhase=ListLinePlot[Transpose@{posx[[unwrapPeak[[1,1]]+1;;unwrapPeak[[  
2,1]]]],newPhase[[unwrapPeak[[1,1]]+1;;unwrapPeak[[2,1]]]]},ptPLStyle,PlotLegends->{  
"Part unwrapped phase"}]  
Show[plotNewphase,plotunwrapPhase]//Rasterize
```

### ***Linear fitting on the unwrapped phase***

```
unwraplf=LinearModelFit[Transpose@{posx[[unwrapPeak[[1,1]]+1;;unwrapPeak[[2,1]]  
]],newPhase[[unwrapPeak[[1,1]]+1;;unwrapPeak[[2,1]]]]},x,x]  
umwrapfitPhase=ListLinePlot[Transpose@{posx[[unwrapPeak[[1,1]]+1;;unwrapPeak[[2,  
1]]]],unwraplf/@posx[[unwrapPeak[[1,1]]+1;;unwrapPeak[[2,1]]]]},PlotStyle->Green,Pl  
otTheme->"Scientific",ptPLStyle,PlotLegends->{"Linear fitting"}];
```

### ***Get the residual and convert to um***

```
unwrappradresidual=unwraplf["FitResiduals"]>(*rad*)  
unwrapumresidual=unwraplf["FitResiduals"]*4400/2/Pi>(*convert rad to um*)
```

### ***Plot the residual in Rad***

```
umwrapplotLfResidual=ListLinePlot[Transpose@{posx[[unwrapPeak[[1,1]]+1;;unwrapP  
eak[[2,1]]]],unwrappradresidual},ImageSize->Medium,PlotRange->All,PlotTheme->"Deta  
iled",PlotLegends->{"Linear fitting residuals"},FrameLabel->{"Time (s)", "Phase error  
(Rad)"},LabelStyle->Directive[{FontFamily->"Arial",FontSize->14,Black}];
```

### ***Plot the residual in um***

```
umwrapplotumResidual=ListLinePlot[Transpose@{posx[[unwrapPeak[[1,1]]+1;;unwrap  
Peak[[2,1]]]],unwrapumresidual},ImageSize->Medium,PlotRange->All,PlotLegends->{"Li  
near fitting residuals"},PlotTheme->"Detailed",FrameLabel->{"Time (s)", "Phase error  
(um)"},LabelStyle->Directive[{FontFamily->"Arial",FontSize->14,Black}];
```

### ***Compare the encoder difference and the linear fitting residual***

```
phaseShow=Show[plotNewphase,plotPhase,PlotRange->All]//Rasterize
```

```
Show[plotNewphase,plotPhase,PlotRange->All]
```

### ***Get one period of the data and operate linear fitting***

```
pposx=posx[[onepeak[[1,1]]+1;;onepeak[[2,1]]]];
pphase=phase[[onepeak[[1,1]]+1;;onepeak[[2,1]]]];
onePhase=ListLinePlot[Transpose@{pposx,pphase},PlotStyle->Blue,ptPLStyle,PlotLegends->{"One period phase"}];
If=LinearModelFit[Transpose@{pposx,pphase},x,x]
pa=If["ParameterValue"] If["ParameterTable"] If["AdjustedRSquared"]
fitPhase=ListLinePlot[Transpose@{pposx,If/@pposx},PlotStyle->Red,PlotLegends->{"One period phase linear fit"},ptPLStyle];
```

### ***Get the residual***

```
radresidual=If["FitResiduals"];(*rad*)
umresidual=If["FitResiduals"]*4400/2/Pi;(*convert rad to um*)
plotLfResidual=ListLinePlot[Transpose@{pposx,radresidual},ImageSize->Medium,PlotRange->All,PlotTheme->"Detailed",PlotLegends->{"Linear fitting residuals"},FrameLabel->{"Time (s)", "Phase error (rad)"},LabelStyle->Directive[{FontFamily->"Arial",FontSize->14},Black]];
plotumResidual=ListLinePlot[Transpose@{pposx,umresidual},ImageSize->Medium,PlotRange->All,PlotTheme->"Detailed",PlotLegends->{"Linear fitting residuals"},FrameLabel->{"Time (s)", "Phase error (um)"},LabelStyle->Directive[{FontFamily->"Arial",FontSize->14},Black]];
plotFitPhase=Show[onePhase,fitPhase,ImageSize->Medium];
Row[{plotFitPhase,plotLfResidual,plotumResidual}];
```

### ***Implement look up table on the above residual,Get the look up table data from the residual***

```
lenLT=20; ItBit=Floor[Length@radresidual/lenLT];
ind=Range[1,lenLT*ItBit,ItBit]; lookuptable=radresidual[[ind]];
AppendTo[lookuptable,radresidual[[-1]]]; pplut=pphase[[ind]];
AppendTo[pplut,pphase[[-1]]]; ItPosx=pposx[[ind]]; AppendTo[ItPosx,pposx[[-1]]];
plotLT=ListPlot[Transpose@{ItPosx,lookuptable},ImageSize->Medium,PlotTheme->"Detailed",PlotStyle->Red,PlotRange->All,PlotLegends->{"Look up table"}]
Show[plotLfResidual,plotLT] pa=(Normal[If]-If[0])/ .x->1
```

### ***Define look up table function***

```
lookupe[s_]:=
Module[{p1,p2,x1,x2,y1,y2,k},
(*If[Floor[s]≥0,x1=1,x1=Floor[s]]*)
If[pa<0,
If[s<Nearest[pplut,s][[1]],p1=Position[pplut,(Nearest[pplut,s][[1]]],p1=(Position[pplut,(Nearest[pplut,s][[1]]]-1),If[s>Nearest[pplut,s][[1]],
p1=Position[pplut,(Nearest[pplut,s][[1]]],p1=(Position[pplut,(Nearest[pplut,s][[1]]]-1));(*> should be changed according to the sign of the slope*)
If[p1=={{lenLT+1}},p1={{lenLT}},p1=p1];
(*p2=Mod[(p1+1),lenLT+1];*)
p2=p1+1;
```



```
y1=lookuptable[[p1//Flatten]];y2=lookuptable[[p2//Flatten]];
x1=pplut[[p1//Flatten]];x2=pplut[[p2//Flatten]];
k=(y2-y1)/(x2-x1); Return[y1+k*(s-x1)]
```

### ***Apply the look up table function on the residual, plot and compare the results***

```
np=Table[(pphase[[i]]-lookupe[pphase[[i]]][[1]],{i,1,Length[pphase]}];
nlf=LinearModelFit[Transpose@{pposx,np},x,x]
nlfresidual=nlf["FitResiduals"]>(*rad*)
numresidual=nlf["FitResiduals"]*4400/2/Pi>(*um*)
plotLtResidual=ListLinePlot[Transpose@{pposx,nlfresidual},ImageSize->Medium,PlotStyle->{Red},PlotTheme->"Detailed",FrameLabel->{"Time (s)", "Phase error (rad)"},LabelStyle->Directive[{FontFamily->"Arial",FontSize->14},Black],PlotLegends->{"Lookup table correctd residual"}];
plotnumResidual=ListLinePlot[Transpose@{pposx,numresidual},ImageSize->Medium,PlotStyle->{Red},PlotTheme->"Detailed",FrameLabel->{"Time (s)", "Phase error (um)"},LabelStyle->Directive[{FontFamily->"Arial",FontSize->14},Black],PlotLegends->{"Lookup table correctd residual"}];
```

### ***Sinusoidal fitting to analysis the original data acquired using oscilloscope***

```
r1sin=Transpose@{pposx,r1n[[onepeak[[1,1]]+1;;onepeak[[2,1]]]]};
r2cos=Transpose@{pposx,r2n[[onepeak[[1,1]]+1;;onepeak[[2,1]]]]};
```

### ***Apply the fitting***

```
model=a Sin[b*x+c];
fitCos=NonlinearModelFit[r2cos,model,{a,c,b},x]
fitCos["ParameterTable"]
fitCos["RSquared"]
residualCos=fitCos["FitResiduals"];
fitSin=NonlinearModelFit[r1sin,model,{a,c,b},x]
fitSin["ParameterTable"]
fitSin["RSquared"]
residualSin=fitSin["FitResiduals"];
```

### ***Plot the residual***

```
(*Show[ListPlot[{r1sin,r2cos}],Plot[{fitSin[x],fitCos[x]},{x,-1,2},PlotStyle->{Red}]]*)
plotSin=Show[ListLinePlot[{r1sin,r2cos},ptSCStyle,PlotStyle->{{Blue,Thick},{Green,Thick}},ImageSize->Medium],ListLinePlot[{Transpose@{pposx,fitSin/@pposx},Transpose@{pposx,fitCos/@pposx}],PlotStyle->{{Orange,Thick},{Red,Thick}},PlotLegends->{"r1 fitting","r2 fitting"},ptSCStyle,ImageSize->Medium]]
plotSinResidual=ListLinePlot[{Transpose@{pposx,residualSin},Transpose@{pposx,residualCos}},FrameLabel->{"Time (s)", "Residual (V)"},GridLines->Automatic,PlotTheme->"Scientific",PlotLegends->{"r1 residual","r2 residual"},LabelStyle->Directive[{FontFamily->"Arial",ptSCStyle},Black],ImageSize->Large]
```

### ***Circular fitting on the Lissajous curve***

```
r1cir=r1sin[[All,2]];
r2cir=r2cos[[All,2]];
```

```

plotQua=ListLinePlot[Transpose@{r1cir,r2cir},AspectRatio->1,PlotTheme->"Detailed",Axes->True];
cirData=Transpose@{r1cir,r2cir,(r1cir2+r2cir2)};
model=a*(x)2+b*(y)2;
fitCir=NonlinearModelFit[cirData,model,{a,b},{x,y}];
circle=Table[{Sin[t],Cos[t]},{t,-Pi,Pi,2 Pi/(peak[[2,1]]-peak[[1,1]])}];
plotCircle=ListLinePlot[circle,AspectRatio->1,PlotStyle->Red];
fitCir["RSquared"] residualCir=fitCir["FitResiduals"];
resiguanCir=ListLinePlot[{Transpose@{pposx,residualCir}},PlotTheme->"Detailed"];
Grid[{{"Lissajous Circle fit","Residual"},{Show[plotQua,plotCircle],resiguanCir}},Frame->All]

```

### ***Fast Fourier transform(FFT) analysis and phase offset remove***

```

r1cir=r1o[[onepeak[[1,1]]+1;;onepeak[[2,1]]]];
r2cir=r2o[[onepeak[[1,1]]+1;;onepeak[[2,1]]]];
psin=ArcCos[r1cir]/Pi*180;
pcos=ArcSin[r2cir]/Pi*180;
ListLinePlot[{Transpose@{pposx,psin-
pcos},Transpose@{pposx,psin+pcos},Transpose@{pposx,psin},Transpose@{pposx,pcos}
}],PlotTheme->"Detailed",PlotLegends->Automatic]
ffts1=Fourier[r1cir,FourierParameters->{-1,1}];
ffts2=Fourier[r2cir,FourierParameters->{-1,1}];
max=Max[Abs[ffts1]]; pos=First[First[Position[Abs[ffts1],max]]];
phaseDif=Arg[ffts1[[pos]]]-Arg[ffts2[[pos]]]; degDif=phaseDif/Pi*180;
degDif90=90-Mod[degDif//Abs,90]
Print[StringForm["\r Phase difference, rad=`,deg=`,deg=`\r",
phaseDif,degDif90,degDif]]

```

### ***Phase shift correction***

```

Length[r1cir]
degDif90/360*Length[r1cir]//Floor
degDif90=Mod[degDif//Abs,90]
degDif90/360*Length[r1cir]//Floor
r2cirPha=RotateRight[r2cir,degDif90/360*Length[r1cir]//Floor];

```

### ***Calculate phase error after phase shift correction***

```

ffts1=Fourier[r1cir,FourierParameters->{-1,1}];
ffts2=Fourier[r2cirPha,FourierParameters->{-1,1}];
max=Max[Abs[ffts1]];
pos=First[First[Position[Abs[ffts1],max]]];
phaseDif=Arg[ffts1[[pos]]]-Arg[ffts2[[pos]]];
degDif=phaseDif/Pi*180; degDif90=90-Mod[degDif//Abs,90]
Print[StringForm["\r Phase difference,
rad=`,deg90=`,deg=`\r",phaseDif,degDif90,degDif]]

```

### ***Plot Lissajous curve before and after phase correction***

```

plotQua2=ListLinePlot[Transpose@{r1cir,r2cirPha},AspectRatio->1,PlotTheme->"Detailed",
Axes->True,PlotStyle->{Green},PlotLegends->{"qua after phase correction"}];
Show[plotQua,plotQua2,plotCircle]
ptcorPha={ImageSize->Medium,PlotTheme->"Scientific"},FrameLabel->{"Time
(s)","Phase
(Rad)"},GridLines->Automatic,LabelStyle->Directive[{FontFamily->"Arial",FontSize->14},
Black]];

```

### ***Calculated the displacement using arctangent function***

```

corpphase=ArcTan[r2cirPha,r1cir];
plotCorPhase=ListLinePlot[Transpose@{pposx,corpphase},ptcorPha,PlotLegends->{"Phase
after phase correction"},PlotStyle->{Blue}];
corlf=LinearModelFit[Transpose@{pposx,corpphase},x,x]
corlf["ParameterTable"] Normal[corlf];

```

### ***Linear fitting***

```

corfitPhase=ListLinePlot[Transpose@{pposx,corlf/@pposx},PlotStyle->{Red,Dashed},pt
PLStyle,PlotLegends->{"Linear fit after phase correction"}];
corradresidual=corlf["FitResiduals"]>(*rad*)
corumresidual=corlf["FitResiduals"]*4400/2/Pi>(*convert rad to um*)
corplotLfResidual=ListLinePlot[Transpose@{pposx,corradresidual},ImageSize->Medium
,PlotRange->All,PlotTheme->"Detailed",ptcorPha,PlotLegends->{"Phase correctted
residual (rad)"}];
corplotumResidual=ListLinePlot[Transpose@{pposx,corumresidual},PlotStyle->{Black},I
mageSize->Medium,PlotRange->All,PlotTheme->"Detailed",ptcorPha,PlotLegends->{"Li
near fit residual after phase correction"}];
Show[plotLfResidual,corplotLfResidual];

```

## **Appendix B – Datasheets of ICs used in the project**

The datasheets of the ICs used in the project are included for reference.



# Balanced Modulator/Demodulator

Data Sheet

AD630

## FEATURES

Recovers signal from 100 dB noise  
2 MHz channel bandwidth  
45 V/ $\mu$ s slew rate  
Low crosstalk:  $-120$  dB at 1 kHz,  $-100$  dB at 10 kHz  
Pin programmable, closed-loop gains of  $\pm 1$  and  $\pm 2$   
0.05% closed-loop gain accuracy and match  
100  $\mu$ V channel offset voltage (AD630)  
350 kHz full power bandwidth  
Chips available

## APPLICATIONS

Balanced modulation and demodulation  
Synchronous detection  
Phase detection  
Quadrature detection  
Phase sensitive detection  
Lock in amplification  
Square wave multiplication

## GENERAL DESCRIPTION

The AD630 is a high precision balanced modulator/demodulator that combines a flexible commutating architecture with the accuracy and temperature stability afforded by laser wafer trimmed thin film resistors. A network of on-board applications resistors provides precision closed-loop gains of  $\pm 1$  and  $\pm 2$  with 0.05% accuracy (AD630B). These resistors may also be used to accurately configure multiplexer gains of 1, 2, 3, or 4. External feedback enables high gain or complex switched feedback topologies.

The AD630 can be thought of as a precision op amp with two independent differential input stages and a precision comparator that is used to select the active front end. The rapid response time of this comparator coupled with the high slew rate and fast settling of the linear amplifiers minimize switching distortion.

The AD630 is used in precision signal processing and instrumentation applications that require wide dynamic range. When used as a synchronous demodulator in a lock-in amplifier configuration, the AD630 can recover a small signal from 100 dB of interfering noise (see the Lock-In Amplifier Applications section). Although optimized for operation up to 1 kHz, the circuit is useful at frequencies up to several hundred kilohertz.

## FUNCTIONAL BLOCK DIAGRAM

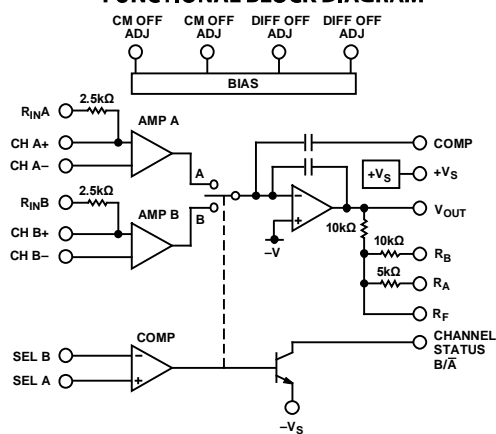


Figure 1.

Other features of the AD630 include pin programmable frequency compensation; optional input bias current compensation resistors, common-mode and differential-offset voltage adjustment, and a channel status output that indicates which of the two differential inputs is active.

## PRODUCT HIGHLIGHTS

1. The application flexibility of the AD630 makes it the best choice for applications that require precisely fixed gain, switched gain, multiplexing, integrating-switching functions, and high speed precision amplification.
2. The 100 dB dynamic range of the AD630 exceeds that of any hybrid or IC balanced modulator/demodulator and is comparable to that of costly signal processing instruments.
3. The op amp format of the AD630 ensures easy implementation of high gain or complex switched feedback functions. The application resistors facilitate the implementation of most common applications with no additional parts.
4. The AD630 can be used as a 2-channel multiplexer with gains of 1, 2, 3, or 4. The channel separation of 100 dB at 10 kHz approaches the limit achievable with an empty IC package.
5. Laser trimming of the comparator and amplifying channel offsets eliminate the need for external nulling in most cases.

Rev. G

Document Feedback

Information furnished by Analog Devices is believed to be accurate and reliable. However, no responsibility is assumed by Analog Devices for its use, nor for any infringements of patents or other rights of third parties that may result from its use. Specifications subject to change without notice. No license is granted by implication or otherwise under any patent or patent rights of Analog Devices. Trademarks and registered trademarks are the property of their respective owners.

One Technology Way, P.O. Box 9106, Norwood, MA 02062-9106, U.S.A.  
Tel: 781.329.4700 ©2015–2016 Analog Devices, Inc. All rights reserved.  
Technical Support [www.analog.com](http://www.analog.com)

## TABLE OF CONTENTS

Features .....	1	Circuit Description .....	13
Applications.....	1	Other Gain Configurations.....	14
Functional Block Diagram .....	1	Switched Input Impedance .....	14
General Description .....	1	Frequency Compensation .....	14
Product Highlights .....	1	Offset Voltage Nulling .....	15
Revision History .....	2	Channel Status Output .....	15
Specifications.....	3	Applications Information .....	16
Absolute Maximum Ratings.....	4	Balanced Modulator.....	16
Thermal Resistance .....	4	Balanced Demodulator.....	16
Chip Availability .....	4	Precision Phase Comparator .....	16
ESD Caution.....	4	Precision Rectifier Absolute Value.....	16
Pin Configurations and Function Descriptions .....	5	LVDT Signal Conditioner .....	17
Typical Performance Characteristics .....	9	AC Bridge .....	17
Test Circuits.....	11	Lock-In Amplifier Applications .....	18
Theory of Operation .....	12	Outline Dimensions .....	19
Two Ways To Look At The AD630 .....	12	Ordering Guide .....	20
How the AD630 Works.....	12		

## REVISION HISTORY

### 12/2016—Rev. F to Rev. G

Changes to Figure 1 .....	1
Changes to Figure 31.....	17
Changes to Figure 35.....	18

### 7/2015—Rev. E to Rev. F

Updated Format.....	Universal
Changes to Features Section, General Description Section, Product Highlights Section, and Figure 1 .....	1
Added Applications Section .....	1
Changes to Table 3.....	4
Added Table 4; Renumbered Sequentially .....	5
Added Figure 4; Renumbered Sequentially and Table 5 .....	6
Added Figure 5 and Table 6.....	7
Added Table 7.....	8
Changes to Figure 7, Figure 8, and Figure 9 .....	9
Changes to Figure 13, Figure 14, and Figure 15 .....	10
Added Test Circuits Section and Figure 16 to Figure 19.....	11
Added Theory of Operation Section .....	12
Change to Figure 24 .....	13
Updated Outline Dimensions .....	19
Changes to Ordering Guide .....	20

### 6/2004—Rev. D to Rev. E

Changes to Ordering Guide .....	3
Replaced Figure 12 .....	9
Changes to AC Bridge Section.....	9
Replaced Figure 13 .....	10
Changes to Lock-In Amplifier Applications.....	10
Updated Outline Dimensions .....	11

### 6/2001—Rev. C to Rev. D

Changes to Specification Table .....	2
Changes to Thermal Characteristics.....	3
Changes to Ordering Guide .....	3
Changes to Pin Configurations .....	3
Changes to Outline Dimensions .....	11

## SPECIFICATIONS

At 25°C and  $\pm V_S = \pm 15$  V, unless otherwise noted.

Table 1.

Parameter	AD630J/AD630A			AD630K/AD630B			AD630S			Unit
	Min	Typ	Max	Min	Typ	Max	Min	Typ	Max	
GAIN										
Open-Loop Gain	90	110		100	120		90	110		dB
±1, ±2 Closed-Loop Gain Error		0.1				0.05		0.1		%
Closed-Loop Gain Match		0.1				0.05		0.1		%
Closed-Loop Gain Drift		2			2			2		ppm/°C
CHANNEL INPUTS										
V <sub>IN</sub> Operational Limit <sup>1</sup>	(−V <sub>S</sub> + 4) to (+V <sub>S</sub> − 1)			(−V <sub>S</sub> + 4) to (+V <sub>S</sub> − 1)			(−V <sub>S</sub> + 4) to (+V <sub>S</sub> − 1)			V
Input Offset Voltage		500			100			500		μV
T <sub>MIN</sub> to T <sub>MAX</sub>		800			160			1000		μV
Input Bias Current	100	300		100	300		100	300		nA
Input Offset Current	10	50		10	50		10	50		nA
Channel Separation at 10 kHz		100			100			100		dB
COMPARATOR										
V <sub>IN</sub> Operational Limit <sup>1</sup>	(−V <sub>S</sub> + 3) to (+V <sub>S</sub> − 1.5)			(−V <sub>S</sub> + 3) to (+V <sub>S</sub> − 1.5)			(−V <sub>S</sub> + 3) to (+V <sub>S</sub> − 1.3)			V
Switching Window		±1.5			±1.5			±1.5		mV
T <sub>MIN</sub> to T <sub>MAX</sub>		±2.0			±2.0			±2.5		mV
Input Bias Current	100	300		100	300		100	300		nA
Response Time (−5 mV to +5 mV Step)		200			200			200		ns
Channel Status										
I <sub>SINK</sub> at V <sub>OL</sub> = −V <sub>S</sub> + 0.4 V <sup>2</sup>	1.6			1.6			1.6			mA
Pull-Up Voltage		(−V <sub>S</sub> + 33)			(−V <sub>S</sub> + 33)			(−V <sub>S</sub> + 33)		V
DYNAMIC PERFORMANCE										
Unity Gain Bandwidth		2			2			2		MHz
Slew Rate <sup>3</sup>		45			45			45		V/μs
Settling Time to 0.1% (20 V Step)		3			3			3		μs
OPERATING CHARACTERISTICS										
Common-Mode Rejection	85	105		90	110		90	110		dB
Power Supply Rejection	90	110		90	110		90	110		dB
Supply Voltage Range	±5		±16.5	±5		±16.5	±5		±16.5	V
Supply Current		4	5		4	5		4	5	mA
OUTPUT VOLTAGE, AT R <sub>L</sub> = 2 kΩ										
T <sub>MIN</sub> to T <sub>MAX</sub>	±10			±10			±10			V
Output Short-Circuit Current		25			25			25		mA
TEMPERATURE RANGES										
N Package	0		70	0		70				°C
D Package	−25		+85	−25		+85	−55		+125	°C

<sup>1</sup> If one terminal of each differential channel or comparator input is kept within these limits the other terminal may be taken to the positive supply.

<sup>2</sup>  $I_{SINK}$  at  $V_{OL} = (-V_S + 1$  V) is typically 4 mA.

<sup>3</sup> Pin 12 open. Slew rate with Pin 12 and Pin 13 shorted is typically 35 V/μs.

## ABSOLUTE MAXIMUM RATINGS

Table 2.

Parameter	Rating
Supply Voltage	$\pm 18$ V
Internal Power Dissipation	600 mW
Output Short-Circuit to Ground	Indefinite
Storage Temperature	
Ceramic Package	$-65^{\circ}\text{C}$ to $+150^{\circ}\text{C}$
Plastic Package	$-55^{\circ}\text{C}$ to $+125^{\circ}\text{C}$
Lead Temperature Range (Soldering, 10 sec)	$300^{\circ}\text{C}$
Maximum Junction Temperature	$150^{\circ}\text{C}$

Stresses at or above those listed under Absolute Maximum Ratings may cause permanent damage to the product. This is a stress rating only; functional operation of the product at these or any other conditions above those indicated in the operational section of this specification is not implied. Operation beyond the maximum operating conditions for extended periods may affect product reliability.

## THERMAL RESISTANCE

Table 3. Thermal Resistance

Package Type	$\theta_{JC}$	$\theta_{JA}$	Unit
20-Lead PDIP (N-20)	24	61	$^{\circ}\text{C}/\text{W}$
20-Lead SBDIP (D-20)	35	120	$^{\circ}\text{C}/\text{W}$
20-Lead LCC (E-20-4)	35	120	$^{\circ}\text{C}/\text{W}$
20-Lead SOIC_W (RW-20)	38	75	$^{\circ}\text{C}/\text{W}$

## CHIP AVAILABILITY

The AD630 is available in laser trimmed, passivated chip form. Figure 2 shows the AD630 metallization pattern, bonding pads, and dimensions. AD630 chips are available; consult factory for details.

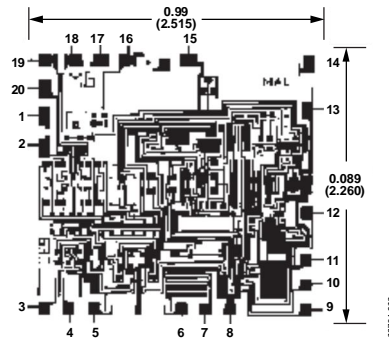


Figure 2. Chip Metallization and Pinout  
Dimensions shown in inches and (millimeters)  
Contact factory for latest dimensions

## ESD CAUTION



**ESD (electrostatic discharge) sensitive device.** Charged devices and circuit boards can discharge without detection. Although this product features patented or proprietary protection circuitry, damage may occur on devices subjected to high energy ESD. Therefore, proper ESD precautions should be taken to avoid performance degradation or loss of functionality.



## PIN CONFIGURATIONS AND FUNCTION DESCRIPTIONS

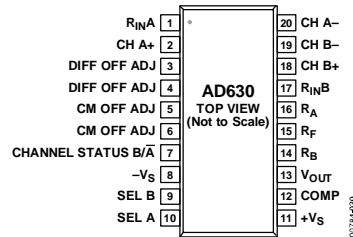


Figure 3. 20-Lead SOIC Pin Configuration

Table 4. 20-Lead SOIC Pin Function Descriptions

Pin No.	Mnemonic	Description
1	R <sub>IN</sub> A	2.5 k $\Omega$ Resistor to Noninverting Input of Op Amp A
2	CH A+	Noninverting Input of Op Amp A
3	DIFF OFF ADJ	Differential Offset Adjustment
4	DIFF OFF ADJ	Differential Offset Adjustment
5	CM OFF ADJ	Common-Mode Offset Adjustment
6	CM OFF ADJ	Common-Mode Offset Adjustment
7	CHANNEL STATUS B/ $\bar{A}$	B or A Channel Status
8	-V <sub>S</sub>	Negative Supply
9	SEL B	B Channel Comparator Input
10	SEL A	A Channel Comparator Input
11	+V <sub>S</sub>	Positive Supply
12	COMP	Pin to Connect Internal Compensation Capacitor
13	V <sub>OUT</sub>	Output Voltage
14	R <sub>B</sub>	10 k $\Omega$ Gain Setting Resistor
15	R <sub>F</sub>	10 k $\Omega$ Feedback Resistor
16	R <sub>A</sub>	5 k $\Omega$ Feedback Resistor
17	R <sub>IN</sub> B	2.5 k $\Omega$ Resistor to Noninverting Input of Op Amp B
18	CH B+	Noninverting Input of Op Amp B
19	CH B-	Inverting Input of Op Amp B
20	CH A-	Inverting Input of Op Amp A

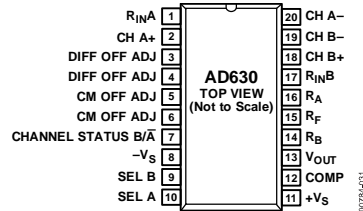


Figure 4. 20-Lead PDIP Pin Configuration

Table 5. 20-Lead PDIP Pin Function Descriptions

Pin No.	Mnemonic	Description
1	R <sub>INA</sub>	2.5 k $\Omega$ Resistor to Noninverting Input of Op Amp A
2	CH A+	Noninverting Input of Op Amp A
3	DIFF OFF ADJ	Differential Offset Adjustment
4	DIFF OFF ADJ	Differential Offset Adjustment
5	CM OFF ADJ	Common-Mode Offset Adjustment
6	CM OFF ADJ	Common-Mode Offset Adjustment
7	CHANNEL STATUS B/ $\overline{A}$	B or A Channel Status
8	-V <sub>S</sub>	Negative Supply
9	SEL B	B Channel Comparator Input
10	SEL A	A Channel Comparator Input
11	+V <sub>S</sub>	Positive Supply
12	COMP	Pin to Connect Internal Compensation Capacitor
13	V <sub>OUT</sub>	Output Voltage
14	R <sub>B</sub>	10 k $\Omega$ Gain Setting Resistor
15	R <sub>F</sub>	10 k $\Omega$ Feedback Resistor
16	R <sub>A</sub>	5 k $\Omega$ Feedback Resistor
17	R <sub>INB</sub>	2.5 k $\Omega$ Resistor to Noninverting Input of Op Amp B
18	CH B+	Noninverting Input of Op Amp B
19	CH B-	Inverting Input of Op Amp B
20	CH A-	Inverting Input of Op Amp A

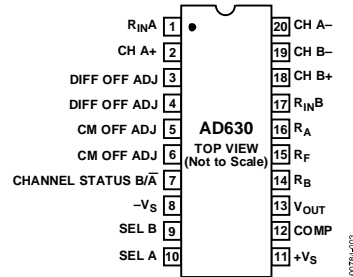


Figure 5. 20-Lead CERDIP Pin Configuration

Table 6. 20-Lead CERDIP Pin Function Descriptions

Pin No.	Mnemonic	Description
1	R <sub>IN</sub> A	2.5 k $\Omega$ Resistor to Noninverting Input of Op Amp A
2	CH A+	Noninverting Input of Op Amp A
3	DIFF OFF ADJ	Differential Offset Adjustment
4	DIFF OFF ADJ	Differential Offset Adjustment
5	CM OFF ADJ	Common-Mode Offset Adjustment
6	CM OFF ADJ	Common-Mode Offset Adjustment
7	CHANNEL STATUS B/ $\overline{A}$	B or A Channel Status
8	-V <sub>S</sub>	Negative Supply
9	SEL B	B Channel Comparator Input
10	SEL A	A Channel Comparator Input
11	+V <sub>S</sub>	Positive Supply
12	COMP	Pin to Connect Internal Compensation Capacitor
13	V <sub>OUT</sub>	Output Voltage
14	R <sub>B</sub>	10 k $\Omega$ Gain Setting Resistor
15	R <sub>F</sub>	10 k $\Omega$ Feedback Resistor
16	R <sub>A</sub>	5 k $\Omega$ Feedback Resistor
17	R <sub>IN</sub> B	2.5 k $\Omega$ Resistor to Noninverting Input of Op Amp B
18	CH B+	Noninverting Input of Op Amp B
19	CH B-	Inverting Input of Op Amp B
20	CH A-	Inverting Input of Op Amp A

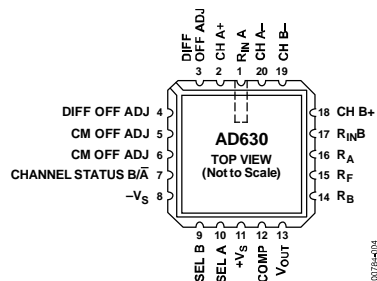


Figure 6. 20-Terminal CLCC Pin Configuration

Table 7. 20-Terminal CLCC Pin Function Descriptions

Pin No.	Mnemonic	Description
1	R <sub>IN</sub> A	2.5 k $\Omega$ Resistor to Noninverting Input of Op Amp A
2	CH A+	Noninverting Input of Op Amp A
3	DIFF OFF ADJ	Differential Offset Adjustment
4	DIFF OFF ADJ	Differential Offset Adjustment
5	CM OFF ADJ	Common-Mode Offset Adjustment
6	CM OFF ADJ	Common-Mode Offset Adjustment
7	CHANNEL STATUS B/ $\overline{A}$	B or A Channel Status
8	-V <sub>S</sub>	Negative Supply
9	SEL B	B Channel Comparator Input
10	SEL A	A Channel Comparator Input
11	+V <sub>S</sub>	Positive Supply
12	COMP	Pin to Connect Internal Compensation Capacitor
13	V <sub>OUT</sub>	Output Voltage
14	R <sub>B</sub>	10 k $\Omega$ Gain Setting Resistor
15	R <sub>F</sub>	10 k $\Omega$ Feedback Resistor
16	R <sub>A</sub>	5 k $\Omega$ Feedback Resistor
17	R <sub>IN</sub> B	2.5 k $\Omega$ Resistor to Noninverting Input of Op Amp B
18	CH B+	Noninverting Input of Op Amp B
19	CH B-	Inverting Input of Op Amp B
20	CH A-	Inverting Input of Op Amp A

## TYPICAL PERFORMANCE CHARACTERISTICS

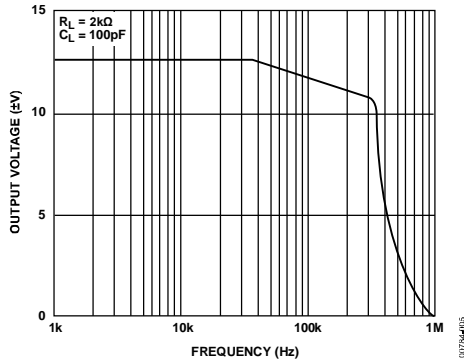


Figure 7. Output Voltage vs. Frequency (See Figure 16)

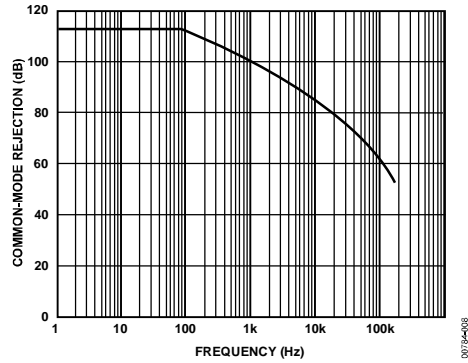


Figure 10. Common-Mode Rejection vs. Frequency

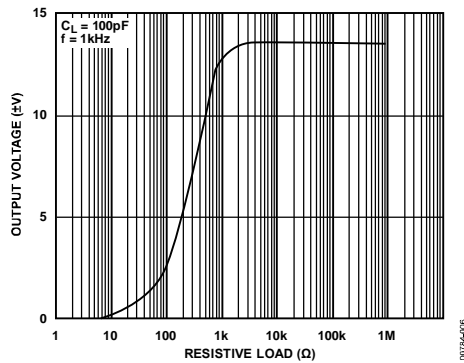


Figure 8. Output Voltage vs. Resistive Load (See Figure 16)

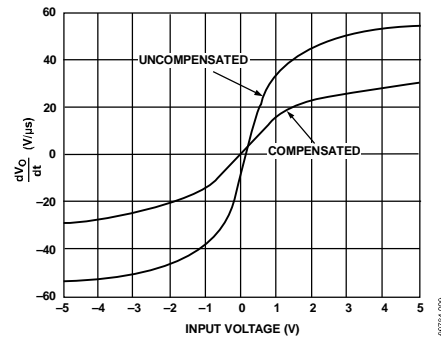
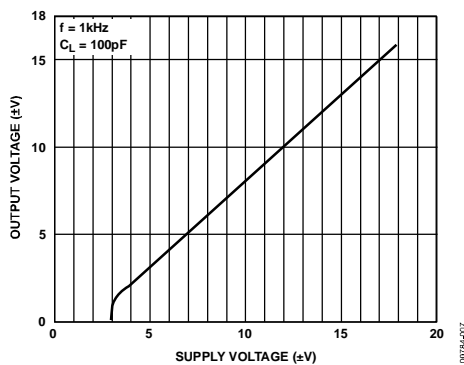
Figure 11.  $\frac{dV_O}{dt}$  vs. Input Voltage

Figure 9. Output Voltage Swing vs. Supply Voltage (See Figure 16)

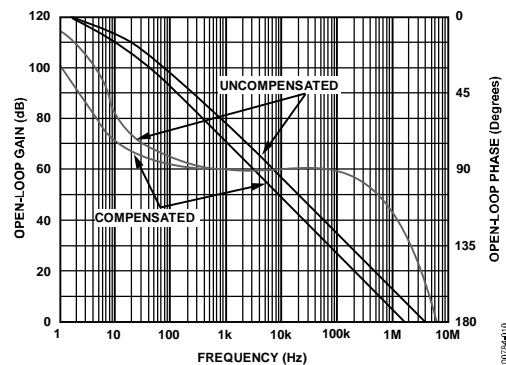


Figure 12. Gain and Phase vs. Frequency

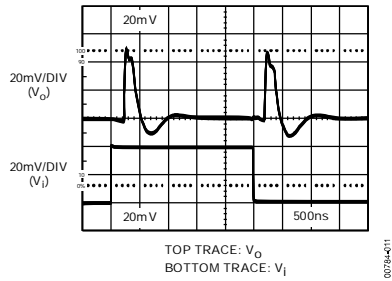


Figure 13. Channel-to-Channel Switch-Settling Characteristic (See Figure 17)

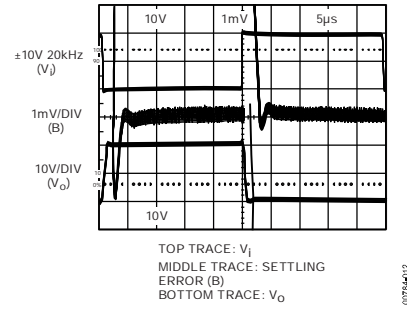


Figure 15. Large Signal Inverting Step Response (See Figure 19)

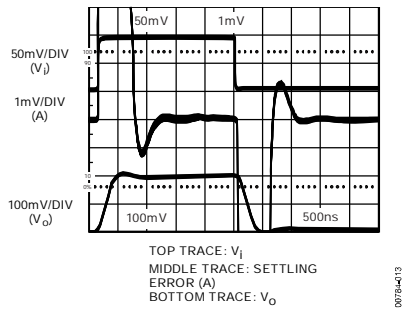


Figure 14. Small Signal Noninverting Step Response (See Figure 18)

## TEST CIRCUITS

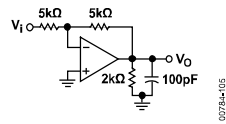


Figure 16. Test Circuit for Output Voltage vs. Frequency, Resistive Load, and Supply Voltage (See Figure 7, Figure 8, and Figure 9)

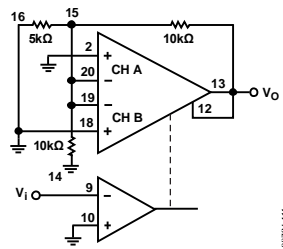


Figure 17. Test Circuit for Channel-to-Channel Switch-Settling Characteristic (See Figure 13)

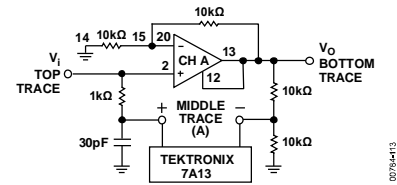


Figure 18. Test Circuit for Small Signal Noninverting Step Response (See Figure 14)

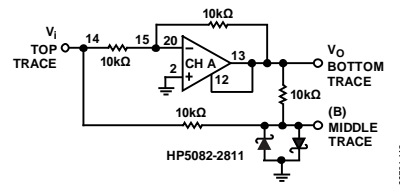


Figure 19. Test Circuit for Large Signal Noninverting Step Response (See Figure 15)

## THEORY OF OPERATION

### TWO WAYS TO LOOK AT THE AD630

The functional block diagram of the AD630 (see Figure 1) shows the pin connections of the internal functions. An alternative architectural diagram is shown in Figure 20. In this diagram, the individual A and B channel preamps, the switch, and the integrator output amplifier are combined in a single op amp. This amplifier has two differential input channels, only one of which is active at a time.

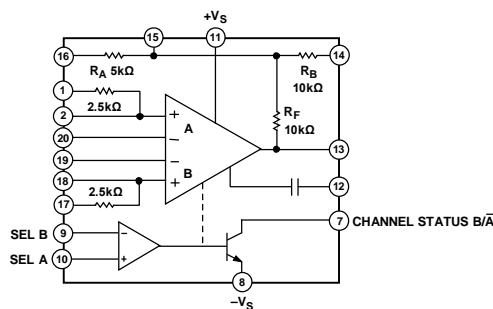


Figure 20. Architectural Block Diagram

### HOW THE AD630 WORKS

The basic mode of operation of the AD630 may be easier to recognize as two fixed gain stages, which can be inserted into the signal path under the control of a sensitive voltage comparator. When the circuit is switched between inverting and noninverting gain, it provides the basic modulation/demodulation function. The AD630 is unique in that it includes laser wafer trimmed thin-film feedback resistors on the monolithic chip. The configuration shown in Figure 21 yields a gain of  $\pm 2$  and can be easily changed to  $\pm 1$  by shifting  $R_B$  from its ground connection to the output.

The comparator selects one of the two input stages to complete an operational feedback connection around the AD630. The deselected input is off and has a negligible effect on operation.

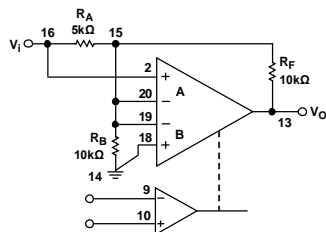


Figure 21. AD630 Symmetric Gain ( $\pm 2$ )

When Channel B is selected, the  $R_A$  and  $R_F$  resistors are connected for inverting feedback as shown in the inverting gain configuration diagram in Figure 22. The amplifier has sufficient loop gain to minimize the loading effect of  $R_B$  at the virtual ground produced by the feedback connection. When the sign of the comparator input is reversed, Input B is deselected and Input A is selected. The new equivalent circuit is the noninverting gain configuration shown in Figure 23. In this case,  $R_A$  appears across the op amp input terminals, but because the amplifier drives this difference voltage to zero, the closed-loop gain is unaffected.

The two closed-loop gain magnitudes are equal when  $R_F/R_A = 1 + R_F/R_B$ , which results from making  $R_A$  equal to  $R_F R_B / (R_F + R_B)$  the parallel equivalent resistance of  $R_F$  and  $R_B$ .

The 5 kΩ and the two 10 kΩ resistors on the AD630 chip can be used to make a gain of 2 as shown in Figure 22 and Figure 23. By paralleling the 10 kΩ resistors to make  $R_F$  equal to 5 kΩ and omitting  $R_B$ , the circuit can be programmed for a gain of  $\pm 1$  (as shown in Figure 28). These and other configurations using the on-chip resistors present the inverting inputs with a 2.5 kΩ source impedance. The more complete AD630 diagrams show 2.5 kΩ resistors available at the noninverting inputs which can be conveniently used to minimize errors resulting from input bias currents.

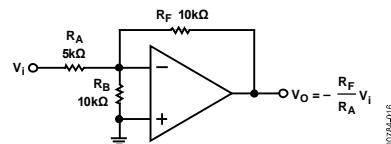


Figure 22. Inverting Gain Configuration

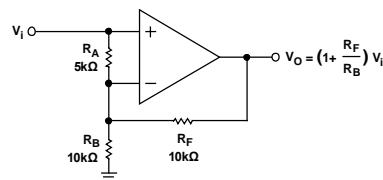


Figure 23. Noninverting Gain Configuration





## INA217 Low-Noise, Low-Distortion Instrumentation Amplifier Replacement for SSM2017

### 1 Features

- Low Noise: 1.3 nV/M  $\sqrt{\text{Hz}}$  at 1 kHz
- Low THD+N: 0.004% at 1 kHz, G = 100
- Wide Bandwidth: 800 kHz at G = 100
- Wide Supply Range:  $\pm 4.5$  V to  $\pm 18$  V
- High CMR: > 100 dB
- Gain Set With External Resistor
- DIP-8 and SOL-16 Widebody Packages

### 2 Applications

- Professional Microphone Preamps
- Moving-coil Transducer Amplifiers
- Differential Receivers
- Bridge Transducer Amplifiers

### 3 Description

The INA217 device is a low-noise, low-distortion, monolithic instrumentation amplifier. Current-feedback circuitry allows the INA217 device to achieve wide bandwidth and excellent dynamic response over a wide range of gain. The INA217 device is ideal for low-level audio signals such as balanced low-impedance microphones. Many industrial, instrumentation, and medical applications also benefit from its low noise and wide bandwidth.

Unique distortion cancellation circuitry reduces distortion to extremely low levels, even in high gain. The INA217 device provides near-theoretical noise performance for 200- $\Omega$  source impedance. The INA217 device features differential input, low noise, and low distortion that provides superior performance in professional microphone amplifier applications.

The INA217 device features wide supply voltage, excellent output voltage swing, and high output current drive, making it an optimal candidate for use in high-level audio stages.

The INA217 device is available in the same DIP-8 and SOL-16 wide body packages and pinouts as the SSM2017. For a smaller package, see the INA163 device in SO-14 narrow. The INA217 device is specified over the temperature range of  $-40^{\circ}\text{C}$  to  $85^{\circ}\text{C}$ .

#### Device Information<sup>(1)</sup>

PART NUMBER	PACKAGE	BODY SIZE (NOM)
INA217	SOIC (16)	10.30 mm x 7.50 mm
	PDIP (8)	9.81 mm x 6.35 mm

(1) For all available packages, see the orderable addendum at the end of the data sheet.



An IMPORTANT NOTICE at the end of this data sheet addresses availability, warranty, changes, use in safety-critical applications, intellectual property matters and other important disclaimers. PRODUCTION DATA.

## INA217

SBOS247C – JUNE 2002 – REVISED NOVEMBER 2015

[www.ti.com](http://www.ti.com)

### Simplified Schematic

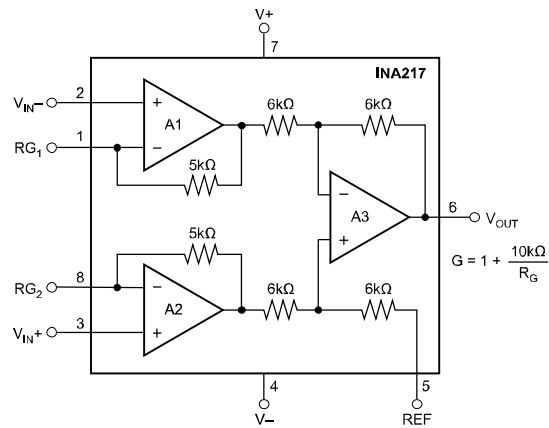


## Table of Contents

<b>1 Features</b> .....	<b>1</b>	7.4 Device Functional Modes .....	<b>12</b>
<b>2 Applications</b> .....	<b>1</b>	<b>8 Application and Implementation</b> .....	<b>13</b>
<b>3 Description</b> .....	<b>1</b>	8.1 Application Information .....	<b>13</b>
<b>4 Revision History</b> .....	<b>3</b>	8.2 Typical Application .....	<b>13</b>
<b>5 Pin Configuration and Functions</b> .....	<b>4</b>	<b>9 Power Supply Recommendations</b> .....	<b>14</b>
<b>6 Specifications</b> .....	<b>5</b>	<b>10 Layout</b> .....	<b>15</b>
6.1 Absolute Maximum Ratings .....	<b>5</b>	10.1 Layout Guidelines .....	<b>15</b>
6.2 ESD Ratings .....	<b>5</b>	10.2 Layout Example .....	<b>15</b>
6.3 Recommended Operating Conditions .....	<b>5</b>	<b>11 Device and Documentation Support</b> .....	<b>16</b>
6.4 Thermal Information .....	<b>5</b>	11.1 Device Support .....	<b>16</b>
6.5 Electrical Characteristics: $V_S = \pm 15\text{ V}$ .....	<b>6</b>	11.2 Documentation Support .....	<b>16</b>
6.6 Typical Characteristics .....	<b>8</b>	11.3 Community Resources .....	<b>16</b>
<b>7 Detailed Description</b> .....	<b>10</b>	11.4 Trademarks .....	<b>17</b>
7.1 Overview .....	<b>10</b>	11.5 Electrostatic Discharge Caution .....	<b>17</b>
7.2 Functional Block Diagram .....	<b>10</b>	11.6 Glossary .....	<b>17</b>
7.3 Feature Description .....	<b>10</b>	<b>12 Mechanical, Packaging, and Orderable Information</b> .....	<b>17</b>

## 4 Revision History

NOTE: Page numbers for previous revisions may differ from page numbers in the current version.

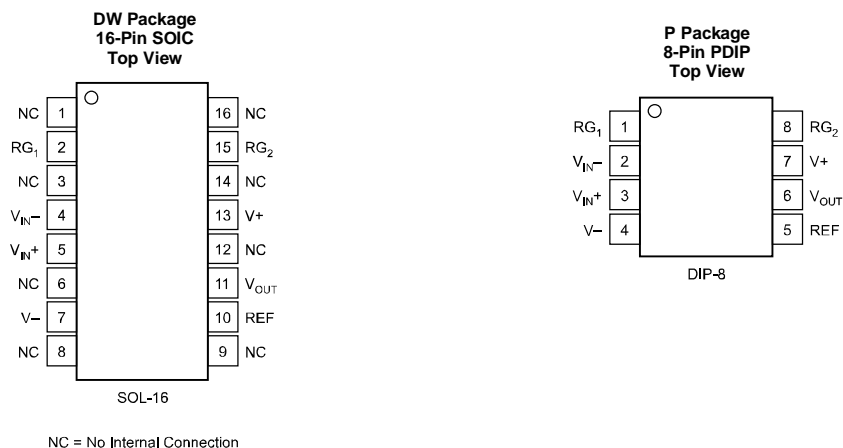
Changes from Revision B (February 2005) to Revision C	Page
<ul style="list-style-type: none"> <li>Added ESD Ratings table, Feature Description section, Device Functional Modes, Application and Implementation section, Power Supply Recommendations section, Layout section, Device and Documentation Support section, and Mechanical, Packaging, and Orderable Information section .....</li> </ul>	<b>1</b>

**INA217**

SBOS247C – JUNE 2002 – REVISED NOVEMBER 2015

[www.ti.com](http://www.ti.com)

## 5 Pin Configuration and Functions



### Pin Functions

Pin Functions

PIN		I/O	DESCRIPTION
NAME	NO.		
PDIP			
NC	1	—	No internal connection
RG1	2	I	Gain setting pin, for gains greater than one, connect an external resistor between pins 2 and 15
NC	3	—	No internal connection
VIN–	4	I	Inverting input
VIN+	5	I	Non-inverting input
NC	6	—	No internal connection
V–	7	I	negative power supply
NC	8	—	No internal connection
NC	9	—	No internal connection
REF	10	I	Reference input
VOUT	11	O	Output
NC	12	—	No internal connection
V+	13	I	Positive power supply
NC	14	—	No internal connection
RG2	15	I	Gain setting pin, for gains greater than one, connect an external resistor between pins 2 and 15
NC	16	—	No internal connection
SOIC			
RG1	1	I	Gain setting pin, for gains greater than one, connect an external resistor between pins 1 and 8
VIN–	2	I	Inverting input
VIN+	3	I	Non-inverting input
V–	4	I	negative power supply
REF	5	I	Reference input
VOUT	6	O	Output
V+	7	I	Positive power supply
RG2	8	I	Gain setting pin, for gains greater than one, connect an external resistor between pins 2 and 15

## 6 Specifications

### 6.1 Absolute Maximum Ratings

over operating free-air temperature range (unless otherwise noted) <sup>(1)</sup>

		MIN	MAX	UNIT
V+ to V–	Supply voltage		±18	V
Signal input terminals	Voltage <sup>(2)</sup>	(V–) – 0.5	(V+) + 0.5	V
	Current <sup>(2)</sup>		10	mA
Output short circuit <sup>(3)</sup>			Continuous	
Operating temperature		–55	125	°C
Junction temperature			300	°C
T <sub>stg</sub>	Storage temperature	–55	150	°C

(1) Stresses beyond those listed under *Absolute Maximum Ratings* may cause permanent damage to the device. These are stress ratings only, which do not imply functional operation of the device at these or any other conditions beyond those indicated under *Recommended Operating Conditions*. Exposure to absolute-maximum-rated conditions for extended periods may affect device reliability.

(2) Input terminals are diode-clamped to the power-supply rails. Input signals that can swing more than 0.5 V beyond the supply rails should be current limited to 10 mA or less.

(3) Short-circuit to ground, one amplifier per package.

### 6.2 ESD Ratings

		VALUE	UNIT
V <sub>(ESD)</sub>	Electrostatic discharge	Human-body model (HBM), per ANSI/ESDA/JEDEC JS-001 <sup>(1)</sup>	±4000
		Charged-device model (CDM), per JEDEC specification JESD22-C101 <sup>(2)</sup>	±1000

(1) JEDEC document JEP155 states that 500-V HBM allows safe manufacturing with a standard ESD control process.

(2) JEDEC document JEP157 states that 250-V CDM allows safe manufacturing with a standard ESD control process.

### 6.3 Recommended Operating Conditions

over operating free-air temperature range (unless otherwise noted)

		MIN	NOM	MAX	UNIT
V+ to V–	Supply voltage	±4.5	±15	±18	V
T <sub>A</sub>	Ambient Temperature	–40	25	85	°C

### 6.4 Thermal Information

THERMAL METRIC <sup>(1)</sup>		INA217		UNIT
		DW (SOIC)	P (PDIP)	
		16 PINS	8 PINS	
R <sub>θJA</sub>	Junction-to-ambient thermal resistance	64.3	46.2	°C/W
R <sub>θJC(top)</sub>	Junction-to-case (top) thermal resistance	24.9	34.5	°C/W
R <sub>θJB</sub>	Junction-to-board thermal resistance	29.4	23.5	°C/W
Ψ <sub>JT</sub>	Junction-to-top characterization parameter	3.3	11.7	°C/W
Ψ <sub>JB</sub>	Junction-to-board characterization parameter	28.8	23.3	°C/W
R <sub>θJC(bot)</sub>	Junction-to-case (bottom) thermal resistance	N/A	N/A	°C/W

(1) For more information about traditional and new thermal metrics, see the *Semiconductor and IC Package Thermal Metrics* application report, [SPRA953](#).

**INA217**

SBOS247C – JUNE 2002 – REVISED NOVEMBER 2015

[www.ti.com](http://www.ti.com)
**6.5 Electrical Characteristics:  $V_S = \pm 15\text{ V}$** 
 $T_A = 25^\circ\text{C}$ ,  $R_L = 2\text{ k}\Omega$ ,  $V_S = \pm 15\text{ V}$ , unless otherwise noted.

PARAMETER		TEST CONDITIONS	$T_A = 25^\circ\text{C}$			UNIT
			MIN	TYP	MAX	
<b>GAIN EQUATION<sup>(1)</sup></b>			$G = 1 + 10\text{k}/R_G$			
Range			1 to 10000			V/V
Gain Error	$G = 1$			$\pm 0.1\%$	$\pm 0.25\%$	
	$G = 10$			$\pm 0.2\%$	$\pm 0.7\%$	
	$G = 100$			$\pm 0.2\%$		
	$G = 1000$			$\pm 0.5\%$		
<b>GAIN TEMPERATURE DRIFT COEFFICIENT</b>						
	$G = 1$	$T_A = -40^\circ\text{C}$ to $85^\circ\text{C}$		$\pm 3$	$\pm 10$	ppm/ $^\circ\text{C}$
	$G > 10$	$T_A = -40^\circ\text{C}$ to $85^\circ\text{C}$		$\pm 40$	$\pm 100$	ppm/ $^\circ\text{C}$
Nonlinearity	$G = 1$			$\pm 0.0003$		% of FS
	$G = 100$			$\pm 0.0006$		% of FS
<b>INPUT STAGE NOISE</b>						
Voltage Noise	$f_O = 1\text{ kHz}$	$R_{\text{SOURCE}} = 0\ \Omega$		1.3		nV/ $\sqrt{\text{Hz}}$
	$f_O = 100\text{ Hz}$			1.5		nV/ $\sqrt{\text{Hz}}$
	$f_O = 10\text{ Hz}$			3.5		nV/ $\sqrt{\text{Hz}}$
Current Noise,	$f_O = 1\text{ kHz}$			0.8		pA/ $\sqrt{\text{Hz}}$
<b>OUTPUT STAGE NOISE</b>						
Voltage Noise,	$f_O = 1\text{ kHz}$			90		nV/ $\sqrt{\text{Hz}}$
<b>INPUT OFFSET VOLTAGE</b>						
Input Offset Voltage		$V_{\text{CM}} = V_{\text{OUT}} = 0\text{ V}$		$50 + 2000/G$	$250 + 5000/G$	$\mu\text{V}$
vs Temperature		$T_A = -40^\circ\text{C}$ to $85^\circ\text{C}$		$1 + 20/G$		$\mu\text{V}/^\circ\text{C}$
vs Power Supply		$V_S = \pm 4.5\text{ V}$ to $\pm 18\text{ V}$		$1 + 50/G$	$3 + 200/G$	$\mu\text{V/V}$
<b>INPUT VOLTAGE RANGE</b>						
Common-Mode Voltage Range		$V_{\text{IN}+} - V_{\text{IN}-} = 0\text{ V}$	$(V+) - 4$	$(V+) - 3$		V
		$V_{\text{IN}+} - V_{\text{IN}-} = 0\text{ V}$	$(V-) + 4$	$(V-) + 3$		V
Common-Mode Rejection	$G = 1$	$V_{\text{CM}} = \pm 11\text{ V}$ , $R_{\text{SRC}} = 0\ \Omega$	70	80		dB
	$G = 100$		100	116		dB
<b>INPUT BIAS CURRENT</b>						
Initial Bias Current				2	12	$\mu\text{A}$
vs Temperature		$T_A = -40^\circ\text{C}$ to $85^\circ\text{C}$		10		nA/ $^\circ\text{C}$
Initial Offset Current				0.1	1	$\mu\text{A}$
vs Temperature		$T_A = -40^\circ\text{C}$ to $85^\circ\text{C}$		0.5		nA/ $^\circ\text{C}$
<b>INPUT IMPEDANCE</b>						
		Differential		$60 \parallel 2$		M $\Omega \parallel \text{pF}$
		Common-Mode		$60 \parallel 2$		M $\Omega \parallel \text{pF}$
<b>DYNAMIC RESPONSE</b>						
Bandwidth, Small Signal, $-3\text{d B}$						
$G = 1$				3.4		MHz
$G = 100$				800		kHz
Slew Rate				15		V/ $\mu\text{s}$
THD+Noise, $f = 1\text{ kHz}$		$G = 100$		0.004%		
Settling Time	0.1%	$G = 100$ , 10V Step		2		$\mu\text{s}$
	0.01%	$G = 100$ , 10V Step		3.5		$\mu\text{s}$
Overload Recovery		50% Overdrive		1		$\mu\text{s}$

<sup>(1)</sup> Gain accuracy is a function of external  $R_G$ .

**Electrical Characteristics:  $V_S = \pm 15\text{ V}$  (continued)**
 $T_A = 25^\circ\text{C}$ ,  $R_L = 2\text{ k}\Omega$ ,  $V_S = \pm 15\text{ V}$ , unless otherwise noted.

PARAMETER	TEST CONDITIONS	T <sub>A</sub> = 25°C			UNIT
		MIN	TYP	MAX	
OUTPUT					
Voltage	R <sub>L</sub> to GND	(V+) − 2 (V−) + 2	(V+) − 1.8 (V−) + 1.8		V V
Load Capacitance Stability			1000		pF
Short Circuit Current	Continuous-to-Common		±60		mA
POWER SUPPLY					
Rated Voltage			±15		V
Voltage Range		±4.5		±18	V
Current, Quiescent	I <sub>O</sub> = 0 mA		±10	±12	mA
TEMPERATURE RANGE					
Specification		−40		85	°C
Operating		−40		125	°C

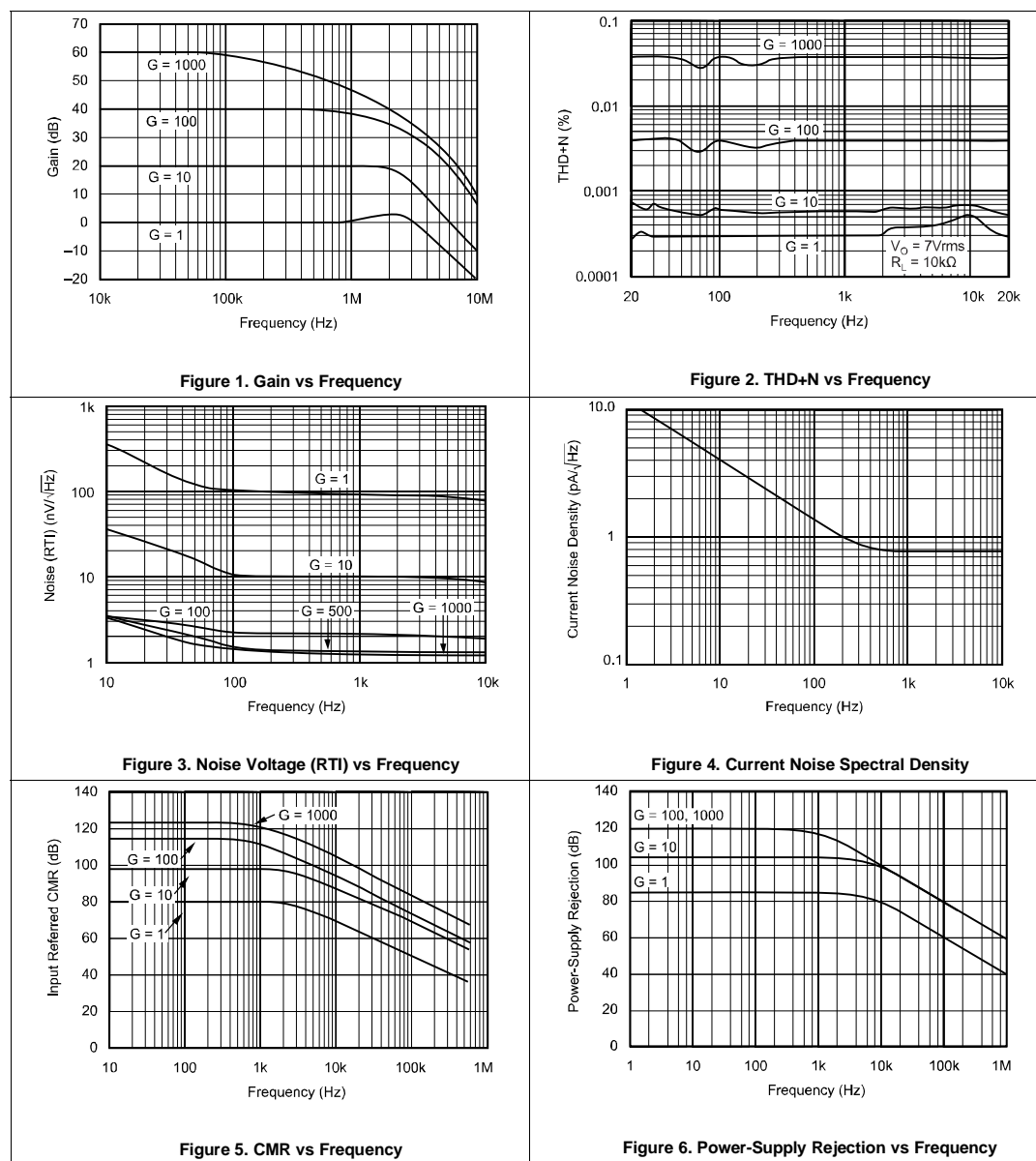
## INA217

SBOS247C–JUNE 2002–REVISED NOVEMBER 2015

www.ti.com

### 6.6 Typical Characteristics

At  $T_A = 25^\circ\text{C}$ ,  $V_S = \pm 15\text{ V}$ ,  $R_L = 2\text{ k}\Omega$ , unless otherwise noted.





## Typical Characteristics (continued)

At  $T_A = 25^\circ\text{C}$ ,  $V_S = \pm 15\text{ V}$ ,  $R_L = 2\text{ k}\Omega$ , unless otherwise noted.

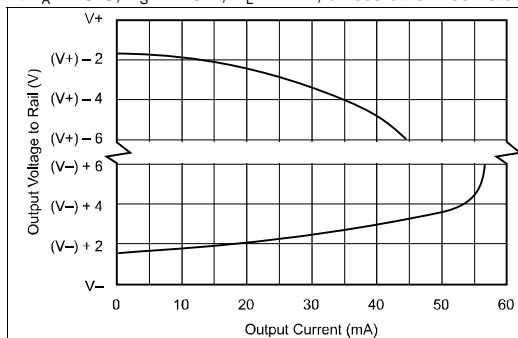


**Figure 7. Output Voltage Swing vs Output Current**

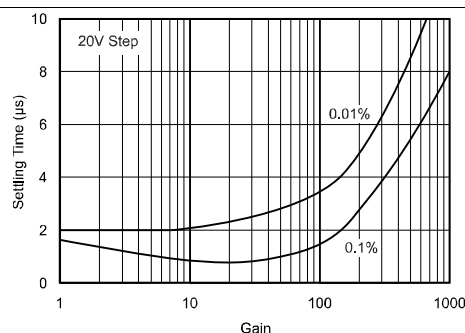


**Figure 8. Settling Time vs Gain**

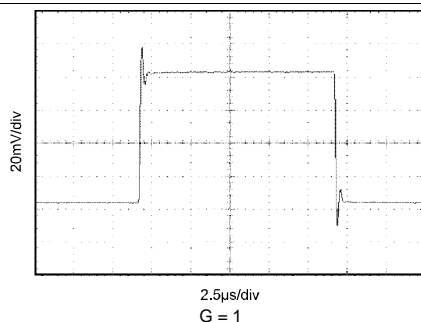


**Figure 9. Small-Signal Transient Response**

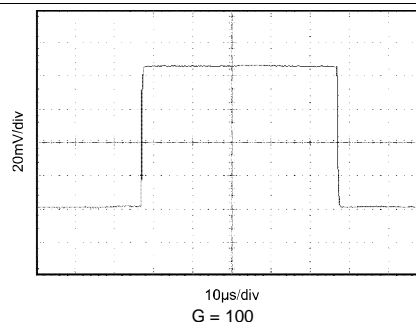


**Figure 10. Small-Signal Transient Response**

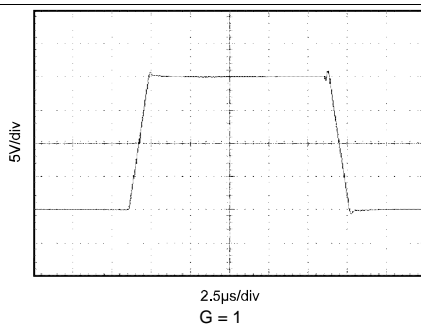


**Figure 11. Large-Signal Transient Response**

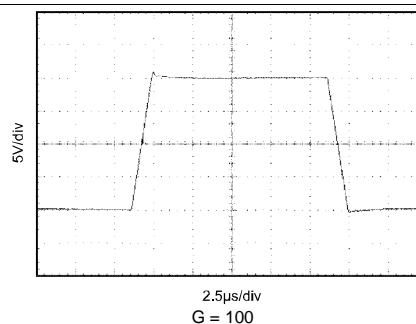


**Figure 12. Large-Signal Transient Response**

## INA217

SBOS247C – JUNE 2002 – REVISED NOVEMBER 2015

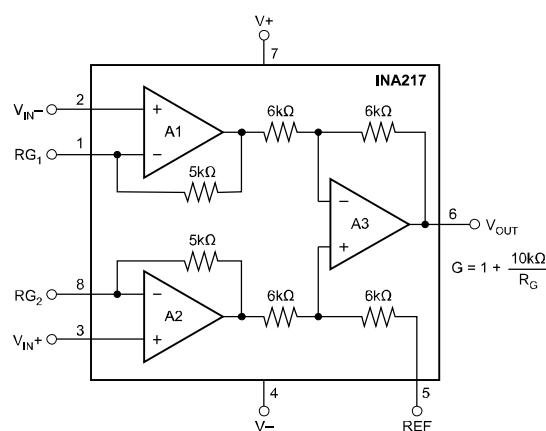
[www.ti.com](http://www.ti.com)

## 7 Detailed Description

### 7.1 Overview

The INA217 is a classical three-amp instrumentation amplifier designed for audio applications. Featuring low noise and low distortion the INA217 is ideally suited for amplifying low level audio signals. With a wide supply voltage, wide output voltage swing, and high output current drive the INA217 is also ideally suited for processing high level audio signals. Specified from  $-40^{\circ}\text{C}$  to  $85^{\circ}\text{C}$  the INA217 is well suited for industrial applications.

### 7.2 Functional Block Diagram



### 7.3 Feature Description

#### 7.3.1 Basic Connections

Figure 13 shows the basic connections required for operation. Power supplies should be bypassed with 0.1- $\mu\text{F}$  tantalum capacitors near the device pins. The output Reference (pin 5) should be a low-impedance connection. Resistance of a few  $\Omega$ s in series with this connection will degrade the common-mode rejection of the INA217.

## Feature Description (continued)

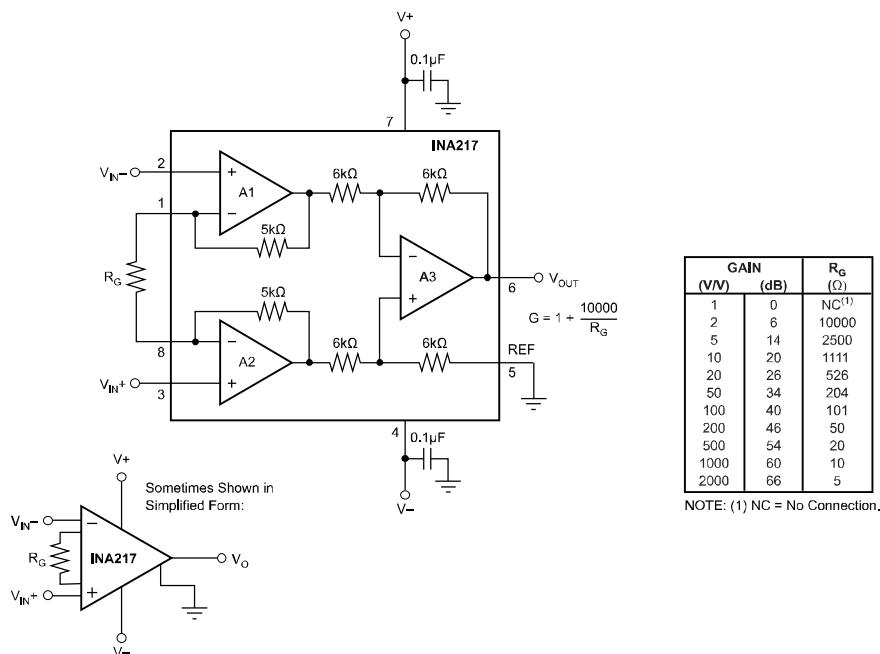


Figure 13. Basic Circuit Connections

### 7.3.2 Gain-Set Resistor

Gain is set with an external resistor,  $R_G$ , as shown in Figure 13. The two internal 5-kΩ feedback resistors are laser-trimmed to 5-kΩ within approximately  $\pm 0.2\%$ . Equation 1 shows the gain equation for the INA217.

$$G = 1 + \frac{10\,000}{R_G} \quad (1)$$

The temperature coefficient of the internal 5-kΩ resistors is approximately  $\pm 25$  ppm/°C. Accuracy and TCR of the external  $R_G$  will also contribute to gain error and temperature drift. These effects can be inferred from the gain equation. Make a short, direct connection to the gain set resistor,  $R_G$ . Avoid running output signals near these sensitive input nodes.

### 7.3.3 Noise Performance

The INA217 provides very low noise with low-source impedance. Its 1.3-nV/M $\sqrt{\text{Hz}}$  voltage noise delivers near-theoretical noise performance with a source impedance of 200 Ω. The input stage design used to achieve this low noise results in relatively high input bias current and input bias current noise. As a result, the INA217 may not provide the best noise performance with a source impedance greater than 10 kΩ. For source impedance greater than 10 kΩ, other instrumentation amplifiers may provide improved noise performance.

### 7.3.4 Input Considerations

Very low source impedance (less than 10 Ω) can cause the INA217 to oscillate. This depends on circuit layout, signal source, and input cable characteristics. An input network consisting of a small inductor and resistor, as shown in Figure 14, can greatly reduce any tendency to oscillate. This is especially useful if a variety of input sources are to be connected to the INA217. Although not shown in other figures, this network can be used as needed with all applications shown.

## INA217

SBOS247C–JUNE 2002–REVISED NOVEMBER 2015

[www.ti.com](http://www.ti.com)

### Feature Description (continued)

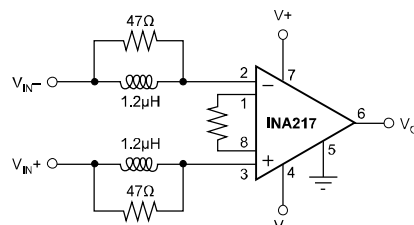


**Figure 14. Input Stabilization Network**

#### 7.3.5 Offset Voltage Trim

A variable voltage applied to pin 5, as shown in [Figure 15](#), can be used to adjust the output offset voltage. A voltage applied to pin 5 is summed with the output signal. An operational amplifier connected as a buffer is used to provide a low impedance at pin 5 to assure good common-mode rejection.

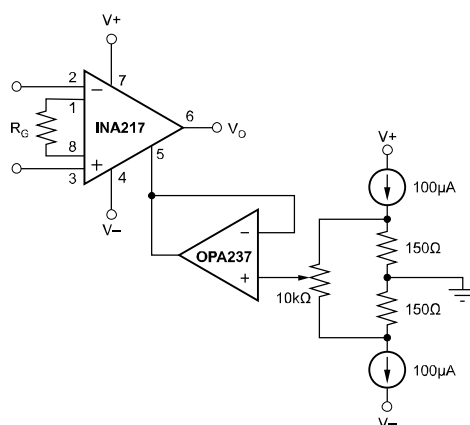


**Figure 15. Offset Voltage Adjustment Circuit**

### 7.4 Device Functional Modes

The INA217 has a single functional mode of operation. The mode is operational when the power supply voltage exceeds  $\pm 4.5$  V. The maximum power supply voltage is  $\pm 18$  V. The INA217 is specified over the temperature range from  $-40^{\circ}\text{C}$  to  $85^{\circ}\text{C}$  and is operational to  $125^{\circ}\text{C}$ .

## 8 Application and Implementation

### NOTE

Information in the following applications sections is not part of the TI component specification, and TI does not warrant its accuracy or completeness. TI's customers are responsible for determining suitability of components for their purposes. Customers should validate and test their design implementation to confirm system functionality.

### 8.1 Application Information

The INA217 is used in professional audio equipment such as professional microphone preamps, moving-coil transducer amplifiers, differential receivers, and bridge transducer amplifiers.

### 8.2 Typical Application

Figure 16 shows a typical circuit for a professional microphone input amplifier.

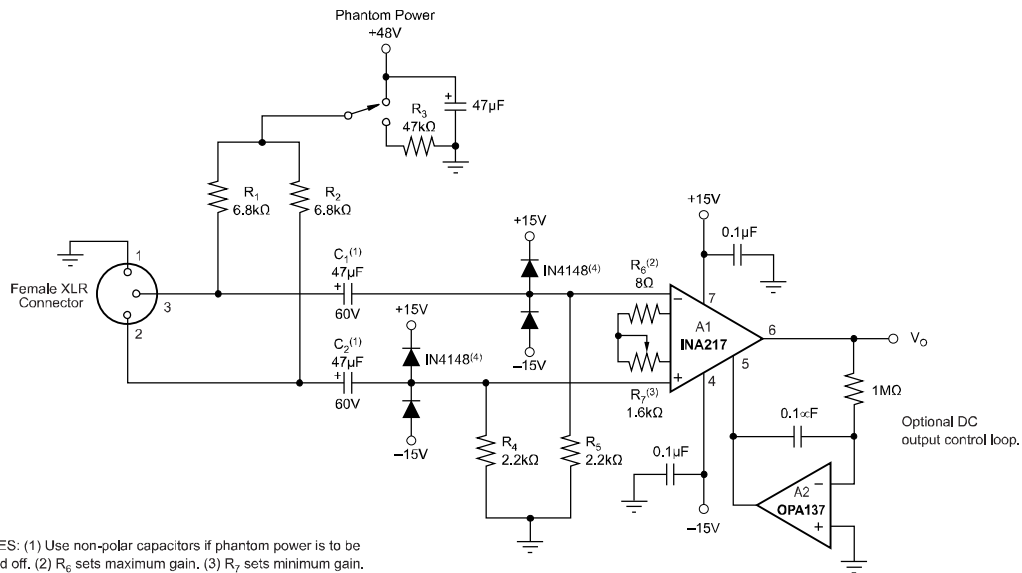


Figure 16. Phantom-Powered Microphone Preamplifier

#### 8.2.1 Design Requirements

- 48-V, Phantom powered, remotely located microphone
- Circuitry operates from  $\pm 15$ -V power supplies
- Low distortion and noise over the audio frequency band
- Gain range from 20 db to 60 db

#### 8.2.2 Detailed Design Procedure

$R_1$  and  $R_2$  provide a current path for conventional 48-V phantom power source for a remotely located microphone. An optional switch allows phantom power to be disabled.  $C_1$  and  $C_2$  block the phantom power voltage from the INA217 input circuitry. Non-polarized capacitors should be used for  $C_1$  and  $C_2$  if phantom power is to be disabled. For additional input protection against ESD and hot-plugging, four IN4148 diodes may be connected from the input to supply lines.

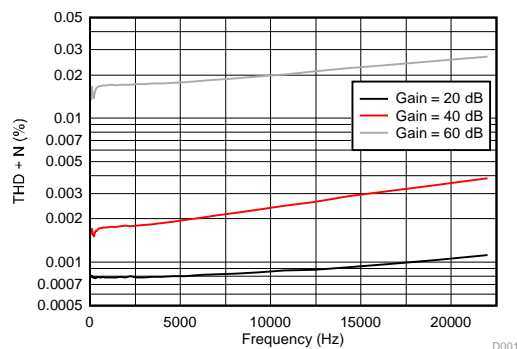
**INA217**

SBOS247C – JUNE 2002 – REVISED NOVEMBER 2015

[www.ti.com](http://www.ti.com)
**Typical Application (continued)**

$R_4$  and  $R_5$  provide a path for input bias current of the INA217. Input offset current (typically 100 nA) creates a DC differential input voltage that will produce an output offset voltage. This is generally the dominant source of output offset voltage in this application. With a maximum gain of 1000 (60 dB), the output offset voltage can be several volts. This may be entirely acceptable if the output is AC-coupled into the subsequent stage. An alternate technique is shown in [Figure 16](#). An inexpensive FET-input operational amplifier in a feedback loop drives the DC output voltage to 0 V. A2 is not in the audio signal path and does not affect signal quality.

Gain is set with a variable resistor,  $R_7$ , in series with  $R_6$ .  $R_6$  determines the maximum gain. The total resistance,  $R_6 + R_7$ , determines the lowest gain. A special reverse-log taper potentiometer for  $R_7$  can be used to create a linear change (in dB) with rotation.

**8.2.3 Application Curve**


**Figure 17. THD + Noise for the Phantom Powered Microphone Circuit**

**9 Power Supply Recommendations**

The INA217 is specified for operation from  $\pm 4.5$  V to  $\pm 18$  V; many specifications apply from  $-40^\circ\text{C}$  to  $85^\circ\text{C}$ . Parameters that can exhibit significant variance with regard to operating voltage or temperature are presented in the [Typical Characteristics](#).

## 10 Layout

### 10.1 Layout Guidelines

For best operational performance of the device, use good PCB layout practices, including:

- Noise can propagate into analog circuitry through the power pins of the circuit as a whole and op amp itself. Bypass capacitors are used to reduce the coupled noise by providing low-impedance power sources local to the analog circuitry.
  - Connect low-ESR, 0.1- $\mu$ F ceramic bypass capacitors between each supply pin and ground, placed as close to the device as possible. A single bypass capacitor from V+ to ground is applicable for single-supply applications.
- Separate grounding for analog and digital portions of circuitry is one of the simplest and most-effective methods of noise suppression. One or more layers on multilayer PCBs are usually devoted to ground planes. A ground plane helps distribute heat and reduces EMI noise pickup. Make sure to physically separate digital and analog grounds paying attention to the flow of the ground current. For more detailed information, see *Circuit Board Layout Techniques*, [SLOA089](#).
- To reduce parasitic coupling, run the input traces as far away from the supply or output traces as possible. If these traces cannot be kept separate, crossing the sensitive trace perpendicular is much better as opposed to in parallel with the noisy trace.
- Place the external components as close to the device as possible.
- Keep the length of input traces as short as possible. Always remember that the input traces are the most sensitive part of the circuit.
- Consider a driven, low-impedance guard ring around the critical traces. A guard ring can significantly reduce leakage currents from nearby traces that are at different potentials.
- TI recommends cleaning the PCB following board assembly for best performance.
- Any precision integrated circuit may experience performance shifts due to moisture ingress into the plastic package. Following any aqueous PCB cleaning process, TI recommends baking the PCB assembly to remove moisture introduced into the device packaging during the cleaning process. A low temperature, post cleaning bake at 85°C for 30 minutes is sufficient for most circumstances.

### 10.2 Layout Example

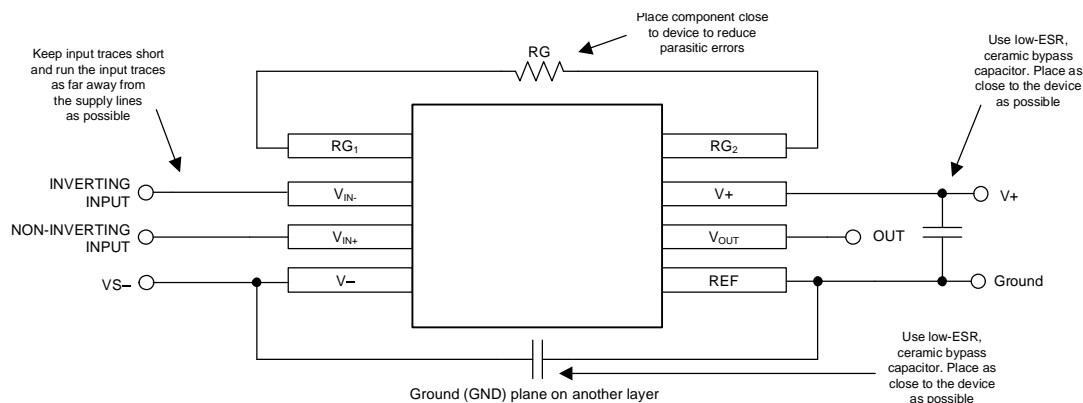


Figure 18. INA217 Layout Example

## 11 Device and Documentation Support

### 11.1 Device Support

#### 11.1.1 Development Support

##### 11.1.1.1 TINA-TI™ (Free Software Download)

TINA™ is a simple, powerful, and easy-to-use circuit simulation program based on a SPICE engine. TINA-TI is a free, fully-functional version of the TINA software, preloaded with a library of macro models in addition to a range of both passive and active models. TINA-TI provides all the conventional dc, transient, and frequency domain analysis of SPICE, as well as additional design capabilities.

Available as a [free download](#) from the Analog eLab Design Center, TINA-TI offers extensive post-processing capability that allows users to format results in a variety of ways. Virtual instruments offer the ability to select input waveforms and probe circuit nodes, voltages, and waveforms, creating a dynamic quick-start tool.

#### NOTE

These files require that either the TINA software (from DesignSoft™) or TINA-TI software be installed. Download the free TINA-TI software from the [TINA-TI folder](#).

##### 11.1.1.2 TI Precision Designs

TI Precision Designs are available online at <http://www.ti.com/ww/en/analog/precision-designs/>. TI Precision Designs are analog solutions created by TI's precision analog applications experts and offer the theory of operation, component selection, simulation, complete PCB schematic and layout, bill of materials, and measured performance of many useful circuits.

##### 11.1.1.3 WEBENCH® Filter Designer

[WEBENCH® Filter Designer](#) is a simple, powerful, and easy-to-use active filter design program. The WEBENCH Filter Designer lets you create optimized filter designs using a selection of TI operational amplifiers and passive components from TI's vendor partners.

Available as a web based tool from the WEBENCH® Design Center, [WEBENCH® Filter Designer](#) allows you to design, optimize, and simulate complete multistage active filter solutions within minutes.

### 11.2 Documentation Support

#### 11.2.1 Related Documentation

For related documentation see the following:

- *Circuit Board Layout Techniques*, [SLOA089](#).
- *Shelf-Life Evaluation of Lead-Free Component Finishes*, [SZZA046](#).

### 11.3 Community Resources

The following links connect to TI community resources. Linked contents are provided "AS IS" by the respective contributors. They do not constitute TI specifications and do not necessarily reflect TI's views; see TI's [Terms of Use](#).

**TI E2E™ Online Community** *TI's Engineer-to-Engineer (E2E) Community*. Created to foster collaboration among engineers. At [e2e.ti.com](http://e2e.ti.com), you can ask questions, share knowledge, explore ideas and help solve problems with fellow engineers.

**Design Support** *TI's Design Support* Quickly find helpful E2E forums along with design support tools and contact information for technical support.



#### 11.4 Trademarks

TINA-TI, E2E are trademarks of Texas Instruments.  
TINA, DesignSoft are trademarks of DesignSoft, Inc.  
All other trademarks are the property of their respective owners.

#### 11.5 Electrostatic Discharge Caution



These devices have limited built-in ESD protection. The leads should be shorted together or the device placed in conductive foam during storage or handling to prevent electrostatic damage to the MOS gates.

#### 11.6 Glossary

[SLYZ022](#) — *TI Glossary*.

This glossary lists and explains terms, acronyms, and definitions.

### 12 Mechanical, Packaging, and Orderable Information

The following pages include mechanical, packaging, and orderable information. This information is the most current data available for the designated devices. This data is subject to change without notice and revision of this document. For browser-based versions of this data sheet, refer to the left-hand navigation.



www.ti.com

## PACKAGE OPTION ADDENDUM

24-Aug-2018

### PACKAGING INFORMATION

Orderable Device	Status (1)	Package Type	Package Drawing	Pins	Package Qty	Eco Plan (2)	Lead/Ball Finish (6)	MSL Peak Temp (3)	Op Temp (°C)	Device Marking (4/5)	Samples
INA217AIDWR	ACTIVE	SOIC	DW	16	2000	Green (RoHS & no Sb/Br)	CU NIPDAU	Level-3-260C-168 HR	-40 to 125	INA217	Samples
INA217AIDWT	ACTIVE	SOIC	DW	16	250	Green (RoHS & no Sb/Br)	CU NIPDAU	Level-3-260C-168 HR	-40 to 125	INA217	Samples
INA217AIP	ACTIVE	PDIP	P	8	50	Green (RoHS & no Sb/Br)	CU NIPDAU	N / A for Pkg Type	-40 to 85	INA217	Samples
INA217AIPG4	ACTIVE	PDIP	P	8	50	Green (RoHS & no Sb/Br)	CU NIPDAU	N / A for Pkg Type	-40 to 85	INA217	Samples

(1) The marketing status values are defined as follows:

**ACTIVE:** Product device recommended for new designs.

**LIFEBUY:** TI has announced that the device will be discontinued, and a lifetime-buy period is in effect.

**NRND:** Not recommended for new designs. Device is in production to support existing customers, but TI does not recommend using this part in a new design.

**PREVIEW:** Device has been announced but is not in production. Samples may or may not be available.

**OBSOLETE:** TI has discontinued the production of the device.

(2) **RoHS:** TI defines "RoHS" to mean semiconductor products that are compliant with the current EU RoHS requirements for all 10 RoHS substances, including the requirement that RoHS substance do not exceed 0.1% by weight in homogeneous materials. Where designed to be soldered at high temperatures, "RoHS" products are suitable for use in specified lead-free processes. TI may reference these types of products as "Pb-Free".

**RoHS Exempt:** TI defines "RoHS Exempt" to mean products that contain lead but are compliant with EU RoHS pursuant to a specific EU RoHS exemption.

**Green:** TI defines "Green" to mean the content of Chlorine (Cl) and Bromine (Br) based flame retardants meet JS709B low halogen requirements of <=1000ppm threshold. Antimony trioxide based flame retardants must also meet the <=1000ppm threshold requirement.

(3) **MSL, Peak Temp. -** The Moisture Sensitivity Level rating according to the JEDEC industry standard classifications, and peak solder temperature.

(4) There may be additional marking, which relates to the logo, the lot trace code information, or the environmental category on the device.

(5) Multiple Device Markings will be inside parentheses. Only one Device Marking contained in parentheses and separated by a "-" will appear on a device. If a line is indented then it is a continuation of the previous line and the two combined represent the entire Device Marking for that device.

(6) **Lead/Ball Finish** - Orderable Devices may have multiple material finish options. Finish options are separated by a vertical ruled line. Lead/Ball Finish values may wrap to two lines if the finish value exceeds the maximum column width.

**Important Information and Disclaimer:** The information provided on this page represents TI's knowledge and belief as of the date that it is provided. TI bases its knowledge and belief on information provided by third parties, and makes no representation or warranty as to the accuracy of such information. Efforts are underway to better integrate information from third parties. TI has taken and



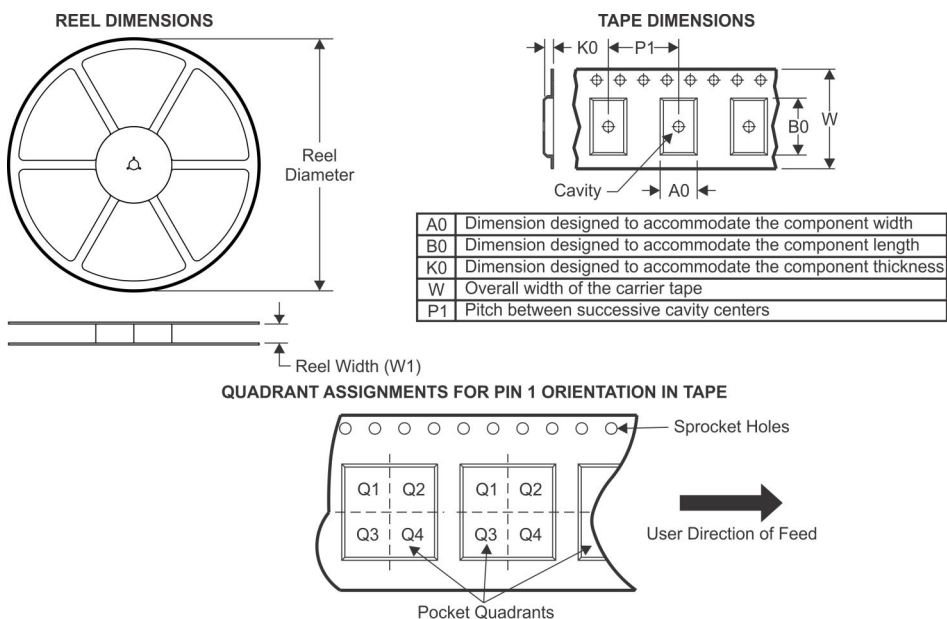
## PACKAGE OPTION ADDENDUM

24-Aug-2018

continues to take reasonable steps to provide representative and accurate information but may not have conducted destructive testing or chemical analysis on incoming materials and chemicals. TI and TI suppliers consider certain information to be proprietary, and thus CAS numbers and other limited information may not be available for release.

In no event shall TI's liability arising out of such information exceed the total purchase price of the TI part(s) at issue in this document sold by TI to Customer on an annual basis.

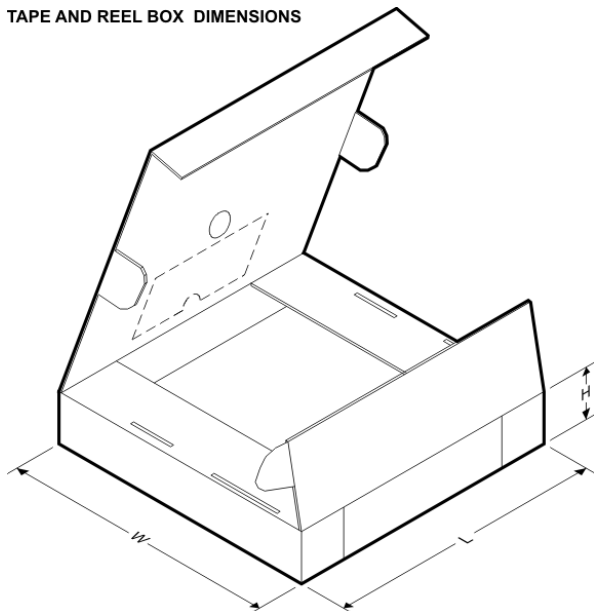
**TAPE AND REEL INFORMATION**



\*All dimensions are nominal

Device	Package Type	Package Drawing	Pins	SPQ	Reel Diameter (mm)	Reel Width W1 (mm)	A0 (mm)	B0 (mm)	K0 (mm)	P1 (mm)	W (mm)	Pin1 Quadrant
INA217AIDWR	SOIC	DW	16	2000	330.0	16.4	10.75	10.7	2.7	12.0	16.0	Q1
INA217AIDWT	SOIC	DW	16	250	180.0	16.4	10.75	10.7	2.7	12.0	16.0	Q1

**TAPE AND REEL BOX DIMENSIONS**

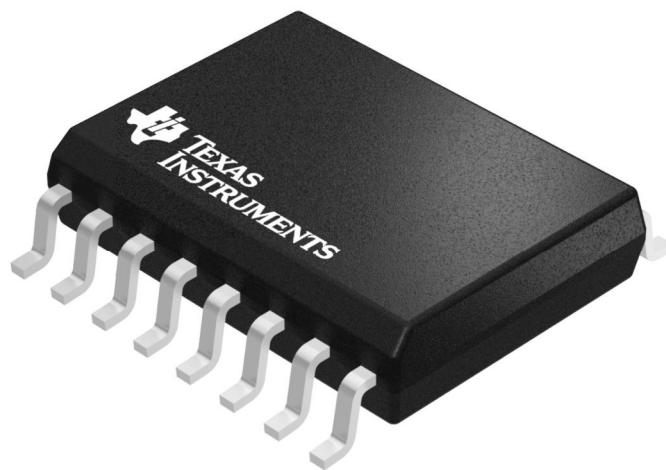


\*All dimensions are nominal

Device	Package Type	Package Drawing	Pins	SPQ	Length (mm)	Width (mm)	Height (mm)
INA217AIDWR	SOIC	DW	16	2000	367.0	367.0	38.0
INA217AIDWT	SOIC	DW	16	250	210.0	185.0	35.0

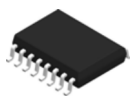
DW 16

GENERIC PACKAGE VIEW  
SOIC - 2.65 mm max height  
SMALL OUTLINE INTEGRATED CIRCUIT



Images above are just a representation of the package family, actual package may vary.  
Refer to the product data sheet for package details.

4040000-2/H

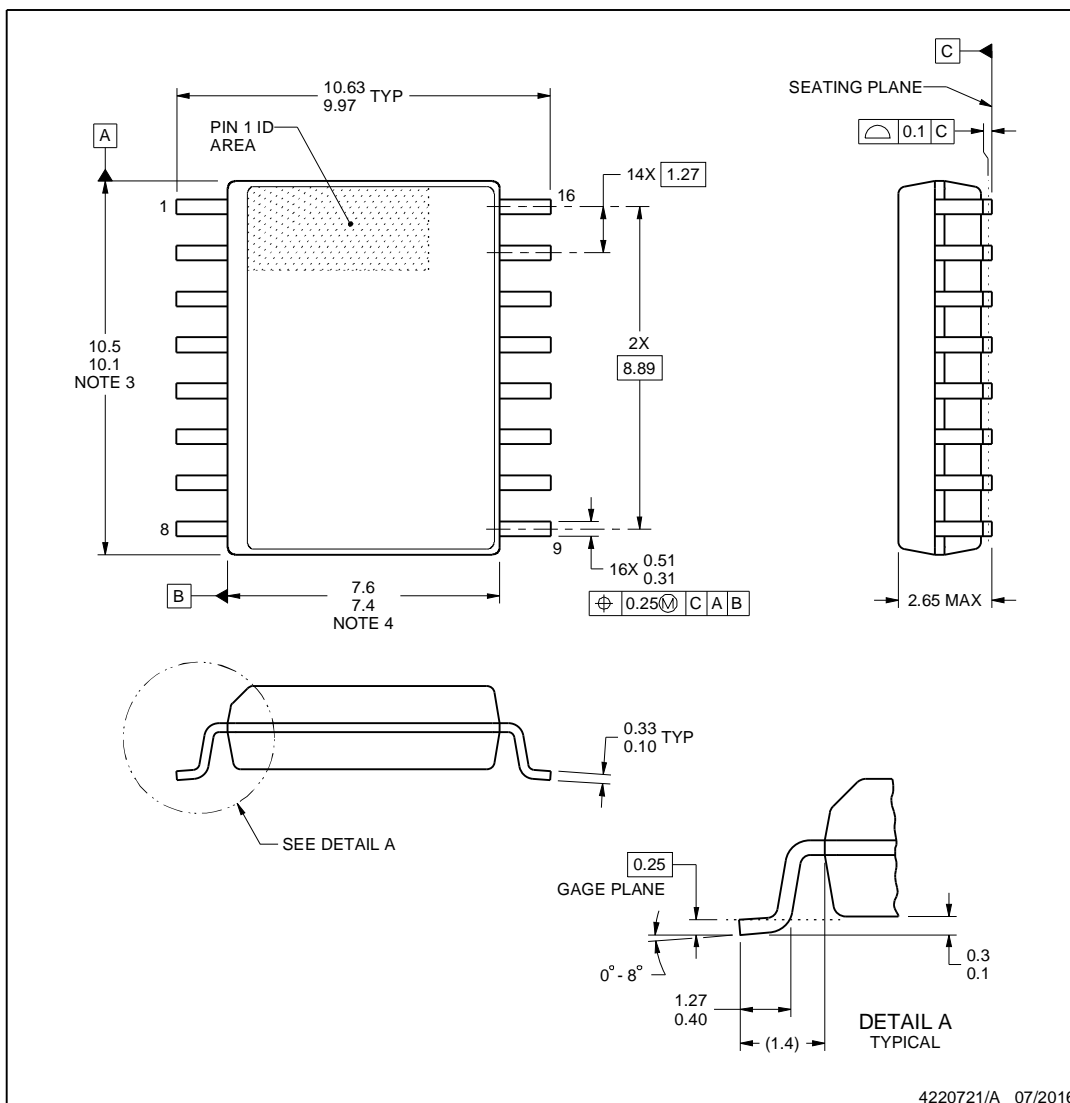


DW0016A

## PACKAGE OUTLINE

SOIC - 2.65 mm max height

SOIC



4220721/A 07/2016

### NOTES:

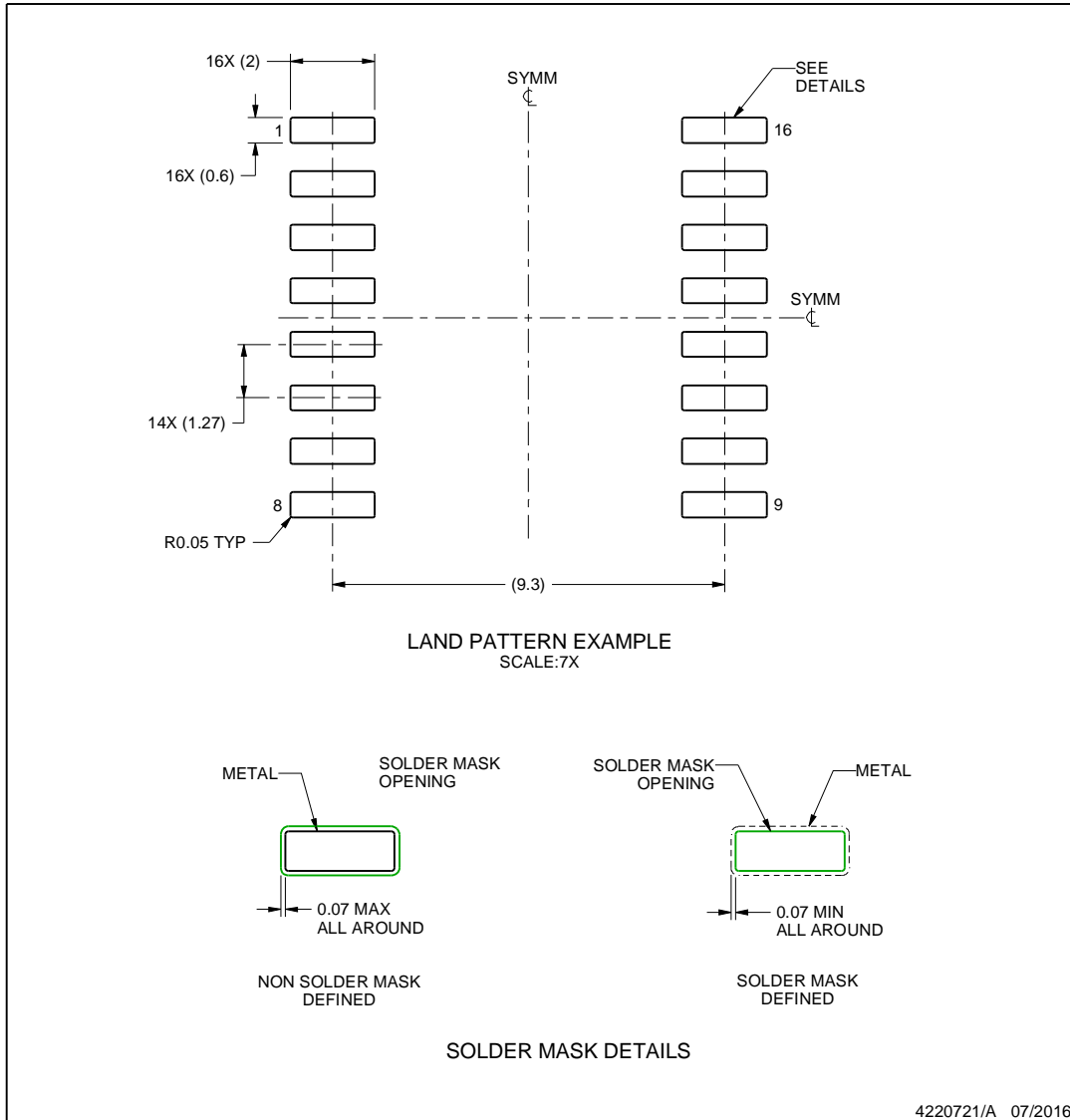
1. All linear dimensions are in millimeters. Dimensions in parenthesis are for reference only. Dimensioning and tolerancing per ASME Y14.5M.
2. This drawing is subject to change without notice.
3. This dimension does not include mold flash, protrusions, or gate burrs. Mold flash, protrusions, or gate burrs shall not exceed 0.15 mm, per side.
4. This dimension does not include interlead flash. Interlead flash shall not exceed 0.25 mm, per side.
5. Reference JEDEC registration MS-013.

## EXAMPLE BOARD LAYOUT

DW0016A

SOIC - 2.65 mm max height

SOIC



NOTES: (continued)

6. Publication IPC-7351 may have alternate designs.

7. Solder mask tolerances between and around signal pads can vary based on board fabrication site.

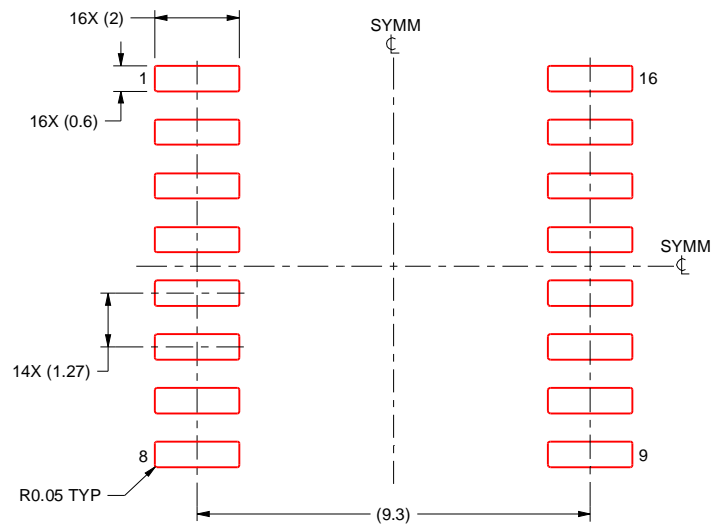


## EXAMPLE STENCIL DESIGN

DW0016A

SOIC - 2.65 mm max height

SOIC



SOLDER PASTE EXAMPLE  
BASED ON 0.125 mm THICK STENCIL  
SCALE:7X

4220721/A 07/2016

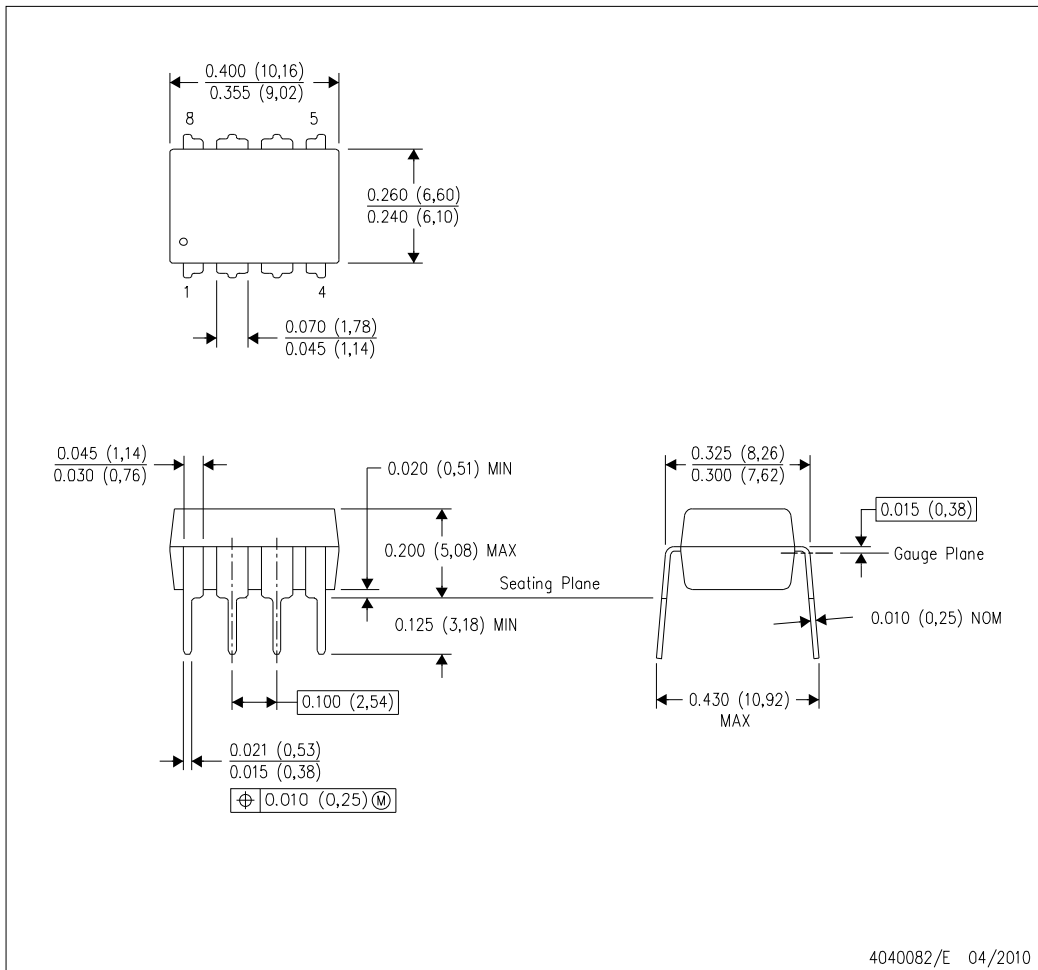
NOTES: (continued)

8. Laser cutting apertures with trapezoidal walls and rounded corners may offer better paste release. IPC-7525 may have alternate design recommendations.
9. Board assembly site may have different recommendations for stencil design.

## MECHANICAL DATA

P (R-PDIP-T8)

PLASTIC DUAL-IN-LINE PACKAGE



- NOTES:
- A. All linear dimensions are in inches (millimeters).
  - B. This drawing is subject to change without notice.
  - C. Falls within JEDEC MS-001 variation BA.

## IMPORTANT NOTICE

Texas Instruments Incorporated (TI) reserves the right to make corrections, enhancements, improvements and other changes to its semiconductor products and services per JESD46, latest issue, and to discontinue any product or service per JESD48, latest issue. Buyers should obtain the latest relevant information before placing orders and should verify that such information is current and complete.

TI's published terms of sale for semiconductor products (<http://www.ti.com/sc/docs/stdterms.htm>) apply to the sale of packaged integrated circuit products that TI has qualified and released to market. Additional terms may apply to the use or sale of other types of TI products and services.

Reproduction of significant portions of TI information in TI data sheets is permissible only if reproduction is without alteration and is accompanied by all associated warranties, conditions, limitations, and notices. TI is not responsible or liable for such reproduced documentation. Information of third parties may be subject to additional restrictions. Resale of TI products or services with statements different from or beyond the parameters stated by TI for that product or service voids all express and any implied warranties for the associated TI product or service and is an unfair and deceptive business practice. TI is not responsible or liable for any such statements.

Buyers and others who are developing systems that incorporate TI products (collectively, "Designers") understand and agree that Designers remain responsible for using their independent analysis, evaluation and judgment in designing their applications and that Designers have full and exclusive responsibility to assure the safety of Designers' applications and compliance of their applications (and of all TI products used in or for Designers' applications) with all applicable regulations, laws and other applicable requirements. Designer represents that, with respect to their applications, Designer has all the necessary expertise to create and implement safeguards that (1) anticipate dangerous consequences of failures, (2) monitor failures and their consequences, and (3) lessen the likelihood of failures that might cause harm and take appropriate actions. Designer agrees that prior to using or distributing any applications that include TI products, Designer will thoroughly test such applications and the functionality of such TI products as used in such applications.

TI's provision of technical, application or other design advice, quality characterization, reliability data or other services or information, including, but not limited to, reference designs and materials relating to evaluation modules, (collectively, "TI Resources") are intended to assist designers who are developing applications that incorporate TI products; by downloading, accessing or using TI Resources in any way, Designer (individually or, if Designer is acting on behalf of a company, Designer's company) agrees to use any particular TI Resource solely for this purpose and subject to the terms of this Notice.

TI's provision of TI Resources does not expand or otherwise alter TI's applicable published warranties or warranty disclaimers for TI products, and no additional obligations or liabilities arise from TI providing such TI Resources. TI reserves the right to make corrections, enhancements, improvements and other changes to its TI Resources. TI has not conducted any testing other than that specifically described in the published documentation for a particular TI Resource.

Designer is authorized to use, copy and modify any individual TI Resource only in connection with the development of applications that include the TI product(s) identified in such TI Resource. NO OTHER LICENSE, EXPRESS OR IMPLIED, BY ESTOPPEL OR OTHERWISE TO ANY OTHER TI INTELLECTUAL PROPERTY RIGHT, AND NO LICENSE TO ANY TECHNOLOGY OR INTELLECTUAL PROPERTY RIGHT OF TI OR ANY THIRD PARTY IS GRANTED HEREIN, including but not limited to any patent right, copyright, mask work right, or other intellectual property right relating to any combination, machine, or process in which TI products or services are used. Information regarding or referencing third-party products or services does not constitute a license to use such products or services, or a warranty or endorsement thereof. Use of TI Resources may require a license from a third party under the patents or other intellectual property of the third party, or a license from TI under the patents or other intellectual property of TI.

TI RESOURCES ARE PROVIDED "AS IS" AND WITH ALL FAULTS. TI DISCLAIMS ALL OTHER WARRANTIES OR REPRESENTATIONS, EXPRESS OR IMPLIED, REGARDING RESOURCES OR USE THEREOF, INCLUDING BUT NOT LIMITED TO ACCURACY OR COMPLETENESS, TITLE, ANY EPIDEMIC FAILURE WARRANTY AND ANY IMPLIED WARRANTIES OF MERCHANTABILITY, FITNESS FOR A PARTICULAR PURPOSE, AND NON-INFRINGEMENT OF ANY THIRD PARTY INTELLECTUAL PROPERTY RIGHTS. TI SHALL NOT BE LIABLE FOR AND SHALL NOT DEFEND OR INDEMNIFY DESIGNER AGAINST ANY CLAIM, INCLUDING BUT NOT LIMITED TO ANY INFRINGEMENT CLAIM THAT RELATES TO OR IS BASED ON ANY COMBINATION OF PRODUCTS EVEN IF DESCRIBED IN TI RESOURCES OR OTHERWISE. IN NO EVENT SHALL TI BE LIABLE FOR ANY ACTUAL, DIRECT, SPECIAL, COLLATERAL, INDIRECT, PUNITIVE, INCIDENTAL, CONSEQUENTIAL OR EXEMPLARY DAMAGES IN CONNECTION WITH OR ARISING OUT OF TI RESOURCES OR USE THEREOF, AND REGARDLESS OF WHETHER TI HAS BEEN ADVISED OF THE POSSIBILITY OF SUCH DAMAGES.

Unless TI has explicitly designated an individual product as meeting the requirements of a particular industry standard (e.g., ISO/TS 16949 and ISO 26262), TI is not responsible for any failure to meet such industry standard requirements.

Where TI specifically promotes products as facilitating functional safety or as compliant with industry functional safety standards, such products are intended to help enable customers to design and create their own applications that meet applicable functional safety standards and requirements. Using products in an application does not by itself establish any safety features in the application. Designers must ensure compliance with safety-related requirements and standards applicable to their applications. Designer may not use any TI products in life-critical medical equipment unless authorized officers of the parties have executed a special contract specifically governing such use. Life-critical medical equipment is medical equipment where failure of such equipment would cause serious bodily injury or death (e.g., life support, pacemakers, defibrillators, heart pumps, neurostimulators, and implantables). Such equipment includes, without limitation, all medical devices identified by the U.S. Food and Drug Administration as Class III devices and equivalent classifications outside the U.S.

TI may expressly designate certain products as completing a particular qualification (e.g., Q100, Military Grade, or Enhanced Product). Designers agree that it has the necessary expertise to select the product with the appropriate qualification designation for their applications and that proper product selection is at Designers' own risk. Designers are solely responsible for compliance with all legal and regulatory requirements in connection with such selection.

Designer will fully indemnify TI and its representatives against any damages, costs, losses, and/or liabilities arising out of Designer's non-compliance with the terms and provisions of this Notice.